NOTICE

The quality of this microform is heavily dependent upon the quality of the original thesis submitted for microfilming. Every effort has been made to ensure the highest quality of reproduction possible.

If pages are missing, contact the university which granted the degree.

Some pages may have indistinct print especially if the original pages were typed with a poor typewriter ribbon or if the university sent us an inferior photocopy.

Reproduction in full or in part of this microform is governed by the Canadian Copyright Act, R.S.C. 1970, c. C-30, and subsequent amendments.

AVIS

La qualité de cette microforme dépend grandement de la qualité de la thèse soumise au microfilmage. Nous avons tout fait pour assurer une qualité supérieure de reproduction.

S'il manque des pages, veuillez communiquer avec l'université qui a conféré le grade.

La qualité d'impression de certaines pages peut laisser à désirer, surtout si les pages originales ont été dactylographiées à l'aide d'un ruban usé ou si l'université nous a fait parvenir une photocopie de qualité inférieure.

La reproduction, même partielle, de cette microforme est soumise à la Loi canadienne sur le droit d'auteur, SRC 1970, c. C-30, et ses amendements subséquents.

Comparison of Flux Line Cutting Behaviour in High T_c and Conventional Type II Superconductors

Thesis submitted to the School of Graduate Studies and Research
of the University of Ottawa in partial fulfilment
of the requirements for the degree
of Master of Science in Physics

Germain Gandolfini
Department of Physics, University of Ottawa
Ottawa, Ontario, Canada

NOTICE

The quality of this microform is heavily dependent upon the quality of the original thesis submitted for microfilming. Every effort has been made to ensure the highest quality of reproduction possible.

If pages are missing, contact the university which granted the degree.

Some pages may have indistinct print especially if the original pages were typed with a poor typewriter ribbon or if the university sent us an inferior photocopy.

Reproduction in full or in part of this microform is governed by the Canadian Copyright Act, R.S.C. 1970, c. C-30, and subsequent amendments.

AVIS

La qualité de cette microforme dépend grandement de la qualité de la thèse soumise au microfilmage. Nous avons tout fait pour assurer une qualité supérieure de reproduction.

S'il manque des pages, veuillez communiquer avec l'université qui a conféré le grade.

La qualité d'impression de certaines pages peut laisser à désirer, surtout si les pages originales ont été dactylographiées à l'aide d'un ruban usé ou si l'université nous a fait parvenir une photocopie de qualité inférieure.

La reproduction, même partielle, de cette microforme est soumise à la Loi canadienne sur le droit d'auteur, SRC 1970, c. C-30, et ses amendements subséquents.

ISBN 0-315-60621-5

UNIVERSITÉ D'OTTAWA
UNIVERSITY OF OTTAWA

ABSTRACT

The magnetic behaviour (magnetization curves, Meissner effect, hysteresis losses, remanent flux and flux line cutting) for high T_c samples of Nd and $YBa_2Cu_3O_{7-x}$ at 77 K, semi-reversible $PbIn$ and hysteretic VTi at 4.2 K have been investigated and compared.

The magnetic behaviour of the high T_c samples and of the $PbIn$ are remarkably similar but contrasts dramatically with the phenomena observed in the VTi.

A hump structure appears in the low field region of the initial magnetization of the high T_c samples. This phenomenon occurs because the sintered samples consist of a compact agglomeration of small irregularly shaped grains which are electrically coupled before the hump structure but are isolated after this feature. We show that the appropriate calibration should be based on the diamagnetic response of the uncoupled grains.

A large ratio of $j_{c\parallel}$ to $j_{c\perp}$ (the critical current densities $\parallel$ and $\perp$ to the flux line density) accounts for the observations on the VTi in the flux cutting regime whereas $j_{c\parallel} \approx j_{c\perp}$ is indicated by the behaviour of the high T_c and $PbIn$ samples.

ACKNOWLEDGEMENTS

I would like to express my gratitude to Dr. Marcel A.R LeBlanc, my thesis director, for his excellent supervision, his keen interest and his encouragement in the accomplishment of this project.

I wish to thank my colleagues, Andrew Golebiowsky, John Sekerka and Richard Lalonde for the friendship, advice and assistance which they provided me during the experiments and computer calculations.

I would like to thank also the supporting staff of the Physics Department, in particular Bob Hart, Ronald Lavigueur and Herve Beaudoin for their contribution in manufacturing and assembling the set-up used in this project.

Finally, I want to dedicate this thesis to my wife, Silvana and my son, Gianmarco for their encouragement throughout this project.

Table of contents

List of tables

List of figures

Chapter 1

Introduction

1.1 General Introduction

After the discovery in 1911 by Heike Kamerlingh Onnes [51] that mercury loses its electrical resistivity when cooled below 4 K, superconductivity above 23 K was not observed until 1986. In spite of this limitation in temperature, superconductivity found application in various, although specialized fields, such as high energy accelerator laboratories and nuclear magnetic resonance imaging. The discovery by Bednorz and Muller[4] in 1986 of a ceramic oxide, $La_{2-x}Ba_xCuO_{4-y}$ with a transition temperature greater than 30 K opened the floodgates to discoveries of new superconductors. Shortly afterwards, Wu et al. [69] discovered a category of similar materials exemplified by $YBa_2Cu_3O_{7-x}$, all with $T_c \approx 93$ K. With these new high T_c materials , a much wider range of applications now becomes possible since these require cooling only to liquid nitrogen temperature (77 K). Driven by scientific curiosity, researchers throughout the World are now devoting considerable resources and time to the study of these ceramic compounds.

It is already well established that these new materials are type II superconductors. A magnetic field between a lower critical value H_{c1} and an upper critical field H_{c2} permeates the samples in the form of flux lines containing one quantum of flux, $\phi_o = h / 2e$. These discrete entities are also called fluxoids, fluxons, flux filaments and vortices. By contrast, the magnetic field exists in type I superconductors only in a thin surface layer called the London penetration depth and denoted λ.

Aside from their incredibly high transition temperatures, are these new materials fundamentally different in their other properties from the previously known type II superconductors ? The latter are now referred to as classical, conventional, standard or low T_c type II superconductors. Many workers have already addressed various aspects of this very broad question both experimentally and theoretically. In this thesis we examine a few features of this vast problem (Meissner effect, trapped flux, Clem valley, hysteresis loops). We also focus on the behaviour of these materials in the flux cutting regime. We investigate this phenomenon macroscopically in two high T_c materials at 77 K in some detail and compare our observations with that obtained under similar flux cutting conditions for two members of the family of low T_c materials at 4.2 K : a semi-reversible (PbIn) and a strongly hysteretic (VTi) specimen. It is not only very convenient and fascinating to study the behaviour of the high T_c materials at 77 K but the reduced temperature $t = T/T_c$ of these measurements is then comparable to that prevailing when the low T_c substances are investigated at 4.2 K. Until very recently, all known high T_c materials exhibited nearly ideal or semi-reversible magnetic behaviour at 77 K. Researchers[31] have now just discovered methods for producing high T_c materials which display appreciable hysteresis at 77K. An extension of our work to these specimens will be of considerable interest and is in progress in our laboratory.

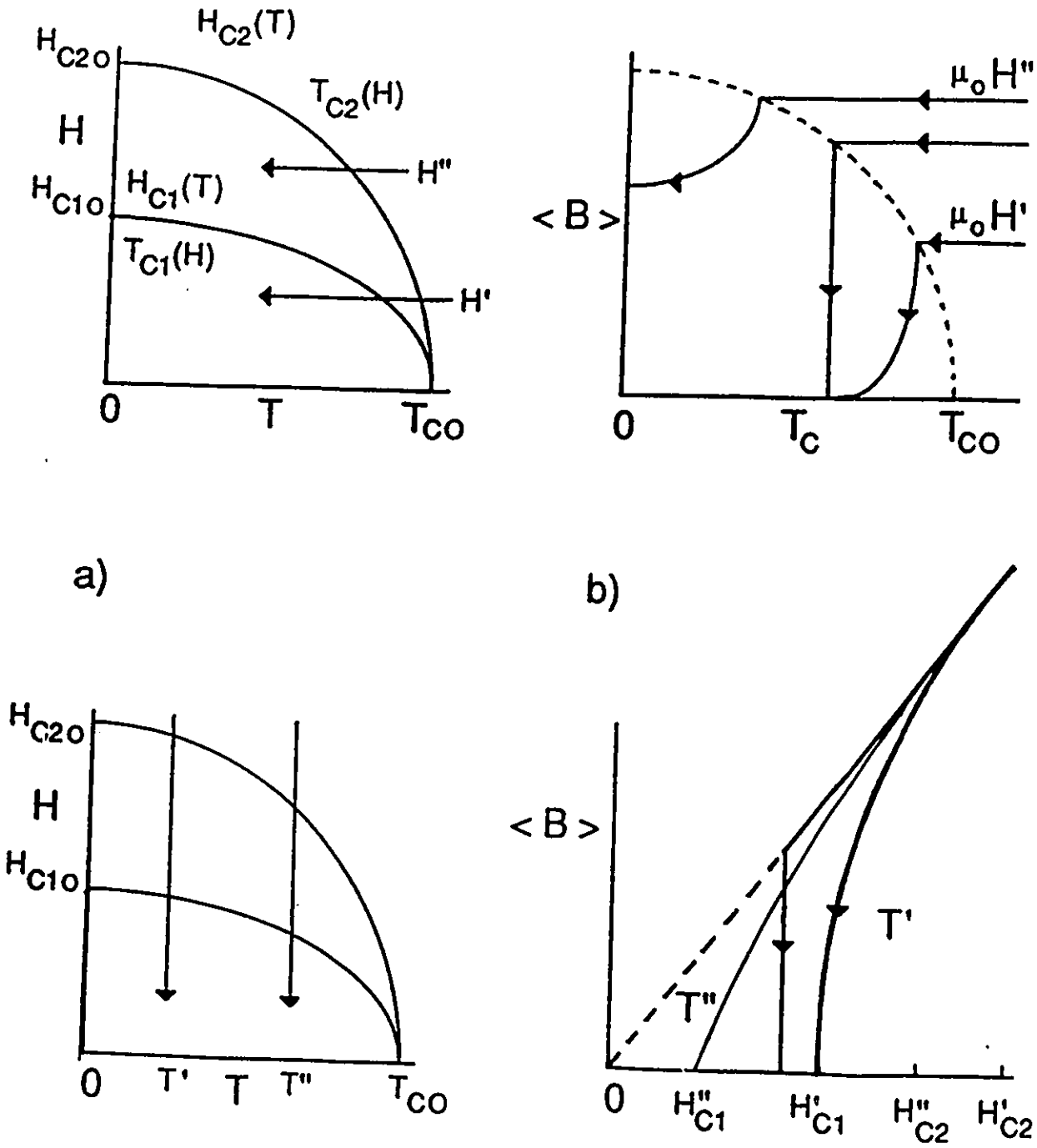

Figure 1: (a) and (c) display paths and phase boundaries in type II superconductors in the H-T plane. The corresponding evolution of $< B >$ versus T in constant H and of $< B >$ versus H at constant T are displayed in (b) and (d) where the behaviour in a type I superconductor is also presented for contrast.

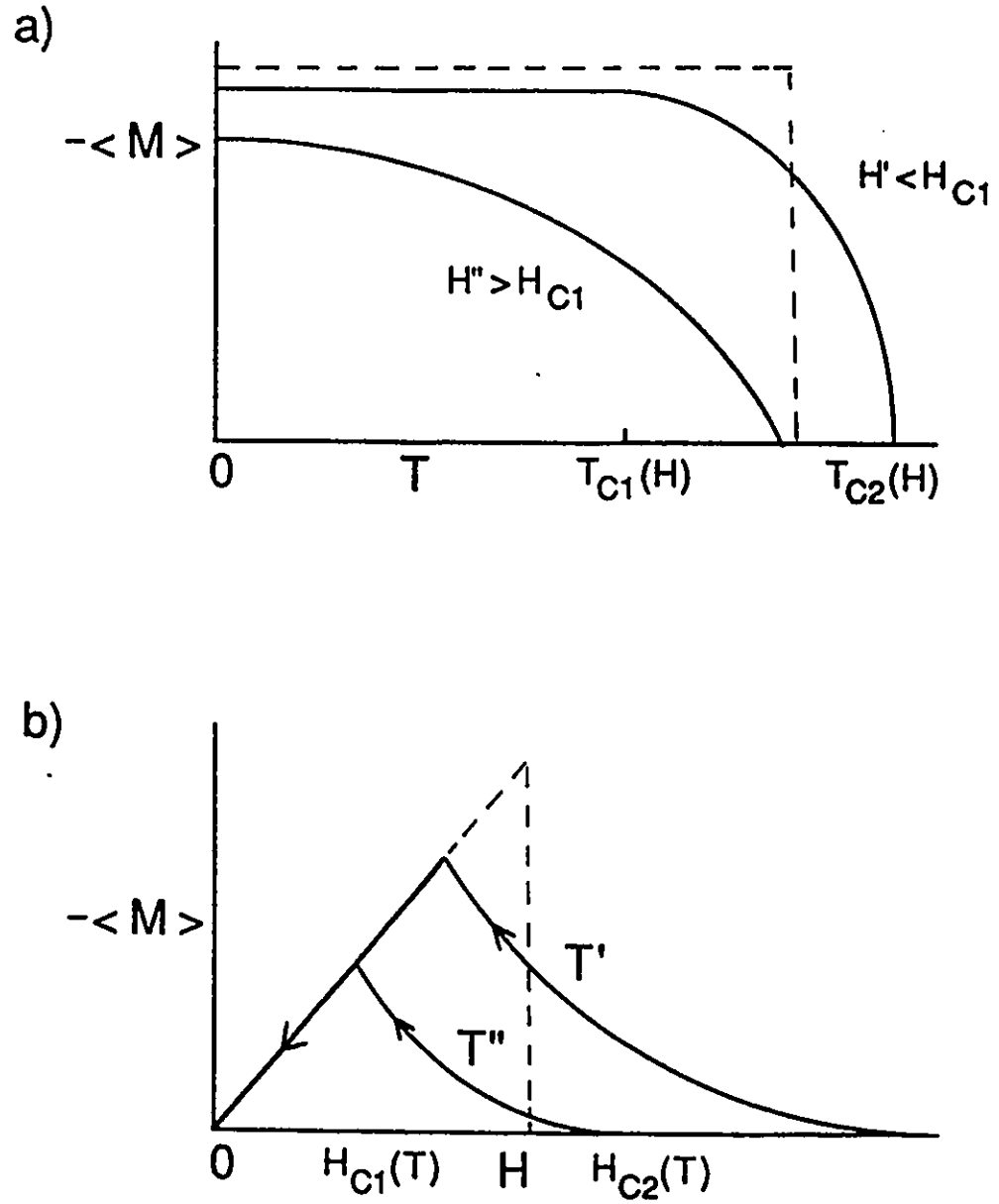

Figure 2: Complements Fig. 1 and displays the locus of the magnetization (magnetic moment per unit volume) versus T at constant H in (a) and versus H at constant T in (b). The dashed curves show the behaviour of a type I material for comparison.

1.2 Meissner Effect in Type II Superconductors

To set the background for our work, it is useful to review the Meissner effect [1], [49] in type II superconductors. Since this phenomenon is reversible, departures from this ideal behaviour provide a measure of irreversibility. Also, the ideal Meissner curve serves as a baseline or frame of reference for gauging the growth in pinning and other contributions to hysteresis.

The Meissner effect in type I and type II superconductors manifests itself in two different ways and we examine each of these modes in succession.

- Firstly, the Meissner effect consists in the expulsion of magnetic flux already permeating the specimen as its temperature is lowered from $T_c(H)$ in a constant applied magnetic field H. This is the better known aspect of the Meissner effect and is illustrated in Figs. 1 (a) and 1 (b). It is not generally appreciated, however, that even in the ideal type II superconductor, this expulsion is never an abrupt occurrence but is a monotonic function of $T_c - T$ regardless of whether H is chosen greater or less than $H_{c1}(T)$ (see Fig. 1(b)). This is in sharp contrast with the behaviour in ideal type I superconductors where the expulsion of flux is sudden and total as T traverses $T_c(H)$ in all fields $H < H_c$. This case is also sketched in Fig. 1 (b).

  In type II superconductors, two situations are encountered dependent on whether H is less or greater than $H_{c1}(T)$.

  1. When $H < H_{c1}(T)$, a gradual ejection of the magnetic flux proceeds as T is lowered from the $T_{c2}(H)$ phase transition curve to the $T_{c1}(H)$ boundary (see lowest curve in Fig. 1 (b)). When the latter boundary

is traversed, the magnetic flux has been completely eliminated from the specimen, i.e. B=0 (except in the penetration depth).

2. When $H_{c1}(T) < H < H_{c2}(T)$, the expulsion of flux is only partial and a considerable fraction of the flux will remain in the ideal specimen even when T reaches absolute zero (see upper curve in Fig. 1 (b)).

- Secondly, the signature of the Meissner effect is seen in the expulsion of magnetic flux from the superconductor as H is reduced with T kept fixed (isothermal case). We refer the reader to Figs. 1(c) and 1(d). Again, in a type I superconductor, the phenomenon here is very dramatic since the magnetic flux is suddenly and completely ejected from the sample when H traverses the $H_c(T)$ frontier (see vertical path in Fig. 1 (d)). This aspect of the Meissner effect in type II superconductors seems to be less well known, perhaps because here it is a somewhat more subtle phenomenon. Magnetic flux in all materials, be they normal conductors, semiconductors, insulators, paramagnets or ferromagnets, will diminish when H is decreased. The difference is that the Meissner effect in type II superconductors causes $< B >$ to **decrease more rapidly** than $\mu_o H$. This is not a spectacular behaviour except that it leads to $< B >= 0$ when H is still appreciable, i.e. $H = H_{c1}(T)$.

The variety of behaviour we have just described is sometimes more conveniently displayed and discussed in terms of the magnetic moment, or equivalently the magnetic moment per unit volume, i.e. the magnetization $< M >$ instead of the average magnetic flux density $< B >$. We recall that the relationship between these quantities can be written,

$$< B >= \mu_o H + \mu_o < M > \qquad (1)$$

when the demagnetization factor is negligible. μ_o is the permeability of free space and has the value $4\pi\ 10^{-7}$ in the S.I. system of units. Fig. 2(a) illustrates the evolution of $< M >$ versus T in fixed H and corresponds to Fig. 1(b). Note that $H' < H_{c1}(T)$ and $H'' > H_{c1}(T)$. Fig. 2(b) shows the variation of $< M >$ versus H descending and complements Fig. 1(d). In these plots, the diamagnetic response is frequently displayed in the first quadrant and we follow that convention.

Since the ideal type II superconductor is reversible, the locus of $< B >$ and of $< M >$ will simply retrace the paths shown in Figs. 1 and 2 if the temperature is now raised instead of lowered and H is made to increase after having been decreased or removed. In other words, the magnetic state of the specimen is entirely determined by the chosen values for H and T and is not affected by the prior variations of these variables (previous history) it has experienced. Thus a single and unique curve of $< M >$ versus H (or $< B >$ versus H) describes the macroscopic configuration of the magnetic flux density in the specimen and its magnetic response at a fixed final temperature. As we shall see later, the behaviour of nonideal, i.e. irreversible (hysteretic) type II superconductors is considerably more complicated. To fully characterize the latter we will need to measure $< M >$ versus H for a variety of paths in the H-T plane since the configurations of magnetic flux and persistent currents in the specimen are now not uniquely linked to H and T but will dramatically depend on the sequences followed in the changes of these variables.

To understand this more intricate behaviour it is useful to outline a qualitative picture of the interactions which are involved in establishing the reversible configurations (states) we have just sketched.

1.3 Basic Interactions and the Meissner Effect

The Meissner effect is a consequence of the interaction between flux vortices with each other and with an external magnetic field [1], [15]. We now explore these basic interactions and look at the Meissner effect in the perspective of these interactions.

The superposition of the magnetic flux densities $\vec{B}_1(r)$ and $\vec{B}_2(r)$ and of the circulating vortex current densities $\vec{j}_1(r)$ and $\vec{j}_2(r)$ of two neighbouring parallel flux lines augments the total magnetic and kinetic energies of the two isolated vortices by terms proportional to :

$$\int \vec{B}_1(r) \,.\, \vec{B}_2(r)\, dv \qquad \text{and} \qquad \int \vec{j}_1(r) \,.\, \vec{j}_2(r)\, dv \tag{2}$$

where the integrations extend over the volume of the specimen. Since these energies diminish as the separation of the flux lines increases, parallel flux lines repel each other. Consequently, in the absence of pinning and of an external magnetic field, flux lines initially threading a type II superconductor will expel each other from the specimen. Thus, the ideal (pinning free) type II superconductor traps no flux. Hence, the residual (remanent) magnetic moment is zero after an excursion of an externally applied field beyond H_{c1}.

An external magnetic field H tends to imprison flux lines inside a type II superconductor. This occurs because the interaction between the external magnetic field and the flux lines is one of mutual repulsion. This interaction can also be readily understood qualitatively. Let $B_M(r)$ denote the magnetic flux density in the penetration depth at the surface of the specimen and let $j_M(r)$ denote the Meissner current density associated with this flux penetration. The superposition of the magnetic flux and circulating vortex current densities of flux lines, $B_1(r)$, $B_2(r)$ etc and $j_1(r)$, $j_2(r)$ etc with $B_M(r)$ and $j_M(r)$ augments the total magnetic and kinetic

energies of the system by terms proportional to :

$$\int \vec{B_M}(r) \,.\, \vec{B_1}(r)\, dv \qquad \text{and} \qquad \int \vec{j_M}(r) \,.\, \vec{j_1}(r)\, dv \tag{3}$$

As a consequence of these energy terms, the applied magnetic field H is said to exert a " pressure " on the lattice of flux lines and tends to confine the latter inside the specimen. The compression of the flux line lattice away from the surface by the action of this " pressure " reduces the overlap energy represented by equation 3 but augments the superposition energy expressed by equation 2. When $H \leq H_{c1}$, the mutual repulsion of the flux lines dominates and overcomes the effort at confinement exerted by the external magnetic field. Equilibrium is reached when the flux lines have all expelled each other from the pinning free specimen, i.e. when $< B >= 0$ (perfect Meissner effect). Pinning, however, will assist H in imprisoning the flux lines in the material and in strong pinning materials, no flux expulsion will occur. These materials will then exhibit zero Meissner effect even when $H < H_{c1}$.

For the ideal (pinning free) specimen in an applied magnetic field in the range $H_{c1} < H < H_{c2}$, the equilibrium density of flux lines in the specimen is also determined by the balance between their mutual repulsion and the confining pressure exerted by H. This equilibrium is attained after a fraction of the flux permeating the sample in the normal state has been ejected. The fraction of flux lines which have to be expelled before equilibrium is reached diminishes as H approaches H_{c2}. Thus, the Meissner effect in the ideal, reversible specimen is always less than 100 % when $H > H_{c1}$ and diminishes monotonically to zero as H rises from H_{c1} to H_{c2}. When pinning is present, the Meissner effect is diminished from the ideal fraction and vanishes entirely in strong pinning samples.

1.4 Hysteresis in Type II Superconductors

Although magnetic irreversibility is not easily quantified and amenable to a rigorous definition, it is nevertheless a useful property for the classification of the vast spectrum of type II superconductors, whether classical or high T_c. In type II superconductors as in ferromagnetic substances, the magnetic flux density $< B >$ permeating the specimen is not a unique function of the externally applied magnetic field H. The physical basis for this phenomenon is, of course, very different in these two classes of substances. As a consequence of the dependence of $< B >$ on previous history, the locus of $< B >$ when H is made to undergo cyclical variations traces a curve in the $< B >$ versus H plane called a hysteresis loop. The area embraced by the hysteresis loop is a direct measure of the energy dissipated in the material per cycle. Consequently, measurements of hysteresis curves provide important data for eventual applications of type II superconductors.

In type II superconductors, the magnetic irreversibility arises from pinning of flux lines by various physical and chemical imperfections. These pinning sites impede the movement of the flux lines inside the superconductor. Consequently, they oppose the entry and penetration of magnetic flux into the specimen when H is increasing and oppose the outward migration and exit of the flux lines when H is decreased. As a result, the flux density $< B >$ in the material lags below the applied flux density $\mu_o H$ when H is rising and exceeds it when H is descending. The similarity of the $< B >$ versus H curves observed for strong pinning type II superconductors with that measured for ferromagnetic substances is indeed remarkable although the physics involved is very different.

Since in type II superconductors, the irreversibility (hysteresis) is a manifestation of pinning of flux lines, it can therefore serve as a measure of the pinning strength, i.e. of the density of the pinning sites or imperfections. Pinning is also intimately linked to the capacity of the material to support lossless persistent currents and hence a critical transport current I_c. We now outline the relationship between these various properties.

1.5 The Critical State Model

As we have seen, at equilibrium, a flux line in the interior of the pinning free material experiences no net force, being pushed equally in all directions by its neighbours. Here, interior means all of the volume beyond a few penetration depths λ from the surface. The sheets of flux lines adjacent to the surface also experience no net force, being repelled outwards by the flux lines in the interior but also by an equal but inwards force provided by the magnetic pressure exerted by the external magnetic field. In the event that the external magnetic field is now augmented, new flux lines are nucleated at the surface and penetrate the specimen until a new uniform equilibrium distribution is achieved. If, instead, the external field is lowered, thereby reducing the retaining magnetic pressure, flux lines migrate out of the sample until equilibrium is restored. We restrict our attention to rates of change such that viscous effects can be ignored and the adjustments in flux line density occur on a time scale that is negligible compared with that of the measurements.

To illustrate the effect of pinning on the scenario outlined above, we focus on several particular situations in succession. First, we consider that H is impressed from zero to a "virgin" specimen, i.e. a specimen containing no vortices, hence

one that has just cooled from T_c to T in $H = 0$. When H exceeds H_{c1}, flux lines begin to nucleate and penetrate the specimen. If the specimen were pinning free (ideal), these flux lines would distribute uniformly throughout its cross-section and we would monitor $< M >$ versus H displayed in Fig. 2(b). Pinning forces however will oppose the penetration and migration of the flux lines. Consequently, the flux line distribution is not uniform and a critical gradient is established in the profile of the flux density.

It is instructive to examine the forces acting on a single flux line (or on a sheet of flux lines) in such a nonuniform configuration. We ignore the effect of the magnetic pressure from the external H since we regard the army of invading flux lines as having already penetrated a distance of several λ's from the surface. Due to their mutual repulsion, each flux line experiences an inward (forward) push from the flux lines behind it and an outward (backward) push from the flux lines in front. A net force will arise however if the packing or concentration of flux lines varies along the path of advance, i.e. a flux line density gradient dB/dx develops. The net (repulsive) force acting on a stationary flux line which is on the threshold of being displaced is balanced by the maximum pinning force density, $F_p(B)$, furnished by the pinning sites. Any incremental advance by the army of flux lines requires that the pinning obstacles or impediments be surmounted over the entire volume occupied by the invading hordes of flux lines. Thus dB/dx must exist in a critical state over the entire space between the front and rear of the procession.

Alternatively and equivalently, the invasion of the flux lines can be viewed in the context of induced persistent currents. Over the range $0 < H < H_{c1}$, the Meissner screening current I_M restrains the entry of the applied magnetic induction to the penetration depth region. When H exceeds H_{c1}, the effective Meissner shielding

current is now diminishing in magnitude and can no longer protect the interior against penetration by the applied magnetic flux. Consequently, by Faraday's law of induction, $\epsilon = -d\phi_M / dt$, persistent currents must now be generated in the body or bulk of the specimen to oppose the entry of the magnetic flux ϕ_M. When the density j of such persistent currents exceeds a limit or ceiling, energy dissipation sets in. The induced current decays to the lossless critical value j_c. Concurrently, the induced emf ϵ with its associated electric field E diminish and disappear in accord with the Maxwell-Faraday equation :

$$\nabla \times \vec{E} = -\frac{\partial \vec{B}}{\partial t} \tag{4}$$

A configuration ensues where the profile of the magnetic flux density and the associated pattern of induced persistent currents are in a critical state. Thus the Maxwell-Ampere equation now reads :

$$\nabla \times \vec{B} = \mu_o \vec{j_c} \tag{5}$$

which simplifies to

$$\frac{dB}{dx} = \pm \mu_o j_c \tag{6}$$

for planar geometry where $\vec{B}$ is directed in the $y-z$ plane.

In isotropic materials, the induced electric field $\vec{E}$ and the critical current density $\vec{j_c}$ are orthogonal to the flux line density $\vec{B}$, hence are denoted $E_\perp$ and $j_{c\perp}$. The critical current density $j_{c\perp}$ is linked to the threshold force for depinning of flux lines and is attained when the Lorentz like driving force density,

$$\vec{F_L} = \vec{j} \times \vec{B} \tag{7}$$

surmounts the pinning force density $\vec{F_p}$.

The static critical state can therefore be written

$$\vec{j_c} \times \vec{B} + \vec{F_p} = 0 \tag{8}$$

As the increase of H proceeds beyond H_{c1}, the advancing flux front eventually reaches the center of the specimen (the midplane for a slab or the axis for a cylinder). The corresponding H is called the first full penetration field and denoted $H_\star$ in this thesis. $< M >_\star$, the magnitude of the magnetization at this juncture as well as $H_\star$ provide complementary data from which $< j_{c\perp} >$, the spatial average of the critical current density can be extracted. Methods and criteria for ascertaining that the flux front has fully penetrated the specimen, hence that $< M > = < M >_\star$ and $H = H_\star$ will be described below.

We now examine the sequences of configurations of magnetic flux density and the patterns of circulating persistent currents generated when the increase of H is interrupted and the direction of its swing is reversed.

Firstly, we note that Meissner current I_M is thermodynamically reversible i.e. its sense of circulation is entirely dictated by $\vec{H}$ and is independent of the previous history of $\vec{H}$, hence is not affected by $\mid d\vec{H}/dt \mid$ and whether $\mid \vec{H} \mid$ is being made to increase or decrease. Consequently I_M not only continues to circulate in a field shielding (diamagnetic) sense when H is being reduced, but rises in magnitude as H is decreased to H_{c1}. Subsequently when H falls below H_{c1}, I_M stays in step with H, diminishing as H diminishes in the range $0 \leq H \leq H_{c1}$. We stress that, when H is decreasing, $\vec{j_M}$, the density of the Meissner current, is directed opposite to the electric field $\vec{E}$ in the penetration depth. Thus, the kinetic energy $\int \vec{E}.\vec{j}\, dt$ given to the Cooper pairs by the electric field when H was impressed is now returned to the source when H is removed, thereby insuring reversibility.

The currents induced in the bulk however are associated with pinning forces,

hence are thermodynamically irreversible and dissipate energy. Their sense of circulation is entirely prescribed by the direction of the electric field as in normal metals. The crucial difference with normal metals is that these irreversible currents are lossless, hence persist, provided their density does not exceed $j_{c\perp}$.

We have now identified the three ingredients which govern the macroscopic magnetic behaviour of non ideal type II superconductors :

- The critical state concept that $j_\perp = j_{c\perp}$ wherever changes in magnetic flux density have been made to occur, hence electric fields have been generated.
- The laws of electromagnetic induction.
- The dependence of the magnitude of the diamagnetic Meissner current on H.

  In S.I. units, one can write,

$$I_M = < M >_{ideal} \tag{9}$$

  where I_M is the current per unit length of the surface along z and $< M >_{ideal}$ is the reversible $< M >$ versus H curve for the type II superconductor under scrutiny.

A careful application of these three prescriptions allows us to map out the vast spectrum of magnetization curves encountered in the study of real type II superconductors, be they classical or high T_c. We proceed to show this schematically.

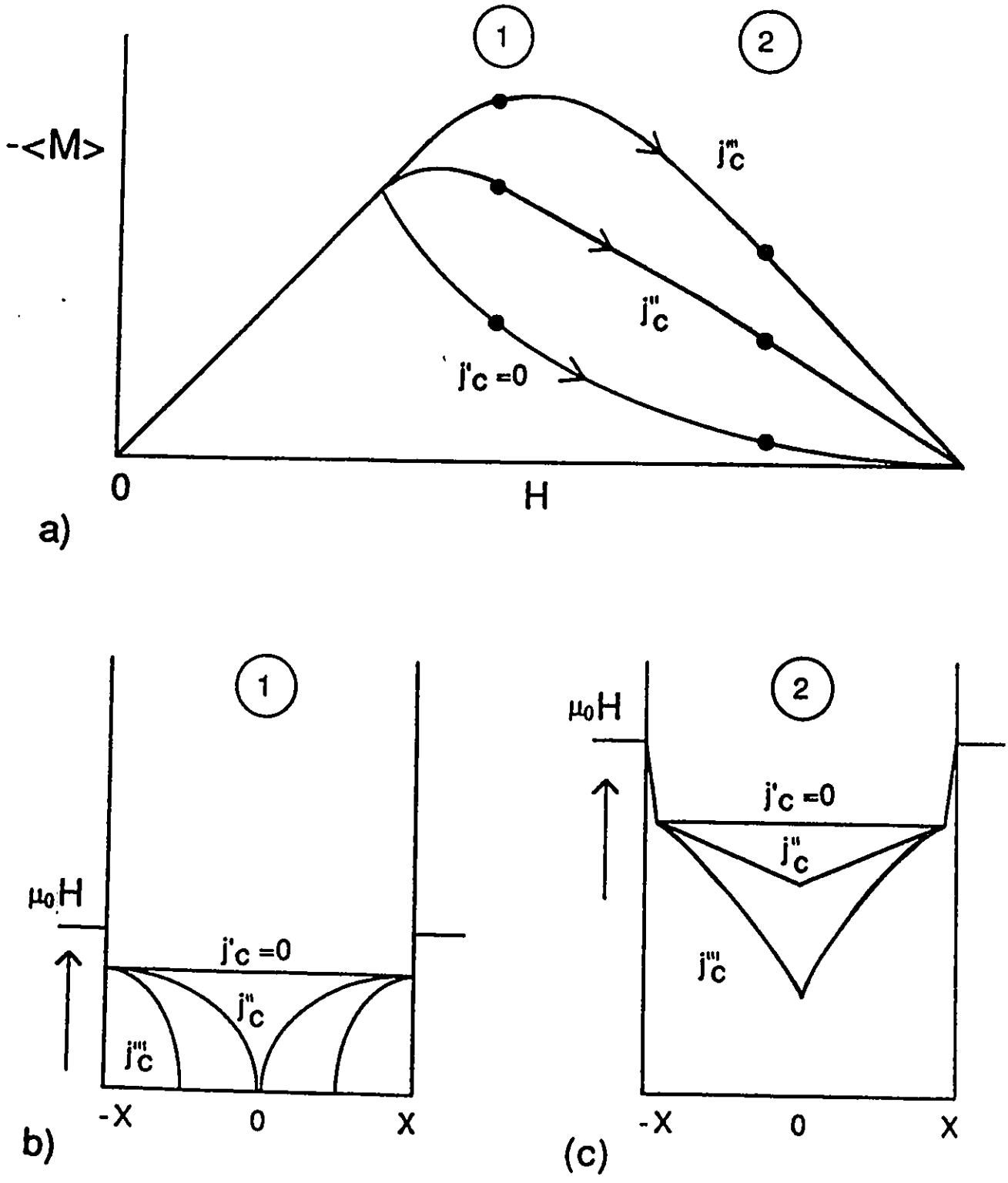

Figure 3: Compares the behaviour of $< M >$ vs. H increasing and the configurations of the B profiles for zero, weak and strong pinning (j_c', j_c'' and j_c''') in intermediate and strong fields.

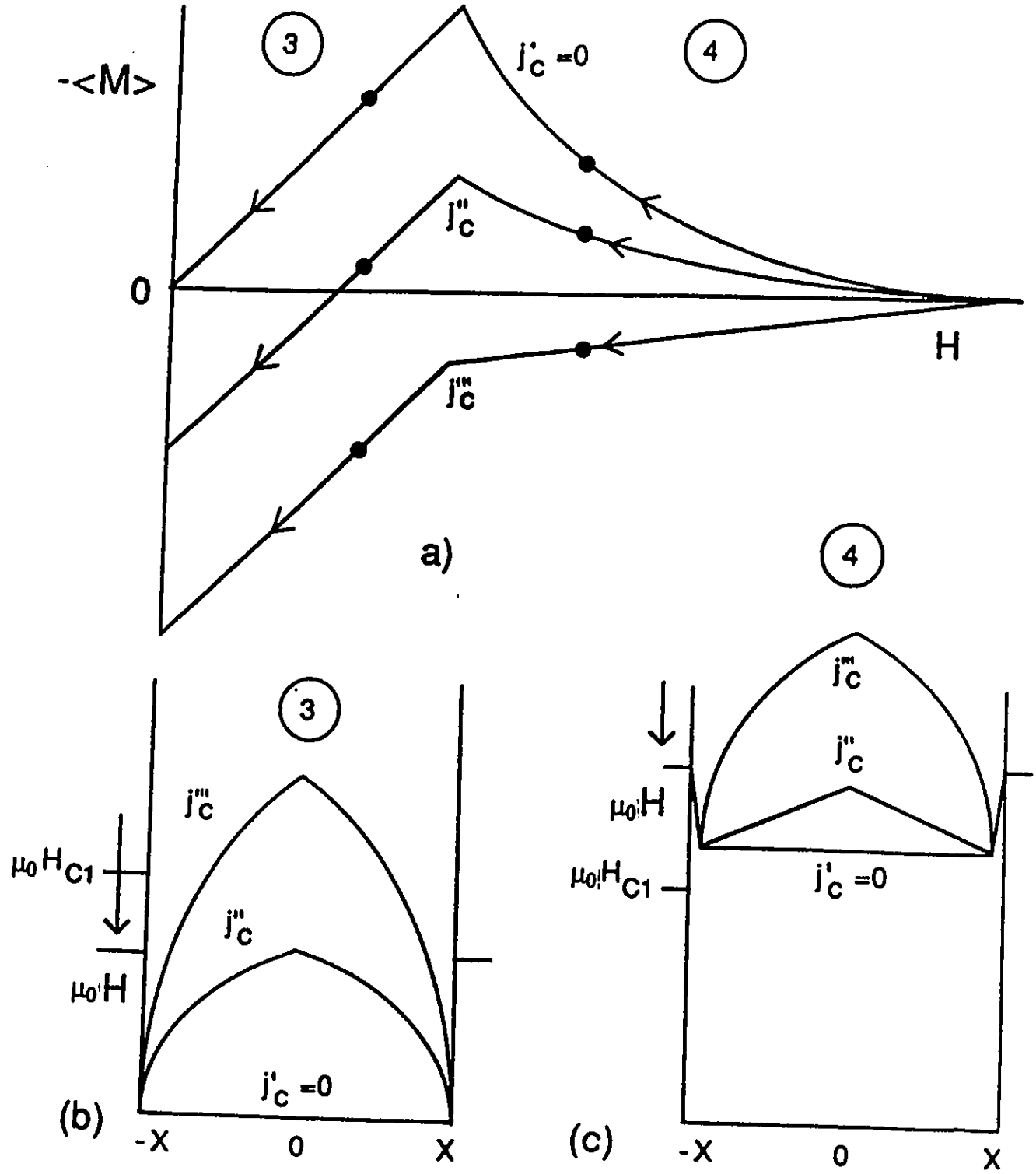

Figure 4: Complements Fig. 3. Compares the behaviour of $< M >$ vs. H decreasing and the configurations of the B profiles for zero, weak and strong pinning (j_c', j_c'' and j_c''') when H is below and above H_{c1}.

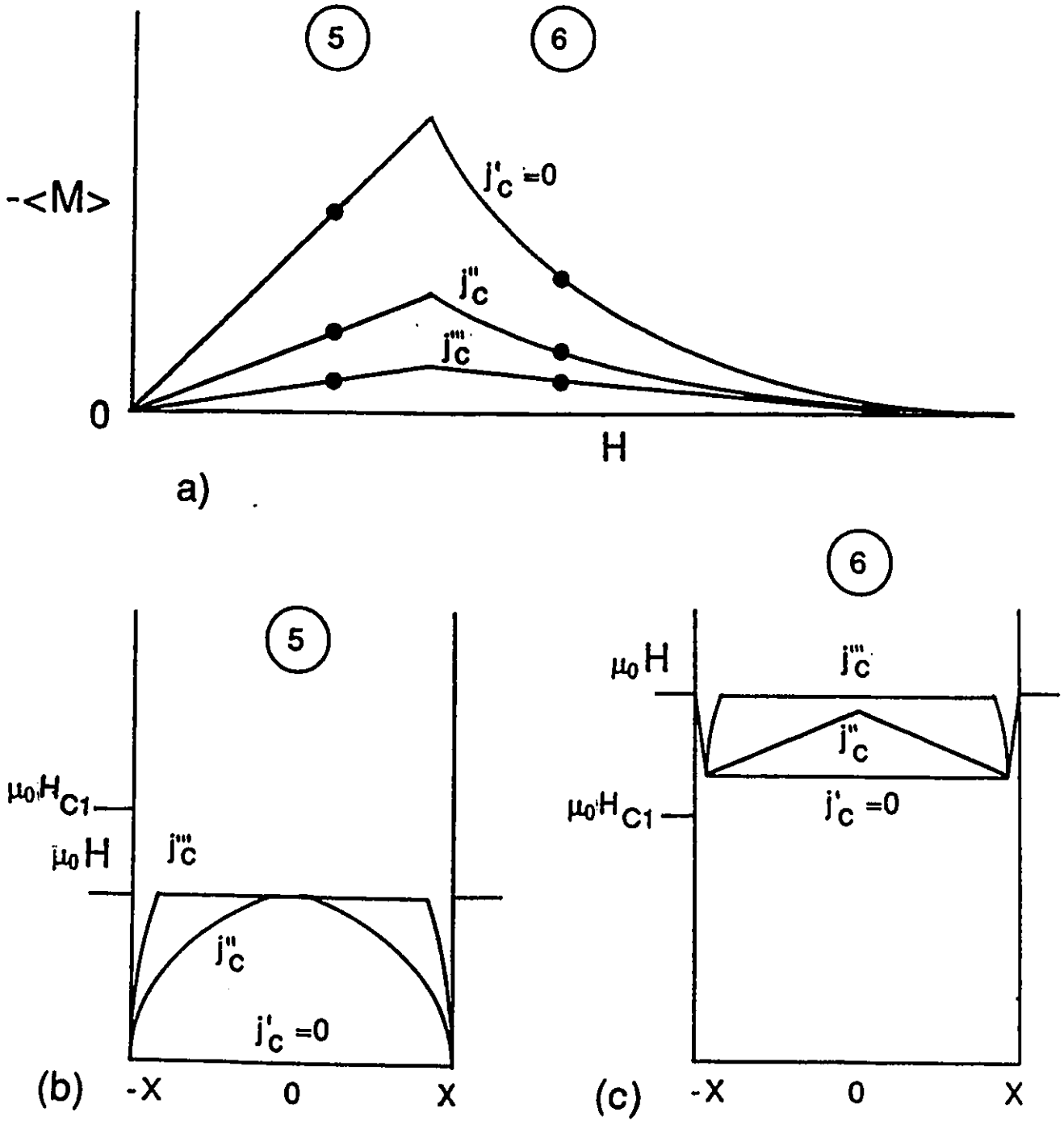

Figure 5: Complements Figs. 3 and 4. Compares the flux expulsion magnetization (Meissner effect) and the B profiles for zero, weak and strong pinning (j'_c, j''_c and j'''_c) when H is below and above H_{c1}.

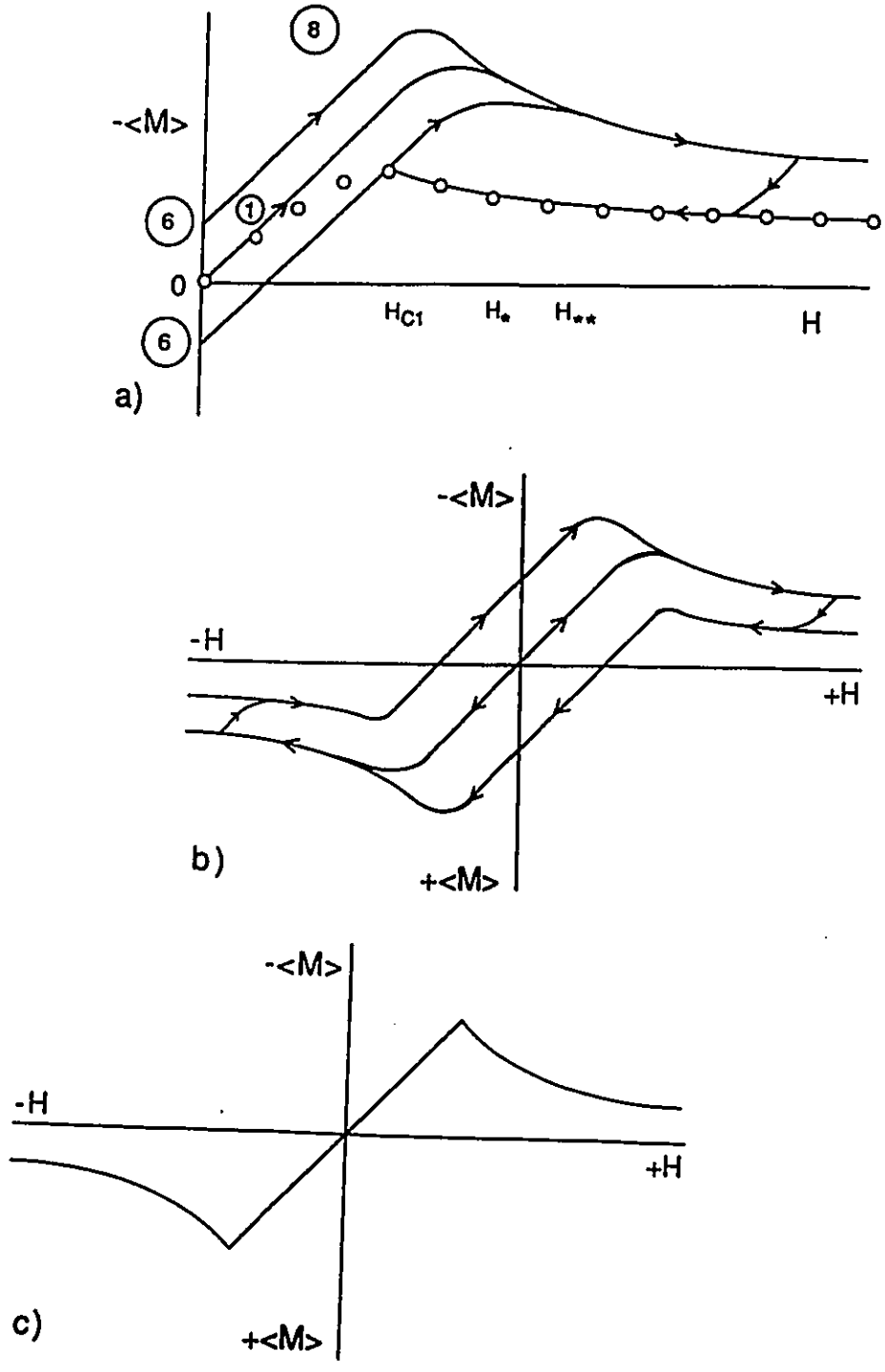

Figure 6: The curves of $< M >$ vs. H for the weak pinning material (j_c'') which are displayed in Figs. 3, 4 and 5 are now combined in (a). Those for the zero pinning material are shown in (c). We stress that a single unique curve ensues. (b) shows the same information as (a) but uses a 4 quadrant format.

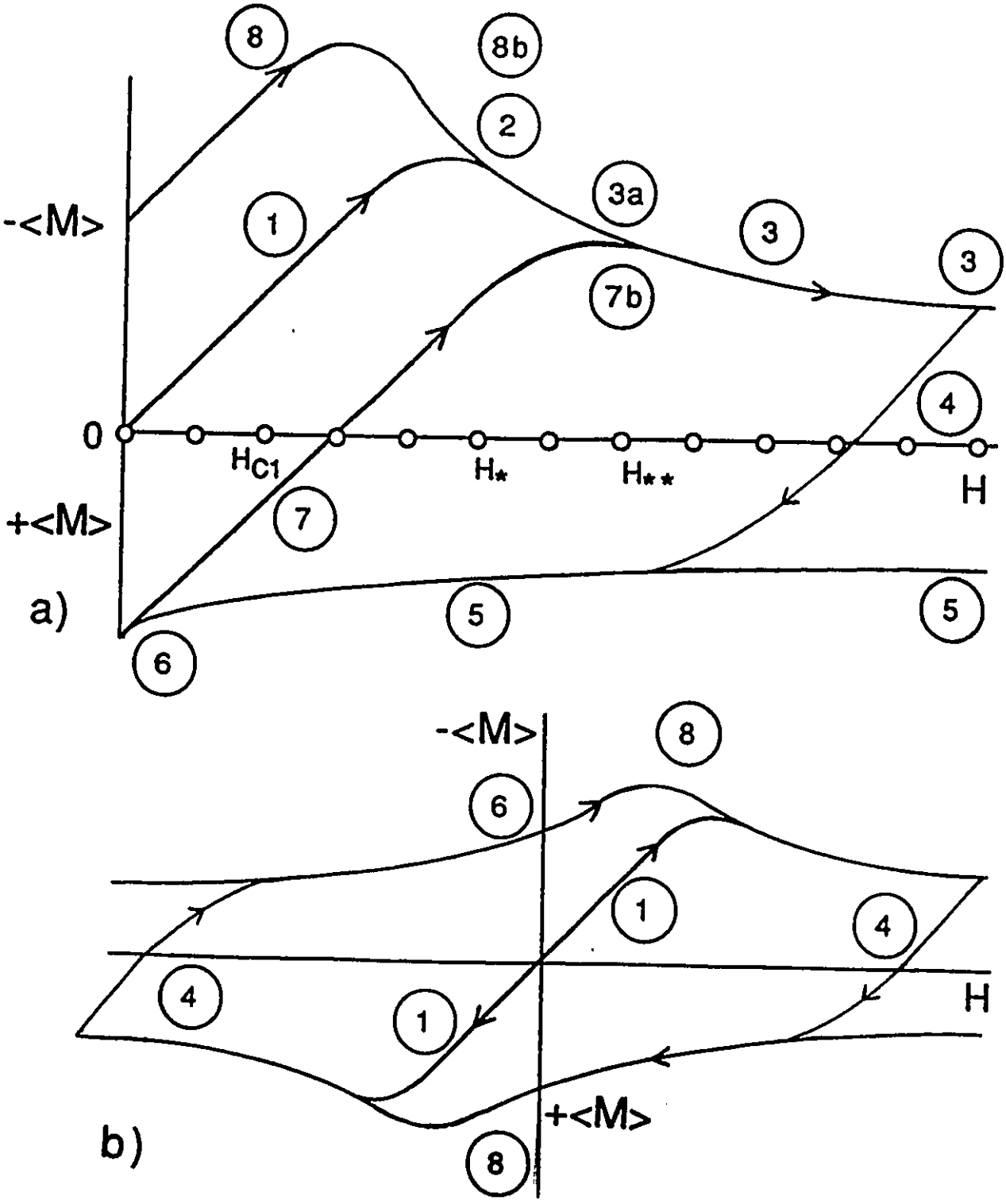

Figure 7: The curves of $< M >$ vs. H for the strong pinning material (j_c''') which are displayed in Figs. 3, 4 and 5 are now combined in (a). The numbers refer to the B profiles sketched in Fig. 8. Again (b) shows the same information as (a) but uses a 4 quadrant format.

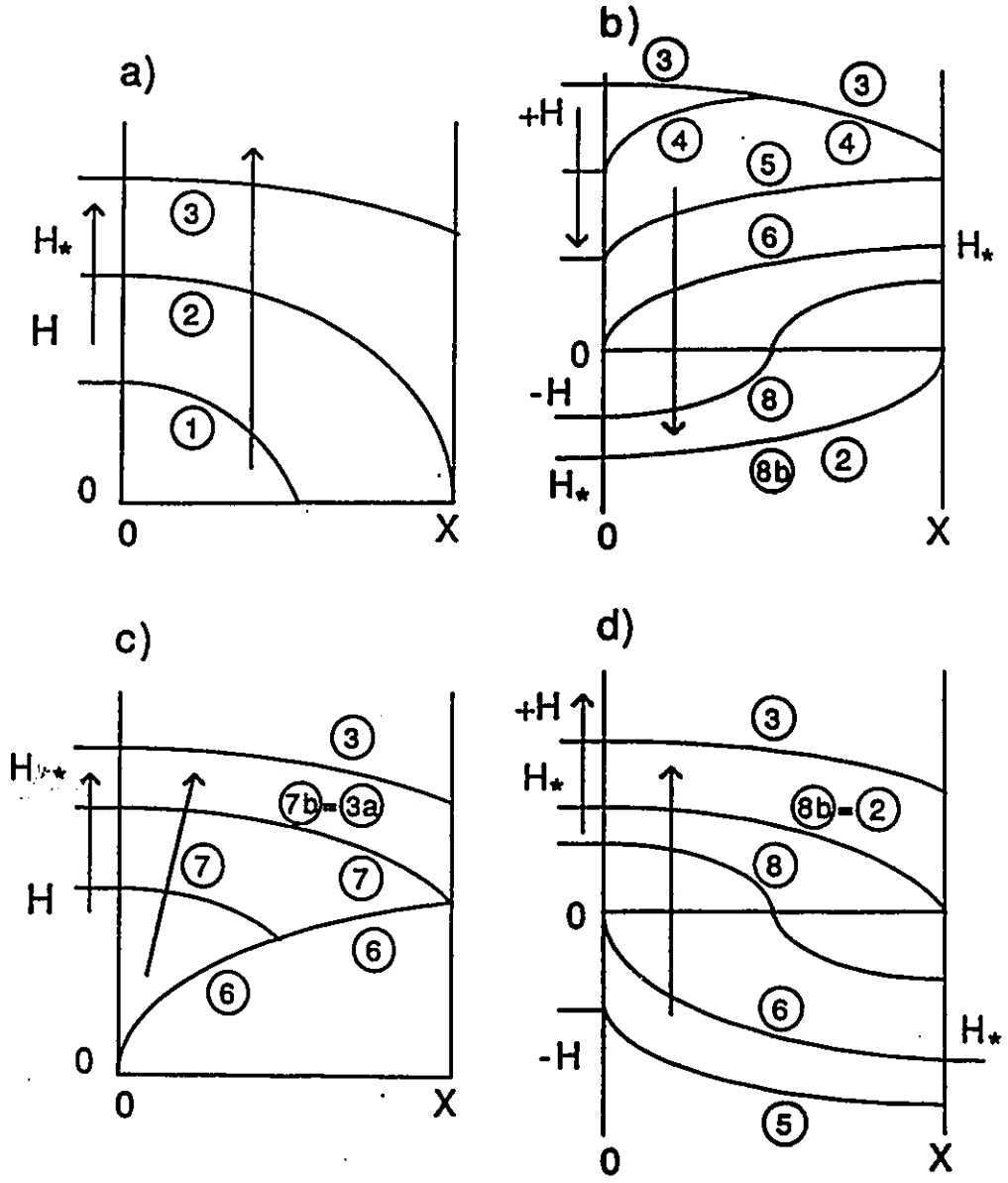

Figure 8: Sequences of B profiles for the following. In (a) H increases from zero with the specimen in the virgin. In (b) the upward swing of H has been stopped and H is now being reduced to zero and then continues to move in the opposite direction attaining H_*. In (c) a downward sweep of H is reversed at $H = 0$. In (d) H is moving from a large negative value through zero to a large positive value. The numbers refer to segments or points indicated in Figs. 6 and 7.

1.5.1 Effect of Pinning ($j_{c\perp}$) on Magnetization curves

We now apply the three rules listed above to illustrate how pinning, hence $j_{c\perp}$, modifies the ideal magnetic behaviour of type II superconductors and leads to a growth in irreversibility. In each of figs. 3, 4 and 5, we compare $< M >$ versus H for :

- a reversible material, i.e. no pinning, hence $j'_{c\perp} = 0$.
- a semi-reversible specimen, i.e. modest pinning, $j''_{c\perp} > 0$.
- a very irreversible sample, i.e. strong pinning, hence $j'''_{c\perp} \gg j''_{c\perp}$.

To avoid cluttering the displays, we dedicate a figure to each of the three major paths in the $H - T$ plane, namely where;

1. H is impressed from zero to the "virgin" specimen (Fig. 3). In the recent literature, this is labelled the zero-field cooled magnetization.
2. H is decreased from H_{c2} to zero (Fig. 4).
3. the sample cools from T_c to T in various static H (Fig. 5). Referred to as the field-cooled magnetization in the recent literature.

The numbers along the magnetization curves refer to the accompanying sketches which display the corresponding distributions of the magnetic flux density $B(x)$ (B profiles) across the specimen. To fix ideas and for convenience we view the specimen to be an infinite slab of thickness $2X$ where $\vec{H}$ is directed along the parallel surfaces in the $y - z$ plane.

The figures should be self-explanatory but a few comments are in order.

In Fig. 3, we chose H to correspond to H_* (full penetration field) for the situation where $j_c = j_c''$ in (b) in order to illustrate this particular case.

In Fig. 4, we note that $< M >$ versus H traces a " straight line " of slope -1 in the range $0 < H < H_{c1}$. This is often referred to as the perfect diamagnetic slope, although when $j_c \neq 0$ magnetic flux is trapped in the specimen. This idealized behaviour has never been encountered experimentally and, in practice, the slope in this region is always smaller than unity. This means that flux is "leaking" out of the specimen as H is lowered from H_{c1} to 0, whereas all existing models envisage no flux leakage in this range. The reason for this discrepancy continues to elude workers in this field. The magnetization associated with the magnetic flux trapped in the specimen when H reaches zero, in Fig. 4 is often referred to as the residual or remanent magnetization and the corresponding flux is called the residual or remanent flux. This quantity is very useful in estimating $j_{c\perp}$ in weak B.

The height of the plateaus in the profiles of Fig. 5 (b) are shown equal to the strength of the uniform applied magnetic induction when $j_c' \neq 0$ and the specimen became superconducting as it cooled through T_c in a static H. When there is no pinning ($j_{c\perp} = 0$), the expulsion of flux due to the mutual repulsion of the flux lines leads to a final uniform equilibrium distribution for $B(x)$ where $B(x) = 0$ when $H < H_{c1}$. For weak pinning, the mutual repulsion of the flux lines can succeed in expelling some flux from the entire specimen. Because of pinning, however, the flux density is nonuniform and a gradient arises in $B(x)$. Nevertheless, at the center of the specimen B is lower than $\mu_o H$. We note that the existence of this type of B profile reveals itself in the following way. The curve of $< M >$ versus H for H descending (see Fig. 4 (a)) overlaps in the range $H_{c1} < H < H_{c2}$ with the flux expulsion curve (see Fig. 5 (a)) over the corresponding range. We will see in the

next chapter that the high T_c materials exhibit such a region of overlap at 77 K. We must then conclude that $j_{c\perp}$ is not very large in these samples at that temperature. For strong pinning, the mutual repulsion succeeds in expelling flux lines only from the vicinity of the surface and the Meissner effect disappears in very strong pinning (highly irreversible or hysteretic) materials, regardless of whether H is above or below H_{c1}. In the recent literature, the Meissner flux expulsion magnetization is called the field-cooled-magnetization.

In order to get a "composite" picture of the behaviour for each category of specimen, we now transfer the three curves which display the behaviour for a weak pinning material in Figs. 3, 4, 5 to Fig. 6. Similarly we combine the three curves showing the response of a strong pinning sample in Fig. 7. Now the flux expulsion (Meissner effect or field-cooled) magnetization is displayed using data points. This makes it easier to identify and corresponds to the experimental situation since, here, one does not measure a continuous curve of $< M >$ versus H but rather we observe final values of $< M >$ for the chosen T in various fixed magnetic fields. Also, we have moved H_{c2} beyond the field of view in Figs. 6 and 7 in order to make room for other aspects of hysteretic behaviour which we now examine.

1.5.2 Hysteresis Loops

The uppermost and lowest curves in Figs. 6 and 7 are referred to as the envelopes of the magnetization curves. The envelopes are also called the upper and lower branches of the major symmetric hysteresis loop. These extreme or boundary curves are also displayed in part (b) of the figures. The reader should note that all of the information exhibited in four quadrants in parts (b) of Figs. 6 and 7 can be displayed using only two quadrants as in parts (a) of these figures. For economy

of space we will generally use the latter format in the remainder of this thesis. The four quadrant representation is useful pedagogically since it helps the reader to understand the origin and meaning of the segment of the envelope numbered (8) in Figs. 6 and 7. Also the four quadrant scheme makes clear the equivalence of the magnetic moments labelled (6) in these two figures. The locus of $< M >$ along segment (8) is traced when H is reduced from a large value of arbitrary polarity through zero and then raised with the polarity now reversed. Since the polarity of H is arbitrary and relative, it is evident that the upper and lower branches (envelopes) of hysteresis loops in a four quadrant representation are identical and equivalent. In other words, quadrant 3 repeats quadrant 1 and similarly quadrant 4 repeats 2. Consequently, there is redundancy of information in a four quadrant format which can be eliminated by retaining the first and fourth quadrants only.

The important feature of the magnetic moments on the envelopes is that here the entire specimen is filled with persistent currents which all circulate in one sense only (say clockwise) along the upper branch and in the opposite direction (counterclockwise) for the lower branch (envelope). As a consequence, the magnitude of the magnetic moment or magnetization along the envelopes can readily be exploited to extract information on $< j_{c\perp} >$ versus $< B >$ for the specimen under study. We will pursue this crucial aspect further in this thesis. In Fig. 8, we display a variety of sequences of configurations of B profiles corresponding to various segments of the envelope of the magnetization curves. The numbers along the B profiles indicate the corresponding segment of the locus of $< M >$ versus H along the envelopes. For economy of space in Fig. 8, we present only one half of the infinite slab since the configuration of $B(x)$ in the other half is the mirror image. We note that here the surface is situated at $x = 0$ and the midplane at

$x = X$. Also to avoid cluttering the sketches, we do not show the " discontinuity " in magnetic field at the surface caused by the Meissner current I_M.

Any magnetic moment which lies inside the boundaries of the envelopes can be generated by a suitable choice of path in the $H - T$ plane. Indeed, for a given hysteretic specimen, an infinite variety of configurations of persistent currents and associated flux density distribution can correspond to any chosen magnetic moment in the $< M > - H$ space. For these magnetic moments, the specimen may contain regions where no persistent currents are flowing. This is the case, for instance, along the initial magnetization curve, labelled (1) in Figs. 6 and 7. Alternatively, the specimen will contain a region where the current is circulating clockwise surrounded by a region where the persistent current is flowing in the opposite sense (counterclockwise). This is the situation which prevails along the curves labelled (4) and (7) in Fig. 7. As noted above, the maximum or limiting symmetric hysteresis loops stretches between + and $-H_{c2}$. Since this value can be extremely large for many type II superconductors it may not be feasible to trace the entire loop and the researcher must be content with a more limited range. Even if H_{c2} is accessible with the source of magnetic field available in the laboratory, it is not necessary to trace out the entire symmetric hysteresis loop to obtain a complete set for the upper and lower envelopes. Indeed this can be accomplished by mapping out a hysteresis loop which spans the range between $+H_{c2}$ and $-H_{**}$ or equivalently between $-H_{c2}$ and $+H_{**}$. The configuration of magnetic flux corresponding to H_{**}, after increasing H from zero, is displayed in Fig. 8(c). The value of H_{**} can be established experimentally using two different procedures;

1. By determining H where the curve labelled (8) in Fig. 7 merges with the curve labelled (7).

2. By measuring the swing of H, starting from zero, which induces the maximum amount of trapped flux in the virgin specimen.

The essential reason for taking H_{**} as a lower boundary for the hysteresis loop is to ensure that point (6), the starting point of segment (8) in Figs. 6 and 7, constitutes a maximum residual magnetization, hence a configuration where the sample is entirely filled with persistent currents circulating in a flux retaining sense. This sense of circulation is also frequently referred to as paramagnetic.

Quite generally, for cylindrical or rectangular rods of infinite length in a uniform applied magnetic field $\vec{H}$ directed along the length of the sample, we can write

$$H_{**} = I_{M**} + I_{b*} + I_{b**} \tag{10}$$

where I_{M**}, I_{b*} and I_{b**} denote absolute values. Equation 10 follows directly from integrating Maxwell's equation, $dH_z/dx = j_{c\perp}$. Hence,

$$I_{b*} = < j_{c\perp} >_* X = < j_{c\perp} >_* R \tag{11}$$

$$I_{b**} = < j_{c\perp} >_{**} X = < j_{c\perp} >_{**} R \tag{12}$$

where X is the half thickness of a rectangular rod whose width $Y > 2X$ and R is the radius of the cylinder. Here, by definition

$$< j_{c\perp} > = \frac{1}{X} \int_0^X j_{c\perp}\, dx = \frac{1}{R} \int_0^R j_{c\perp}\, dr \tag{13}$$

Thus $< j_{c\perp} >_*$ is the average $j_{c\perp}$ when $H = H_*$ and the specimen is entirely in a flux screening configuration. These same conditions apply for $< j_{c\perp} >_{**}$ except that now $H = H_{**}$.

It is remarkable that the width $Y \gg 2X$ of the infinite rectangular rod plays no role in these expressions. Consequently equation (10) applies also to a slab of infinite width Y. This interesting and novel result is developed in appendix A.

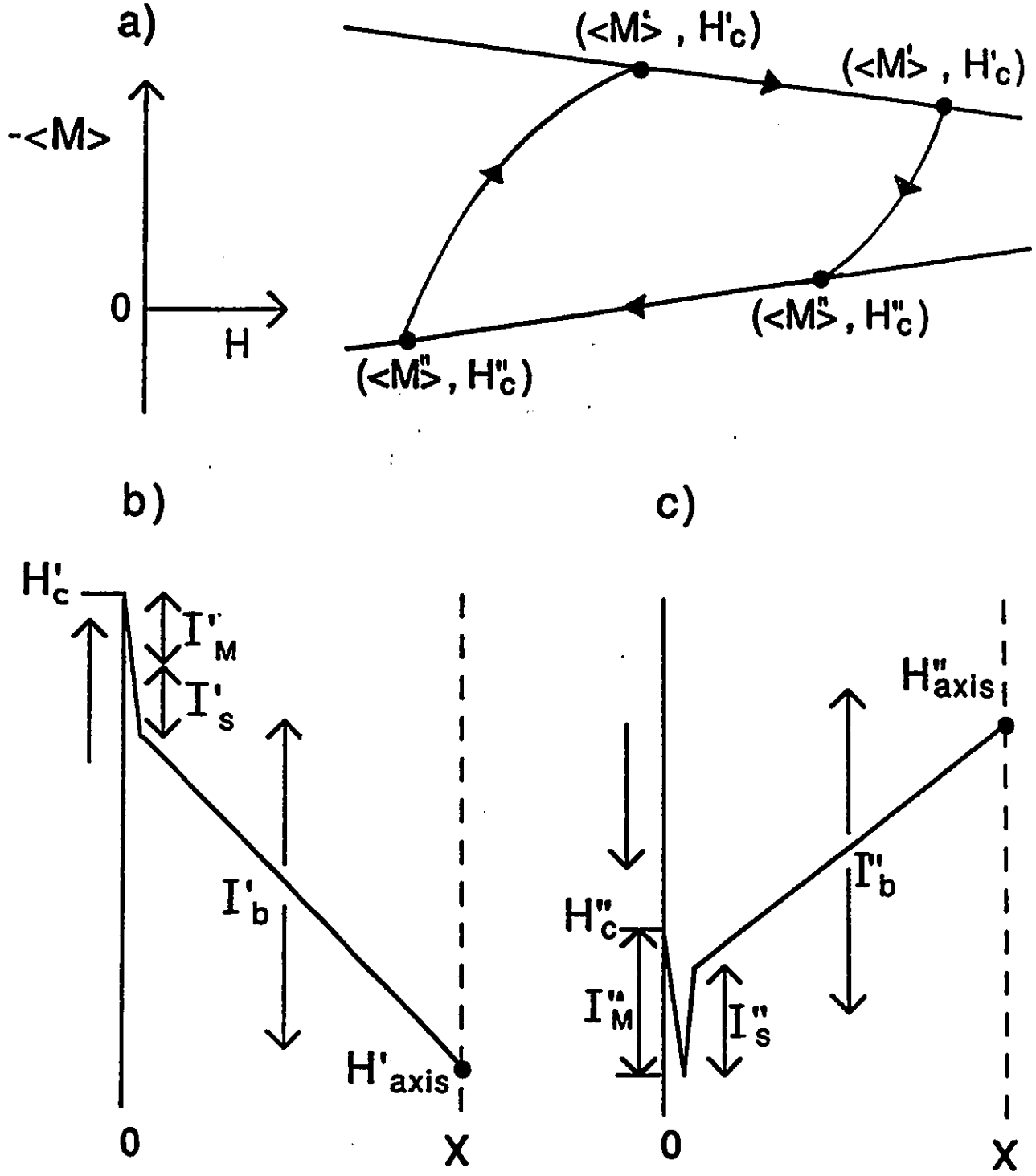

Figure 9: (a) Sketch of two traversals between the upper and lower envelopes (branches) of the major hysteresis loop. (b) B profile when H increasing attains H_c' thereby causing $< M >$ to reach the upper envelope. (c) B profile when H decreasing attains H_c'' thereby causing $< M >$ to reach the lower envelope. I_M, I_s and I_b denote the Meissner, irreversible surface and bulk currents.

1.5.3 Bridges between Branches (ΔH_c)

The curves numbered 4 and 7 in Fig. 7 show the locus of $< M >$ versus H when the sweep of H is interrupted and the direction of its swing is reversed. As we will see later in this thesis, a detailed examination of these traversals from one branch of the major hysteresis loop to the other provides information on the existence and magnitude of surface barriers to flux entry and exit in type II superconductors.

Further,

$$\Delta H_c = \mid H_c^{'} - H_c^{''} \mid \tag{14}$$

The range over which H must be varied in order that the locus of $< M >$ migrate from one branch or envelope, yields data on $< j_{c\perp} >$ for the corresponding average range of H, namely

$$H_{av} = \frac{\mid H_c^{''} \mid + \mid H_c^{'} \mid}{2} \tag{15}$$

Here $H_c^{'}$ and $H_c^{''}$ indicate the magnetic field at the upper and lower boundaries of the traversal or bridge between the envelopes. To avoid various complications, we take $H_c^{'}$ and $H_c^{''}$ to have the same polarity and to exceed H_{c1}.

Quite generally, for the geometries mentioned above, Maxwell's equation, $\nabla \times \vec{H} = \vec{j}$ and the critical state condition that $\vec{j} = \vec{j_{c\perp}}$, after stepwise integration and summation lead to,

$$H_{axis}^{'} = H_c^{'} - I_M^{'} - I_s^{'} - I_b^{'} \tag{16}$$

$$H_{axis}^{''} = H_c^{''} - I_M^{''} + I_s^{''} + I_b^{''} \tag{17}$$

where all the symbols represent absolute quantities. We refer the reader to Fig. 9 for aid in understanding these several terms which we now describe. $I_M^{'}$ and $I_M^{''}$ are the Meissner currents (per unit length along $\vec{H}$) in equilibrium with $H^{'}$ and $H^{''}$

respectively. I_s'' is a surface barrier (thermodynamically irreversible critical surface current) opposing flux exit and I_s' is a surface barrier opposing flux entry. I_b'' and I_b' are flux retaining (paramagnetic) and flux screening (diamagnetic) critical currents circulating in the bulk (volume) of the specimen. Equations similar to 11, 12 and 13 formally define I_b' and I_b''. We stress that the sense of circulation (diamagnetic or paramagnetic) and the ambient magnetic field should be specified in identifying critical bulk and surface persistent currents in hysteretic type II superconductors. H'_{axis} and H''_{axis} denote the magnetic field intensity at the center of the specimen. Equations 16 and 17 are valid along the upper and lower branches of hysteresis curves respectively for the infinite slab, infinite rectangular rod and infinite cylinder where $\vec{H}$ is uniform and directed along the infinite dimension. Also we stress that, (i) H', H'' and H'_{axis} must have the same sign and (ii) $H' > H_{c1}$, in order that these expressions be applicable.

According to critical state ideas, at the threshold of the completion of a traversal from one branch of the major hysteresis loop to the other, (see Figs. 7 and 9 (a)), the condition,

$$H''_{axis} = H'_{axis} \tag{18}$$

prevails. Introducing this condition into equations 16 and 17 and combining yields,

$$\Delta H_c = \mid H'_c - H''_c \mid = (I'_b + I''_b) + (I'_s + I''_s) + (I'_M - I''_M) \tag{19}$$

where $H'' = H''_c$ and $H' = H'_c$ indicate a set of limits to a traversal or bridge.

Equation 19 contains so many quantities that its usefulness is not evident. It is therefore worthwhile to examine the three bracketed terms separately. For samples with dimensions large compared with λ, the initial linear portion of a traversal between the envelopes has a slope $d < M > /dH = -1$ since the flux screening or flux trapping arises from surface currents. The sweep of ΔH occupied by this linear

segment yields ($I_s'' + I_s'$). By exploiting lock-in A.C. techniques this quantity can be determined with great precision. We will see later in this thesis that our high T_c samples display no such region, hence possess no significant surface barriers when $H \geq H_{c1}$.

Generally, when ΔH_c is small compared to H_{c2} but appreciable relative to H_{c1}, the Meissner current I_M is slowly varying with H. Consequently $I_M'' \approx I_M'$ and the difference ($I_M' - I_M''$) is negligible and can be ignored. Consequently, measurements of ΔH_c yield good estimates of ($I_b'' + I_b'$). This combination is of particular interest since it corresponds to the total lossless transport current which the bulk of the specimen can support in the corresponding average H.

In all of the pertinent literature we have surveyed, the information which this important quantity (ΔH_c) contains has been ignored. Indeed, the need and the usefulness of measuring (ΔH_c) has been overlooked. Workers have focused instead on the determination of the magnitudes of the envelopes of the major hysteresis curves for their specimens. This is a useful and important exercise since the envelopes also contain information on I_b, I_M and I_s provided that the calibration of $< M >$ versus H is valid, reliable and appropriate. Thus the major hysteresis curves (the envelopes) and the compilation of ΔH_c versus H_{av} complement each other. We will develop this complementary aspect in some detail in this thesis.

In much of the recent literature on high T_c materials, the measurements of ΔH_c are frequently inconsistent with the observations reported for the magnitudes of $< M >$ versus H for the envelopes. This inconsistency appears in every instance not to have been noticed by the authors. A major purpose of our investigation has been to address this discrepancy, examine the reasons for its occurrence and propose a possible resolution of this problem.

Before proceeding further on this vital topic we wish to complete our discussion of another feature of Fig. 7 which sets the framework for another part of our work. We wish to draw the attention of the reader to a special situation which occurs when a traversal between the envelopes commences at $H' = 0$ (see the path labeled (8) in Fig. 7 and the corresponding sequence of B profiles in Fig. 8 (d)). The reader will note that the initial magnetization curve (labeled (1)) merges with path (8) at a point designated (2). The configuration of the flux density at this juncture leads to the expression;

$$H_\star = I_{M\star} + I_{b\star} \tag{20}$$

We note that $I_{b\star}$ also appears in the expression (eqn 10) for $H_{\star\star} = I_{M\star\star} + I_{b\star} + I_{b\star\star}$, another readily measured quantity. In strongly hysteretic samples, $I_{b\star}$ dominates $I_{M\star}$, hence, eqn 20 simplifies to,

$$H_\star \approx I_{b\star} \tag{21}$$

Similarly $(I_{b\star} + I_{b\star\star})$ dominates $I_{M\star\star}$, hence, eqn 10 simplifies to,

$$H_{\star\star} \approx I_{b\star} + I_{b\star\star} \tag{22}$$

Consequently, measurements of $H_\star$ and $H_{\star\star}$ readily yield good estimates for $I_{b\star}$ and $I_{b\star\star}$.

Further we note that measurements of the residual (remanent) magnetic moment also contain information on $j_{c\perp}$ over the range $0 < H < H_\star$ (see the profiles numbered 6 in Figs. 8 (b) and (c)), hence these measurements, relate to $I_{b\star}$.

These various quantities and their relationships will be seen to play important roles in our efforts to resolve the major inconsistency mentioned above and achieve a reliable and appropriate calibration of magnetization envelopes in high T_c superconductors.

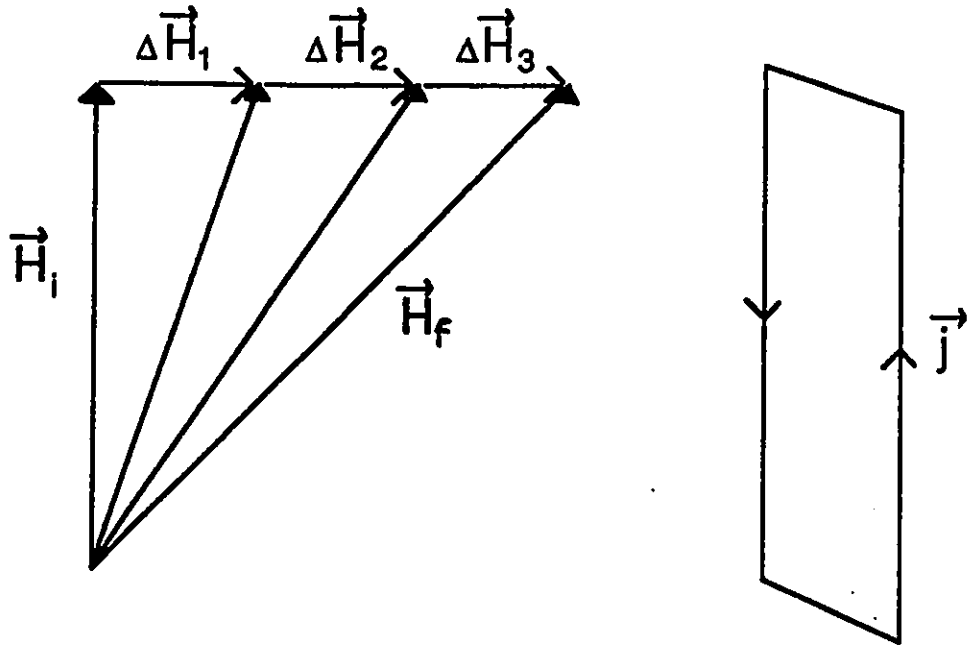

Figure 10: Shows schematically that varying $\vec{H}$ from $\vec{H}_i$ to $\vec{H}_f$ by increments $\Delta\vec{H}$ orthogonal to $\vec{H}_i$ induces a current to flow with a component parallel to $\vec{H}$.

1.6 Flux Cutting Regime

In the foregoing we have focused on situations where the net repulsive force acting on flux lines in type II superconductors is sufficiently strong to cause the lattice of flux lines to become unpinned and to migrate. Such a net repulsive force arises when the gradient of the flux line density exceeds a threshold value. By the Maxwell-Ampere equation $\nabla \times \vec{B} = \mu_o \vec{j}$ this entails that the current density surpasses a critical value $j_{c\perp}$ since it is the component of $\vec{j}$ flowing transverse to $\vec{B}$ which generates the flux density gradient. These situations are referred to as the flux transport, flux depinning or flux flow regimes. These cases are also sometimes denoted the collinear regime. The reason for the latter label is that experimentally, the migration, entry and exit of the flux is brought about by an increment $\Delta\vec{H}$ which is superimposed upon and collinear with the existing $\vec{H}$.

We now address the broader spectrum of situations where the increment $\Delta\vec{H}$ is not directed along the existing $\vec{H}$, hence are called the noncollinear regime. To fix ideas, we focus on a special case of the vast noncollinear landscape, namely where the series of increments $\Delta\vec{H}$ are directed orthogonal to the initial $\vec{H}$ denoted $\vec{H}_i$. This arrangement is straightforward to implement experimentally and also corresponds to situations of particular interest.

Consider a straight ribbon or wire immersed in a stationary magnetic field $\vec{H}_a$ directed along the length of the ribbon or axis of the wire. When a transport current I_{tr} is now made to flow along this ribbon or wire via leads attached to the ends and connected to a current source; the magnetic field H_I generated by the current I_{tr} will, by the right hand rule, be directed orthogonal to $\vec{H}_a$. Consequently I_{tr} flows with a component of its current density parallel to the resultant magnetic

field $\vec{H}_f = \vec{H}_a + \vec{H}_I$. It is frequently more convenient, however, to generate both $\Delta\vec{H}$ and $\vec{H}_a$ externally by an orthogonal pair of magnet coils. The latter technique has been exploited in our work.

By Faraday's law of induction, the persistent currents induced to circulate in an isotropic material by the application of $\Delta\vec{H}$ will flow with a component directed along the total

$$\vec{H}_f = \vec{H}_i + \sum \Delta\vec{H} \tag{23}$$

over most of the volume of the specimen as sketched in Fig. 10. By the laws of electromagnetism, the presence of such a current flowing along the flux lines means that the direction or orientation of the flux lines must vary with depth in the material. For planar geometry, the Maxwell-Ampere equation, $\nabla \times \vec{B} = \mu_o \vec{j}$, now reads,

$$\frac{dB}{dx} = -\mu_o j_\perp \tag{24}$$

and

$$B \frac{d\alpha}{dx} = \mu_o j_\parallel \tag{25}$$

where $\alpha(x)$ indicates the direction of the magnetic flux density in the $y-z$ plane and $j_\parallel$ denotes the component of $\vec{j}$ flowing parallel to $\vec{B}$.

We have seen that there is a ceiling on the current density $j_\perp$ which can flow, without energy loss, perpendicular to the flux line density. When $j_\perp$ exceeds a critical limit $j_{c\perp}$, the flux lines become unpinned, flux line migration takes place and energy dissipation occurs. Similarly, there exists a physical limit $j_{c\parallel}$ to the current density which can flow without loss hence before the onset of resistance parallel to the flux lines. In the framework of the Maxwell-Ampere equation, this signifies that there exists also a critical value, $(d\alpha/dx)_c$, for the spatial variation of the orientation of the flux lines (see equation 25).

Theoretical investigation of the basic interactions between flux lines reveals that as the angle $\Delta\alpha$ subtended by adjacent sheets of flux lines is augmented, their mutual repulsion diminishes monotonically and an attractive interaction sets in when a critical angle $\Delta\alpha_c$ is attained [12], [24]. This turn of events should not be surprising since it is well known that anti-parallel flux lines attract and will annihilate each other if unrestrained by pinning forces [15].

A major portion of this thesis is dedicated to our investigation of macroscopic behaviour encountered when a critical current density $j_{c\|}$, hence critical orientation gradients $(d\alpha/dx)_c$ are generated in type II superconductors. Such situations have been labeled the flux cutting regime [5] - [12], [15] - [26] , [50], [52] - [54], [64], [67], [68] for reasons which we will try to explain shortly.

We focused on the study of flux cutting phenomena in semi-reversible (weak pinning) type II superconductors. Our motivation here was twofold. Firstly, all high T_c materials known when our project was initiated and completed, exhibited semi-reversible behaviour at 77 K. Secondly, the flux cutting regime in classical semi-reversible type II superconductors was essentially unexplored when our research was launched.

Thus this part of our work has two objectives; (i) determine the response of high T_c materials and classical semi-reversible samples in the flux cutting regime and then (ii) compare these responses for similarities and differences. For completeness we also performed identical measurements on a highly irreversible (strong pinning) classical type II superconductor (VTi), although the flux cutting behaviour in this category of materials had already been extensively studied in our laboratory. Consequently we also present some of our observations on this material. These results illustrate that dramatic differences in flux cutting behaviour arise from changes

in the pinning strength, hence $j_{c\perp}$. The high T_c materials and the semi-reversible $PbIn$, however, show only minor differences in their responses.

1.6.1 Flux Line Cutting (Vortex Reconnection) Process

Although the related parameters $j_{c\|}$ and $(d\alpha/dx)_c$ suffice to account for the macroscopic behaviour encountered in the flux cutting regime, it is of some interest to examine the processes envisaged to occur when $j_\|$ exceeds $j_{c\|}$; hence $(d\alpha/dx) > (d\alpha/dx)_c$.

Although it is frequently convenient to describe the behaviour of type II superconductors in terms of persistent current densities $j_\perp$ and $j_\|$ induced by changes in the magnitude and orientation of the external magnetic field $\vec{H}$, we must always bear in mind that in these materials, the magnetic flux exists in the form of discrete entities (quantized vortices or flux lines). Once the sample is in the superconducting state, these entities can only enter or exit at its surfaces. Further, although adjacent sheets of flux lines can repel or attract each other, depending on the angle subtended between them, they exert no torque, torsional shear or turning forces on each other. Consequently mechanisms whereby flux lines undergo changes of orientation inside the superconductor, hence $d\alpha/dx$ diminishes to $(d\alpha/dx)_c$ and $j_\|$ relaxes to $j_{c\|}$ must be elaborated within this framework. The process of flux line cutting or vortex reconnection was proposed to account for these events.

To describe the accepted picture we return to and focus on the specific situation illustrated in Fig. 10. The increase in the magnitude of $\vec{H}$ eventually nucleates a sheet of flux lines directed along $\vec{H}_i + \Delta\vec{H}$ and drives these into the specimen. Since this new sheet of lines differs in orientation from that already existing in the sample in the vicinity of the surface , we see that $d\alpha/dx \neq 0$, hence $j_\| \neq 0$ in

that region. It is instructive to examine various possibilities.

First, if $d\alpha/dx < (d\alpha/dx)_c$, hence $j_{||} < j_{c||}$, the interaction between the sheets of flux lines is repulsive. Thus the situation essentially corresponds to that already examined earlier in this chapter, although we have focused on the simple configuration where the flux lines all possessed the same direction, i.e. $d\alpha/dx = 0$ and $j_{||} = 0$. The circumstances where $d\alpha/dx \neq 0$ but $d\alpha/dx < (d\alpha/dx)_c$, hence $j_{||} \neq 0$ but $j_{||} < j_{c||}$ can occur and are of considerable interest. Here flux lines will migrate in the specimen without changing direction, hence without undergoing flux cutting. This state of affairs has been examined in some detail by Lachaine [34], Lorrain [46] and LeBlanc [45]. We will return to this type of situation later in this thesis, since straightforward considerations of these events will provide us with the code for deciphering the signature of flux cutting.

Secondly, it is important to note that a lattice of non parallel flux lines may initially exist in a subcritical configuration (i.e. where $d\alpha/dx \neq 0$ but $d\alpha/dx < (d\alpha/dx)_c$) but be transformed to an overcritical state (i.e. where $j_{||} > j_{c||}$). This can be accomplished by compressing the lattice of flux lines. The analogy with an accordion is useful in this context. Such a compression, (i) increases the flux line density $B(x)$ and (ii) also increases $d\alpha/dx$ since the separation Δx between adjacent sheets thereby diminishes but the angle , $\Delta\alpha$, which they subtend, remains fixed. Turning to equation 25 ($B\, d\alpha / dx = \mu_o j_{||}$), we see that these two factors can contribute to augment $j_{||}$ and drive this quantity above the critical threshold.

Finally, we turn to the processes whereby flux lines finding themselves in an overcritical configuration where $d\alpha/dx > (d\alpha/dx)_c$, hence $j_{||} > j_{c||}$, relax and reorient until a critical state is established with $d\alpha/dx = (d\alpha/dx)_c$, thus $j_{||} = j_{c||}$. The initial overcritical situation may occur at the time of nucleation or may arise

later after the flux line lattice has undergone compression.

We consider two adjacent sheets of flux lines subtending an angle $\Delta\alpha_{1\,2} > \Delta\alpha_c$ with respect to each other. The sequence of events is portrayed schematically in Fig. 11. The two sheets are drawn side by side in Fig. 11(a) but should be visualized as superimposed and lying one above and one below the plane of the paper. Since $\Delta\alpha_{1\,2} > \Delta\alpha_c$, the two sheets attract each other. Consequently, they will move towards each other under the influence of their mutual attraction, making contact at an array of points of intersection as displayed in Fig. 11(b). At these points of contact, the flux lines temporarily fuse and form doubly quantized regions. The resulting regions are energetically expensive, hence unstable and cannot persist. Consequently the unions will break up with segments from one sheet now attached to the adjacent segments from the other sheet. This situation is sketched in Fig. 11(c). The process where two lattices of flux lines intersect and cross join is called flux line cutting or vortex reconnection.

The process we have just described is not unique to type II superconductors. The concept of vortex reconnection is encountered in magneto hydrodynamics (solar flares, astrophysics, aurora borealis) superfluid helium and recently in the theory of strings (we refer the reader to Fig. 4 on page 33 of the March 1989 issue of Physics Today).

The immediate result of the vortex reconnection is a dense sheet of zig zag flux lines as depicted in Fig. 11(c). This zig zag configuration is energetically unfavorable and the pattern straightens out to reduce the line tension energy (see Fig. 11(d)). Since the flux lines become shorter as they straighten, the volume of flux, $\phi_v = \int \phi_o dl$ is consequently diminished. Here ϕ_o is the flux quantum and dl is an element of length along the flux line. Flux is said to be consumed by the process of flux line

cutting since the total volume amount of flux is reduced. In another perspective, we note that it is the transverse component of the flux line density of the initially separate sheets which has been made to vanish. The number of flux lines, however, is conserved in the process just described.

The ensuing densely packed sheet of flux lines shown in Fig. 11(d) is unstable because of the large mutual repulsion. Consequently, these separate into two adjacent sheets which occupy the volume initially filled by the two sheets before their merger. The separated sheets are displayed side by side in Fig. 11 (e) but should again be viewed in three dimensions, with one sheet above and the other below the plane of the paper.

We note that D_f, the final separation between the flux lines in each of the resulting two sheets is larger than the original separation D_i, although the total number of flux lines is conserved. Simple trigonometric considerations lead to the relation,

$$D_f = \frac{D_i}{\cos(\Delta\alpha/2)} \tag{26}$$

The motion of flux lines or of flux line segments dissipates energy since a force $\vec{F}$ (whether it is repulsive or attractive) acts along the displacements $\vec{ds}$. Therefore energy is dissipated when, (i) the sheets of flux lines approach each other, (ii) the zig zag configuration straightens out and (iii) the ensuing densely packed sheet of flux lines separates into two sheets. Processes (i) and (ii) can be shown to generate a net electric field $E_{||}$ directed upwards in Fig. 11, hence parallel to $j_{||}$. The energy dissipation can also be viewed in terms of $\int dt \int E_{||} j_{||} dv$.

We now visualize that the two sheets of flux lines whose interaction history we have just chronicled are situated at the edge or frontier of a lattice of flux lines consisting of sheets initially subtending an angle $\Delta\alpha_{ij} = \Delta\alpha_c$ with respect to their

nearest neighbours. Clearly then after sheets $i = 1$ and $j = 2$ which we have just looked at, have undergone the process described above, $\Delta\alpha_{2\,3}$, the angle subtended by sheets 2 and 3 is now overcritical since it has increased from $\Delta\alpha_c$ to 3/2 $\Delta\alpha_c$. Hence, sheets 2 and 3 will go through the ritual just outlined. As a consequence, $\Delta\alpha_{3\,4}$ now becomes overcritical and so on. The disturbance in orientation of the flux lines thereby propagates throughout the volume of a lattice initially at the critical angular threshold, causing a change of orientation of the flux lines throughout the critical region. After the passage of each "wave" of angular adjustment, things quiet down until a new perturbation is introduced at the surface of the specimen by an increment $\Delta\vec{H}$.

In this thesis we report on our observations of the evolution of the magnetic flux in type II superconductors, both classical and high T_c, when subjected to changes in the externally applied magnetic field $\vec{H}$ which are designed to induce flux line cutting.

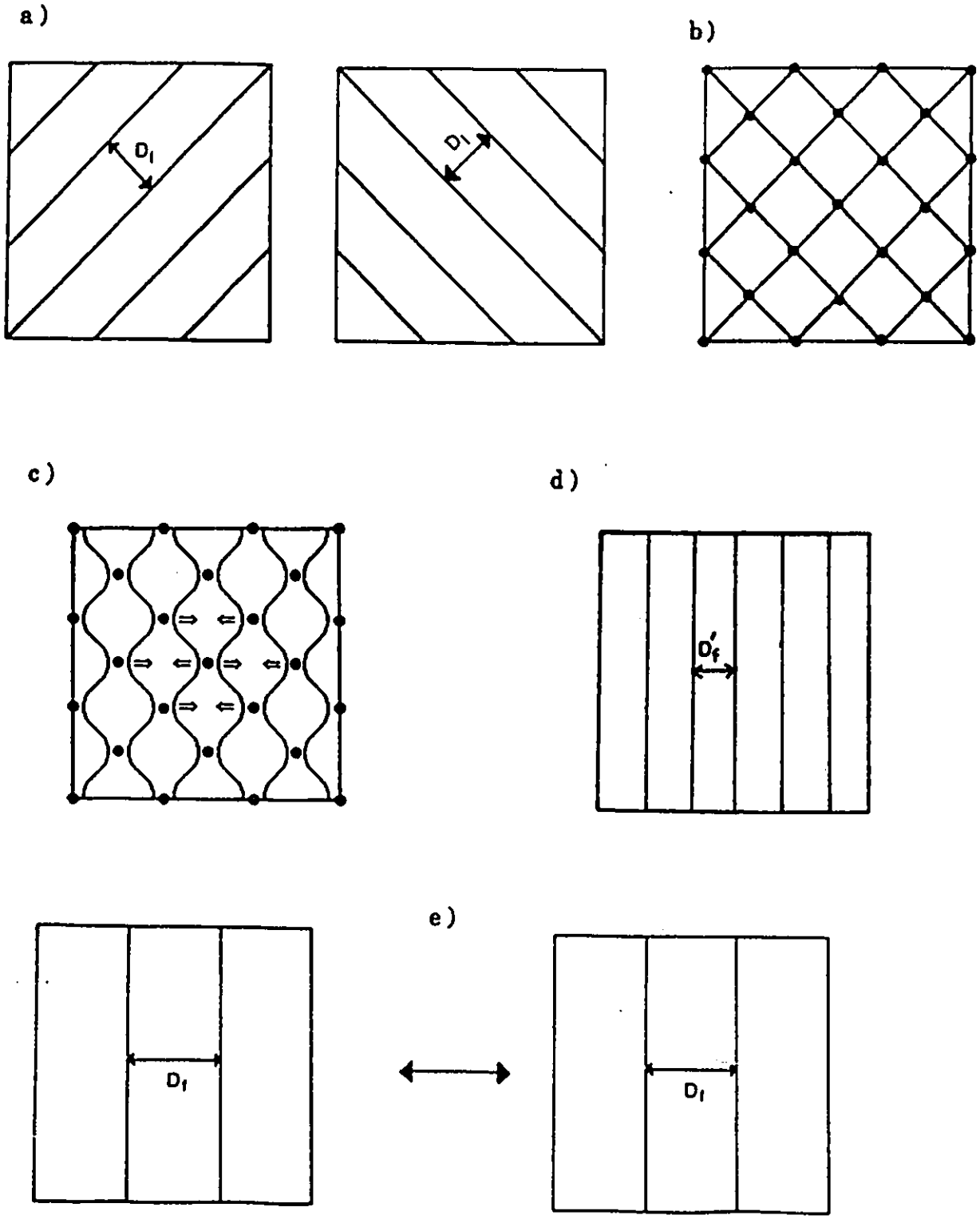

Figure 11: Shows schematically the sequence of intersection, cross joining, straigthening and separation of two sheets of flux lines. This process is called flux line cutting.

Chapter 2

Experimental Procedures

2.1 Description of Samples Employed

Each sample is a rectangular slab with its length Z and width Y large compared with the thickness X thereby ensuring a small demagnetization factor for an externally applied magnetic field $\vec{H}_a$ directed along the $Y-Z$ plane. The dimensions of the four samples we studied are listed in table 1 which also indicates the exact composition of the four materials. For brevity, in the text we will generally refer to the high T_c samples as the 123 compounds and denote them individually as the Yttrium or Nd samples. Also for simplicity, the conventional superconducting alloys will be abbreviated to $PbIn$ and VTi.

Sample	Thickness (cm)	Width (cm)	Length(cm)
$YBa_2Cu_3O_{7-x}$	.16	1.2	2.8
$NdBa_2Cu_3O_{7-x}$	.22	1.2	2.4
$Pb_{0.46}In_{0.54}$	.075	1.0	3.0
$V_{0.24}Ti_{0.76}$	.15	.51	3.6

Table 1: Sample Dimensions.

All of the samples were prepared from high purity starting materials. The VTi ingot was prepared by the Materials Research Corporation by repeated arc melting of the appropriate mixture. The $PbIn$ ingot was prepared in our laboratory by melting an intimate mixture of the ingredients in an evacuated and sealed pyrex tube. The melted ingot was cooled to 120 ^oC by turning off the furnace and annealed at that temperature for 24 hours.

The slab samples were cut from these ingots using a wire saw. The measurements reported by Lachaine [33],[34] and by Lorrain [45],[46] on VTi were performed on this specimen. Sekerka [61] has also carried out extensive measurements on disks cut from the same $PbIn$ ingot.

The 123 samples were prepared by Christian Moreau at the Institut de Génie des Matériaux, Boucherville, Québec using a standard prescription for preparing these high T_c compounds starting with oxides of the constituents.

2.2 Experimental Arrangement and Procedure

2.2.1 Description of the Heater-Sample Unit

In the previous chapter we have stressed the importance of controlling the path followed by nonideal type II superconductors in the $H - T$ plane. This requires that the specimen be made to cool from above T_c to the ambient temperature in a chosen $\vec{H}_a$ within a conveniently short interval of time. Consequently, the specimen must be in fairly intimate thermal contact with the cryogenic bath. On the other hand, it is also very useful in the measurements of the "final" magnetic moment of the specimen to be able to raise its temperature from ambient to above T_c with ease and rapidly.

These objectives are attained by winding an electric heater directly on the sample and interposing a minimal thermal barrier between the sample-heater unit and the cryogenic bath. Of course a compromise must be struck between these conflicting desires since a weak thermal barrier, hence rapid cooling, implies that a large heating rate will be needed in order to raise the sample temperature from ambient to T_c. Such a large heat input is particularly undesirable in expensive liquid helium. Mainly for this reason we have not pursued measurements on the high T_c materials at 4.2 K.

The electric heater consists of manganin wire wound non inductively (i.e. bifilarly) as a single layer covering the entire surface of the specimen. By using a simple layer we ensure the most intimate contact between the heater and the sample. The bifilar noninductive arrangement assures that a current flowing in the heater generates no magnetic moment and no resultant magnetic field. Manganin wire is used

because it is not magnetic and has a large resistivity. The latter property is most useful since it means that a small current will provide the desired joule heat input (I^2R) thus at the same time minimizing the generation of any magnetic moment and magnetic field by the heater.

The sample-heater assembly is painted with a thin layer of epoxy. This provides the desired thermal barrier and ensures against unravelling of the heater. If necessary, one or more layers of masking tape are wrapped around the unit to augment the thermal barrier. As noted above, this is a major consideration when the cryogenic bath is precious liquid helium.

The sample-heater unit fits tightly inside a slot at the center of the main transverse pickup coil as shown schematically in Fig. 12. The bakelite sample holder is designed to ensure that the YZ plane of the slab specimen is easily, accurately and rigidly aligned with respect to the externally applied magnetic field $\vec{H}_a$.

2.2.2 The $H_{\|}$ and $H_{\perp}$ Magnet Coils

We desire to immerse the specimens in an external magnetic field $\vec{H}$ which can be varied simultaneously in strength and direction. This is very conveniently accomplished by separately generating two orthogonal magnetic fields, one directed along the length Z of the specimen and denoted $H_{\|}$, the other directed along its width Y and denoted $H_{\perp}$. In our arrangement $H_{\|}$ is produced by a long multi- layer solenoid and $H_{\perp}$ by a rectangular coil which tightly embraces the solenoid as sketched in Fig. 13. The solenoid fits tightly inside the rectangular coil and the two are rigidly clamped together since they will exert a large torque upon each other when both are simultaneously energized.

Two such similar arrangements were constructed, one using coils wound with

superconducting commercial multifilamentary $NbTi$ wire for the measurements at 4.2 K and the other using coils wound with 16 gauge copper wire for the studies on high T_c materials at 77 K. The bores of the copper and $NbTi$ solenoids are 3.7 cm and 2.5 cm respectively. The outer diameter and the length of the copper solenoid are appreciably larger than that of the $NbTi$ solenoid. Nevertheless the maximum magnetic induction $\mu_o H_{\|}$ which can be obtained by the former (2 Tesla) is much greater than can be produced by the copper solenoid ($\approx$ 0.3 Tesla). The superconducting solenoid produces $45mT/A$ whereas the copper solenoid provides only $20mT/A$.

The rectangular copper coil is consequently larger in dimensions and considerably more massive than its $NbTi$ counterpart, nevertheless the former generates only $3.67mT/A$ while the latter provides $17mT/A$. The frame of the rectangular coils was made by machining a thick slab of aluminum.

Outer Length	Inner Length	Outer Width	Inner Width	Thickness	Depth
28.10 cm	23 cm	13.97 cm	9.05 cm	3.17 cm	2.22 cm
20.5 cm	15 cm	8.5 cm	4.0 cm	2.2 cm	2.2 cm

Table 2: Dimensions of the copper rectangular coil (upper) and $NbTi$ rectangular coil (lower)

2.2.3 The Pick up Coil System

We wish to measure the evolution of the magnetic flux density both along the length ($< B_z >$ or $B_{\|}$) and along the width ($< B_y >$ or $B_{\perp}$) of the slab samples

simultaneously and separately. This is accomplished using two orthogonal pick up coils one embracing the length of the specimen (the Z or longitudinal coil) and the other its width (the Y or transverse coil).

In practice, it is generally more convenient to measure the components of the magnetic moment or magnetization of the specimen rather than the components of the magnetic flux density. Since $\mu_o\vec{M} = \vec{B} - \mu_o\vec{H}$, this means that the contribution of the applied magnetic field $\vec{H}$ to the magnetic flux density must be instrumentally subtracted from the measurement. This is readily accomplished by introducing bucking or balancing coils which monitor $\vec{H}$ but do not embrace or "see" the sample. Such bucking coils are series opposition connected to the corresponding main or detector coil which embraces the sample. The set up is displayed schematically in Fig. 12 and Fig. 13.

In our arrangement each main coil is "balanced" by a pair of identical bucking coils which are symmetrically placed on each side of the main coils. This configuration minimizes the sensitivity of the balancing to variations of position along the z axis since both $H_{\parallel}(z)$ and $H_{\perp}(z)$ vary symmetrically with respect to the midpoint of the solenoid and rectangular coil.

The balancing of a pickup coil is perfect when

$$N_1 < A_1 > = N_2 < A_2 > \tag{27}$$

where N_1 and N_2 denote the number of turns of the main coil and its bucking coils, $< A_1 >$, the average area embraced by N_1 and $< A_2 >$, the average area embraced by N_2. By Faraday's law of induction, the emf's generated in each coil as H is varied, read

$$\mathcal{E}_i = -\mu_o N_i < A_i > \frac{dH}{dt} \tag{28}$$

when the coils embrace no sample (or a non magnetic material). Since the coils are connected in series, but the sense of their windings are opposite, no net emf is generated when the sample exhibits no magnetic moment.

It is difficult to balance the coils exactly, hence a small background signal due to imperfect cancellation and a small net emf is generally present. Since the samples we have studied are non magnetic in the normal state, this background signal is determined for each "run" with the sample in place but maintained at a temperature above T_c using the heater. Further, for superconducting coils, H is not exactly a linear function of the energizing current I, and indeed H versus I exhibits a sometimes not negligible dependence on the previous history of $\vec{H}$ experienced by the coil in the superconducting state. Consequently, we monitor this "background" signal for each specified path in the $H_{\|} - H_{\perp}$ plane in order to identify this spurious contribution and extract it from our raw data. The history dependence or irreversibility of superconducting coils and consequent non linearity is unfortunately frequently ignored in much of the published research.

2.2.4 Monitoring of $< M_z >$ and $< M_y >$

We monitor the components of the magnetization (magnetic moment per unit volume) $< M_z >$ and $< M_y >$ separately and continuously as, (i) $\vec{H}$ is varied at constant T or, (ii) T is varied at constant $\vec{H}$. We recall that,

$$\mu_o < M_z > = < B_z > - \mu_o H_{\|} \tag{29}$$

$$\mu_o < M_y > = < B_y > - \mu_o H_{\perp} \tag{30}$$

where $< B_z >$ and $< B_y >$ denote the spacial average of the magnetic flux density threading the specimen along its length and width. $H_{\|}$ and $H_{\perp}$ are the

corresponding components of the externally applied magnetic field.

Each balanced pickup coil feeds an electronic integrator/amplifier. These drive the Y axis of $X-Y$ recorders.

Since the net emf

$$\mathcal{E}_{\parallel}(t) = N < A > \frac{d}{dt}(< B_z > - \mu_o H_{\parallel}) \tag{31}$$

is integrated by the operational amplifier, the signal $S(t)$ at the output of the integrator/amplifier reads,

$$S_{\parallel}(t) = k \int_0^t \mathcal{E}_{\parallel}(t')\, dt' = \mu_o < M_z(t) > k\, N < A > \tag{32}$$

hence, the evolution of $< M_z >$ with time. Thus the effects of $\vec{H}(t)$ or $T(t)$ are registered. Here we suppose that the coils are perfectly balanced, hence $N < A >$ applies to either the main coil or the bucking coils. k is an amplification factor. Evidently, expressions similar to equation 31 and equation 32 can be written for $< M_y >$.

The X axes of the two $X-Y$ recorders are driven by a signal proportional to either the longitudinal magnetic field $H_{\parallel}$ or to the transverse magnetic field $H_{\perp}$ depending on the investigation in progress. The desired signals are provided by the voltage drop along a standard calibrated shunt placed in each of the circuits connected to separate power supplies and feeding current to the magnet coils. The operation of the complete system of magnet coils, current sources, shunt voltages, pickup coils, amplifier/integrator and $X-Y$ recorders is shown schematically in Fig. 14.

The measurements on the high T_c superconductors were carried out in an open plastic encased styrofoam dewar with the sample-coil assembly submerged in liquid nitrogen at atmospheric pressure (hence at $\approx$ 77 K).

The cryogenic environnement for the measurements on the conventional superconductors was appreciably more sophisticated since these measurements were carried in liquid helium. Many complications however were avoided by electing to pursue the work in liquid helium at atmospheric pressure (hence at ≈ 4.2 K).

The cryogenic system consist of two nesting glass dewars, an outer one filled with liquid nitrogen and an inner one containing the liquid helium at a level well above the top of the magnet coil assembly. The liquid nitrogen environnement is needed here to reduce heat flow by radiation into the helium bath. This thermal enclosure at 77 K reduces the radiation heat input by a factor ≈ 250 according to the Stefan-Boltzmann T^4 radiation law.

Initially, a small residual air pressure exists between the walls of the helium dewar. This residual air provides for the transfer of heat by conduction from the contents of the helium dewar (magnet coils, sample assembly) to the surrounding liquid nitrogen. When the transfer of liquid helium begins, this residual air quickly freezes on the inner wall of the helium dewar and the vacuum between the walls of this dewar becomes nearly perfect. This process for creating a vacuum is called cryopumping. Now, the contents of the helium dewar are thermally isolated from the outside world except for heat input by radiation from the 77 K liquid nitrogen enclosure and from the top of the dewar at 300 K. Metal baffles are placed in the helium dewar to reduce the latter source of heat input.

Liquid helium is transferred into the experimental dewar using a sealed double walled siphon; the air between the walls having been evacuated. Since the latent heat of evaporation of liquid helium is very small, the transfer of liquid helium must not proceed too rapidly in order to optimize the exploitation of the large heat capacity of the cold helium vapor in cooling the apparatus from 77 K to 4.2 K.

2.2.5 Calibration Procedure

Following standard procedure, the magnetization of the $PbIn$ and VTi samples was calibrated on the well verified assumption that the virgin specimen shields perfectly against entry of magnetic flux in the range of $H_a < H_{c1}$. The penetration depth is negligible compared to the thickness of our slab samples, hence $< B >$ can be taken to be identically zero under these circumstances. H_{c1} for nonideal materials is generally identified with the applied field where the locus of the magnetization versus H_a ceases to be linear.

For the sintered 123 specimens, the linear region is relatively minute at 77 K, spanning a small range between 0 and $\approx$ 1.5 mT. This introduces some sensitivity problems in obtaining an accurate calibration. The major problem which arises, however, is that this calibration criterion leads to significant inconsistencies in the interpretation of two related and complementary observations, namely, (i) ΔH_c discussed in the previous chapter and (ii) the magnitudes assigned to the magnetization on the basis of this calibration. We will examine this important discrepancy in some detail in this thesis.

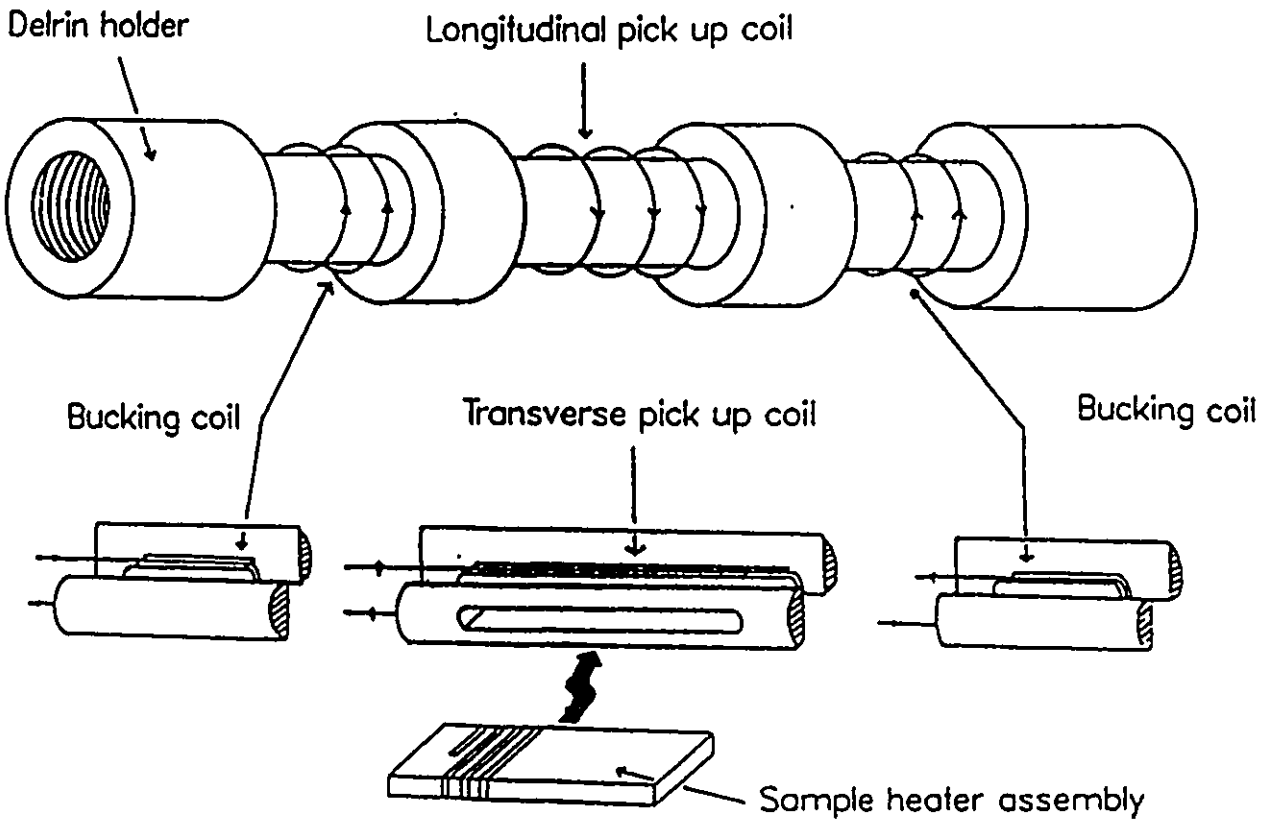

Figure 12: Schematic of longitudinal and transverse pick up coil assembly.

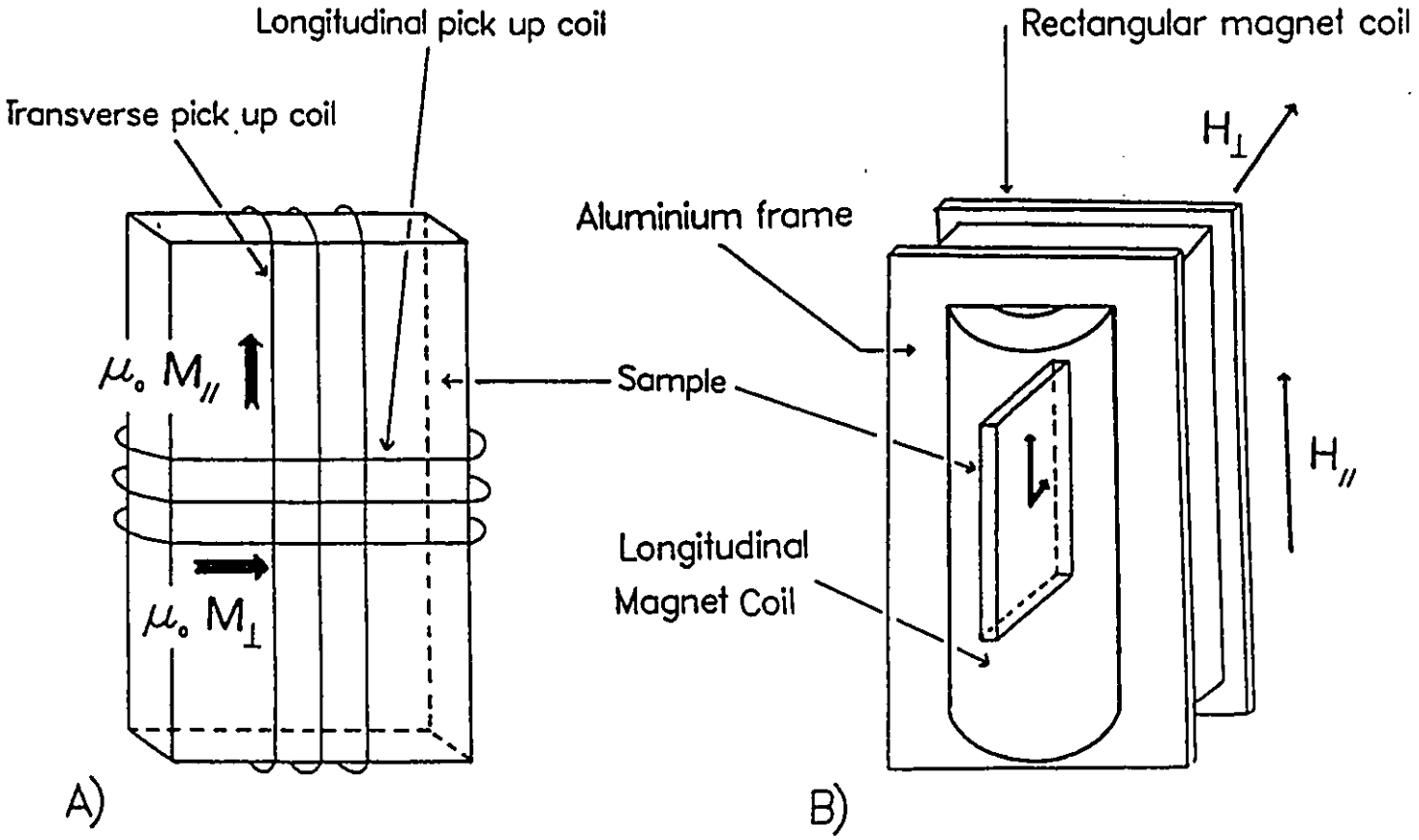

Figure 13: Schematic of the arrangement of the pick up coils and magnets.

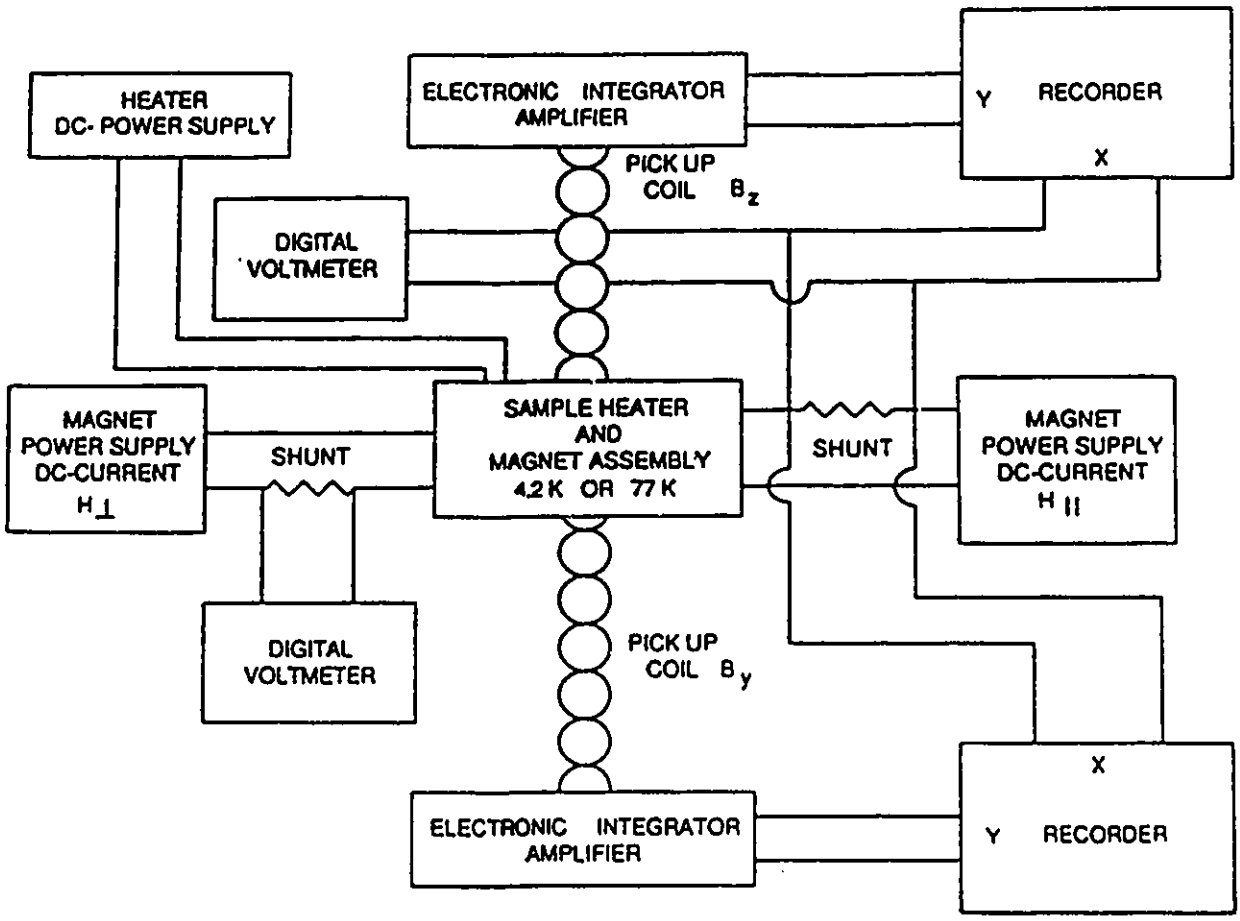

Figure 14: Schematic of experimental set up.

Chapter 3

Standard Magnetization Curves

3.1 Introduction

We have emphasized in the first chapter that the magnetic response of real type II superconductors is not a single-valued function of the intensive variables H and T but depends on the path followed in the $H - T$ plane, hence on the previous history in the superconducting state. Consequently in order to fully characterize the magnetic properties of a specimen and identify various important parameters (i.e. $H_\star$, $H_{\star\star}$, maximum trapped flux, ΔH_c etc ...) several major data curves should be mapped out. Unfortunately many workers neglect to measure or fail to report some of the important features of this panoply of complementary and useful magnetization data.

A complete catalogue of the pertinent information should include the following.

- The initial magnetization curve when H_a is first impressed upon the virgin specimen (i.e. a sample cooled in zero field).
- The upper and lower envelopes of the symmetric major hysteresis loop.
- The traversal between the upper and lower envelopes when the sweep of H is reversed at $H_a = 0$.
- Traversals between the upper and lower envelopes starting at various H_a extending from 0 to H_{c2} or the largest value accessible.
- The magnitude of the flux expulsion (Meissner effect) observed upon cooling from T_c to the chosen ambient temperature in various static magnetic fields.

3.2 Magnetic Characterization of our Samples

Figures 15 through 21 display some of the magnetic behaviour of the four samples we have investigated. In these figures we focus on the response in the range of low fields in order to bring out several features more clearly. In each case, however, the maximum H_a exceeds H_{**}, hence this important quantity can readily be identified and estimated as well as H_*. Also $< M >_*$ and $< M >_{**}$, the magnetization at H_* and H_{**}, and finally $< M >_{res}$, the maximum residual or remanent magnetization can be evaluated.

These parameters are listed in table 3.

Sample	$H_*(mT)$	$H_{**}(mT)$	$< M >_*(mT)$	$< M >_{**}(mT)$	$< M >_{res}(mT)$
$YBa_2Cu_3O_{7-x}$	12.8	22	9.5	9.5	2.9
$NdBa_2Cu_3O_{7-x}$	14.5	17.2	8.5	8.5	3.7
$Pb_{0.46}In_{0.54}$	14.2	16.1	12	9.9	2
$V_{0.24}Ti_{0.76}$	60.6	72.6	22	17.4	36

Table 3: Magnetization Parameters. (*For brevity the μ_o factor has been omitted*)

In order to ascertain whether our samples are isotropic we have measured the magnetization curves both along the length and along the width. The corresponding magnetization curves overlap within experimental accuracy for all of the samples except the VTi ribbon which displays some anisotropy. The anisotropic behaviour of this specimen has been examined by Lorrain [46]. For economy of space and since the data curves for the other samples essentially coincidence we present the magnetic response along the length of the ribbons in this thesis.

Figs. 16 and 15 both display the same data on the magnetic behaviour of the Nd specimen. Our purpose in presenting both figures is to iilustrate once again the feature noted in chapter 1 that a 4 quadrant format is needlessly repetitious since the information contained in the 3^{rd} quadrant duplicates that already contained in the 1^{st} and similarly the 2^{nd} quadrant is a reproduction of the 4^{th} . The 2 quadrant format is evidently more "economical". Further this format is clearer since the picture is now enlarged. In the remainder of this thesis we will avoid the redundancy of the 4 quadrant format and display the pertinent information using only the more convenient 2 quadrant picture.

Indeed, an important feature which is almost imperceptible in Fig. 15 becomes more evident in the two quadrant display of Fig. 16. We draw the attention of the reader to the structure displayed by the Nd specimen in the low field region of the initial magnetization curve (i.e. the curve starting at $< M >= 0$, the virgin state). The low field data is shown on an expanded scale in Fig. 17. We note that the slope undergoes dramatic changes in the vicinity of $H \approx 2mT$. This interesting structure or hump is also encountered in the magnetic response of the Yttrium specimen (see Fig. 18). It is less prominent here since it appears at a lower field. Consequently, to give a better view of this feature in the latter specimen, the low field data is shown on a much enlarged scale in Fig. 19.

A variety of complementary investigations in several laboratories have established the following account for this low field structure or hump in sintered high T_c materials.

These sintered samples are seen to consist of a compact agglomeration of small irregularly shaped grains with typical dimensions in the range of a few microns. In very weak fields these grains are electrically interconnected or coupled by superconducting bridges at points or areas of contact. The lossless current carrying capacity of these surfaces of contact (the intergrain critical current density $j_{c\perp}$) is not very large ($\lesssim 10^3\ A/cm^2$) and is also very sensitive to weak magnetic fields ($\mu_o H_a \lesssim$ a few milliteslas or even a fraction of a millitesla).

As a consequence, an applied magnetic flux easily quenches or at least appreciably diminishes the magnitude of the macroscopic persistent currents flowing from grain to grain and readily penetrates the space between the individual grains (the matrix). The decline in the slope of $< M >$ versus H testifies to this collapse of the intergrain persistent currents and the consequent invasion of the matrix by

magnetic flux. The sintered specimen can now be correctly regarded as a collection of electrically separate (uncoupled) irregularly shaped particles packed closely together.

The available evidence indicates that $\mu_o H_{c1}$ of the individual grains of the 123 compounds at 77 K is $\approx$ 10 mT. The critical flux depinning current density, $j_{c\perp}$, which grains of these materials can sustain at 77 K can vary by several orders of magnitude depending on the techniques and procedures of fabrication as well as the composition. These conclusions have emerged from extensive studies of powdered (isolated particles) and sintered samples in many laboratories including ours. Since a magnetic flux density of a few milliteslas effectively destroys the intergrain persistent currents, the size and behaviour of the envelopes of the magnetization curves carries the desired information on the intragrain $j_{c\perp}$. In order to extract estimates of $j_{c\perp}$ versus B from these data we require, (i) a reliable calibration of the magnetization and (ii) information on the average size of the particles. The latter can be readily determined by a microscopic analysis. In this thesis we will address the problem of finding an acceptable and appropriate calibration.

In our view, a calibration based on the initial weak field magnetic response, hence perfect shielding of the entire volume of the sintered specimen by the macroscopic persistent currents flowing from grain to grain along its periphery is inappropriate for the analysis of the behaviour of the isolated particles. It appears to us more logical and self-consistent that the diamagnetic moment after the intergrain currents have been quenched, should be used for calibration of the data pertaining to the uncoupled grains. Indeed, this is in effect the approach used in measurements on collections of isolated grains. Here the hump does not appear and the question of using the initial slope of this structure for calibration does not even arise to cloud or

confuse the issue. The calibration is then based solely on the diamagnetic response of the uncoupled grains. For sintered samples, this response of the uncoupled grains appears after the hump. Figs. 15 through 19 were calibrated on this basis.

Unfortunately, this approach introduces some uncertainty in the calibration. The particles in sintered samples exhibit a variety of geometries and orientations as well as sizes. A consequence of the irregularities in shape and orientation is that the demagnetization factor of the individual grains spans a wide spectrum. These various features cause the locus of $< M >$ versus H (after the hump) to deviate from linearity well before the ideal H_{c1} is reached. Further the relationship between the effective field and the applied magnetic field is uncertain and can only be estimated. This arises because the magnetic flux density threading the space between the grains (the matrix) is not only made non uniform but also augmented above $\mu_o H_a$ by the "return" flux generated by the shielding currents circulating around the individual grains. As is well known, the magnitude of this return flux density at the surface of spheres and rods can be comparable to $\mu_o H_a$.

We have not attempted to estimate an effective or average demagnetization factor for the collection of uncoupled particles comprising our sintered samples. For simplicity, we have ignored these complications and assumed $H_{effective} = H_a$ in these figures. Our purpose at this stage is mainly to focus on the qualitative similarities and differences of the materials under scrutiny. We will return to the problem of calibration of the sintered specimens in a later chapter.

It is however of interest to record the quantitative transformation brought about by calibrating as we have done, (using $< M >$ and/or $d < M > / dH$ immediately after the hump) instead of using the initial linear region before the hump. As a consequence, the magnitude assigned to the magnetic moment of the collection of

uncoupled grains is augmented by a factor of 2.5 for the Nd specimen and a factor of 1.5 for the Yttrium sample. Equivalently, the inverse of these ratios can be regarded as indicating that the superconducting volume of the uncoupled particles comprises $\approx 40\%$ of the total volume of the Nd slab and $\approx 66\%$ of the Yttrium slab specimen.

Since the effect of the non negligible demagnetization factor of the particles is to augment $H_{effective}$ relative to H_a, the ratios quoted above would consequently be increased. Estimating $H_{effective} / H_a \approx 3/2$ therefore leads to magnetic moments further enlarged by this factor of 3/2 and effective superconductive volumes further diminished by a factor of 2/3.

It is well known that the sintered high T_c materials are quite porous. Our analysis of the calibration indicates however that the superconducting fraction is much smaller than the actual volume occupied by the particles or grains.

3.3 Comparison of Magnetic Responses

An inspection of Figs. 16, 18, 20 and 21 reveals that the overall behaviour of the two high T_c materials at 77 K is very similar to that of the $PbIn$ while the magnetic properties of this threesome differ markedly from that of the VTi which is clearly quite hysteretic.

Firstly, the 123 compounds and the $PbIn$ exhibit an appreciable Meissner effect. We stress that for an ideal type II superconductor this phenomenon peaks at H_{c1}. In sharp contrast, the VTi sample shows no flux expulsion, within experimental accuracy ($\lesssim 0.01$ mT), upon cooling from T_c to 4.2 K.

Although the ratios of the maximum Meissner moment to the maximum diamagnetic response (≈ 0.4 , 0.26 and 0.33 for the Nd, Y and $PbIn$ samples respectively)

are comparable, the critical current density $j_{c\perp}$ against depinning is inferred to be appreciably larger for the 123 compounds than for the *PbIn*. The significant difference in the estimates for $j_{c\perp}$ even though the Meissner magnetizations are similar arises because of the efficacy of pinning in opposing the Meissner flux expulsion is sample size dependent. We develop this feature in the next paragraph and the accompanying sketch.

The solid curves in the drawing schematically display the B profile in a "thick" slab after cooling from T_c in an arbitrary field $H_a < H_{c2}$. This is to be compared with the B profile (illustrated by the dashed curves) which is encountered if this "thick" slab has been sliced $\parallel$ to $\vec{B}$. Now the specimen consists in a juxtaposition of three separate, electrically uncoupled slabs with the same total thickness. We note that the total magnetic flux which is expelled in the latter configuration is much greater than in the former case. Here, for simplicity and ease of comparison we have taken $j_{c\perp}$ to be uniform and the same in both instances. We have seen earlier that the particles or grains of the sintered samples become electrically isolated at 77 K when $\mu_o H_a \gtrsim 2mT$. The pertinent dimension then is the cross section of the grains with a typical diameter of a few microns. This is to be compared with the thickness of about a millimeter for the *PbIn* ribbon. The latter acts as a single entity. The observation of comparable Meissner magnetizations therefore indicates that $j_{c\perp}$ of the isolated grains of the 123 materials is considerably larger than that of the *PbIn*. The higher $j_{c\perp}$ "compensates" for the much smaller size of the grains and yields similar spatial averages for the flux expulsion magnetizations.

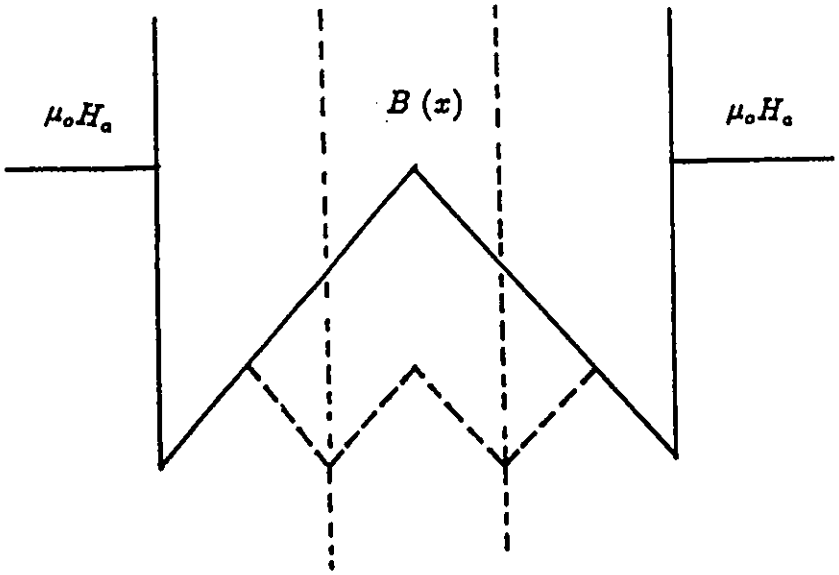

The observation that the *VTi* expels no magnetic flux upon cooling from T_c indicates that a large surface barrier and/or strong pinning in the bulk, hence a large $j_{c\perp}$, successfully suppress the expulsion of magnetic flux (Meissner effect). This "null" result, however, provides to quantitative guide to the precise values for $j_{c\perp}$ or the height of the surface barrier. The nonlinearity of the traversals between the magnetization envelopes indicate the absence of a surface barrier, hence, show that the Meissner effect is inhibited by a strong bulk pinning (large $j_{c\perp}$) only.

The observation that, for the 123 materials and the *PbIn* sample, the locus of $< M >$ versus H_a descending coincides closely with the Meissner magnetization in the range $H_a > H_{c1}$ classifies these specimens as semi-reversible since here, the dependence on previous history in the $H - T$ plane is not pronounced. This correspondence shows that the peak in the corresponding B profiles cannot exceed

$\mu_o H_a$. This feature provides semi quantitative information on $j_{c\perp}$ in these specimens.

In contrast, the locus of $< M >$ versus H_a for the VTi sample swings steeply from the diamagnetic (upper) to the paramagnetic (lower) quadrant when H_a is removed. This very irreversible behaviour again indicates strong pinning. We will show in a later chapter how estimates of $j_{c\perp}$ can be extracted from the "distance" or separation between the upper and lower envelopes.

Finally we note that the remanent magnetization for the VTi is considerably larger than that for the three other samples. The large amount of trapped flux indicates a high density of flux lines imprisoned in the material and made unable to escape by strong pinning. This powerful confinement is associated with steep gradients in the B profile, hence large $j_{c\perp}$.

3.4 Conclusion

Extensive data on the magnetic properties of our samples in the superconducting state has been compiled and catalogued. A survey of these results brings out the similarities in semi- reversible behaviour of the classical $PbIn$ and the two high T_c materials at 77 K as well as the sharp differences these exhibit compared to the very hysteretic VTi. The physical import of various salient features has been outlined.

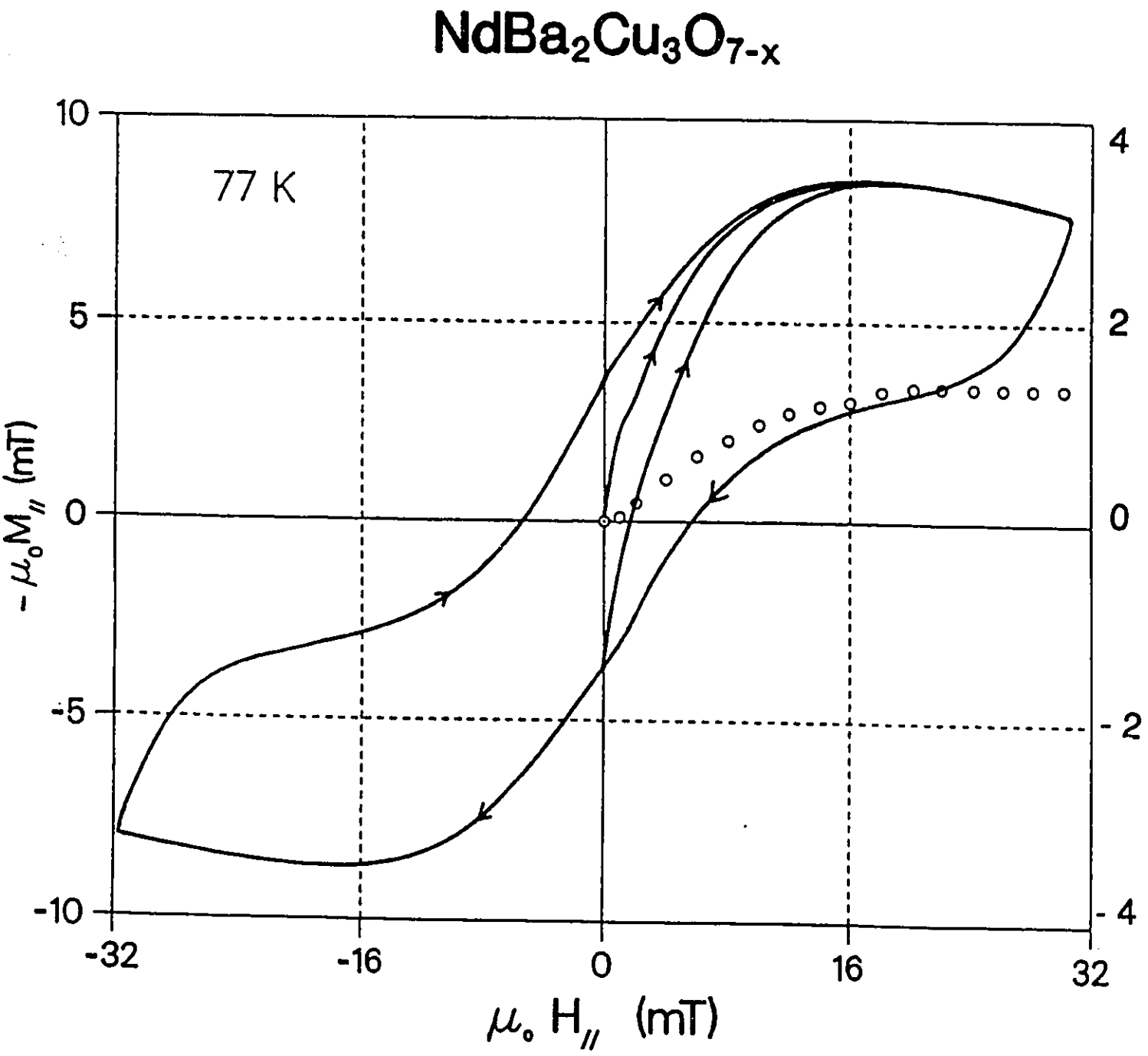

Figure 15: Displays a symmetric hysteresis loop for $NdBa_2Cu_3O_{7-x}$ where H swings beyond H_{**}. The initial magnetization curve and a traversal between the envelopes which start at $H = 0$ are also shown. The open circles show the flux expulsion (Meissner effect) upon cooling from T_c to 77 K.

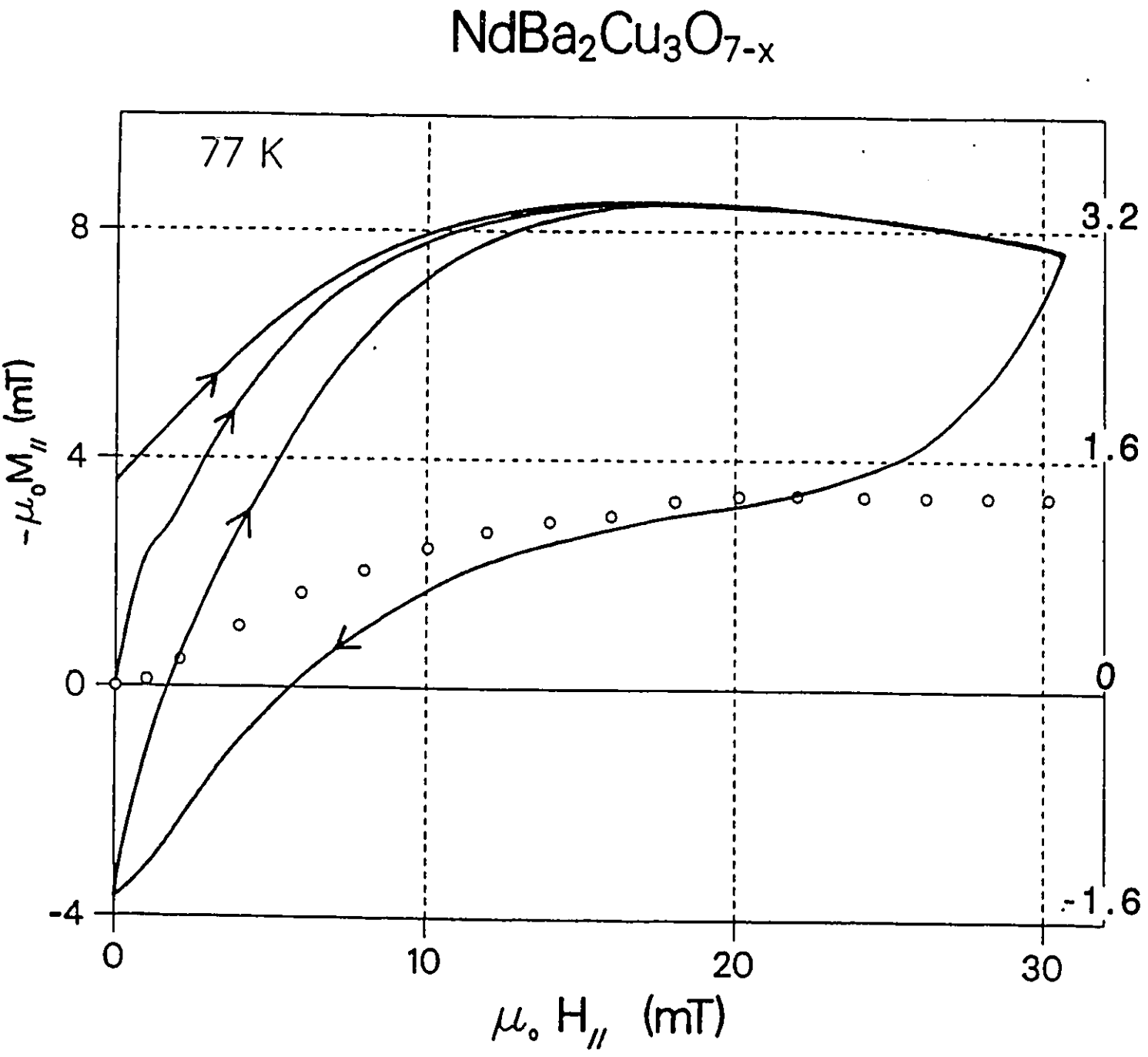

Figure 16: Displays the same information as the previous figure but uses the more economical and therefore expanded scale of a two quadrant format. As discussed in the text, the calibration shown on the left hand side assumes perfect shielding by the isolated grains immediately after the hump structure, that on the right is based on the initial low field response before the hump.

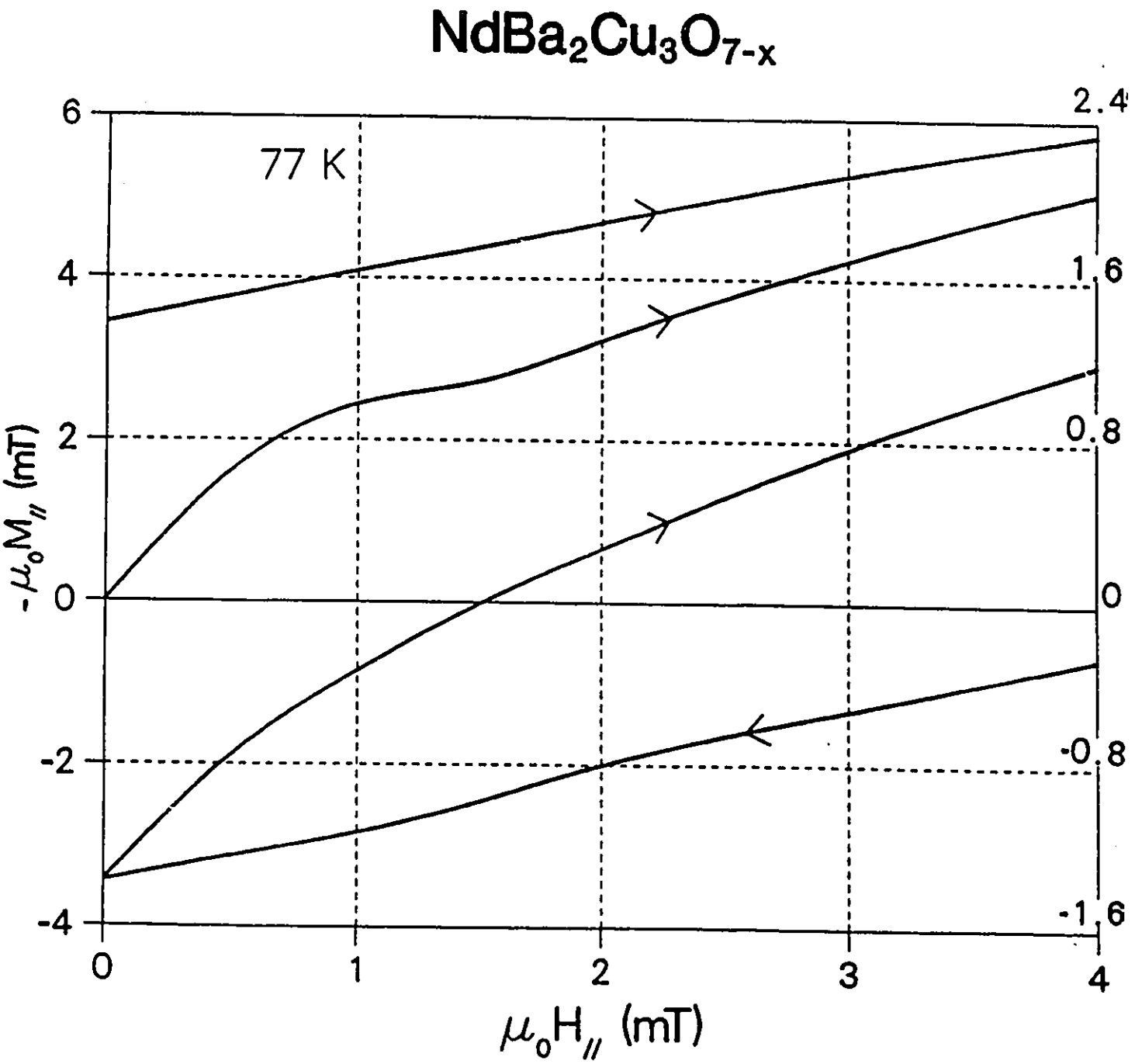

Figure 17: The low field region of the previous figure is shown enlarged to focus on the hump structure.

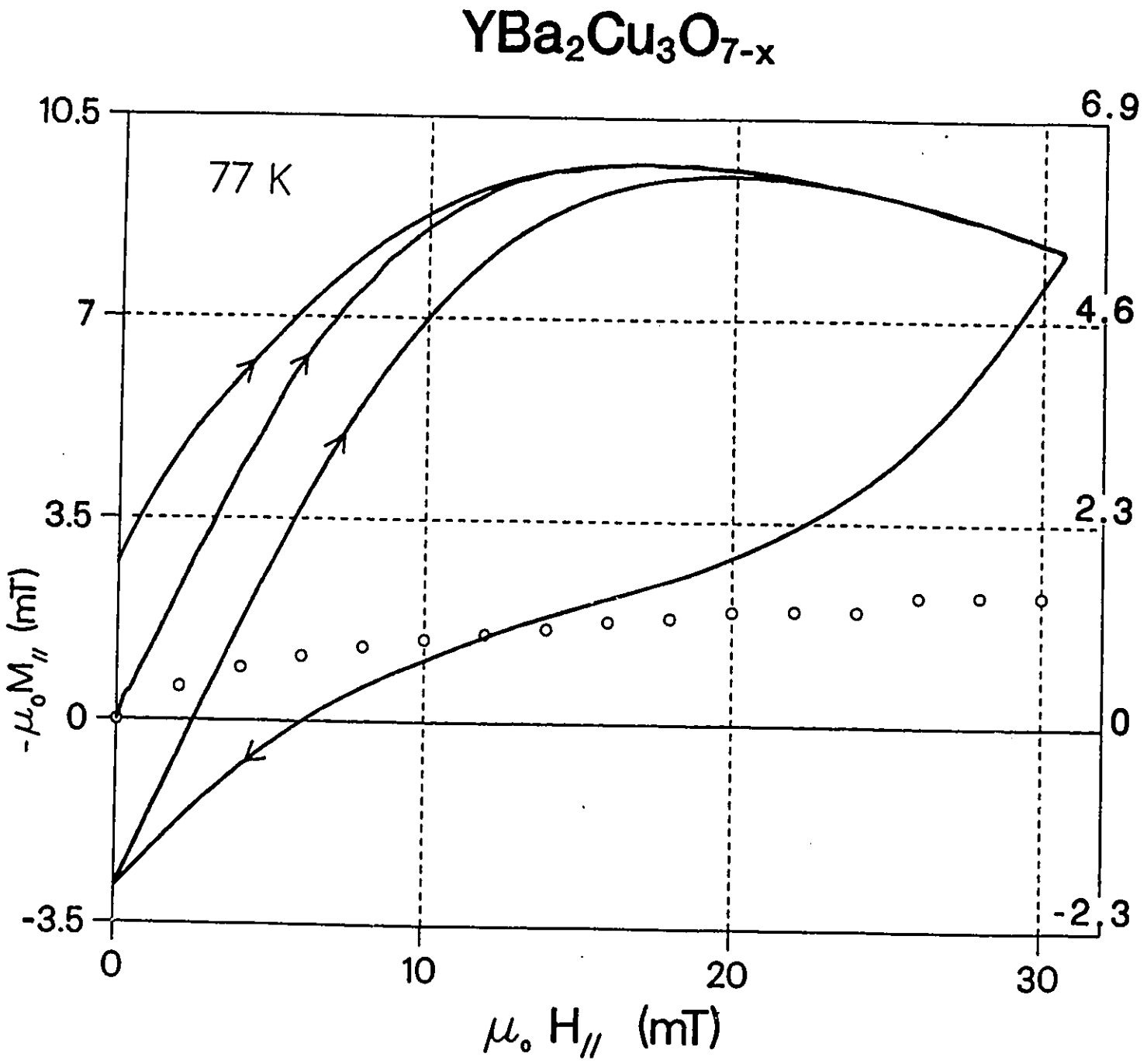

Figure 18: Displays half of a symmetric hysteresis loop for $YBa_2Cu_3O_{7-x}$. The initial magnetization curve and a traversal between the envelopes which start at $H = 0$ are also shown. The open circles show the flux expulsion (Meissner effect) upon cooling from T_c to 77 K.

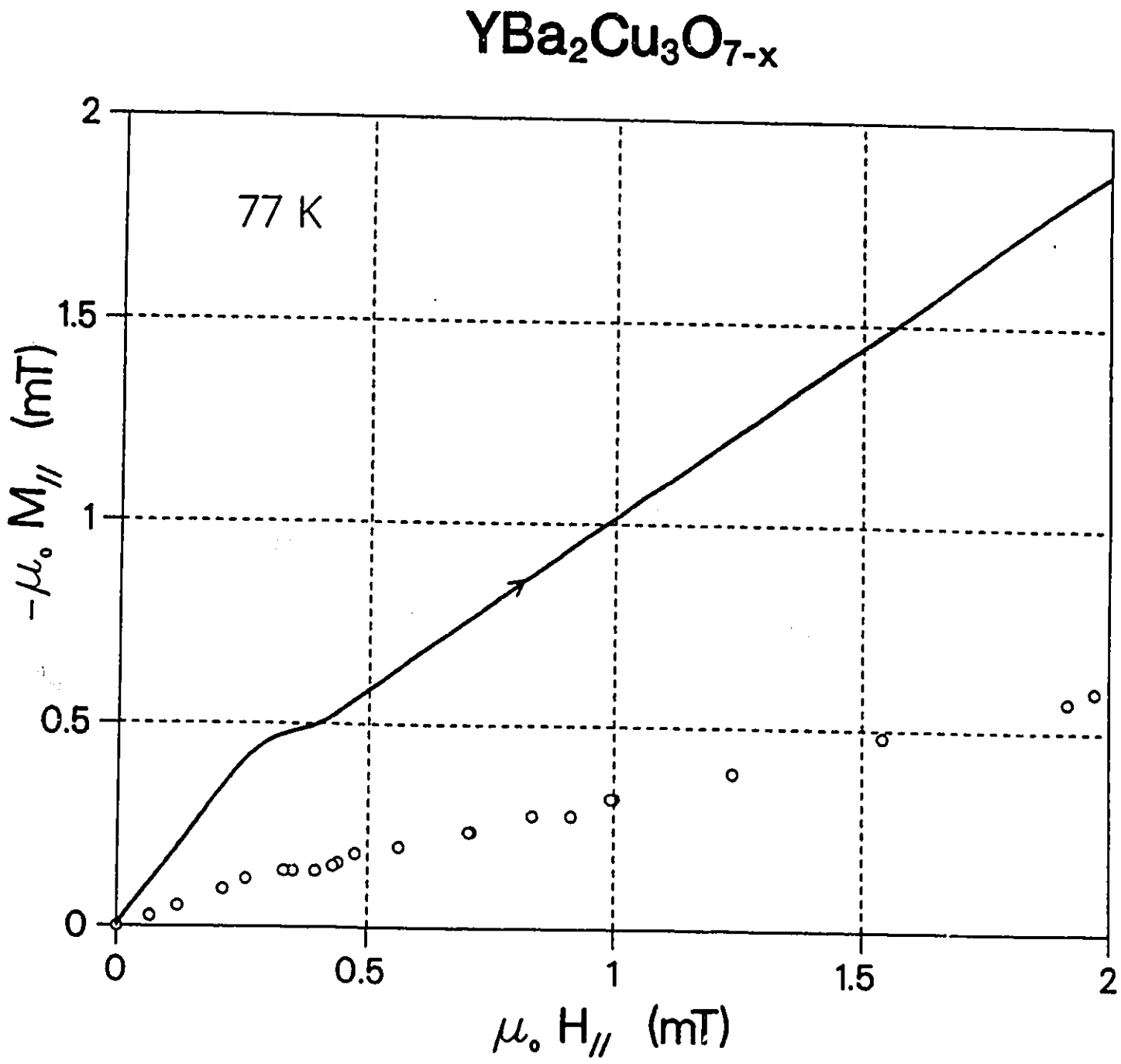

Figure 19: Enlargement of initial magnetization curve and Meissner effect data of previous figure.

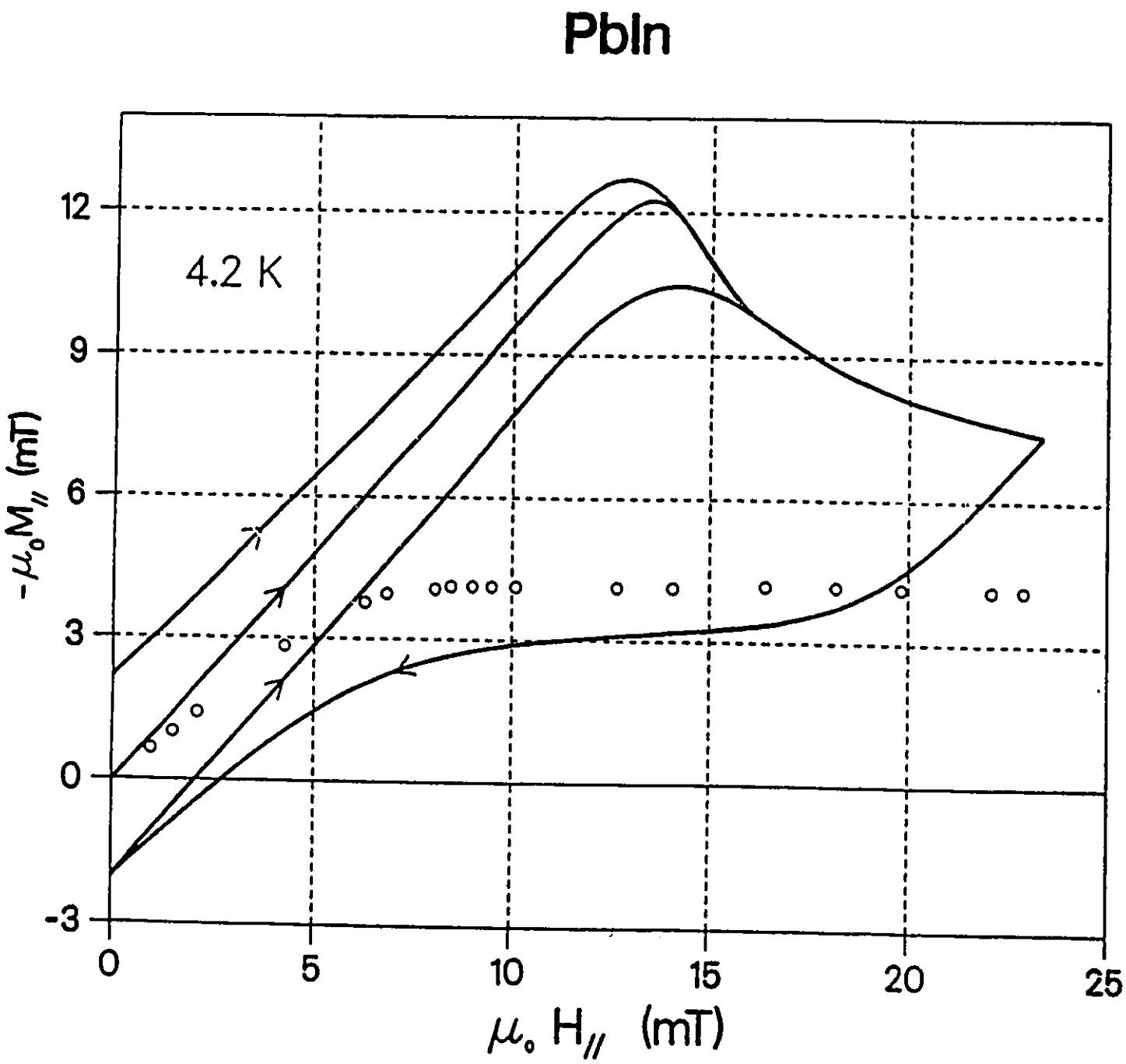

Figure 20: Displays half a symmetric hysteresis loop for the *PbIn* sample. The initial magnetization curve is also shown. The point where this curve touches the envelope determines H_* and $< M >_*$. The traversal between the envelopes which starts at $H = 0$ is also shown. The point where this curve touches the upper envelope defines H_{**} and $< M >_{**}$. The open circles display the Meissner effect flux expulsion upon cooling from T_c to 4.2 K.

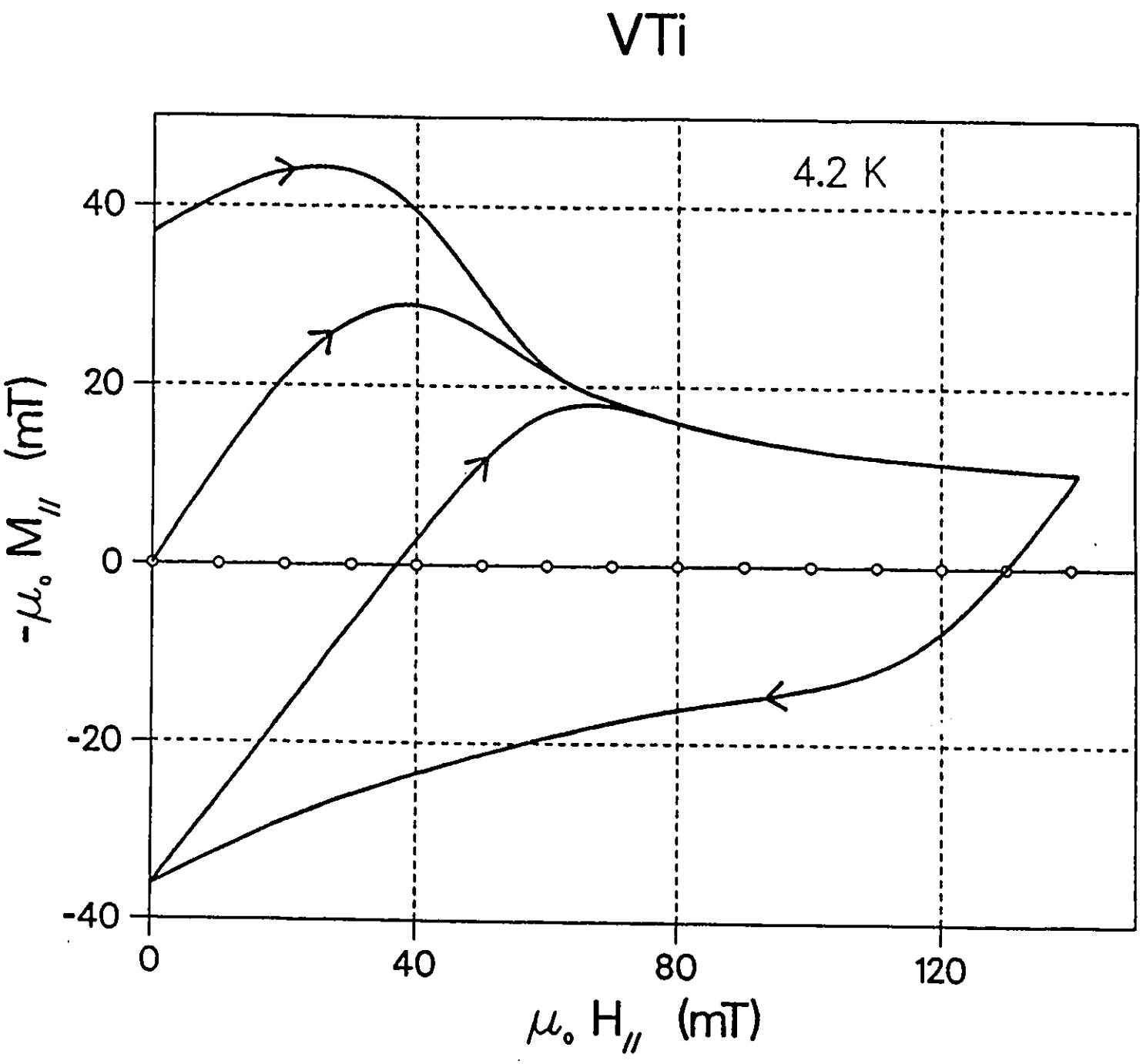

Figure 21: Displays half a symmetric hysteresis loop for the VTi sample. The initial magnetization curve and a traversal between the envelopes starting at $H = 0$ are also shown. The points of merger determine H_{*}, $< M >_{*}$, H_{**} and $< M >_{**}$. The residual magnetization is seen to exceed H_{c1}. No flux expulsion (Meissner effect) occurs upon cooling from T_c to 4.2 K in any field.

Chapter 4

Meissner Effect Revisited

4.1 Introduction

The expulsion of magnetic flux from type II superconductors during cooling from T_c in a static applied field H_a (the Meissner effect) is hindered by pinning in the bulk or volume of the specimen. The pinning forces oppose the mutual repulsion of the flux lines and assist the external field in confining the flux lines.

Schweitzer and his collaborators [56]-[60] have presented measurements on several classical type II superconductors indicating that the surface acted as a powerful barrier both against the entry and the exit of magnetic flux throughout the range $0 < H_a < H_{c3}$. The upper critical field for the destruction of surface superconductivity is denoted by H_{c3}. Experiment and theory have shown that $H_{c3} \approx 1.7\, H_{c2}$ where H_{c2} is the upper critical field for suppression of superconductivity in the bulk of the specimen. The $< M >$ versus H_a curves which Schweitzer et al displayed as evidence for a surface barrier frequently failed to exhibit the required slopes $d < M > /dH = -1$, the criterion for surface shielding or flux retaining persistent

currents. Subsequently, other groups confirmed that the surface could indeed shield against flux entry well beyond the Meissner current but appeared to be ineffective in opposing flux exit in the range $0 < H_a < H_{c2}$ [13], [14], [66].

The picture of a semi-permeable surface barrier opposing flux entry but allowing flux exit thus came to prevail. This consensus was fortified by the theoretical explanations of the surface barrier. Bean and Livingston [3] developed the concept of an image force. In this analysis, the deformation of a flux line parallel to and adjacent to the surface is described by the superposition of the undistorted flux line and its hypothetical image outside the specimen and situated on equal distance from the surface. The attraction of the flux line to its image can then be computed. This attraction creates a surface barrier against flux entry which can eventually be overcome by the magnetic pressure exerted by an externally applied magnetic field. De Gennes [30] examined the barrier height in the perspective of the energy required to nucleate the first sheet of flux lines at the surface and showed that this required a threshold magnetic field $H_a = H_c$, the thermodynamic critical field. Further analysis by Ternovski [62] and by Clem [27] indicate a small barrier against flux exit.

LeBlanc and Mattes [42] and LeBlanc et al [43] presented evidence that the surface can also oppose the expulsion of the magnetic flux during cooling below T_c and thereby reduce the manifestation of the Meissner effect. Indeed, their measurements reveal that the barrier against flux exit is comparable to that against flux entry. Further LeBlanc and his collaborators [41] have shown that the surface barrier against flux exit can be appreciably diminished and effectively suppressed when a small component of the magnetic flux density permeating the specimen is made to pierce the flat surfaces of type II superconducting ribbons.

The nature and origin of the surface barrier remains to be elucidated. Matsushita et al [48] have presented good evidence that pinning at the surface can be considerably stronger than in the bulk and thereby give rise to a surface barrier. This picture however does not account for all of the surface phenomena reported to date.

4.2 Background and Results

LeBlanc et al. [41] discovered that the expulsion of magnetic flux upon cooling of ribbon samples of type II superconductors in a magnetic field $\vec{H}_a$ (Meissner effect) can be greatly enhanced when the magnetic field instead of being directed exactly parallel to the length of the specimen was tilted at a small angle with respect to the broad surfaces of the ribbon. When $\vec{H}_a$ is tilted, the component H_x of $\vec{H}_a = \vec{x}H_x + \vec{z}H_z$, pierces the flat faces of the ribbon.

These workers investigated this behaviour in several materials and in Fig. 22 we reproduce one pair of their data curves which illustrates this effect quite spectacularly. The lower data curve in Fig. 22 displays the expulsion of flux (diamagnetic magnetization) observed along $\vec{H}_a$ versus H_a when $H_x = 0$, hence the angle of tilt is zero. The upper data curve shows the diamagnetic magnetization along $H_z(H_{||})$ versus $H_z(H_{||})$ when a component H_x is present as the sample is cooled from T_c. Clearly, the Meissner moment along H_z is greatly amplified by the "bias" magnetic field H_x.

This phenomenon is attributed to the presence of a surface barrier whose capacity, I_s, to oppose the expulsion of flux is sensitive to both the magnitude of $\vec{H}_a$ and θ, its orientation with respect to the broad faces of the slab specimen. From

families of data curves such as displayed in Fig. 22 measured with various values chosen for H_x and exploiting the idea of a surface barrier, these workers extracted detailed information on the quantity $I_s(H_a, \theta)$ for the specimens they studied.

We deemed it worthwhile to investigate whether our high T_c samples would exhibit the phenomenon just described.

The solid circles in Fig. 23 display the expulsion of flux (Meissner effect) observed on cooling from T_c to 77 K for the Yttrium specimen versus $H_{||}$ when $H_x = 0$, i.e. $\vec{H}_a$ is directed along the length of the slab specimen. The squares show the Meissner magnetization measured along the length of the slab with $\mu_o H_x = 20\,mT$. It is evident from these two sets of data that the presence of H_x, hence tilting $\vec{H}_a$ so that it pierces the broad surfaces of the specimen, does not enhance the Meissner effect. Measurements carried out with various values of H_x confirm this "null" result.

The open circles in Fig. 23 display the Meissner magnetization observed when the magnetic field is tilted in the $y-z$ plane by a component $H_y = 20\,mT$ directed along the width of the slab. Here $\vec{H}_a = \vec{y}\,H_y + \vec{z}\,H_z$. Under these circumstances, LeBlanc et al [41] found a weak enhancement of the Meissner moment in their classical type II superconducting ribbons. They also attributed this effect to lowering or suppression of the surface barrier along the narrow sides of the slab since now $\vec{H}_a$ is tilted to pierce these side surfaces. This is less effective in allowing the release of flux lines since the sides constitute only a small fraction of the total surface area. Our measurements again show a "null" result in this arrangement.

The observations in the $y-z$ plane are useful however in providing information on any anisotropy in the bulk pinning forces opposing the expulsion of flux lines by their mutual repulsion. If the slab specimen is isotropic, the Meissner magnetization

in a field $\vec{H}_a$ of fixed magnitude will be independent of the orientation of $\vec{H}_a$ in the $y-z$ plane. In this plane, the demagnetization factor is negligible since the Y and Z dimensions of the slab are large compared to its thickness along X. (The demagnetization factor along the thickness is not negligible. This will give rise to anisotropic behaviour when $\vec{H}_a$ is directed in the $x-z$ plane.) The dashed curve traced in Fig. 23 verifies the isotropy of the Meissner effect in the specimen in the following way. The magnetic moments, $< M_z >_{H_a=H_z}$, observed along the Z axis when $\vec{H}_a = \vec{z}H_z$, hence $H_y = 0$, $H_x = 0$, are then taken as inclined in the yz plane and aligned parallel to the corresponding tilted $\vec{H}_a = \vec{y}H_y + \vec{z}H_z$. The dashed curve then maps out $< M_z >_{H_a\,tilted}$, the expected component along the z axis when $\vec{H}_a$ is tilted, according to the Pythagorean prescription that,

$$< M_z >^2_{H_a\,tilted} + < M_y >^2_{H_a\,tilted} = < M_z >^2_{H_a=H_z} \qquad (33)$$

The close correspondence between this projected component and that actually observed (the open circles) indicates that the specimen is isotropic.

The data displayed in Fig. 23 is illustrative and comprises only a fraction of the pertinent measurements we have carried out. Observations were made for various H_y and H_x. These results confirm the message contained in Fig. 23 and are not shown. We have also carried out identical measurements, although in less detail, on the Nd specimen. These measurements yield similar results and therefore lead to the same conclusions for this sample. In both materials, (i) no enhancement of the Meissner effect is encountered when $\vec{H}_a$ pierces the broad surfaces of the slab specimens and (ii) the samples are isotropic as regards the Meissner effect in the $y-z$ plane.

4.3 Discussion

The absence of any enhancement of the Meissner effect by tilting $\vec{H}_a$ to pierce the broad surfaces of the slab samples of the two high T_c samples (our "null" result) is not surprising in light of our present knowledge of these sintered materials. As noted in the previous chapter, these materials become a compact collection of electrically isolated particles when H_a exceeds a very small threshold value. The continuous "visible" surface of the slab specimen then loses its physical meaning and effects associated with such a superconducting surface will vanish. This is presumably the situation we encountered in this investigation.

In the work reported in this chapter we are presumably observing the average Meissner effect for an agglomeration of individual grains of a variety of shapes, sizes and orientation. Due to the irregular geometry of these particles, $\vec{H}_a$ pierces most of their surfaces regardless of its orientation in the $y-z$ or $x-z$ plane. In a sense then, $\vec{H}_a$ is always "tilted" with respect to the grains and its orientation vis á vis the boundaries of the slab is not pertinent.

It is now well established that the superconductivity properties of individual grains are highly anisotropic. The isotropic behaviour we observe is only apparent and results from averaging the behaviour of a multitude of randomly oriented grains in sintered samples.

In the range $0 < H_a \lesssim 1\,mT$, where the surface of the slab is continuous and plays an important role, the Meissner magnetization is correspondingly small and inadequate to provide clear cut data.

Measurements of the type we have described in this chapter on single crystals

or strongly coupled sintered materials should provide useful and interesting information.

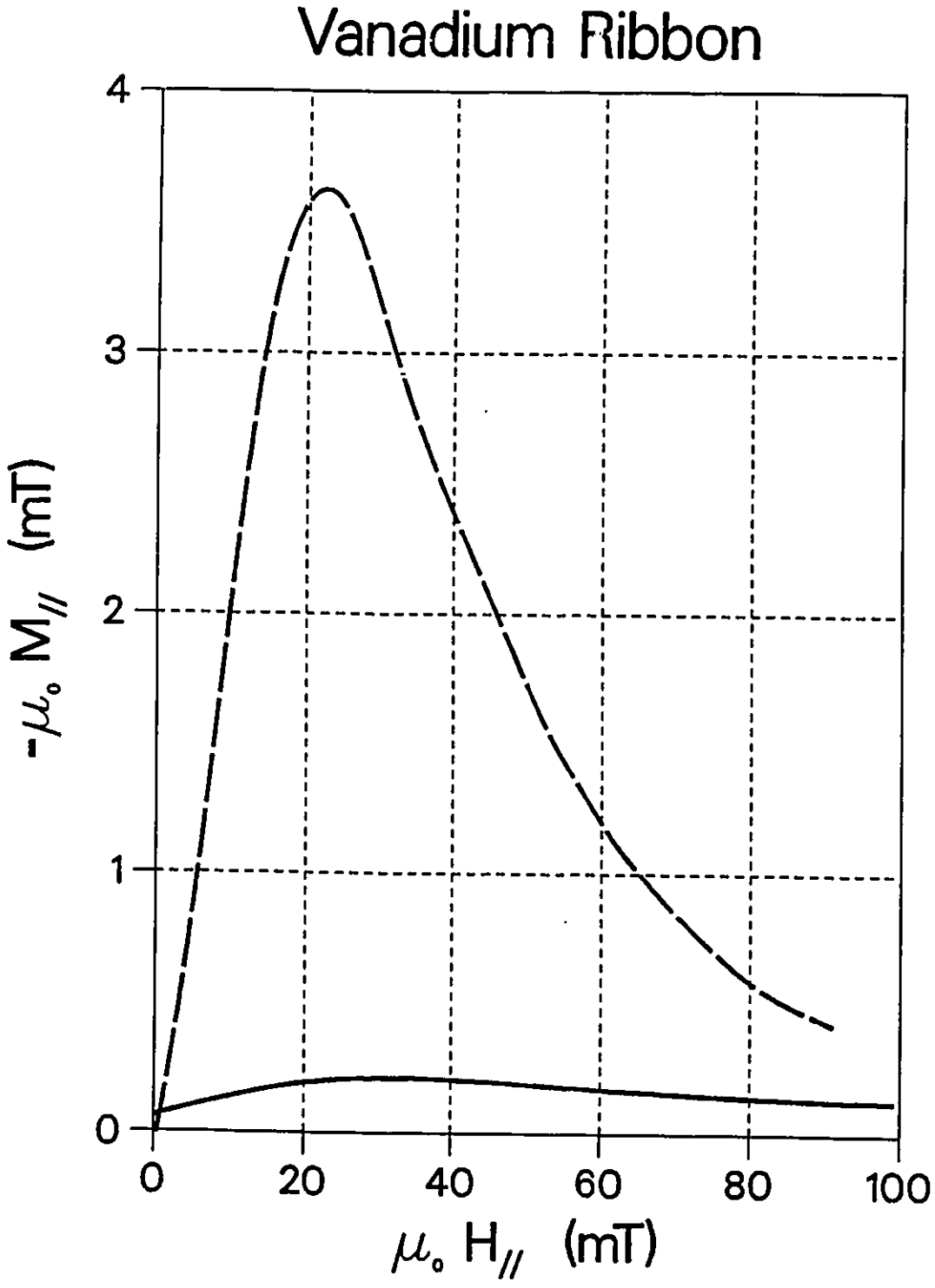

Figure 22: Flux expulsion magnetization measured along the length of Vanadium ribbon upon cooling from T_c to 4.2 K vs $H_{||}$ in $\mu_o H_\perp =$, 0 and 18 mT for the solid and dashed curves respectively.

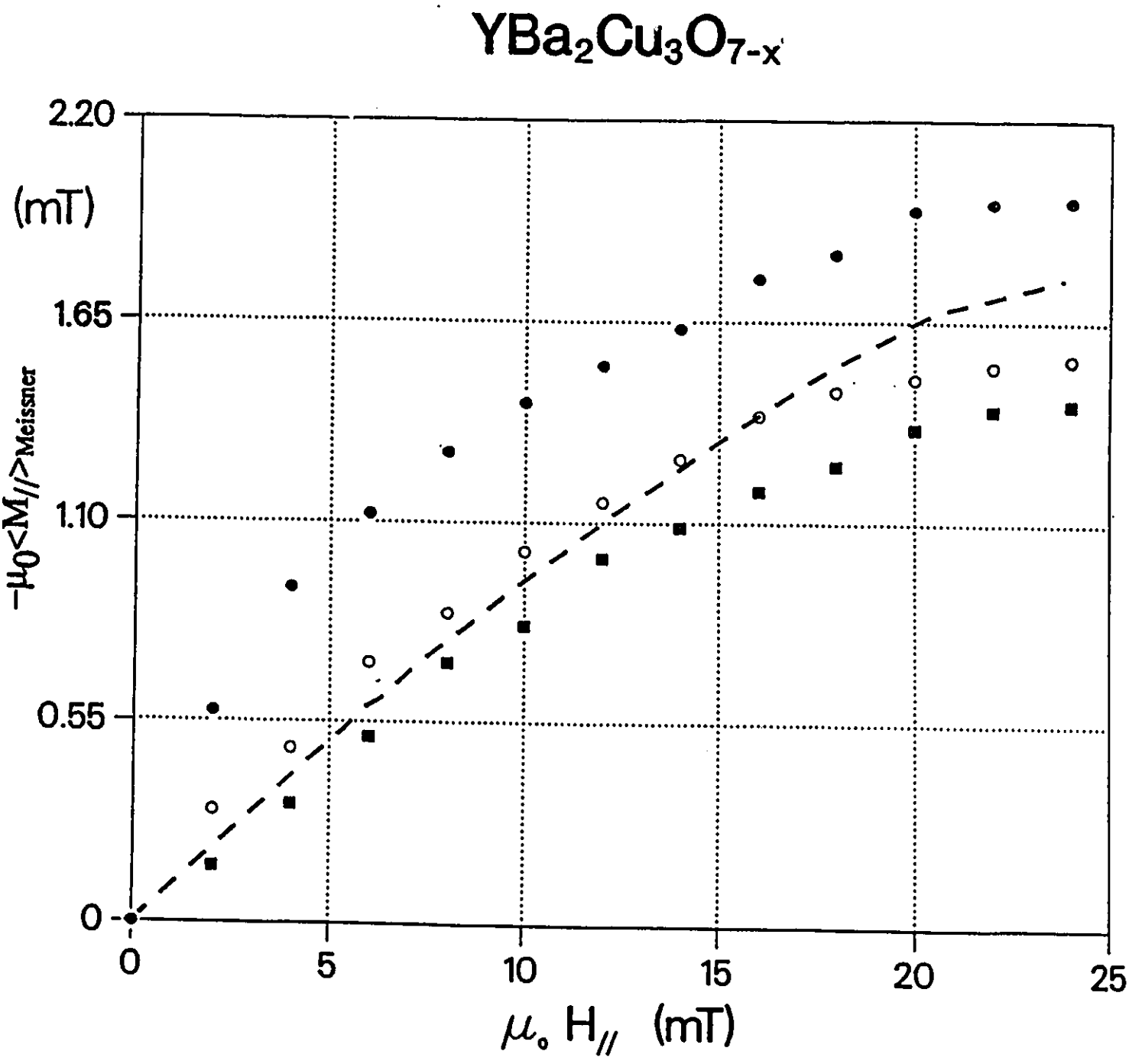

Figure 23: Meissner effect magnetization along the length of the specimen from flux expulsion upon cooling from T_c to 77 K versus $H_{||}$, the component of $\vec{H}_a$ directed along the length. No bias field is present for • data points ($H_a = H_{||}$). A bias field of 20 mT is directed along the width and along the thickness of the sample for the o and ■ data points. The dashed curve is calculated as described in the text. The correspondence of the o and ■ data points with this curve indicates the ideal isotropic case.

Chapter 5

Search for the Clem Valley

5.1 Introduction

Clem and his collaborators [26], [63] discovered in 1979 that hysteresis losses in some type II superconductors measured at a fixed amplitude $h_o \lesssim H_\star$ traversed a valley when a bias magnetic field H_b was introduced and directed along h_o. The minimum in the valley occurs when $H_b \approx 0.5\, H_\star$. This phenomenon is referred to as the Clem valley [33], [40]. This behaviour is of practical as well as academic interest since it reveals a simple technique for minimizing hysteresis losses in various A.C. applications of these materials.

The physical origins of this phenomenon have been well identified by Clem [26]. The account however is not readily amenable to a qualitative explanation. The behaviour arises from the dependence of the critical current density $j_{c\perp}$ and of the surface barrier I_s on the magnetic flux density B. The Clem valley has been observed and investigated in several classical type II superconductors (eg. $NbGe$, Nb_3Sn, NbN, $NbTi$, VTi). In Fig. 24, we display some of the data obtained by

Lorrain [46] in our laboratory on a ribbon sample of VTi to illustrate this effect. We were not and are not aware, at this time, of any report on the occurrence of this valley in high T_c materials. We undertook to determine whether our high T_c samples exhibited this phenomenon.

5.2 Procedure and Results

It is well known that the area enclosed by a hysteresis loop is a measure of the dissipation of energy in the specimen per cycle of the externally applied magnetic field H_a. It is convenient to write,

$$H_a = H_b + h_o f(t) \tag{34}$$

where H_b is a static bias magnetic field directed parallel to the amplitude h_o. Here $f(t)$ denotes an arbitrary function of time varying monotonically between plus and minus one. Let $W(h_o, H_b)$ denote the hysteresis losses per cycle as a function of h_o and H_b. Fig. 24 displays an example of the Clem valley observed in a classical type II superconductor. Each data point is obtained by measuring the area embraced by a closed hysteresis curve such as displayed in Figs. 15 through 21. The area can be measured using a planimeter or some other technique. Alternatively, the loss per cycle can be monitored using a wattmeter or a calorimeter. The upper and lower limits of the swing of H_a, denoted H_{max} and H_{min} determine H_b and h_o since

$$\begin{aligned} H_{max} &= H_b + h_o \\ H_{min} &= H_b - h_o \end{aligned} \tag{35}$$

We note from Fig. 24 that $W(h_o, H_b)$ plotted versus H_b for a fixed h_o exhibits a minimum. The structure of the valley, its depth and position vary with H_b and h_o.

We note that these features are independent of the calibration.

Our data on hysteresis losses in the Yttrium specimen are displayed in Fig. 25. We oriented H_b and h_o along the length of the slab (z axis) since the sensitivity of our detecting system is greater along this direction. Thus here, $H_{||}$ and H_b denote the same quantity. The continuously monitored curves of $< M_z >$ versus H_a as the latter was cycled were digitized, stored in the computer memory and the area enclosed by the hysteresis loops computed numerically. Our measurements span the range expected from previous work on classical materials for the Clem valley, namely, $0 < H_b = H_{||} < H_\star$. Here $H_\star \approx 15\,mT$. The Clem valley is known to become more pronounced as the amplitude h_o is made small relative to $H_\star$. The hysteresis losses, however, vary approximatively as the square of the amplitude in this range. Since the optimum sensitivity of our detection system is fixed, the data becomes proportionately less accurate as the amplitude is chosen smaller. Consequently a compromise must be made. We selected $h_o / H_\star \approx 1/3$ and $1/2$ for our investigation. From inspection of Fig. 25 we conclude that the Yttrium specimen exhibits no Clem valley. Since the specimen has been shown to be isotropic on a macroscopic average, we have not deemed it worthwhile to repeat the measurements along its width. Also because of the similarity in behaviour of the two high T_c materials we did not pursue this investigation on the Nd specimen.

5.3 Discussion

The absence of a Clem valley in the hysteresis losses of the sintered high T_c specimen is consistent with our understanding of this phenomenon and our knowledge of the properties of these materials.

Clem [26] has examined the contribution of the surface barrier to the occurrence and evolution of the valley. The sintered samples however appear to have no surface barrier (at least when $\mu_o H_a$ exceeds $\approx$ 1 millitesla). We conjecture that the magnetic field H_a suppresses the surface barrier by piercing most of the surface of the irregularly shaped and randomly oriented grains.

LeBlanc et al [40] have investigated the effect of the dependence of $j_{c\perp}$ on B in modifying the structure or appearance of the valley. Their work shows that the Clem valley becomes shallower when $j_{c\perp}$ is insensitive to the strength of the magnetic flux density B and that the valley vanishes in the limit where $j_{c\perp}$ is independent of B. This is often referred to as the Bean limit or approximation [2]. We will see in the next chapter that the intragrain $j_{c\perp}$ appears to vary very slowly as a function of B in the range $0 < H_a < H_*$. The "null" result reported in this chapter is consequently in agreement with the observations we present in the next chapter.

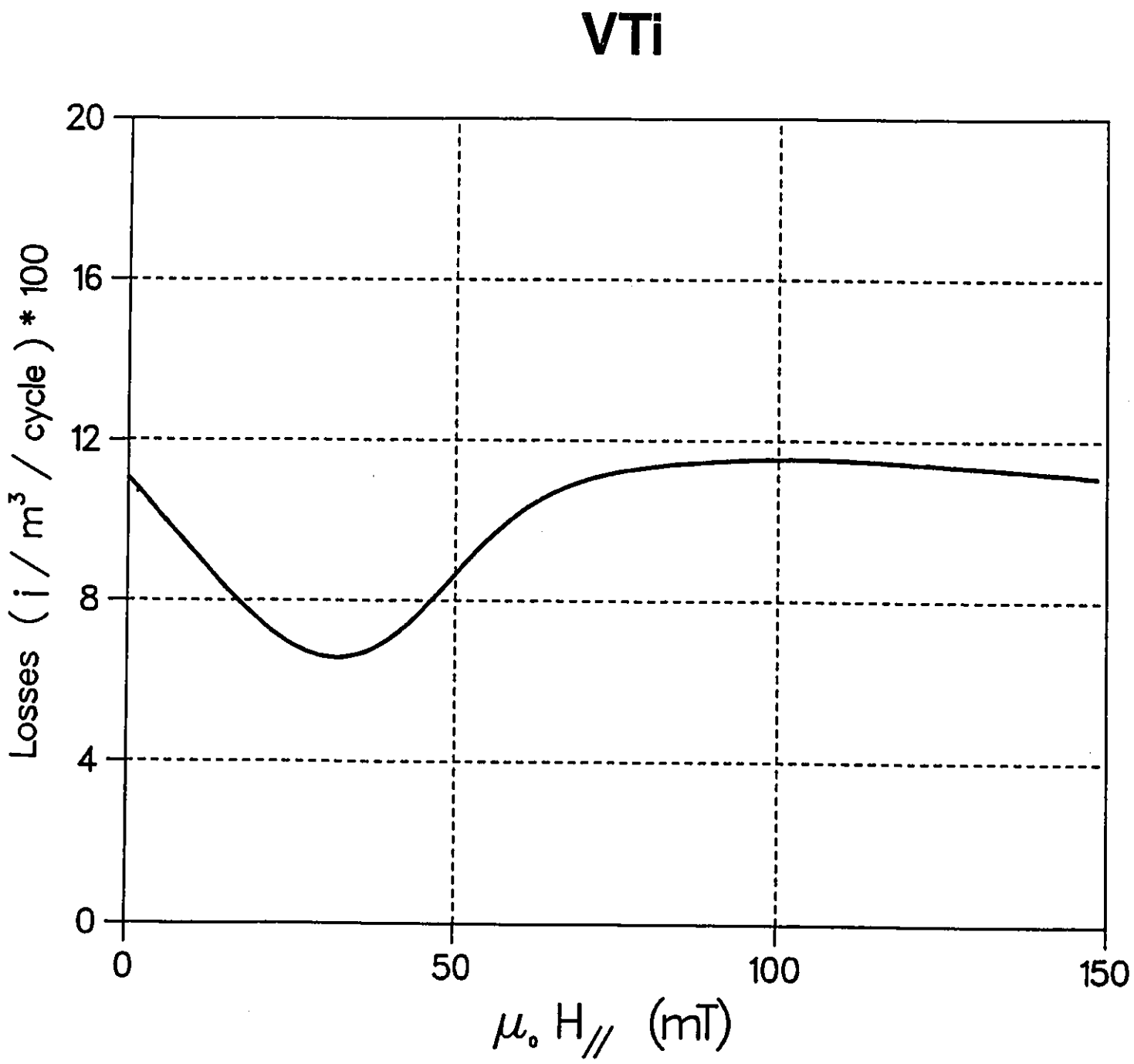

Figure 24: Typical Clem valley. Displays hysteresis losses observed with a constant amplitude ($\mu_o h_o = 45\,mT \approx \mu_c H_\star$) vs. a bias magnetic field $H_{||}$ directed along h_o. Data curve for VTi is copied from Lorrain's thesis

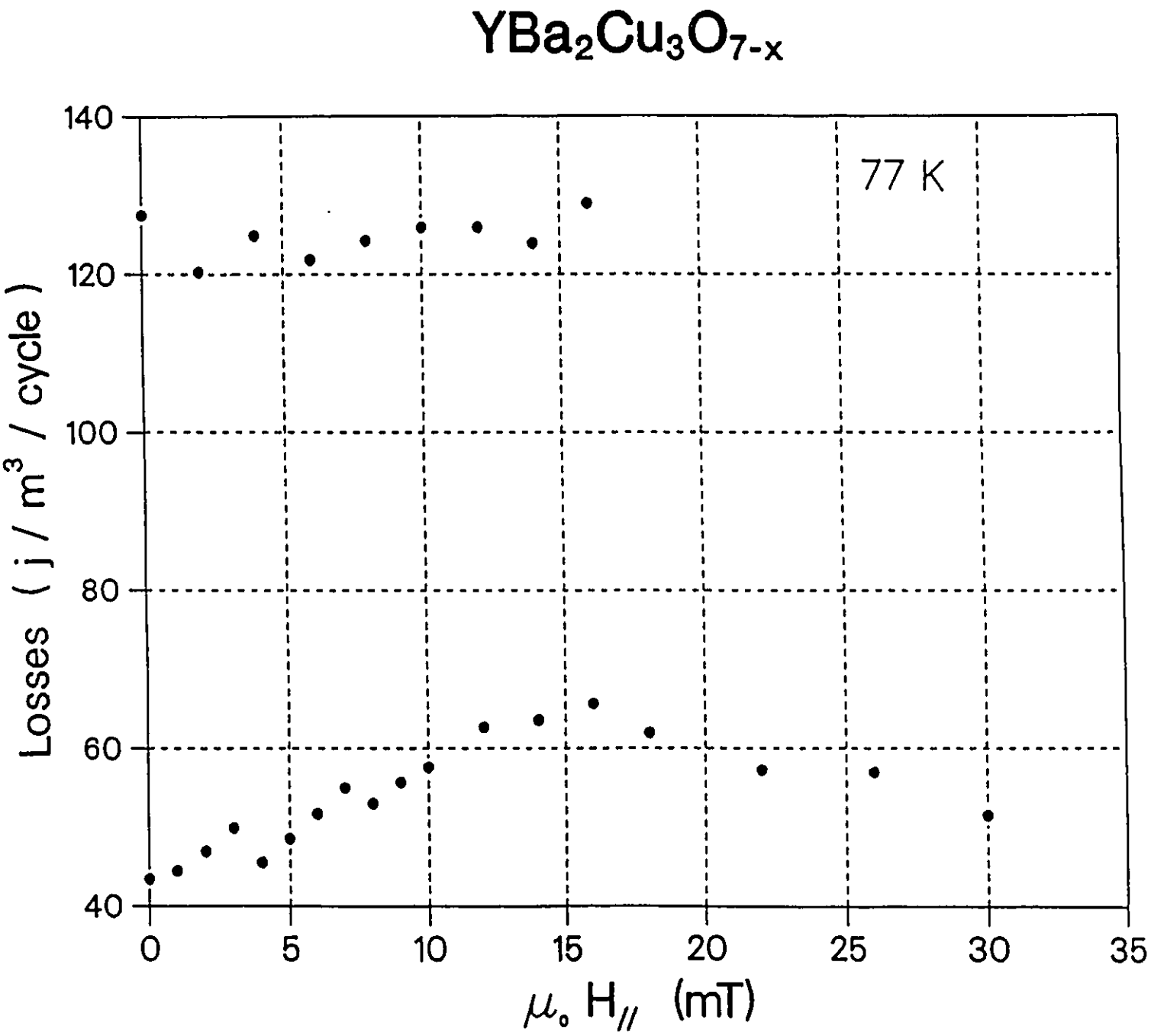

Figure 25: Hysteresis losses measured for $YBa_2Cu_3O_{7-x}$ ribbon versus bias field $H_{||}$ directed along the length of the sample and the varying field of amplitude $\mu_o h_o = 8\,mT < \mu_o H_*$ for the upper data points and $5\,mT$ for the lower data points.

Chapter 6

Flux Trapping in Sintered High T_c Specimens

6.1 Introduction

In principle, the maximum residual trapped flux, or equivalently, the largest remanent magnetic moment exhibited by a type II superconductor provides a relatively direct and clear measurement of the capacity of the specimen to support persistent circulating currents in zero externally applied magnetic field H_a. Although H_a is zero, the circulating lossless currents bathe in the magnetic field which they themselves generate, hence $< H(x) >$ and $< B(x) >$, the spatial averages of the magnetic field and magnetic flux density can be appreciable. Indeed, according to prevailing views, $B(x)$ at the peak(s) of the trapped flux profile will attain $\mu_o H_\star$. Although, neither the $B(x)$ profiles nor its peak values are readily accessible to measurement, the spatial average of the trapped flux is easily determined and can readily be analyzed to yield $< j_{c\perp} >$, the spatial average of the depinning critical

current density for the corresponding range of B.

Two standard procedures or paths in the $H - T$ plane are generally followed to generate the residual magnetic moment. We will describe these processes below and show that one procedure leads to a determination of H_*. The other approach yields a measurement of H_{**}, which we have seen, is related to H_*. Both H_* and H_{**} contain information on and readily lead to estimates of $< j_{c\perp} >$ over the range $0 < B < \mu_o H_{**}$. These various routes have been exploited in the study of classical type II superconductors and provide results in agreement with each other and with answers obtained via other techniques. In the light of this self-consistency and harmony, the critical state picture has become firmly entrenched and universally accepted.

We have pursued two standard procedures for trapping flux in our high T_c specimens. The critical state model is seen to describe the "evolution" of the trapped flux as a function of the excursions of H_a remarkably well in both instances. We encounter, however, a major discrepancy between the magnitude of the residual magnetization and the excursions of the magnetic field required to achieve these results. We argue that either, the enshrined critical state picture must be radically reformed or that an appropriate calibration of the residual magnetization be introduced. We propose that self-consistency be allowed to dictate the answer. This, in our view, means that the calibration of the magnetization needs to be amended and adjusted.

6.2 Procedure and Results

First we describe the two standard procedures followed to trap the flux and thereby generate the residual magnetic moments. These are conveniently called the field cooled and the field cycling approach and labeled H_{cool} and H_{cycle} procedures.

H_{cool} Procedure, H^*_{cool} and H_*.

As the name indicates, in the field cooled approach, the sample is allowed to cool from T_c to the ambient temperature T in a static magnetic field H_a denoted H_{cool}. Some of the magnetic flux permeating the specimen is expelled by the Meissner effect during the cooling. Subsequently H_{cool} is removed. This generates persistent currents which attempt to retain the magnetic flux inside the specimen. Since $j_{c\perp}$ is finite, however, the induced persistent currents will allow some of the magnetic flux threading the specimen after the Meissner flux expulsion to escape now. Figs. 26 (a) and (b) schematically display the B profiles envisaged to exist in the specimen after H_{cool} has been removed. The residual amount of flux trapped in the specimen by pinning, hence by the circulation of $j_{c\perp}$, will evidently depend on H_{cool}. The variation of the amount of trapped flux with H_{cool} is illustrated in Figs. 26 (a) and (b). These sketches apply either to the individual grains when these are electrically isolated or to the entire slab specimen when it is responding as a single connected entity.

The essential features relating the amount of trapped flux to H_{cool} are now listed and described. We note that, here the remanent magnetic moment and the residual trapped flux are identical ($H_a = 0$). Also, since $H_a = 0$, the residual magnetic flux density $< B >_{res}$ and $\mu_o < M >_{res}$, the remanent magnetizations are the same.

- According to the critical state concept and the laws of electromagnetic induction, the B profile in the volume from which flux has leaked out or escaped when H_{cool} was removed, will exist in a critical state where the flux retaining persistent circulating current density $j_\perp = j_{c\perp}$ and $dB/dx = (dB/dx)_c$.

- A "core" region may exist from which no flux escaped during the removal of H_{cool}. As H_{cool} is removed, the configuration of the magnetic flux (B profile) remains unchanged in this core volume. This is possible because this core volume is protected from experiencing the surrounding events by the induced circulating persistent currents which embrace it. The magnitude and configuration of the B profile in this "core" volume are determined by the strength of H_{cool} and the corresponding Meissner effect.

- No "core" region will remain after removal of a very large H_{cool} since, under these circumstances, some flux will have escaped from the entire specimen and its entire volume will be filled with flux retaining, persistent, circulating currents at the critical density, $j_{c\perp}$. This is referred to as the saturated critical state (see dashed-solid curve in Fig. 26 (b)).

- There is therefore a threshold or minimum H_{cool}, denoted H^*_{cool}, which will ensure that a saturated critical state is established after H_a is removed. Let B_* denote the magnetic flux density at the center or peak(s) of the resulting B profile. We note that when $H_a = H_*$ is applied to a virgin specimen, the magnetic flux density just inside the surface will correspond to B_* and the B profile will descend from this value at the surface to zero at the center of the specimen. In other words, the B profile just described is an image or reversed

saturated state. Consequently,

$$H^*_{cool} \lesssim H_\star \tag{36}$$

- Choosing $H_{cool} > H^*_{cool}$ will not lead to any increase in the residual trapped flux since now, upon reducing H_a to zero, the specimen is left, in every case, in the same saturated critical state. We therefore, expect and find that a plot of the residual trapped flux versus H^*_{cool} will map out a plateau. The edge of this plateau defines H_{cool}, hence provides a good approximation to $H_\star$. The solid circles in Fig. 27 display our data for the Yttrium specimen. The Nd sample exhibits similar behaviour.

H_{cycle} Procedure, H^*_{cycle} and $H_{\star\star}$

In this procedure, the virgin specimen is subjected to one excursion or swing of the externally applied magnetic field. Here the latter is made to vary from zero to H_a and then back to zero, hence the label H_{cycle} for H_a under these circumstances. Evidently, H_{cycle} may range from very small to beyond H_{c2}.

When H_{cycle} exceeds H_{c1}, magnetic flux is made to enter the specimen and some of this flux will be retained (imprisoned or trapped) by the sample after the cycle is completed. Figs. 26 (c) through (e) schematically display the configurations of the magnetic flux density (B profiles), (i) when H_{cycle} attains the top of its excursion (upper solid curves) and, (ii) after the swing has been completed (shaded areas). Clearly, the amount of the residual flux grows as the magnitude of H_{cycle} is chosen larger. However, a saturated critical state will be generated by this procedure when H_{cycle} exceeds a threshold level denoted H^*_{cycle}.

This saturated critical state where the specimen is filled with flux retaining,

persistent, circulating currents $j_\perp$ at the critical density $j_{c\perp}$ will be identical to that achieved in the H_{cool} procedure.

We then expect a plot of the residual trapped flux versus H_{cycle} to attain and trace a plateau. Also we anticipate that the height of this plateau should correspond to that encountered through the H_{cool} procedure when $H_{cool} > H^*_{cool}$. The edge of this plateau defines H^*_{cycle}. An examination of Fig. 26 (f) and the configuration of magnetic flux which is established when H_a attains $H_{\star\star}$ reveals that

$$H^*_{cycle} = H_{\star\star} \tag{37}$$

This procedure just outlined therefore provides another method of determining $H_{\star\star}$. (In chapters 1 and 3, we described a criterion or procedure for measuring this quantity.)

6.3 Results and Discussion

Our data on flux trapping with the H_{cool} and H_{cycle} procedures for the Yttrium specimen are displayed in Fig. 27 . We note that both procedures generate a plateau and that the two plateaus overlap as expected. We estimate where the edges of the two plateaus occur and thus evaluate $\mu_o H^*_{cool} \approx 18\,mT$ and $\mu_o H^*_{cycle} \approx 26\,mT$. As anticipated, these values correspond respectively with $H_\star$ and $H_{\star\star}$ determined by other procedures in chapter 3. The Nd specimen shows similar behaviour and agreement.

Two sets of values are indicated for the residual magnetizations. As indicated in chapter 3, many workers base the calibration of sintered samples on the diamagnetic response of the virgin specimen in the weak field region below the "hump" structure.

The set of smaller numbers on the right side correspond to this calibration criterion. The set of larger numbers on the left are based on the magnetic momemt observed immediately after the "hump" structure in the initial magnetization. As discussed previously, the latter procedure assumes perfect shielding by the isolated grains, in the low field range. Let $< M >_r^{'}$ denote the former and $< M >_r^{''}$ the latter values for the remanent magnetization. We stress that $< M >_{rMax}$, the magnitude of the maximum residual magnetization (i.e. the height of the plateau) based on the $< M >_r^{'}$ scale is grossly inconsistent with the observed H^*_{cool} (hence H_*) and H^*_{cycle} (hence H_{**}). This disparity emerges without detailed calculations since the average density of the trapped magnetic flux should be approximatively 1/2 of B^*.

Detailed calculations of $< M >_r$ require that the appropriate geometry be identified and that the dependence of $j_{c\perp}$ on B be known. The irregular geometry and random orientation of the isolated grains in sintered materials present a formidable, indeed intractable, problem. Answers however can readily be obtained for standard basic geometries, the infinite slab and cylinder with H_a directed parallel to the height or length. In appendix B we develop analytic expressions for $< M >_r$ versus H_{cool} and versus H_{cycle} for both of these geometries.

In order to mathematically model the variety of B profiles sketched in Fig. 26, it is necessary that the variations of the gradient, hence $j_{c\perp}$, be specified. For our analysis we have stipulated that;

$$\mu_o j_{c\perp} = -\left(\frac{dB}{dx}\right)_c = \alpha_B \tag{38}$$

where α is a constant. This is referred to as the Bean-London approximation [2], [36], [44] (or Bean approximation for brevity). We have also explored the behaviour assuming that,

$$\mu_o j_{c\perp} = \left(\frac{dB}{dx}\right)_c = \frac{\alpha_K}{B} \tag{39}$$

This is labeled, the Kim-Anderson approximation [32], [55] (or Kim approximation for brevity). We note that these two approximations constitute extrema for the expected dependence of $j_{c\perp}$ on B. As a consequence the behaviour which ensues from a set of calculations with these two approximations will define the limits of the anticipated response.

The essential features of the derivations and the assortment of closed form expressions which we have obtained in this exercise are presented in appendix B. The curves calculated from these expressions are displayed in Figs. 28 and 29. In the calculation B^* is taken equal to 20 mT and $B_{**} = 28\,mT$. For purpose of comparison with the observations, the calculated residual magnetizations are normalized to the measured value $\mu_o < M >_{rMax} = 3.0\,mT$. We stress that the model does not specify whether the specimen is composed of one single entity (the entire slab sample) or a juxtaposition of isolated identical units (grains or particles) with the idealized geometry.

The theoretical curves are seen to reproduce the experimental behaviour quite well for both the H_{cool} and H_{cycle} procedures. This agreement, in our view, indicates that the basic picture is correct, i.e. the configurations of the B profiles as a function of H_{cool}/H_* and H_{cycle}/H_* develop as predicated. The structure appearing in the low field range of the H_{cycle} data is attributed to flux trapping in the matrix of the sintered high T_c materials by the intergrain persistent circulating currents. This contribution has not been introduced in the model which associates all of the trapped flux with the individual grains. The fact that the Bean approximation yields the best fit to the observations for both procedures in Figs. 28 and 29 suggests that the intragrain $j_{c\perp}$ is not sensitive to the magnitude of B in the range $0 < B < B_{**}$.

It is perhaps not surprising that the better correspondence between observations

and the model calculations is obtained in the limit of cylindrical geometry. As shown in appendix A, the magnetic behaviour of a square or cylindrical specimen when B is parallel to their lengths will be identical. The square, however, is readily seen to constitute the limiting case, $b/a = 1$ of the rectangular geometry where b is the width and a is the thickness. The infinite slab, where $b/a = \infty$ represents the other limit. Clearly, a finite ratio $\gtrsim 1$ better corresponds to reality. The finite length of the grains is expected to cause the pertinent variable, H/H_*, to scale by a constant average demagnetization coefficient but should not affect the shape of the calculated curves.

The predictions of the model for the magnitude of the maximum remanent magnetization $\mu_o < M >_{r\,Max}$, normalized to B^*, are tabulated in table 4.

$\mu_o < M >_{r\,Max}/B^*$	Slab	Cylinder
Bean approximation	1/2	1/3
Kim approximation	2/3	8/15

Table 4: Normalized Parameters

We note that the Bean approximation for cylinder (square or rectangular) geometry which leads to the best correspondence with the data in Figs. 28 and 29, also yields the smallest value for $< M >_{r\,Max}/B^*$. This smallest value is nevertheless appreciably too large if the $< M >_r'$ calibration is introduced but corresponds adequately to the $< M >_r''$ calibration.

6.4 Conclusion

The amount of flux trapped in sintered high T_c materials using two different procedures is seen to depend on H_{cool} and H_{cycle} in accordance with the predictions of the critical state model. These data provide estimates of $H_\star$ and $H_{\star\star}$ in agreement with that obtained from other types of magnetization measurements. Comparison of the model calculations with the data indicate that the intragrain $j_{c\perp}$ diminishes only slightly with B in the low field range. The magnitude of the maximum residual magnetization confirms that the calibration stipulating perfect shielding by isolated particles after the hump structure in the initial magnetization curve to be the more appropriate.

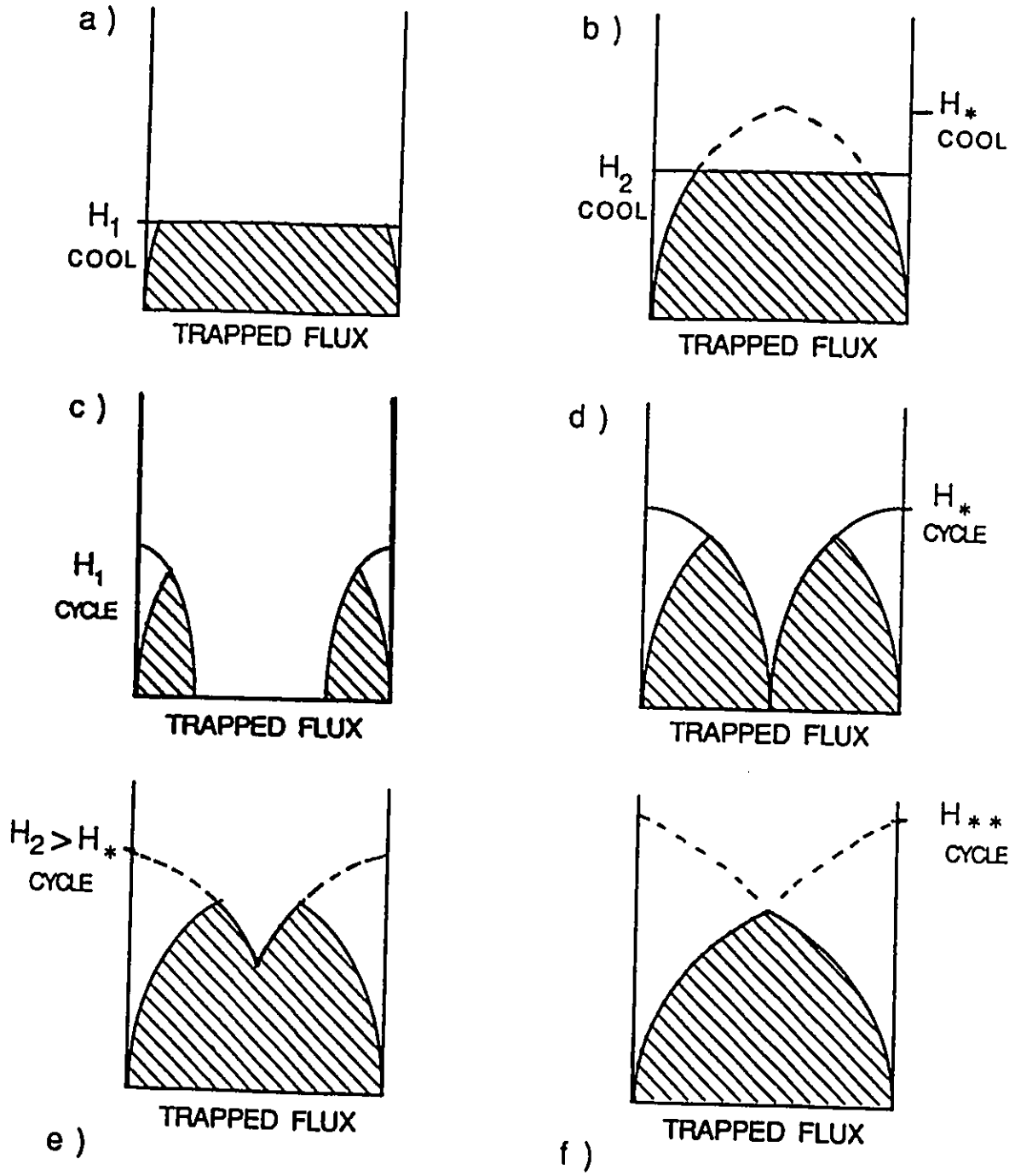

Figure 26: Schematics representing sequences of B profiles in H_{cool} and H_{cycle} procedures.

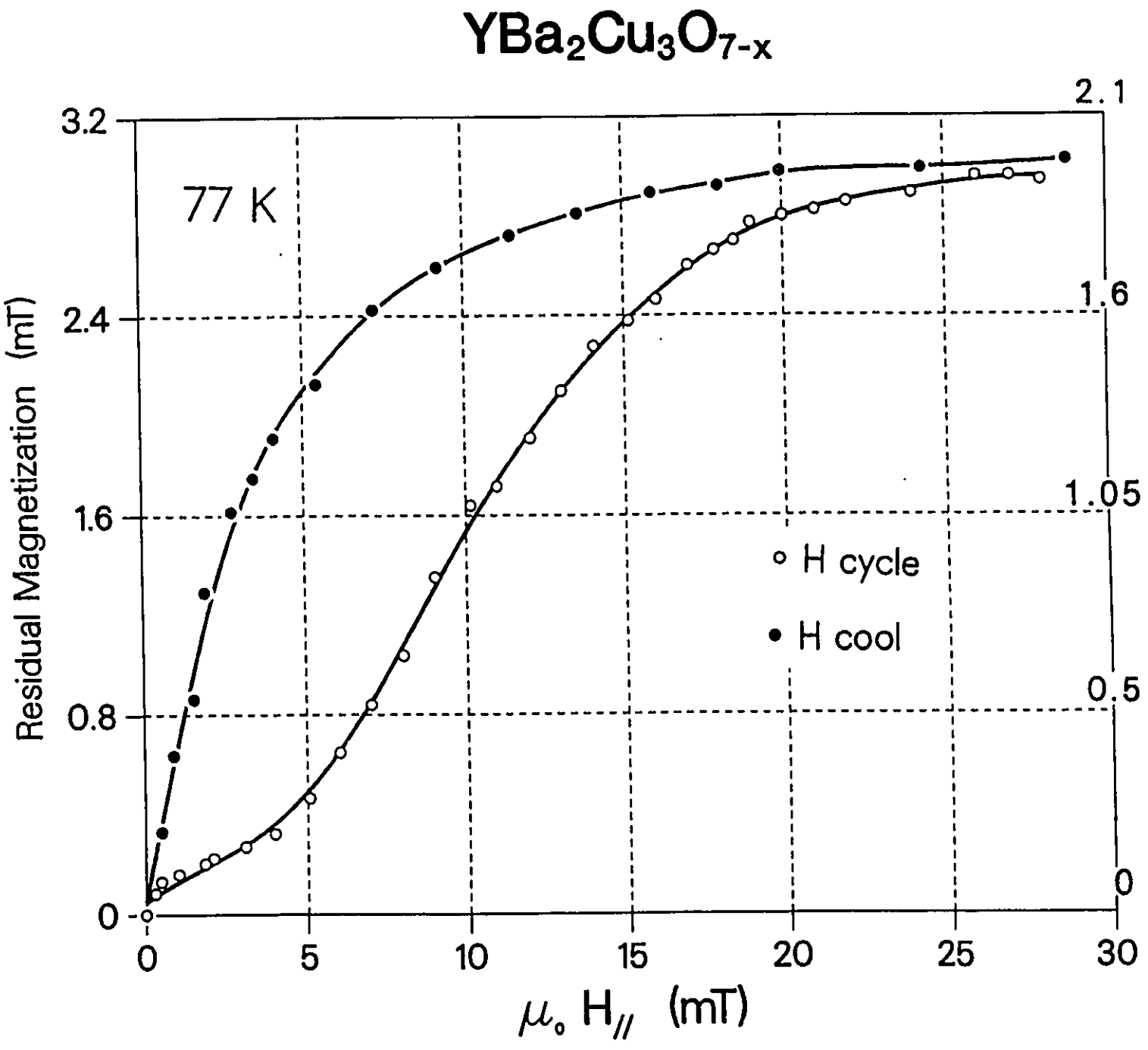

Figure 27: Evolution of the residual trapped flux with H_{cool} and H_{cycle} measured for the $YBa_2Cu_3O_{7-x}$ specimen at 77 K.The full and empty circles represent the experimental data for the H_{cool} and H_{cycle} measurements respectively.

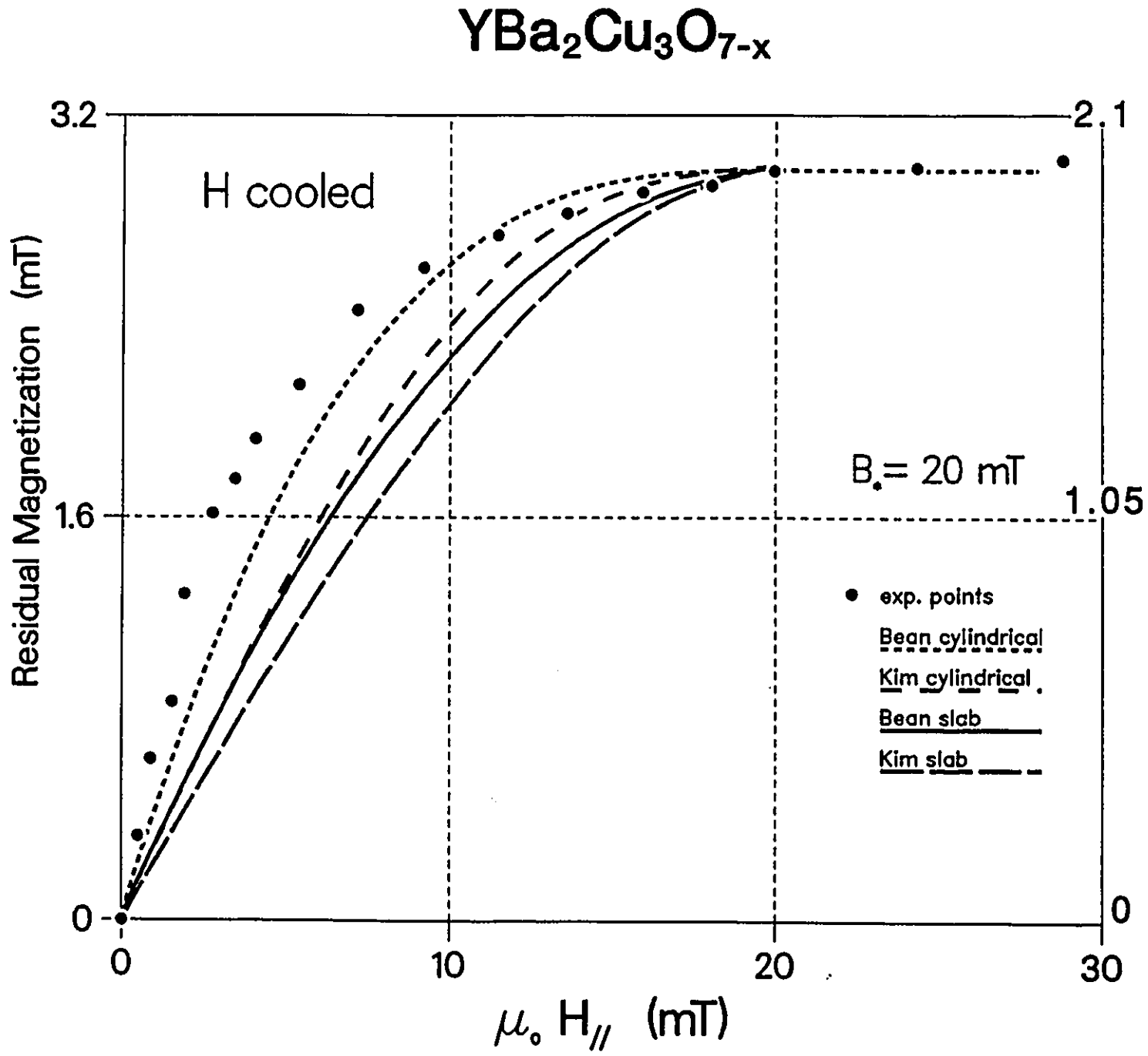

Figure 28: Comparison of the observed evolution of the residual magnetization versus H_{cool} with that predicted by the critical state model for the infinite slab and cylinder exploiting the Bean and the Kim approximations.

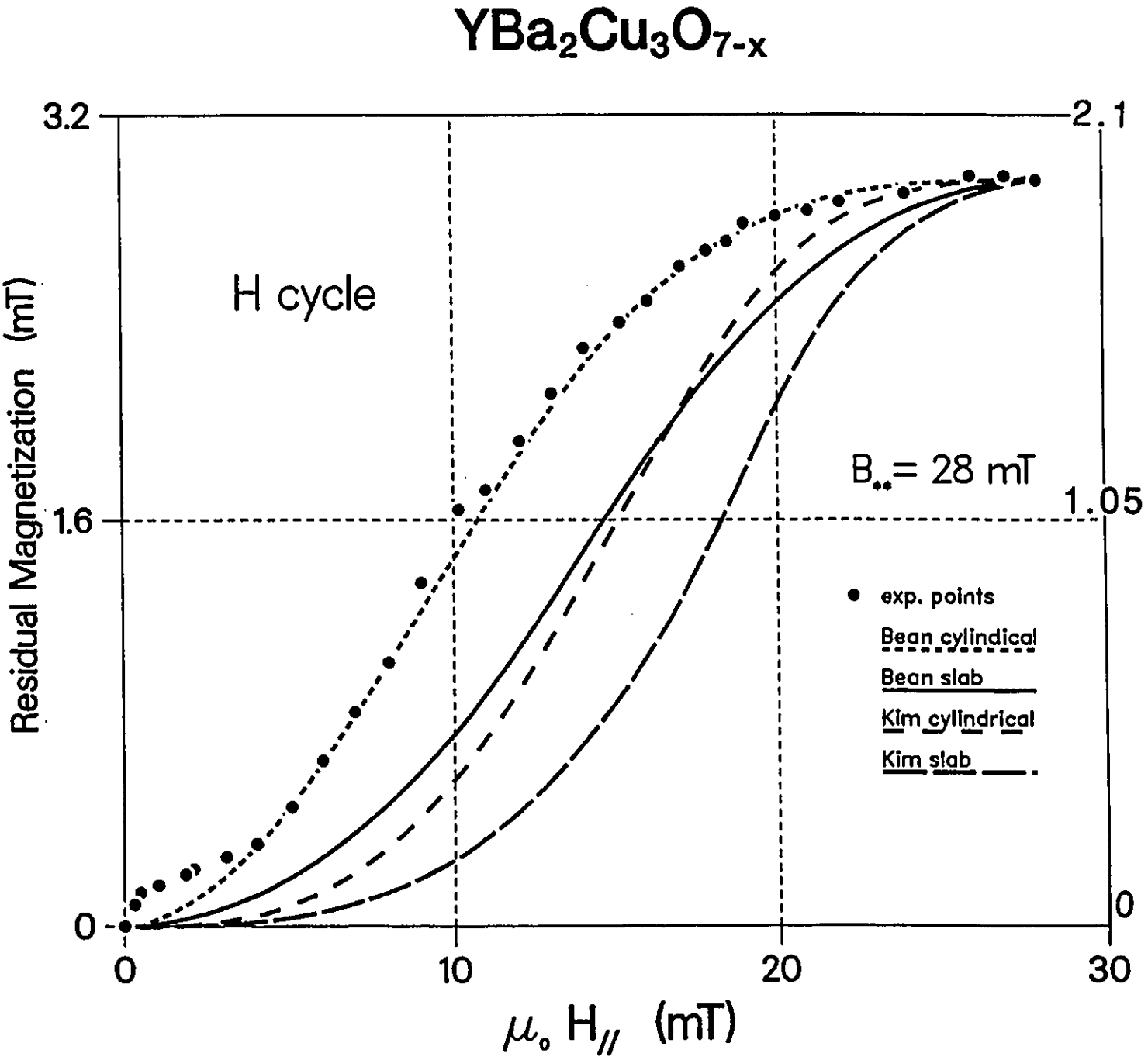

Figure 29: Comparison of the observed evolution of the residual magnetization versus $\mathbf{H_{cycle}}$ with that predicted by the critical state model for the infinite slab and cylinder exploiting the Bean and the Kim approximations.

Chapter 7

I_b and I_M from Magnetization Curves

7.1 Introduction

The magnitude of the magnetic moment of type II superconductors provides information on the depinning critical current provided that the entire volume of the specimen is occupied by critical persistent currents circulating in the same sense. These configurations are labeled saturated critical states. These configurations are encountered only when the locus of the magnetization is situated on either the upper or the lower envelope (or branches) of the major hysteresis curves. In this chapter we will develop expressions relating these saturated magnetic moments to the bulk and surface critical currents.

In the previous chapter we have focused on a special case where by following specific procedures in the $H-T$ plane, the specimen is filled with a residual trapped flux at $H_a = 0$. In these situations when the maximum residual trapped flux is

generated, the sample is occupied by persistent critical currents flowing in a flux retaining sense.

In the introductory chapter we have shown that ΔH_c, the sweep of H_a required to cause the locus of the magnetization to migrate from the upper to the lower magnetization envelope (or vice versa) causes a reversal in the sense of circulation of the bulk and surface critical currents over the entire volume of the specimen. Consequently, ΔH_c also contains information on these quantities.

Since the magnitude of the magnetization along the envelopes and ΔH_c are interrelated and complementary quantities, these data should yield consistent and harmonious results. In the literature on sintered high T_c materials, workers have concentrated on the magnetic moments and ignored the associated ΔH_c. More disturbing, however, when the data on ΔH_c is displayed, it is on careful inspection found not to be in accord with the reported magnitudes of the magnetization by factors which can approach an order of magnitude. In this chapter we report on our observations and again argue that much of the discrepancy may arise from an inappropriate calibration.

7.2 Observations

We focus attention on the high T_c samples at 77 K and the *PbIn* since these exhibit similar semi-reversible magnetic behaviour. Figs. 30 and 31 again display the evolution of the magnetic moment for various important paths in the $H-T$ plane already discussed in some detail in previous chapters. The new feature which we address in this chapter are the minor hysteresis loops which exactly span the distance between the upper and lower envelopes (branches) of the major hysteresis

curve. Only a few such minor hysteresis loops are shown although many others were measured. These illustrate the important features without cluttering the figures. The *Nd* and *Y*ttrium high T_c samples exhibited identical behaviour but only the former is displayed to avoid repetition.

7.3 Discussion and Analysis

7.3.1 Framework of the Analysis

We focus on the magnetic moments at the end or reversal points of the minor hysteresis loops. Since these loops were measured to just bridge the separation between the envelopes of the major hysteresis loop, these end points also belong to the family of magnetic moments of the envelopes. This means that the critical persistent circulating currents all flow in the same sense throughout the volume of the specimen, all either opposing entry of magnetic flux at the upper end or all opposing exit of flux at the lower end.

For completeness, two types of critical currents need to be considered.

- A bulk critical current I_b flowing in the volume of the specimen and associated with flux line pinning, hence an appropriate spatial integral of $j_{c\perp}$.
- A thermodynamically irreversible critical surface current I_s.

The latter is seen to occur in the *PbIn* specimen but shows no evidence of existing in the high T_c samples under the circumstances under scrutiny.

The Meissner current I_M is a thermodynamically reversible current in equilibrium with H_a, hence is not regarded as a "critical" current. This current, as is well

known, always flows in a diamagnetic (field shielding) sense.

The symbols I_b, I_s and I_M each denote a total current circulating in the $x-y$ plane per unit length along z with H_a directed along the z axis. We note that in *S.I.* units, the magnetization $< M >$ (magnetic moment μ per unit volume V), H and I have the same units. This leads to very simple and transparent relationships.

To avoid some complications which arise when $H_a < H_{c1}$, we will confine our analysis to situations where $H_a > H_{c1}$. Here, the sintered high T_c specimens behave as a collection of electrically isolated particles. The expressions we develop will apply either to one "representative" grain of idealized geometry and orientation in the case of these materials or to the entire slab in the case of the *PbIn* specimen.

Let $M_\uparrow$ and $M_\downarrow$ denote the magnetization $< M >$ along the upper and lower envelopes and $H_\uparrow$ and $H_\downarrow$ the corresponding externally applied magnetic field. Let I'_M, I'_b and I'_s denote the Meissner, bulk and surface currents corresponding to $M_\uparrow$, hence $H_\uparrow$, and these double primed quantities for $M_\downarrow$, hence $H_\downarrow$.

Examination of the minor hysteresis loops displayed by the *PbIn* sample reveals that there are sections where the locus of $< M >$ versus H_a is linear and possesses a slope $d < M > / dH_a = -1$. We recall that, $< B >= \mu_o H_a + \mu_o < M >$, hence, $d < M >= -dH_a$, means that $d < B >= 0$. Consequently, the magnetic flux permeating the sample is not changing (except in a minute surface region occupied by the surface current), over the corresponding sweep of H_a. This is the clear signature of a thermodynamically irreversible surface current opposing flux entry when H_a is increasing and flux exit when H_a is decreasing. The minor hysteresis loops of the sintered high T_c materials show no such behaviour. Consequently, we conclude that here I'_s and I''_s are either negligible or zero. As noted previously, this is not surprising, since the magnetic field pierces most of the surface of each grain.

The expressions we develop, will however, for completeness, include I_s' or I_s''.

7.3.2 Simple Expressions for < M >

The "specimen" is visualized to be either, (i) an idealized slab of half thickness X, infinite width along the y axis and infinite heigth along the z axis, or (ii) a solid cylinder of radius R, infinitely long along the z axis. The symbols Y and Z denote arbitrary segments along these respective axis. The quantities $\vec{M}$, $\vec{B}$ and $\vec{H}_a$ are taken to be collinear and directed along the z axis, hence orientation subscripts will usually be omitted.

The idealized planar (slab) geometry is taken to apply to the $PbIn$ specimen and all homogeneous and continuous type II superconducting ribbon samples very large compared with λ. The cylindrical geometry constitutes a limiting case of the infinite slab. Intermediate objects are infinitely long rectangular slabs of width b and thickness a. The results obtained when $b = a$, hence the specimen is a square rod are identical to that for the cylinder of radius $R = a = b$ (see appendix A). Thus the latter limit is regarded as a simple albeit crude, attempt to describe an electrically isolated grain.

Inspection of the magnetization curves reveals that $< M >$ along the envelopes varies quite slowly as a function of H_a, hence $j_{c\perp}$ as well as I_M and I_s are not sensitive to the magnetic flux density in the range $H_a > H_{c1}$. (We have already seen that $j_{c\perp}$ is nearly independent of B even in the range $0 < H_a \lesssim H_\star$.) Consequently, for simplicity, we will assume $j_{c\perp}$ to be uniform (Bean approximation).

Expressions for the magnetization $< M >$ can be developed in two different but complementary contexts.

i) The framework is the well known relationship

$$< M > = \frac{< B >}{\mu_o} - H_a \tag{40}$$

The exercise then consists in deriving expressions for $< B >$, exploiting the definitions,

$$< B_z > = \frac{1}{X} \int_0^X B_z(x)\, dx = \frac{1}{\pi R^2} \int_0^R B_z(r)\, 2\pi r\, dr \tag{41}$$

where the midplane of the slab is situated at $x = 0$ and the surface at $x = X$.

The Maxwell-Ampere equation, $\nabla \times \vec{B} = \mu_o \vec{j}$ and the critical state concept lead to,

$$\begin{aligned} B_z(x) - B_z(X) &= \int_X^x \frac{dB_z}{dx}\, dx = \pm \mu_o \int_X^x j_{c\perp}(x)\, dx \\ B_z(r) - B_z(R) &= \int_R^r \frac{dB_z}{dr}\, dr = \pm \mu_o \int_R^r j_{c\perp}(r)\, dr \end{aligned} \tag{42}$$

The + sign applies when $j_{c\perp}$ flows to retain flux (lower magnetization envelope), the − sign when $j_{c\perp}$ flows to oppose flux entry (upper branch).

Introducing eqn 42 into 41 and exploiting the Bean approximation leads to,

$$< B_z > = B_z(X) \pm \mu_o j_{c\perp} \frac{X}{2} = B_z(R) \pm \mu_o j_{c\perp} \frac{R}{3} \tag{43}$$

We note that the change in geometry causes the coefficient in the second term to vary from 1/2 to 1/3. These numbers therefore bracket the possible range under transformation of the specimen from a slab to a square or circular rod.

Introducing the surface currents I_M and I_s into the Maxwell-Ampere equation leads to,

$$H_a - \frac{B_z(X)}{\mu_o} = I_M \pm I_s = H_a - \frac{B_z(R)}{\mu_o} \tag{44}$$

Noting that,

$$I_b = < j_{c\perp} > X = < j_{c\perp} > R \tag{45}$$

We rewrite eqn 43 to read,

$$\frac{< B_z >}{\mu_o} = H_a - I_M \pm I_s \pm f I_b \tag{46}$$

Hence returning to eqn 40 we obtain

$$M_\uparrow = - I_M - I_s' - f I_b' \tag{47}$$

$$M_\downarrow = - I_M + I_s'' + f I_b'' \tag{48}$$

where f varies between 1/3 and 1/2 depending on the choice of geometry. Eqns 47 and 48 are depicted schematically in Fig. 32 (a) and (b).

When the specimen has cooled in a static field $H_a > H_{c1}$, the Meissner effect magnetization; M_M can be written,

$$M_M = - I_M + I_s'' + f I_b'' \tag{49}$$

Here, the surface current I_s'' and the bulk current I_b'' oppose the expulsion of the flux lines. This is identical to eqn 48 and applies when the peak of the B profile lies below $\mu_o H_a$. This is the configuration which must arise when the Meissner magnetization is observed to coincide with the lower envelope (see Figs. 30 and 31). Stated mathematically, this condition reads,

$$I_M > I_s'' + f I_b'' \tag{50}$$

We have presented evidence that $I_s \approx 0$ in sintered high T_c materials, presumably because the magnetic field pierces most of the grain surface. Consequently here, eqn 50 is qualitatively and semi quantitatively very instructive since it provides an upper limit for the intragrain bulk pinning current, namely,

$$I_b < \frac{I_M}{f} \tag{51}$$

The Meissner current I_M, however, can never exceed H_{c1}. Taking $\mu_o H_{c1} \approx 10\,mT$, and estimating the average grain radius R or thickness X to be ≈ 10 microns leads to a maximum $j_{c\perp} \approx (2 \text{ or } 3)\,10^9\,A/m^2$ at 77 K, quite an appreciable upper limit.

Now, since the $< M >$ versus H descending curve (the lower envelope) falls below the Meissner flux expulsion when $H_a \lesssim H_{c1}$, (see Fig. 30) we can conclude that the B profiles change from the lower to the upper configuration sketched in Fig. 32(d) when $H_a \approx H_{c1}$. Therefore, when $H_a \approx H_{c1}$, hence $I_M \approx H_{c1}$, eqn 50 becomes an equality for the high T_c materials (and the $PbIn$ also). Thus the upper limit evaluated above corresponds to the actual estimate. In the case of the $PbIn$ specimen, since here the pertinent dimension is the thickness $X \approx 1\,mm$, the same considerations and estimate for H_{c1} lead to $j_{c\perp} \approx 2 \times 10^7\,A/m^2$. This is much too modest a value for applications whereas the estimate for the high T_c materials approaches the range required for technological applications.

ii) An alternative framework for developing expressions for $M_\uparrow$, $M_\downarrow$ and M_M is provided by the following definitions. The magnetization can be written,

$$\vec{M} = \frac{\vec{\mu}}{V} \tag{52}$$

where $\vec{\mu}$ is a magnetic moment occupying a volume V. The total magnetic moment $\vec{\mu}$ may be regarded as the sum or integral of constituents, thus ,

$$\vec{\mu} = \sum \Delta\vec{\mu} \tag{53}$$

where,

$$\Delta\vec{\mu} = \vec{A}\,\Delta I \tag{54}$$

Here $\vec{A}$ is the area embraced by the element of current ΔI. For critical currents circulating in the bulk, this reads

$$\Delta I = \vec{j}_{c\perp} \cdot \Delta\vec{S} \tag{55}$$

Again, we stipulate that $\vec{M}$, $\vec{B}$ and $\vec{H}$ are collinear and directed along the $z-axis$ and we will now omit the vector notation.

For cylindrical geometry where,

$$A = \pi r^2 \qquad V = \pi R^2 Z \qquad \Delta S = Z \Delta r \tag{56}$$

the magnetization $< M >_b$ arising from the persistent currents circulating in the bulk, using eqns 52 through 56, reads,

$$< M >_b = \frac{\int_0^R (\pi r^2) (j_{c\perp} Z \, dr)}{\pi R^2 Z} = \frac{j_{c\perp} R}{3} = \frac{I_b}{3} = f I_b \tag{57}$$

when $j_{c\perp}$ is taken to be uniform.

For planar geometry where,

$$A = 2xY \qquad V = 2XYZ \qquad \Delta S = Z \Delta x \tag{58}$$

and again assuming $j_{c\perp}$ to be uniform, the set of definitions lead to,

$$< M >_b = \frac{\int_0^X (2xY) (j_{c\perp} Z \, dx)}{2XYZ} = \frac{j_c X}{2} = \frac{I_b}{2} = f I_b \tag{59}$$

The surface currents I_M and I_s embrace the total area

$$A_t = \pi R^2 \qquad \text{or} \qquad A_t = 2XY \tag{60}$$

thus generate magnetic moments,

$$\mu_M = I_M A_t Z \qquad \text{and} \qquad \mu_s = I_s A_t Z \tag{61}$$

Consequently in view of eqn 52, their respective contribution to the magnetization simply reads,

$$I_M \qquad \text{and} \qquad I_s \tag{62}$$

We stress that I_b, I_M and I_s are currents flowing per unit length Z.

Combining these three contributions to the magnetic moment, hence to the magnetization, eqns 47, 48 and 49 are again obtained for $M_\uparrow$, $M_\downarrow$ and M_M respectively.

7.3.3 Application of the Expressions for < M >

In the literature, a "two tier" perspective is frequently exploited in the analysis of the magnetic behaviour of type II superconductors. Although $j_{c\perp}$ is expected to decrease as a function of B, hence with H_a, in a first approximation, $j_{c\perp}$ is regarded as constant throughout the specimen in a chosen H_a. Consequently, the B profiles are taken to be linear (constant slope). This picture is often called the Bean model. This approximation is valid when ΔB, the maximum variation of B across the B profile satisfies the condition,

$$\Delta B = \mu_o < j_{c\perp} > X \ll < B > \tag{63}$$

However, as the examination of the magnetic moments proceeds along the magnetization envelopes, the slope of the succession of linear B profiles, hence $j_{c\perp}$, are regarded as varying with $< B >$, hence H_a. As a result, estimates of $< j_{c\perp} >$ versus $< B > \approx \mu_o H_a$, yield data on the dependence of $j_{c\perp}$ on B. We will adopt this standard hierarchy of approximations in our analysis.

Taking a pair of $M_\uparrow$ and $M_\downarrow$ measured in the same H_a, equations 47 and 48 can be combined in two ways. This addition yields,

$$\frac{M_\uparrow + M_\downarrow}{2} = -I_M - \frac{(I_s' - I_s'')}{2} - \frac{f(I_b' - I_b'')}{2} \tag{64}$$

For classical type II superconductors, the surface current I_s' opposing flux entry

has been shown to compare in magnitude with I_s'' opposing flux exit for a corresponding H_a, hence, the term,

$$\Delta I_s = I_s' - I_s'' \tag{65}$$

can be neglected.

For the sintered high T_c materials, we have found no evidence of irreversible surface currents, hence $I_s' \approx 0$ and $I_s'' \approx 0$, thus, a fortiori, ΔI_s can be ignored.

Taking $j_{c\perp}$, hence I_b' and I_b'' to be weakly dependent on B, thus letting

$$I_b' = I_b'' = I_b \tag{66}$$

the third term on the right hand side can be dropped. This neglect is further justified by noting that the coefficient $f/2 \approx 1/6$ to $1/4$. Consequently, eqn 64 can be simplified to read,

$$\frac{M_\uparrow + M_\downarrow}{2} = -I_M \tag{67}$$

This is useful and frequently exploited first approximation, valid when $H_a > H_{c1}$ and eqn 63 is satisfied.

Subtraction eqn 47 from 48 yields,

$$M_\downarrow - M_\uparrow = (I_s' + I_s'') + f(I_b' + I_b'') \tag{68}$$

For the *PbIn* specimen and materials with similar behaviour, both terms on the right hand side must be retained. However, taking $I_s' \approx I_s'' \approx I_s$ and $I_b' \approx I_b'' \approx I_b$, eqn 68 can be simplified to read,

$$M_\downarrow - M_\uparrow = 2I_s + 2fI_b \tag{69}$$

For the sintered high T_c materials, eqn 68 reduces to,

$$M_\downarrow - M_\uparrow = f(I_b' + I_b'') \tag{70}$$

since the surface currents I_s' and I_s'' are either absent or suppressed. Again, in the context that $j_{c\perp}$, hence I_b are slowly varying with B, eqn 70 simplifies to,

$$M_\downarrow - M_\uparrow = 2 f I_b \tag{71}$$

This last relationship has been extensively exploited in the recent flurry of research on high T_c materials. Clearly any conclusions regarding I_b which exploit this equation must rely on a valid and appropriate calibration of $M_\downarrow$ and $M_\uparrow$. Care must also be exercised in assigning the correct geometry factor f. For sintered materials, when the grains are electrically uncoupled, the external shape of the specimen will no longer provide the relevant geometry factor.

We now turn our attention to pairs of $M_\uparrow$ and $M_\downarrow$ which are measured at the reversal points of minor hysteresis loops which exactly straddle the magnetization envelopes. Let H_c' denote H_a at the reversal point touching the upper envelope and H_c'' denote H_a for the contact point on the lower envelope. Provided that,

$$\Delta H_c = H_c' - H_c'' < \frac{H_c' + H_c''}{2} \tag{72}$$

we may continue to exploit the expressions developed above although now the magnetic moments no longer correspond to the same H_a.

At first glance it may seem that using $M_\uparrow$ and $M_\downarrow$ measured at the extremes of a minor hysteresis loop where the corresponding H_a are different could introduce some additional inaccuracy compared with the standard situation where $M_\uparrow$ and $M_\downarrow$ are measured in the same H_a. The important feature, however, is that $< B >$, the spatial average of the various B profiles under scrutiny be comparable. An examination and comparison of the pertinent B profiles sketched in Fig. 32 shows that these are comparable in both approaches. Fig. 32 (a) and (b) displays the B profiles for the same H_a while Fig. 32 (c) shows the B profiles at H_c' and H_c''.

The equivalence of these two perspectives also emerges from a consideration of the locus of $< B >$ versus H_a instead of $< M >$ versus H_a. For this reason we display these two modes of presentation side by side in the accompanying sketch.

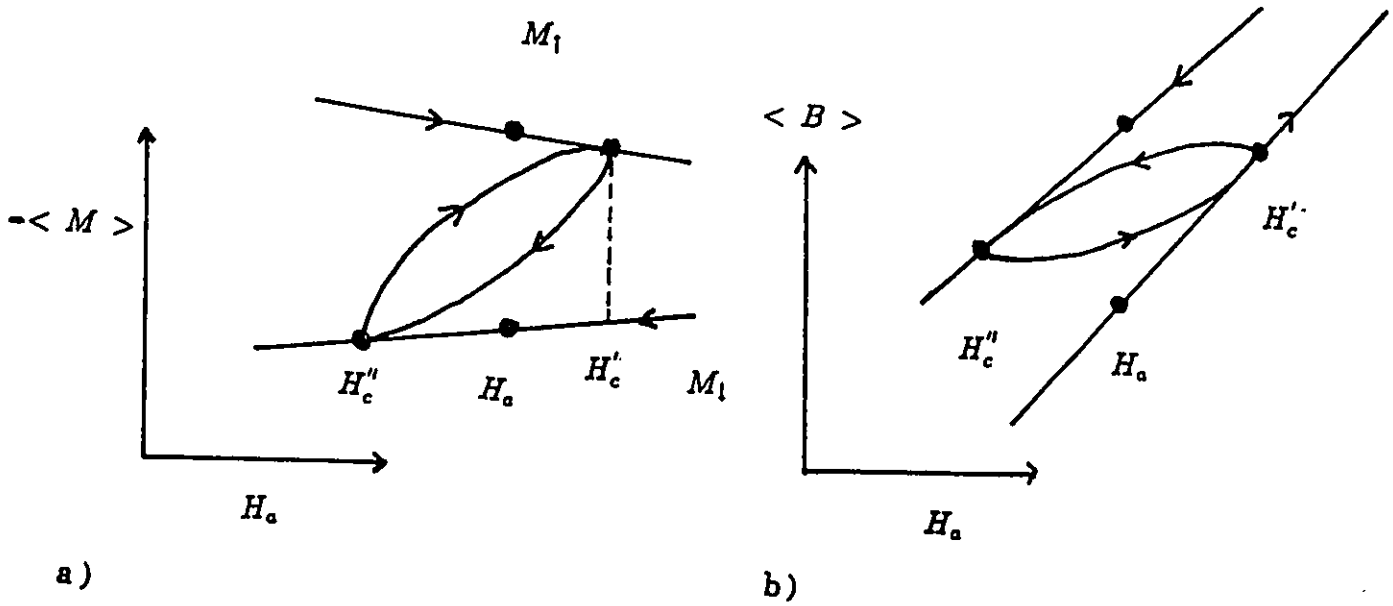

In chapter 1 we have shown that,

$$\Delta H_c = (I'_M - I''_M) + (I'_s + I''_s) + (I'_b + I''_b) \tag{73}$$

We have seen that this follows from combining the Maxwell-Ampere eqn with the critical state picture and can be obtained from careful inspection of Fig. 32 (c) together with the definition,

$$\Delta H_c = H'_c - H''_c \tag{74}$$

In those circumstances where ΔH_c is small compared to the average $H_a = (H'_c + H''_c)/2$, the first bracketed term is negligible and eqn 73 simplifies to,

$$\Delta H_c = 2 I_s + 2 I_b \tag{75}$$

where we have also regarded $I'_s \approx I''_s$ and $I'_b \approx I''_b$. For the $PbIn$ specimen where, $f = 1/2$, is known without any ambiguity from the geometry of the specimen,

equation 75 together with eqn 69 can be exploited to yield both I_s and I_b versus H_a from the data on ΔH_c, $M_\uparrow$ and $M_\downarrow$ from various minor hysteresis loops. Further the estimates of $2\,I_s$ extracted from this exercise can be directly compared with the linear segments of the hysteresis loops. Since $\Delta H_a = 2\,I_s$, this also provides a separate and direct measure. Finally, I_s and I_b obtained from this exercise can be compared with data from four probe (voltage versus current) measurements. For the *PbIn* and other classical type II superconductors, such measurements yield harmonious and consistent results.

For the sintered high T_c materials where I_s is absent or suppressed, eqn 75 reduces to,

$$\Delta H_c = 2\,I_b \tag{76}$$

We stress that eqns 71 and 76 are based on the same physical model, hence are complementary and should be regarded as equally valid. Equations 75 and 76 have been ignored in the recent literature on high T_c materials and attention has focused exclusively on eqns 67 and 71, namely, $M_\uparrow + M_\downarrow = -2\,I_M$ and $M_\downarrow - M_\uparrow = 2\,f\,I_b$. Furthermore, the geometric factor f associated with the external shape of the agglomeration of grains has been used in the analysis. Workers have focused on the envelopes of the magnetization curve and failed to recognize that complementary information is contained in the traversals between the envelopes, hence in minor hysteresis loops which just bridge the magnetization envelopes. In numerous instances, when data on ΔH_c appears in published papers (usually incidentally included), I_b which ensues from application of eqn 76 is appreciably larger, sometimes by almost an order of magnitude, than I_b extracted from the same article using eqn 71.

We examine whether our data on the sintered high T_c materials yields self-consistent information on I_b. The results will be self-consistent when they yield the

same I_b, hence when,

$$\frac{\Delta M_c}{\Delta H_c} = \frac{M_\downarrow - M_\uparrow}{\Delta H_c} = f \tag{77}$$

Some uncertainty exists regarding the appropriate average geometric factor f for the isolated grains in sintered samples. As discussed previously we expect this factor to fall between 1/3 (square or cylindrical rods) to 1/2 (platelets with a large widths / thickness ratio).

We have explored the merits of two different calibrations for the magnetization of our specimens.

- One stipulated perfect shielding against flux entry by lossless currents flowing at the surface of the sample regarded to be homogeneous and electrically connected. This response was associated with the locus of $< M >$ versus H_a below the observed hump structure.

- The other calibration was predicated on perfect shielding by electrically isolated grains. This situation was associated with the locus of $< M >$ versus H_a immediately after the hump feature. The numbers listed on the right (left) of Fig. 31 correspond to the former (latter).

Inspection of the minor hysteresis loops, a few of which are displayed in Fig. 31 by way of illustration, we find $\Delta M_c / \Delta H_c \approx 0.44$ when the calibration shown on the left is used and $\approx$ 0.18 when that on the right is relied upon. The latter falls significantly below the minimum for the expected range. These observations, in our view, again confirm our thesis that the low field calibration is inappropriate for the analysis of the magnetic behaviour of sintered high T_c materials when $H_a \geq H_{c1}$.

7.4 Concluding Remarks

The experimental quantities, ΔH_c and ΔM_c are complementary and intertwined. Recently, workers have focused almost exclusively on ΔM_c. This quantity, however, (i) contains a geometric factor f whose effective value is not known exactly for isolated grains in sintered materials and, (ii) requires an appropriate calibration.

We urge that both quantities be measured and analysed in the established framework to yield self consistent results for I_b. This two pronged approach also provides a check on the validity of the calibration and an estimate of the average geometric factor f of the compact collection of grains in sintered high T_c materials. This two front approach is also applicable and important in the study of single crystal samples and thin films. There is growing evidence that in these cases, internal superconducting boundaries are suppressed by the magnetic field thereby destroying its integrity and homogeneity. As a consequence the specimen becomes a juxtaposition of superconducting islands.

Finally it is important to emphasize that the uncertainty in the calibration pertains to the magnetization $M = \mu/V$, hence the appropriate volume V and not to the magnetic moment μ. Essentially then what is at stake is the correct determination of V_{eff}, the volume (or mass) of the specimen which is superconducting and supporting the persistent circulating currents. It is well known that sintered high T_c materials are porous. The total volume of the pores for our samples is estimated to be ≤ 15 % of the external volume. For the Nd specimen, requiring that the ΔM_c data be consistent with the observations on ΔH_c indicates that $V_{eff} \approx 40\%$ of the external V.

We note that researchers exploiting other techniques for investigating magnetic

properties of type II superconductors (eg. Squid magnetometers, torque magnetometers, Gouy balances, susceptometers, mutual inductance apparatus, etc $\cdots$) do not avoid the problem we have identified and examined. Indeed in all of these techniques, the calibration procedure implicitly or explicitly associates the measured magnetic moment with the external volume (or the total mass) of the specimen.

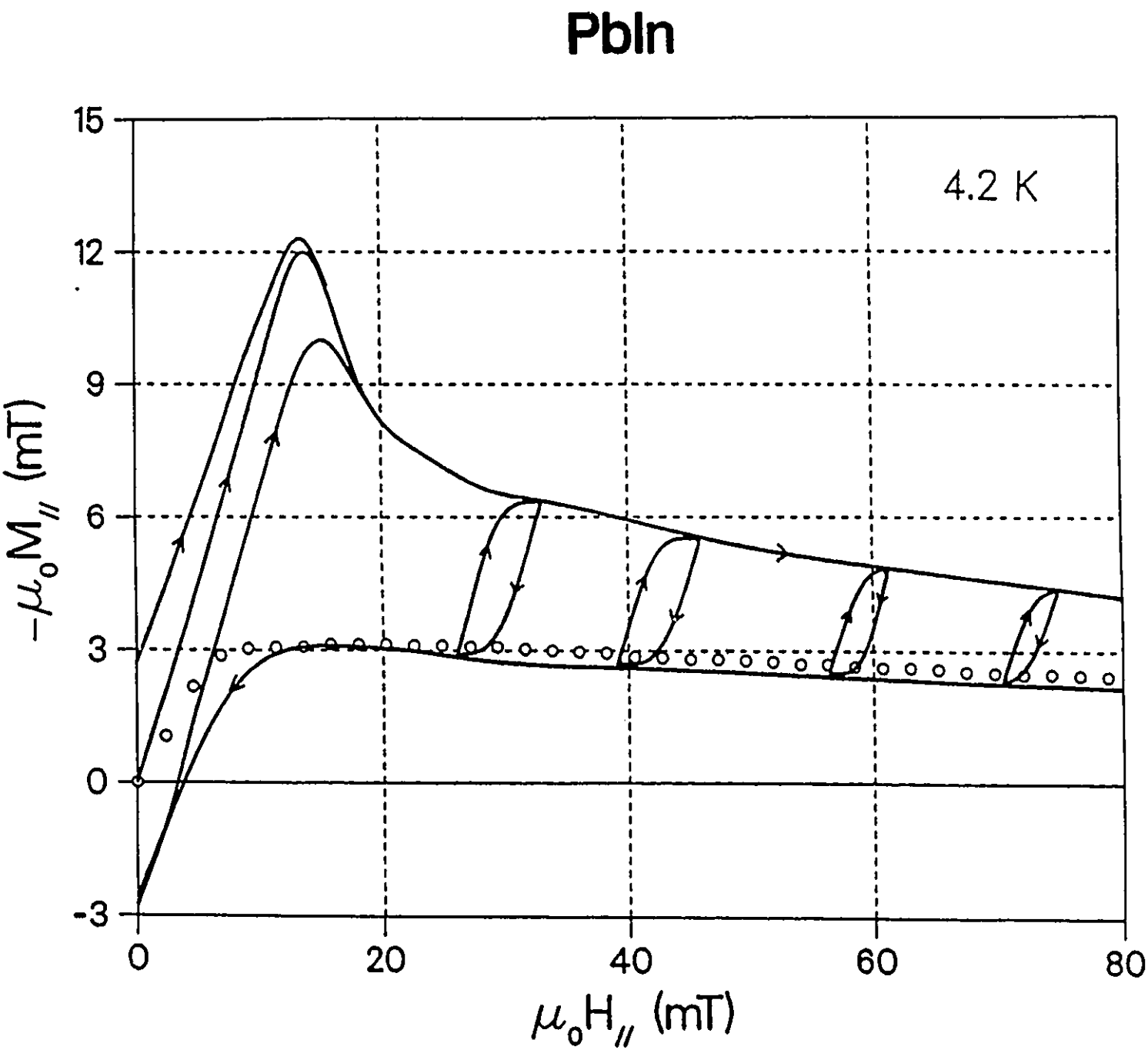

Figure 30: Standard magnetization curves of the *PbIn* at $4.2K$ including typical minor hysteresis loops.

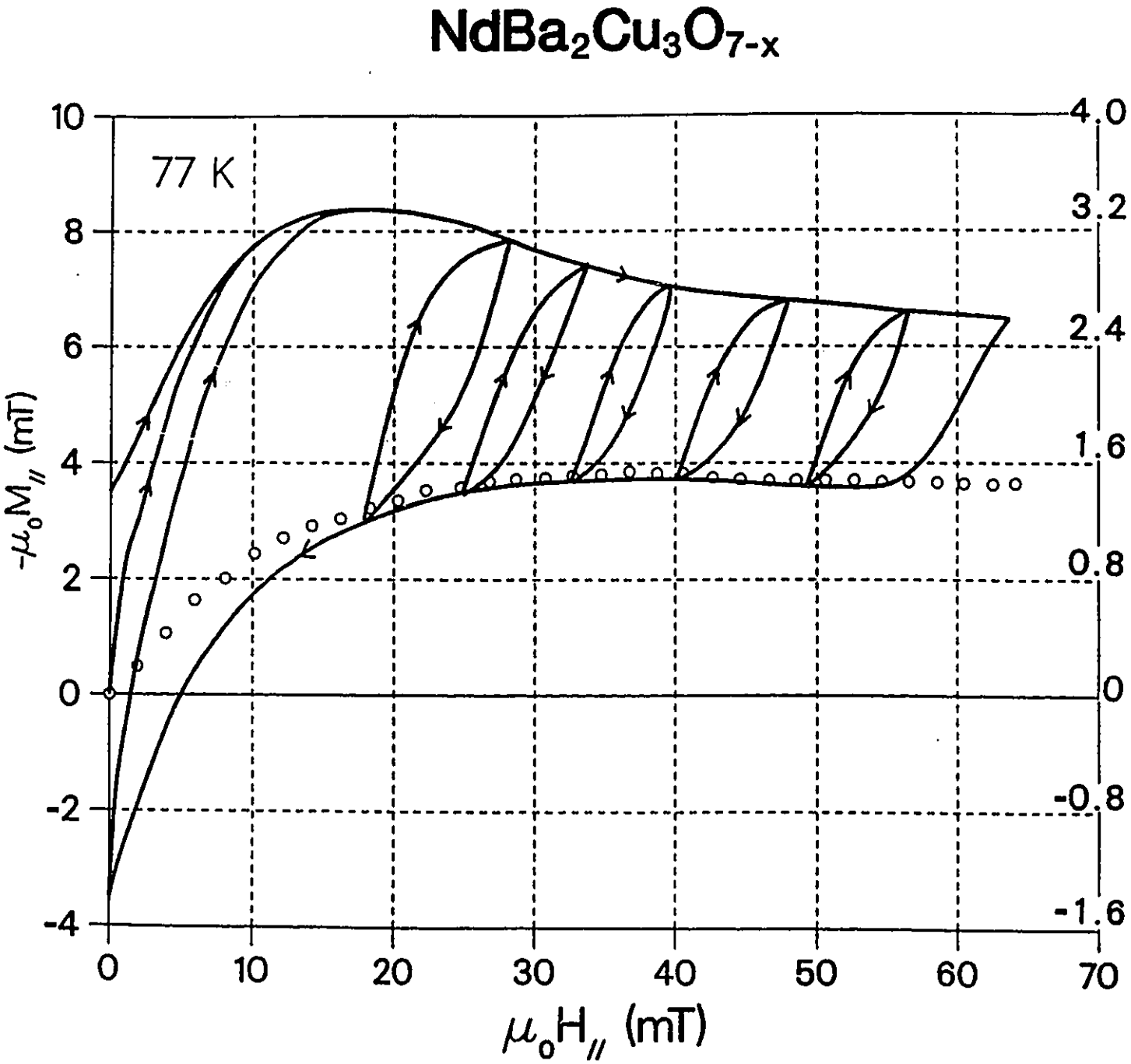

Figure 31: Standard magnetization curves of the $NdBa_2Cu_3O_{7-x}$ at $77K$ including typical minor hysteresis loops.

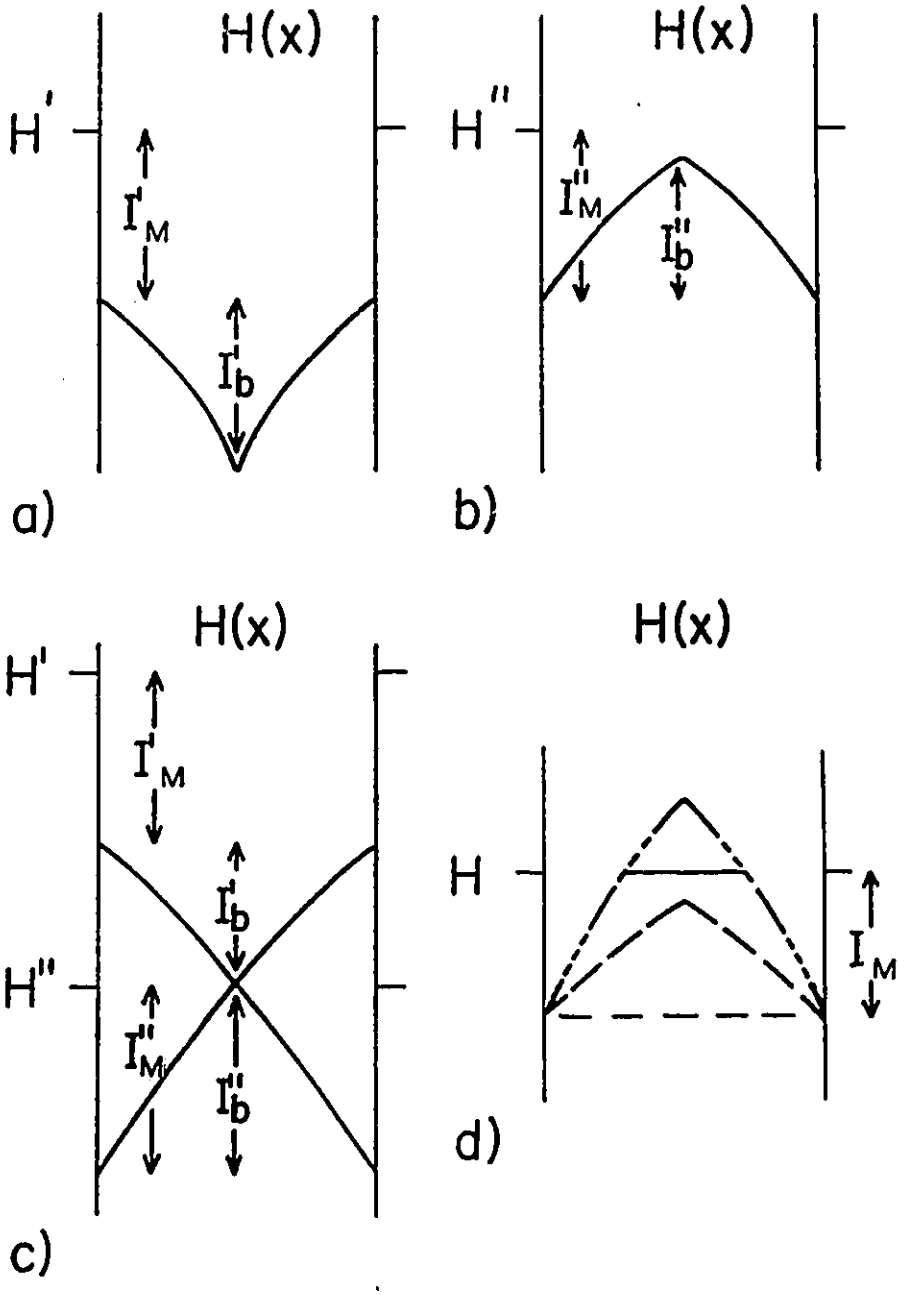

Figure 32: Schematics of B profiles of the magnetic flux density of a type II superconductor in critical state configurations.

Chapter 8

Flux Line Cutting Behaviour

8.1 Introduction

Flux line cutting is believed to take place in type II superconductors when changes in the direction of the external magnetic field $\vec{H}$ induce electric currents to flow with a component parallel to the magnetic flux density $\vec{B}(x)$ in the material [5]-[12], [15]-[26], [29], [35], [37], [38], [52]-[54], [65], [67], [68]. According to the Maxwell-Ampere equation, $\nabla \times \vec{B} = \mu_o \vec{j}$, any spatial variation of $d\theta / dx$, the direction of the magnetic flux density is associated with a current density $\vec{j_{\|}}$ flowing along the flux lines. When $j_{\|}$ exceeds a critical threshold $j_{c\|}$, the phenomenon of flux line cutting is thought to occur causing $j_{\|}$ to relax to $j_{c\|}$, hence $d\theta / dx$ to decay towards a critical configuration $(d\theta / dx)_c$.

The macroscopic magnetic behaviour of strongly hysteretic classical type II superconductors in the flux cutting regime has been extensively examined [7], [18], [20], [29], [33]-[35], [40], [45], [46], [65]. These phenomena in semi-reversible materials are currently under investigation in our laboratory in a variety of situations.

For instance, flux cutting can be induced by slowly rotating a disk of a type II superconductor in a stationary magnetic field directed $\perp$ to the axis of rotation and $\parallel$ to the flat faces of the disk. Sekerka [61] in his thesis reports on his study of *PbIn* disks under these circumstances. Lalonde is also investigating the behaviour of disks of sintered high T_c materials with this arrangement.

In this thesis we focus on flux line cutting generated when a magnetic field, denoted $H_\perp$, is superimposed and varied orthogonally to a constant bias magnetic field denoted $H_\parallel$. Here $H_\parallel$ and $H_\perp$ are directed along the broad surfaces of the rectangular slab specimens and both $M_\parallel$ and $M_\perp$, hence $< B_z >$ and $< B_y >$ are continuously monitored as the externally applied magnetic field

$$\vec{H}_a = \vec{y} H_\perp + \vec{z} H_\parallel$$

is varied in the prescribed manner.

We examine the effect of the magnitude of the bias magnetic field $H_\parallel$ on the response of the specimens and also the effect of the magnitude of the excursion of $H_\perp$. The evolution of the configurations of the magnetic flux during the initial swing of $H_\perp$ and also during subsequent cyclic variations of $H_\perp$ is also explored. Finally we also investigate the phenomena when $H_\perp$ is made to swing between 0 and some $H_{\perp max}$ (half-wave oscillations) and between + and $-H_{\perp_{max}}$ (full- wave oscillations). All of these situations are of interest and provide different insights into the behaviour of flux lines in the flux cutting regime. Further these procedures relate to the variety of circumstances encountered in applications and technology.

For every procedure, we report on the behaviour observed for the *Nd* and *Yttrium* high T_c materials, the *PbIn* and *VTi* samples. Our objectives in this chapter are to catalogue the salient features of our observations and inspect the variety of responses for similarities and differences. A quantitative analysis of this

vast assortment of results is beyond the scope of this *M.Sc.thesis*. We will however present a physical account or qualitative description of some major aspects of the phenomena.

8.2 Results and Discussion

We examine and compare the response of our specimens as the magnitude of the variables $H_\perp$ and $H_\parallel$ relative to the first full penetration field $H_\star$ is modified. However since $H_\star$ is not known accurately we do not present the data normalized to this quantity.

We stress that, for each measurement sequence, the sample becomes superconducting in the stationary magnetic field labelled $H_\parallel$ which is maintained fixed at the chosen value throughout the subsequent history. Now a component transverse to $H_\parallel$ and denoted $H_\perp$ is impressed and removed, then again impressed and removed, etc ..., i.e. $H_\perp$ is cycled between 0 and the chosen maximum $H_\perp$. The behaviour during the first swing of $H_\perp$ is "unique" and can be regarded as a transient. The behaviour during the subsequent oscillations repeats, i.e. traces a closed loop. We will see that these curves and closed loops can be very intricate and that the patterns evolve in a complicated manner as the range of $H_\perp$ is extended.

8.3 Magnetization Orthogonal to the Varying Field (// to a Bias Field)

In this section we examine the evolution of a magnetic moment orthogonal to the varying component of $\vec{H}_a$, hence along a static bias field, denoted $H_{||}$. First we focus on the response of the samples during the initial rise of $H_{\perp}$. The starting point is at the upper left in Figs. 33 through 36. The two high T_c materials and the $PbIn$ specimen have expelled some magnetic flux, hence exhibited a Meissner effect as they cooled from T_c to ambient, hence possess a diamagnetic moment when the flux cutting operation commences. The VTi has expelled no magnetic flux, hence shows no magnetic moment at this juncture. We note that the locus of $M_{||}$ versus $H_{\perp}$ traverses a valley for the Nd, Y and $PbIn$ samples but traces a peak for the VTi specimen. We will explain shortly that both of these features carry the signature of flux cutting.

It is perhaps instructive at this point to dwell on the behaviour of an ordinary (normal) isotropic conductor under the circumstances prevailing here. The specimen is permeated by a uniform magnetic flux density $B_{||} = \mu_o H_{||}$. By Faraday's law of induction, the application of $H_{\perp}$ will induce eddy currents which will circulate to oppose the entry of $H_{\perp}$ into the metal. Thus a diamagnetic moment will appear collinear with $H_{\perp}$ and orthogonal to $H_{||}$. This magnetic moment vanishes as the induced currents decay because of the finite resistivity of the normal metal. The important feature is the direction of the decaying magnetic moment during its existence. Since $H_{||}$ is kept fixed along the z axis, (i) no currents are made to circulate in the x-y plane to aid or oppose $H_{||}$, (ii) the magnetic flux density $B_{||} = < B_{||} > = \mu_o H_{||}$ remains unchanged and, (iii) no magnetic moment is generated

along $H_{||}$. Thus, according to classical electrodynamics, the locus of $M_{||}$ versus $H_{\perp}$ for an isotropic normal metal will trace a straight horizontal line fixed at $M_{||} = 0$ in displays such as figures 33 through 36.

Turning now to a superconductor regarded as a metal endowed with zero resistivity (infinite conductivity). Let this material acquire the property of zero resistivity as it is cooled in the presence of a static uniform magnetic field $H_{||}$ directed along the z-axis. Again, from the laws of electromagnetic induction, no response will accompany the appearance of zero resistivity under these circumstances. Thus, at this juncture, $B_{||}$ remains uniform and equal to $\mu_o H_{||}$. Also, by Faraday's law of induction, the application of $H_{\perp}$ will generate electric currents circulating to oppose the change of $H_{\perp}$ and give rise to a magnetic moment directed along $H_{\perp}$. The important feature which we wish to stress is that since $H_{||}$ is kept fixed, conclusions (i), (ii) and (iii) enunciated above will continue to prevail and $M_{||}$ remain zero as $H_{\perp}$ is varied.

We may further stipulate in the foregoing that the resistivity is zero (the conductivity infinite) only until the current density attains a threshold value j_c. This ansatz does not modify the conclusions just enumerated. Introducing a limit j_c on the lossless current density will only affect the time dependence and the magnitude of the magnetic moment generated along $H_{\perp}$ by changes of $H_{\perp}$.

It is evident from a glance at Figs. 33 through 36 that $M_{||}$, the magnetic moment along the fixed $H_{||}$, is drastically affected by changes in $H_{\perp}$. As we have just noted, such behaviour cannot be accounted for by regarding type II superconductors simply as materials possessing the property of zero resistivity until the current density attains a ceiling or critical value j_c.

It is now well established that magnetic flux exists and enters in type II superconductors in the form of discrete flux lines each containing a quantum of magnetic flux $\phi_o = h/2e$. We therefore also examine the behaviour in the framework of flux lines instead of the perspective of induced currents. It is instructive to set the concept of flux line cutting aside and pursue the consequences envisaged in the absence of this process. We stress that this implies that flux lines, once created, cannot rotate and change their direction inside the superconductor. $\Delta H_\perp$, an increment of $\Delta H_\perp$ causes an augmentation ΔH_a in the magnitude of $\vec{H}_a$. This increase of H_a leads to the nucleation and penetration of flux lines in the specimen. In the absence of flux line cutting, the flux lines maintain their integrity and orientation as they migrate and undergo compression in the specimen. Every flux line entering the sample adds a quantum of flux to the reservoir of flux already permeating the specimen. The magnetic flux density threading each flux line is directed along the magnetic field $\vec{H}_a$ existing at the surface of the specimen when the flux line is nucleated. Consequently, $< B_\parallel >$, the component of the magnetic flux density along $H_\parallel$ is increased by the addition of each flux line **even though $H_\parallel$ is maintained constant**. Thus, in the absence of flux line cutting, we expect to see a continuous increase in $< B_\parallel >$, hence of the magnetization $M_\parallel$ along $H_\parallel$ as $H_\perp$, the component of $\vec{H}_a$ orthogonal to the fixed $H_\parallel$, is augmented.

A glance at the uppermost curve in Figs. 33 through 36 reveals that this expectation is realized only along the first part of the initial response of the VTi specimen (see Fig. 36) to the application of $H_\perp$. Only here does the behaviour agree with the scenario sketched above but we see that the rise of $M_\parallel$ soon ceases and the curve then traces a steep descent. Any region exhibiting a horizontal or downward slope in the locus of $M_\parallel$ during the first increase of $H_\perp$ testifies that flux

line cutting is taking place thereby causing a major reorientation of magnetic flux away from $H_{\parallel}$ towards $H_{\perp}$. It is evident from a comparison of Figs. 33, 34 and 35 with Fig. 36 that the three semi-reversible materials are initially more susceptible to flux line cutting than the hysteretic VTi.

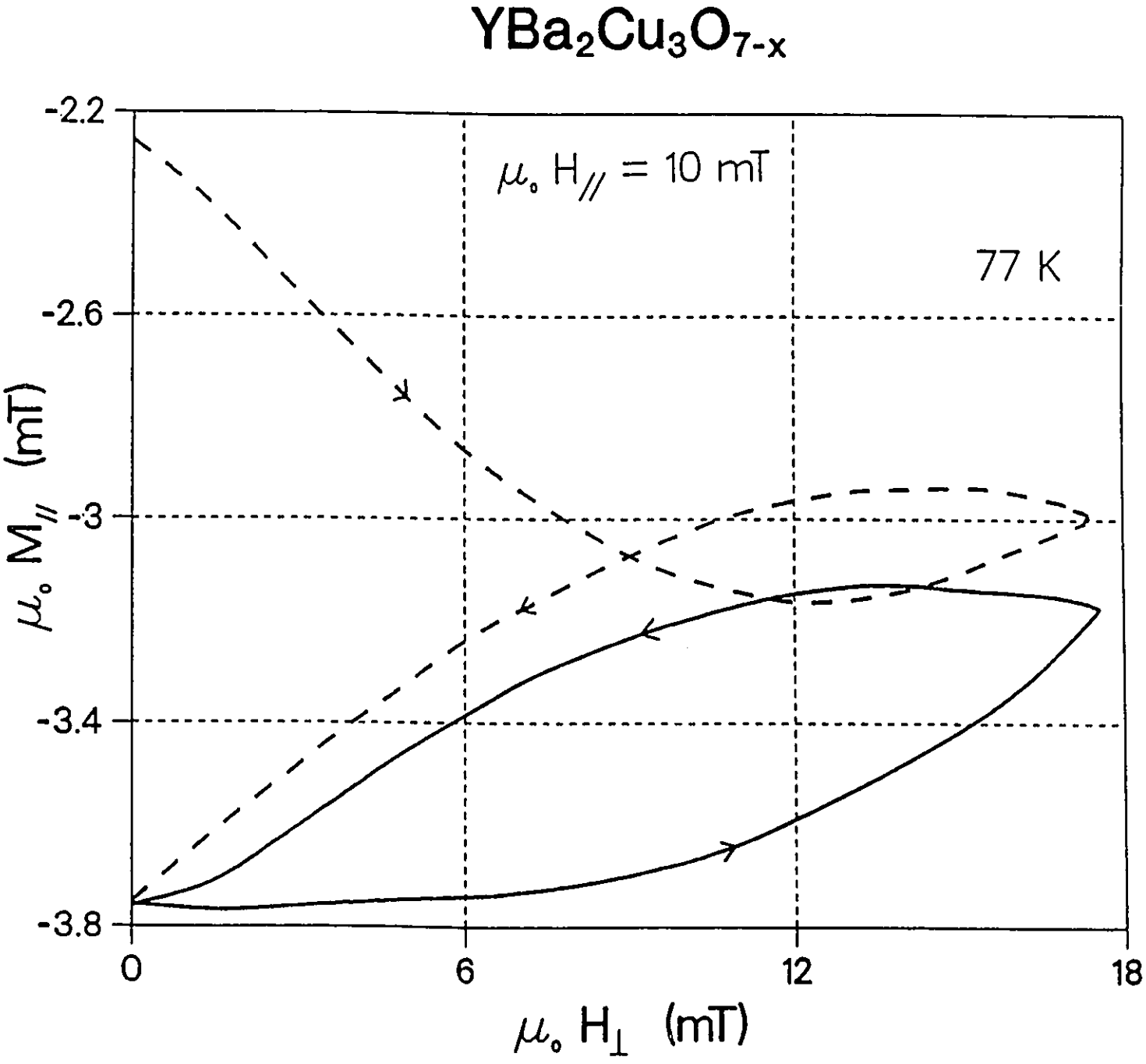

Figure 33: Evolution of $< B_z >$ along the length of the $YBa_2Cu_3O_{7-x}$ sample at 77 K while the applied magnetic field $H_\perp$ is impressed and cycled in the presence of a stationary bias field $H_{||}$.Here $\mu_o H_{||} = 10\ mT$.

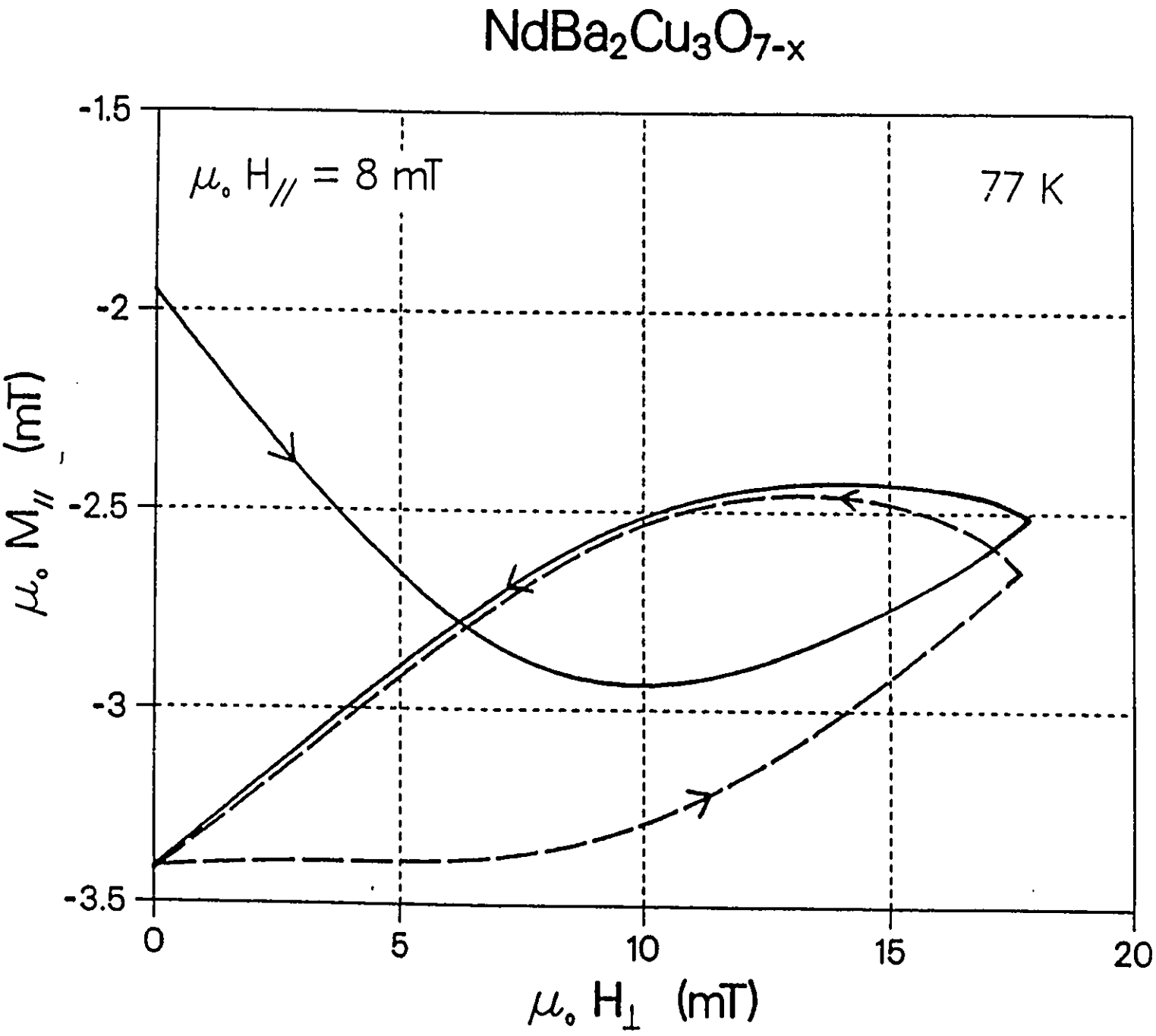

Figure 34: Same as in the previous figure, except that the specimen is $NdBa_2Cu_3O_{7-x}$ with a bias magnetic field of 8 mT.

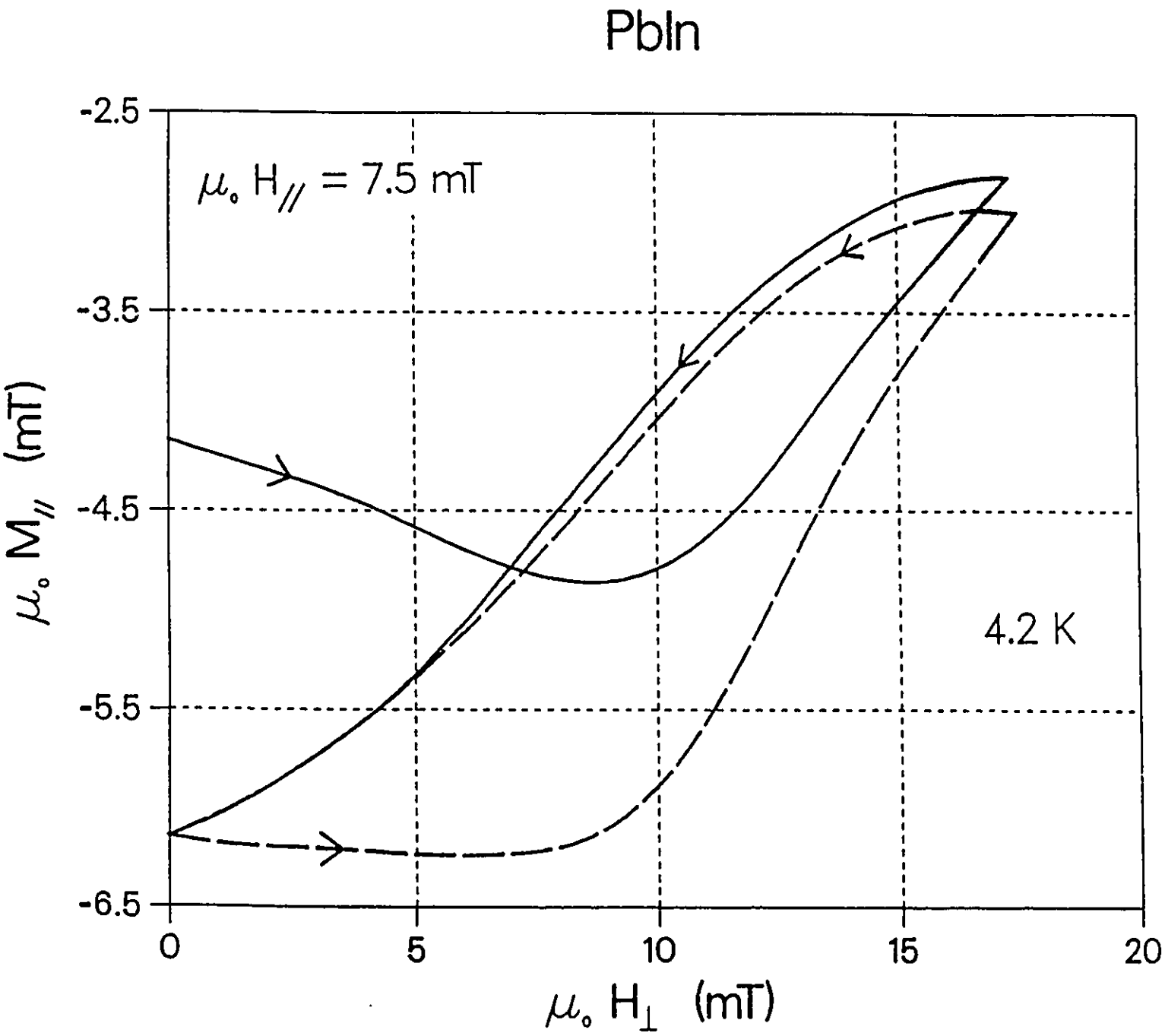

Figure 35: Same as in the previous figure, except that the specimen is *PbIn* at 4.2 K with a bias magnetic field of 7.5 mT.

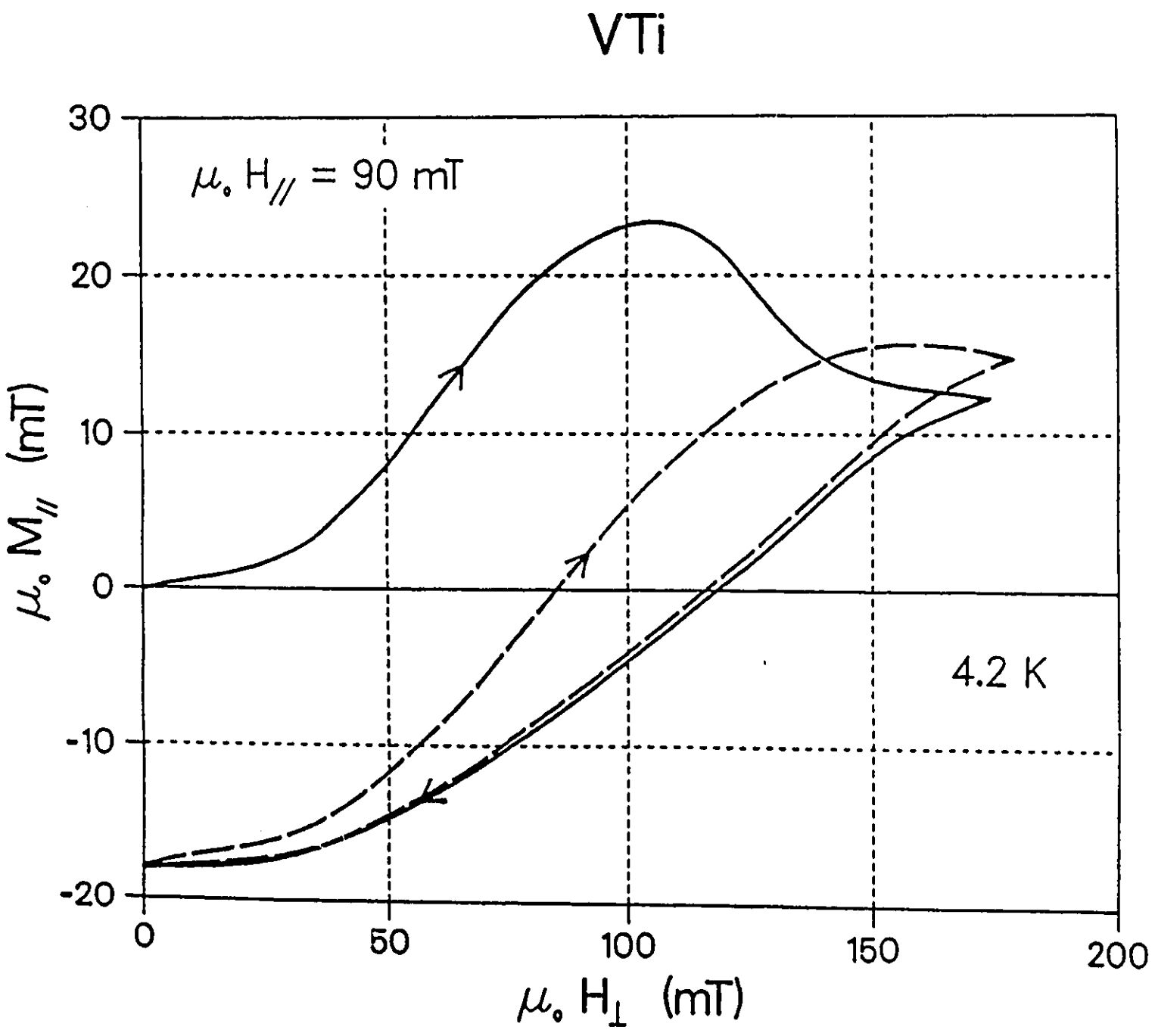

Figure 36: Same as in the previous figure, except that the specimen is *VTi* at 4.2 K with a bias magnetic field of 90 mT.

The locus of $M_{||}$ (hence $B_{||}$) versus $H_{\perp}$ eventually exhibits a rise as the increase in $H_{\perp}$ continues to higher values. This growth of $M_{||}$ is pursued to even larger values of $H_{\perp}$ in Figs. 37 and 38. We note however that $M_{||}$ fails to rise into the positive (paramagnetic) quadrant in both figures. This indicates that the addition of flux lines fails to compensate for the flux line cutting that has taken place. We also draw the attention of the reader to the differences in the position and shape of the "return" curves between the $PbIn$ and the high T_c material.

We now turn our attention to the periodic response of the samples to subsequent half cycles of $H_{\perp}$. This is shown by the closed loops in Figs. 33 through 36. We note that although the ratios of $H_{\perp}$ to $H_{||}$ are comparable in all four displays, the locus of $M_{||}$ versus $H_{\perp}$ circulates counter-clockwise in the first three figures whereas the circulation is clockwise for the VTi specimen. A counterclockwise circulation is observed in the latter specimen also but appears at much smaller ratios of $H_{\perp}$ to $H_{||}$. This mode of circulation can be seen in Fig. 41 (loops labeled A', B', A and C').

The effect of the amplitude of $H_{\perp}$ on the periodic responses (closed loops) is illustrated in Figs. 39, 40 and 41. We note that for the high T_c specimen, the circulation remains counterclockwise and the shape of the loops stays quite simple over the entire range of amplitudes explored (see Fig. 40). In contrast, for both the $PbIn$ and the VTi, the configuration of the loops evolves and becomes quite intricate as a function of growing amplitude of $H_{\perp}$ (see Figs. 39 and 41). In both cases we observe the formation of a "figure eight" loop. In the VTi the lower portion of the "figure eigth" is seen to diminish and gradually disappear as the amplitude is augmented so that eventually the sense of circulation is reversed over the entire loop (compare the loop labeled D' with that labeled B in Fig. 41). In the $PbIn$

however, the lower portion of the "figure eigth" survives, embracing a fixed area, while the upper portion expands with increasing amplitude. In Fig. 40, the loops have been displaced vertically for clarity of presentation. This mode of display is not required for the *VTi* since here the "starting" (lower left) point of the closed loops is seen to shift downwards as the amplitude is chosen larger.

The influence of the strength of the static bias field $H_{\|}$ on the initial response and on the subsequent closed loops is illustrated in Figs. 42 through 47. The trends are seen to be quite similar in both instances for all the samples. The data for the *Yttrium* specimen are essentially identical to that for the *Nd* sample and are not shown.

The beautiful "butterflies" traced by the locus of $M_{\|}$ versus $H_{\perp}$ when the latter is made to oscillate symmetrically between $+H_{\perp max}$ and $-H_{\perp max}$ are displayed in Figs. 48 through 51. Again we note that the sense of circulation in the case of the *VTi* differs from that witnessed with the other three samples although the ratios of $H_{\perp}$ to $H_{\|}$ are comparable in all cases. To emphasize this feature we have displayed "butterflies" observed over a wide range of $H_{\perp}/H_{\|}$ for the *VTi* specimen. The *VTi* sample however is seen to display butterflies with a "reversed" sense of circulation, hence corresponding to that shown in Figs. 48, 49 and 50 when the ratio $H_{\perp}/H_{\|}$ is chosen very small (these curves are not shown).

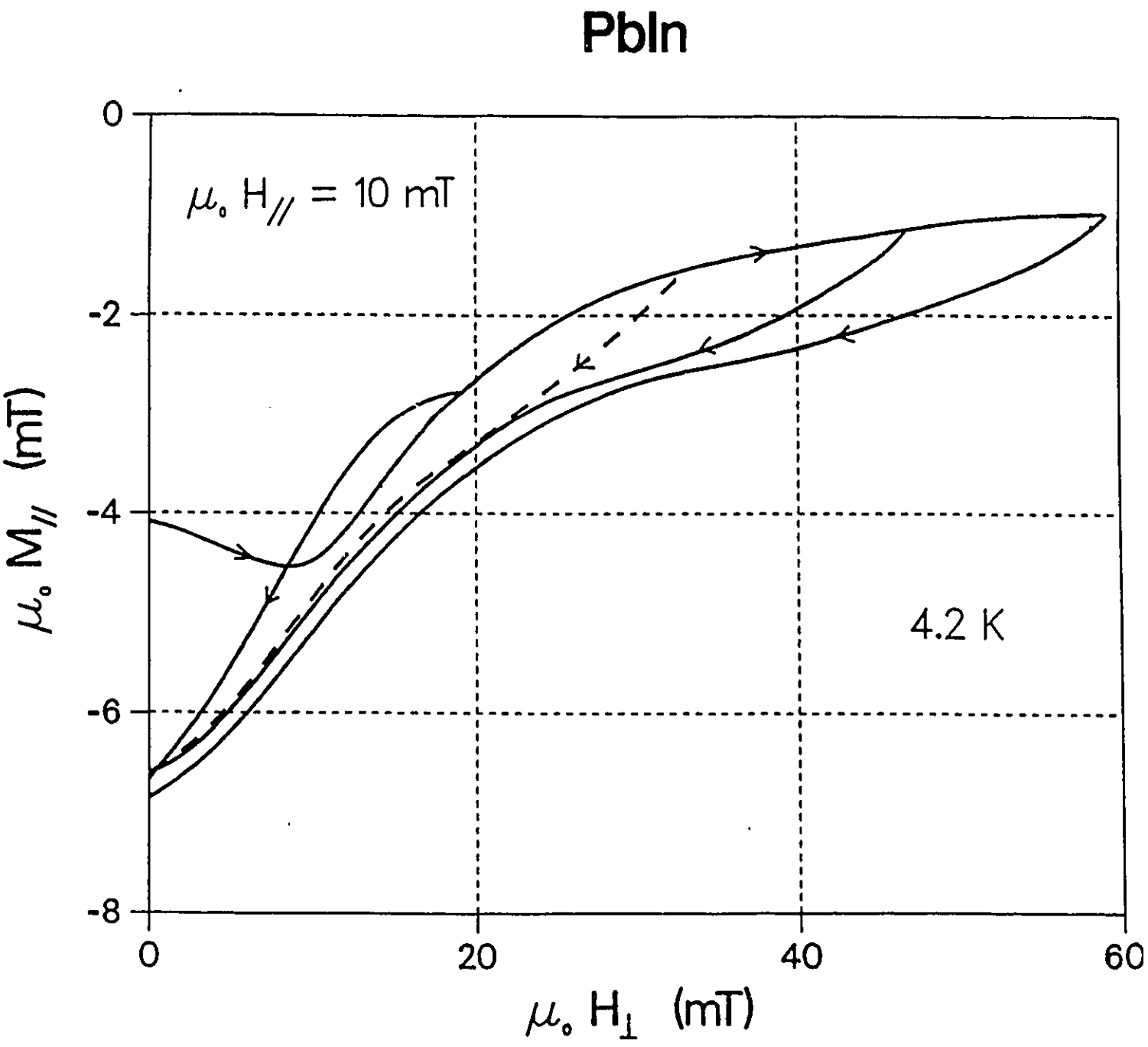

Figure 37: Response of the *PbIn* specimen at 4.2 K to a first application and removal of $H_\perp$ directed perpendicular to a static bias field $\mu_o H_{||} = 10\,mT$. This figure illustrates the effect of increasing the amplitude of $H_\perp$ on the locus of $M_{||}$ vs. $H_\perp$.

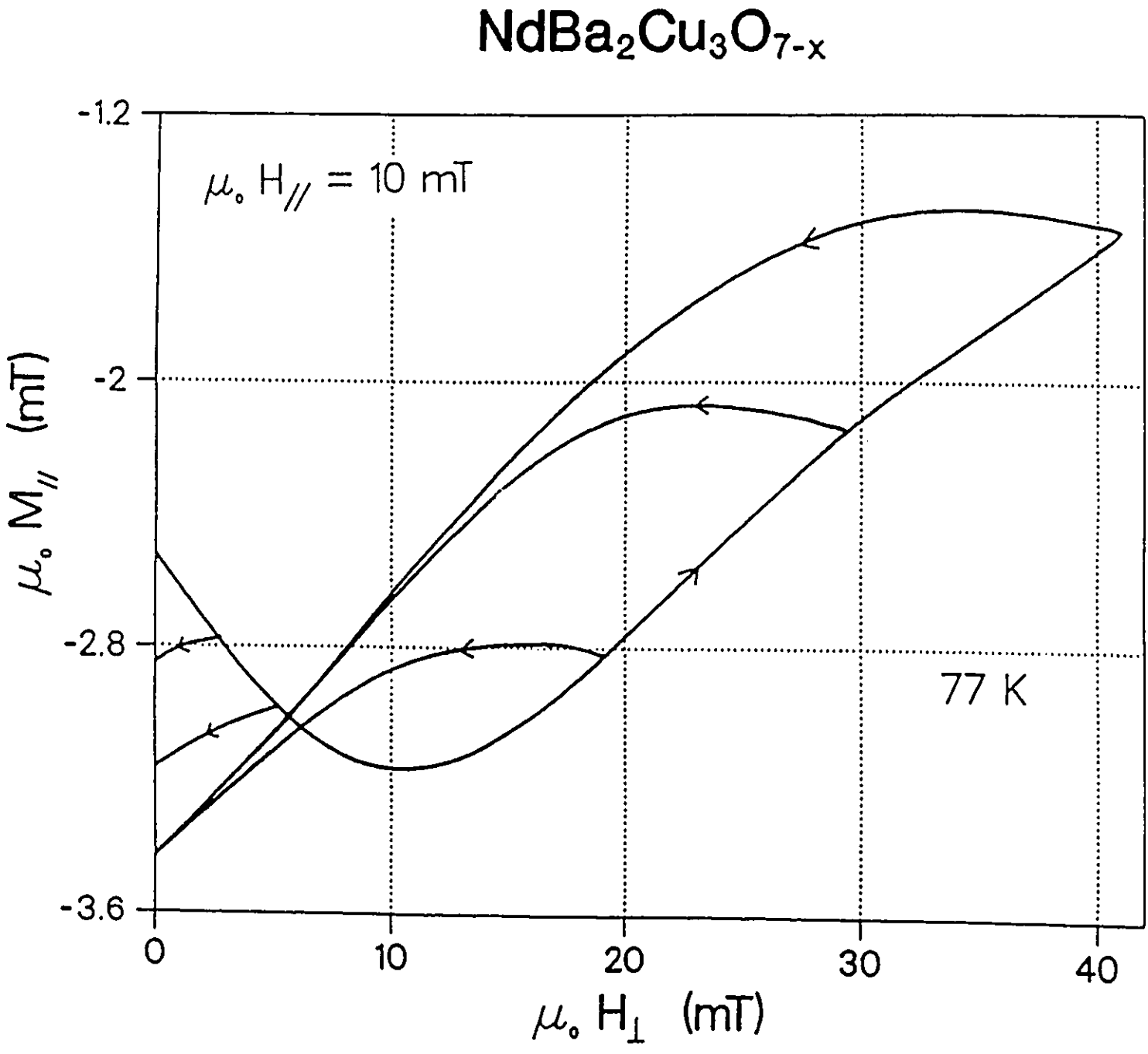

Figure 38: Same as in the previous figure except that here the specimen is $NdBa_2Cu_3O_{7-x}$ at 77 K.

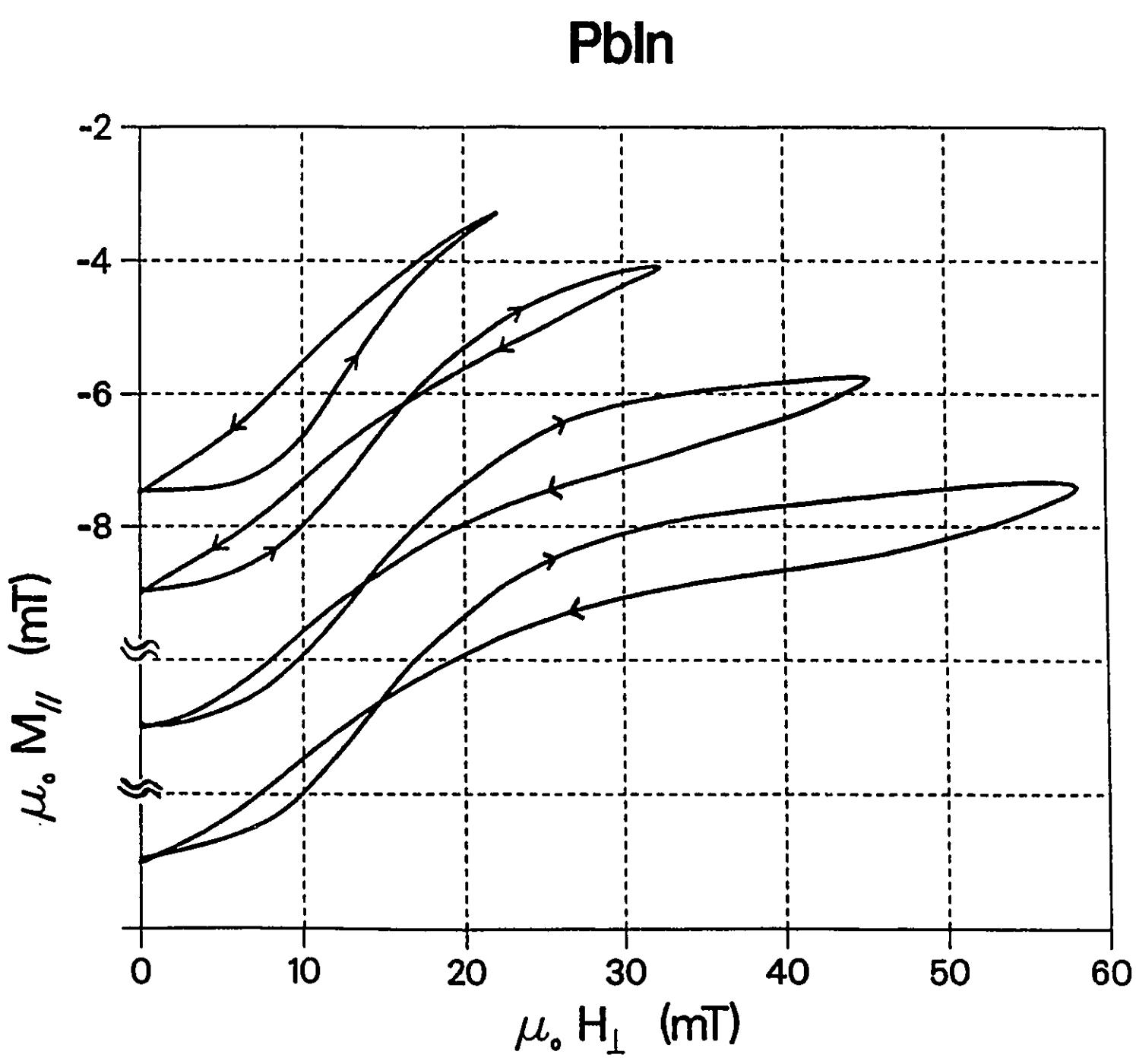

Figure 39: Shows the effect of different amplitudes of half cycles of $H_\perp$ on the periodic response of $M_{||}$ in a static bias field $H_{||}$ for the *PbIn* specimen at 4.2 K. The closed loops all start at the same point but are shown shifted vertically to avoid clutter. Note the appearance and evolution of the figure 8.

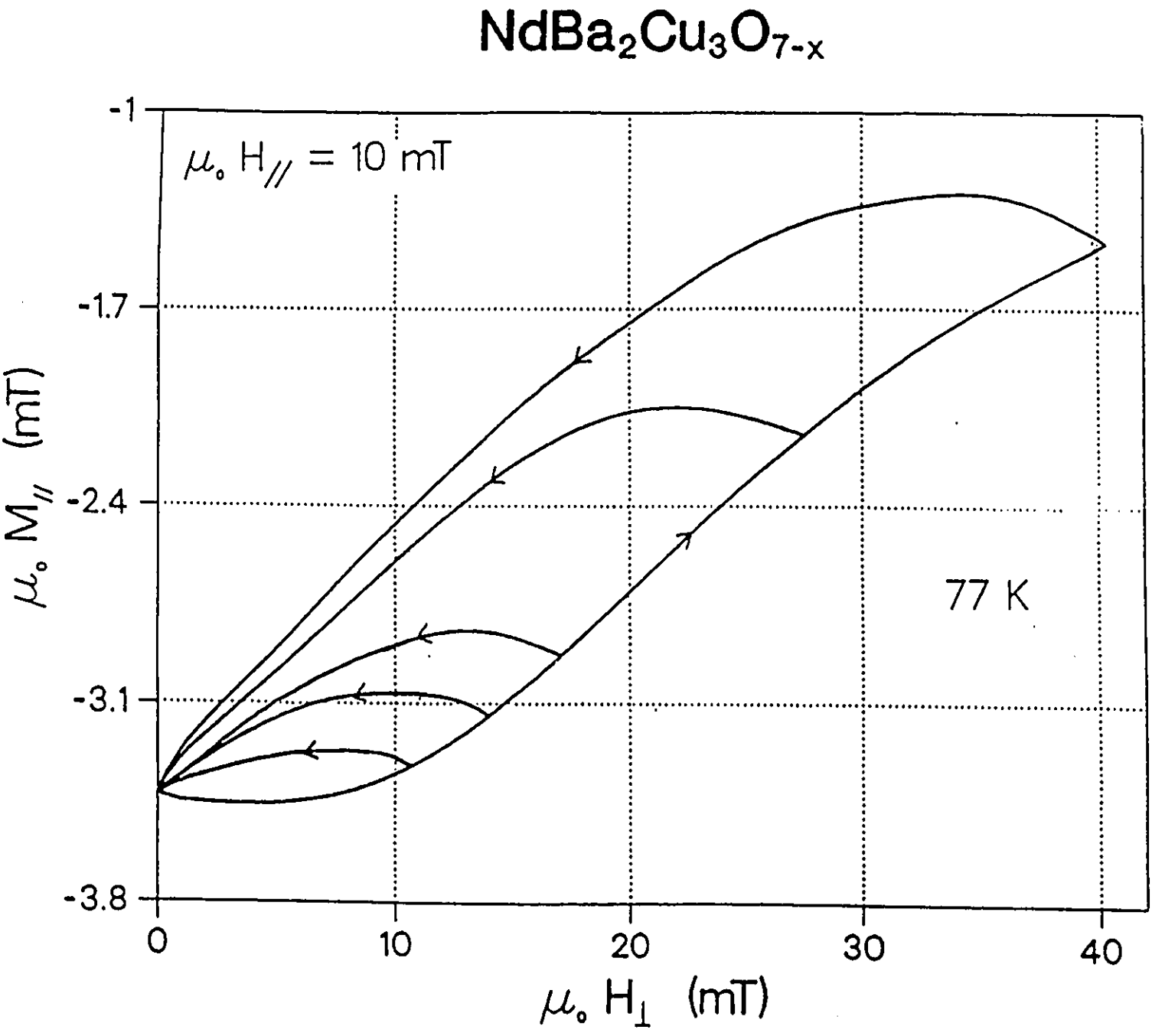

Figure 40: Shows the effect of different amplitudes of half cycles of $H_\perp$ on the periodic response of $M_\parallel$ in a static bias field $H_\parallel$ for the Nd specimen at 77 K. In contrast to the $PbIn$, the closed loops only expand but show no change in their sense of circulation.

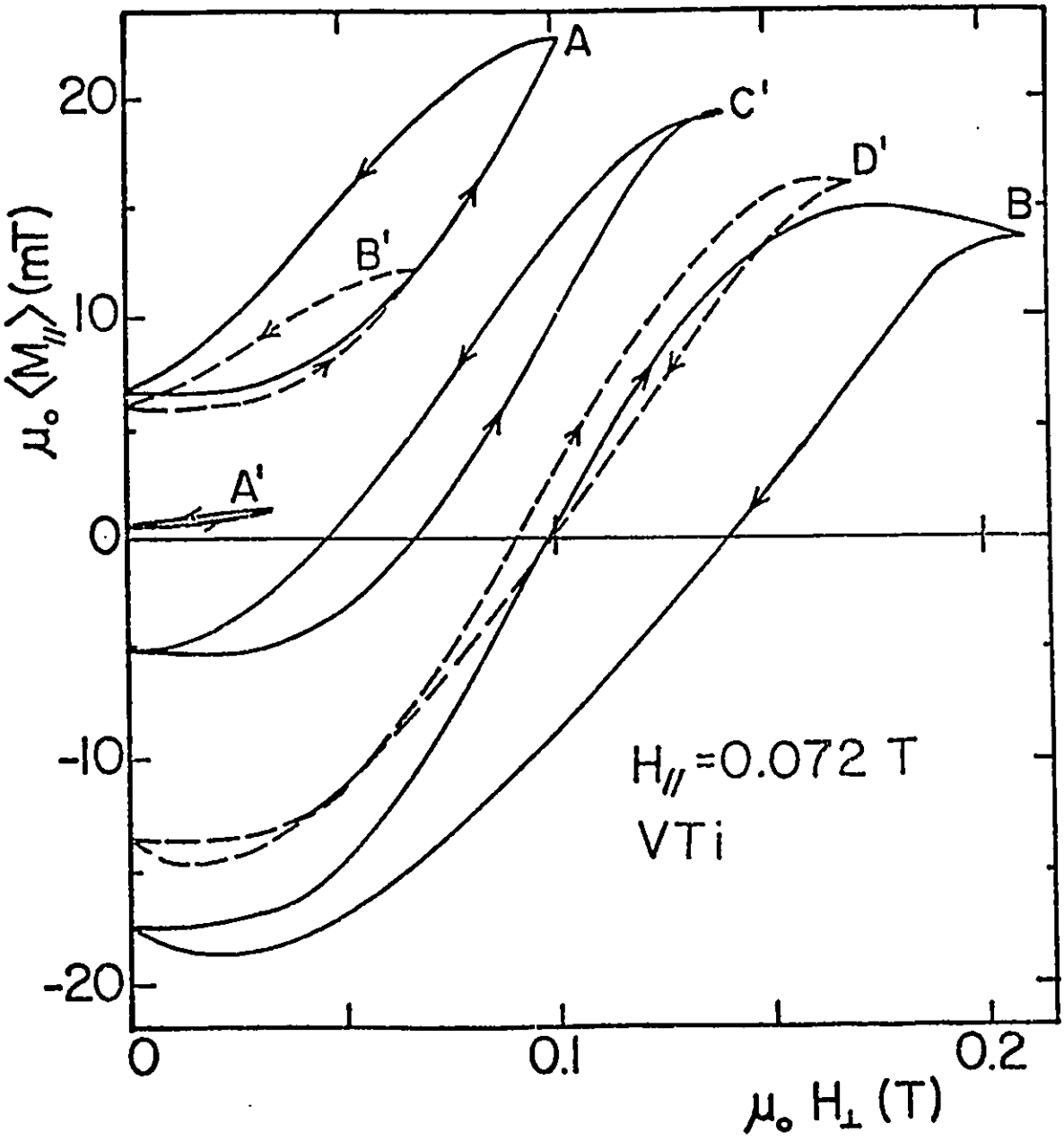

Figure 41: Shows the effect of different amplitudes of half cycles of $H_\perp$ on the periodic response of $< M_{||} >$ in a static bias field $H_{||}$ for the VTi specimen at 4.2 K. Here $\mu_o H_{||} = 72mT$. In contrast to the two previous figures, the starting point is displayed vertically here as a result of the initial half cycle. Note the change in the sense of circulation of the closed loops and the figure 8 (curve D').

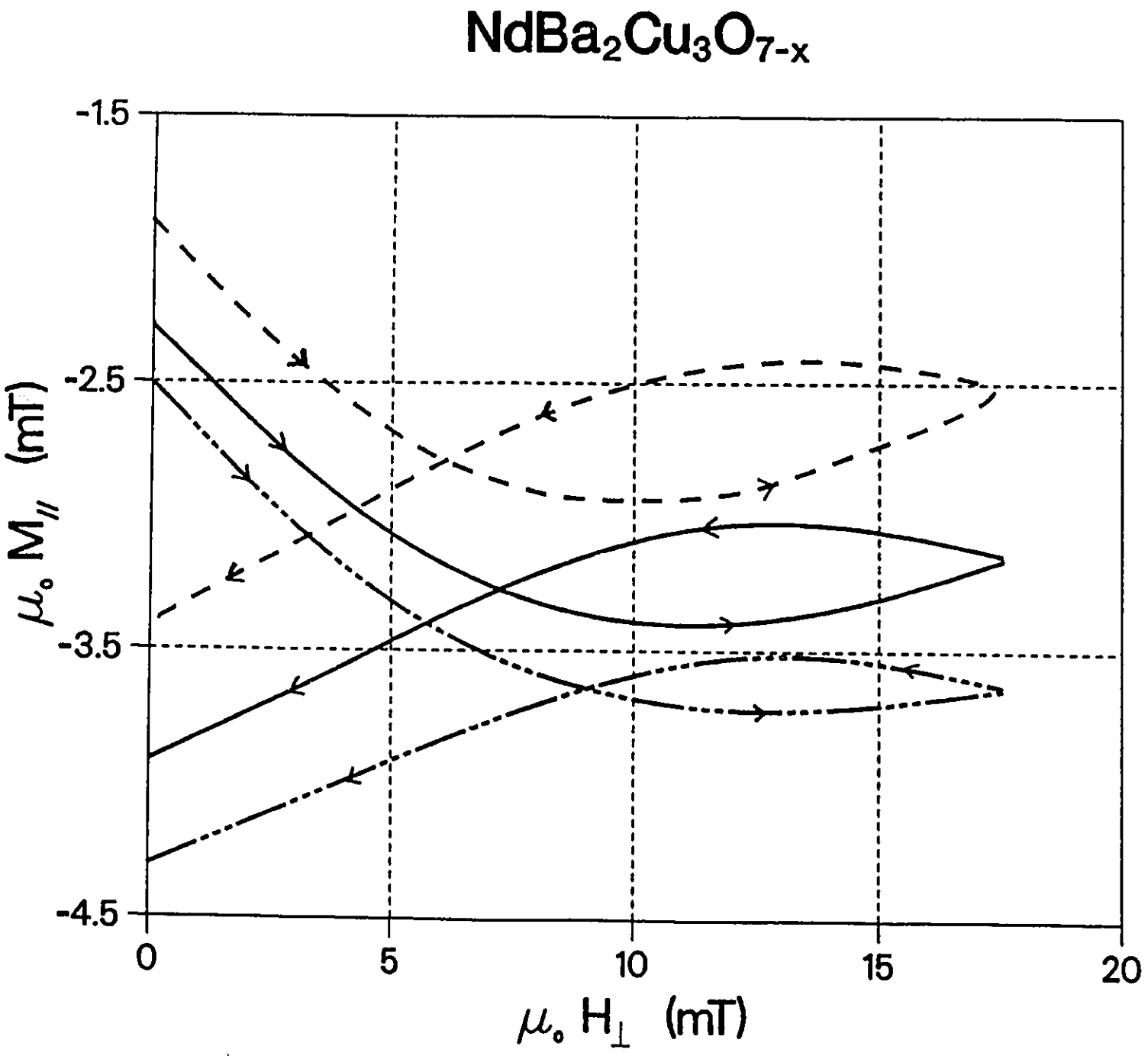

Figure 42: Illustrates the effect of different static bias fields $H_{||}$ on the response of $M_{||}$ to the initial application and removal of $H_{\perp}$ for the Nd specimen. $\mu_o H_{||} = 8$, 12 and 15.5 mT for the - - - - - - - , ——————— , — - — - — - — curves respectively.

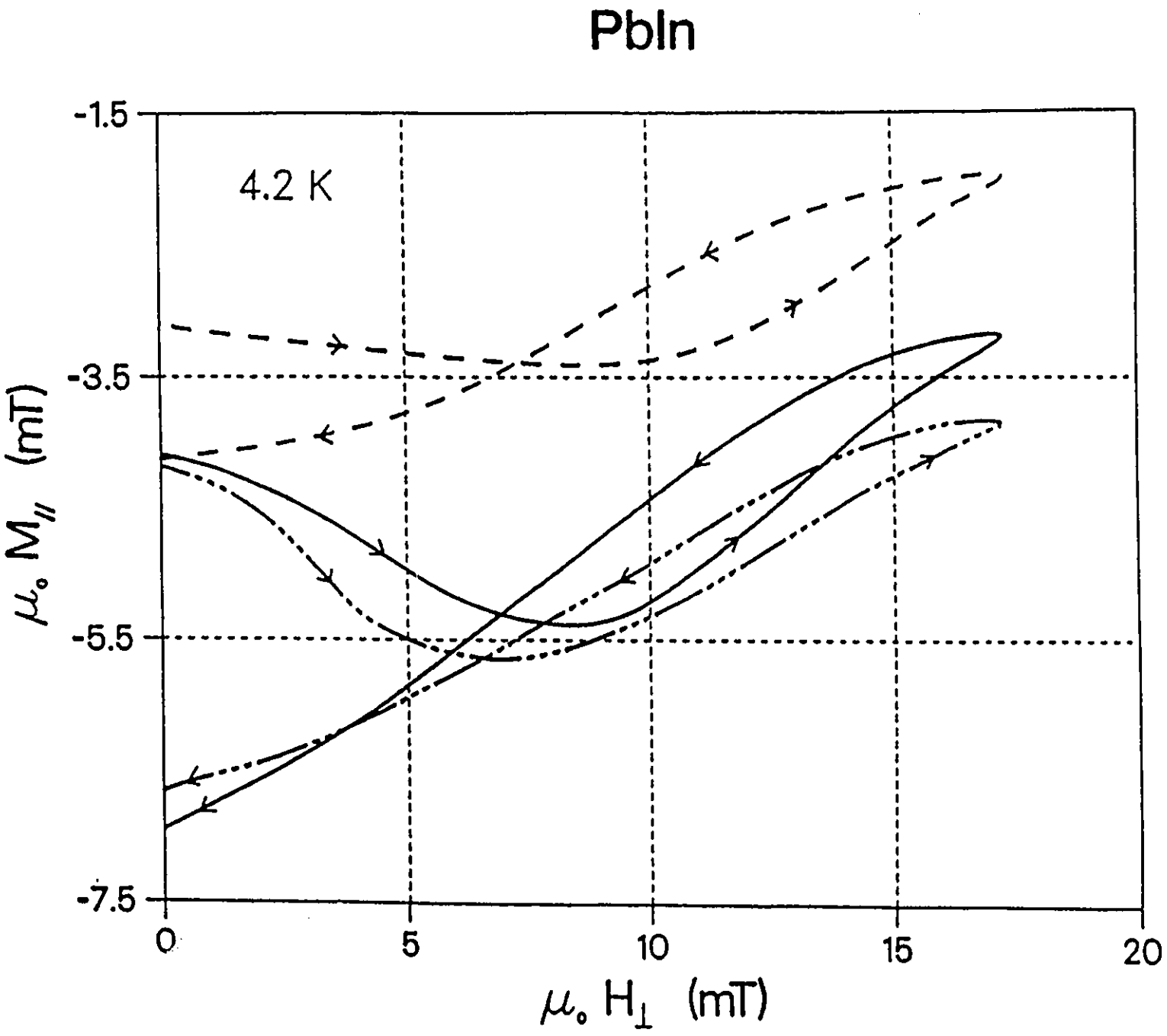

Figure 43: Illustrates the effect of different static bias fields $H_{||}$ on the response of $M_{||}$ to the initial application and removal of $H_\perp$ for the *PbIn* specimen. $\mu_o H_{||} = 5$, 10 and 15 mT for the - - - - - - - , ———— , — - — - — - — curves respectively.

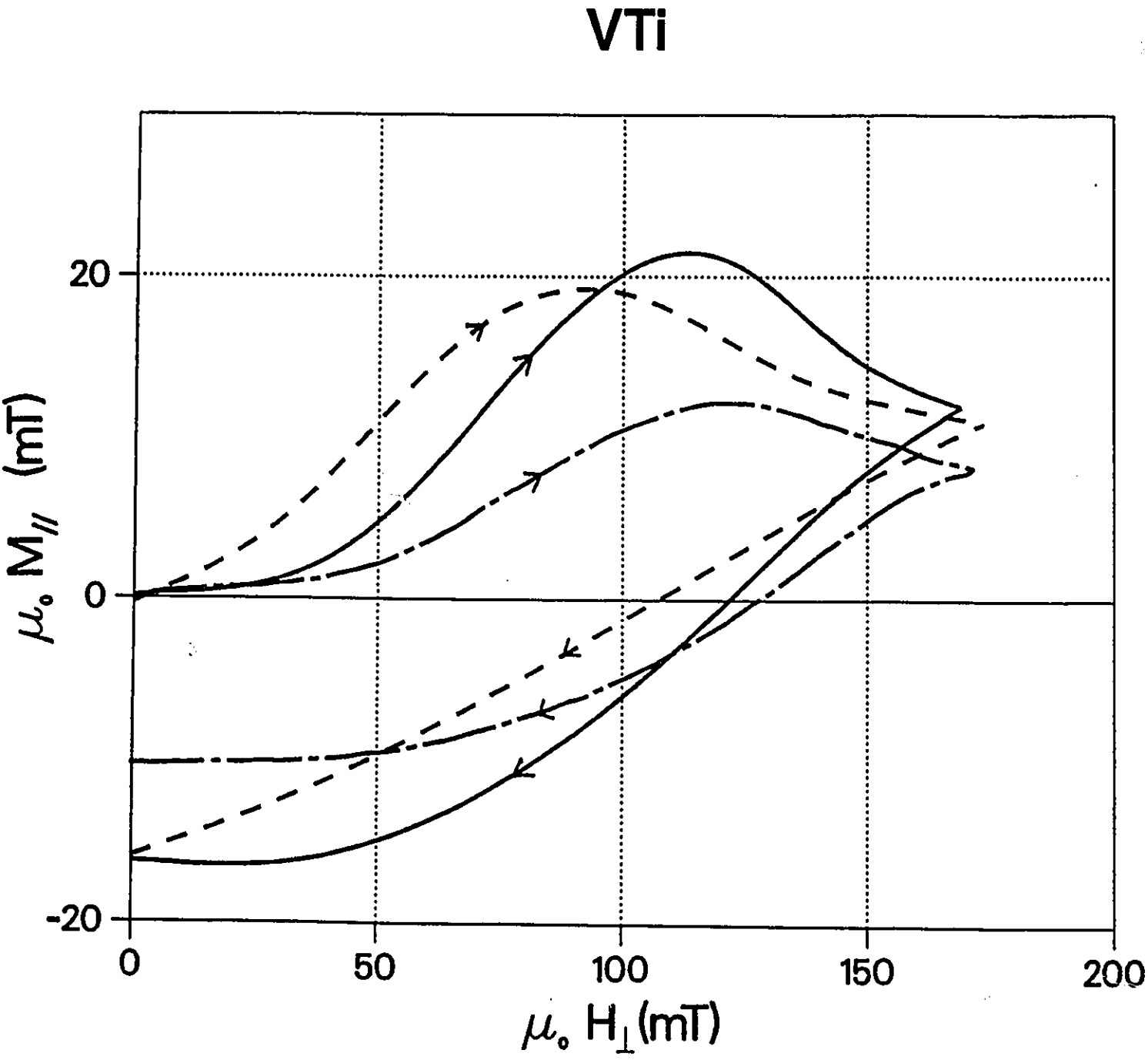

Figure 44: Illustrates the effect of different static bias fields $H_{||}$ on the response of $M_{||}$ to the initial application and removal of $H_\perp$ for the VTi specimen. $\mu_o H_{||} = 45$, 158 and 340 mT for the - - - - - - - , ———— , — - — - — - — curves respectively.

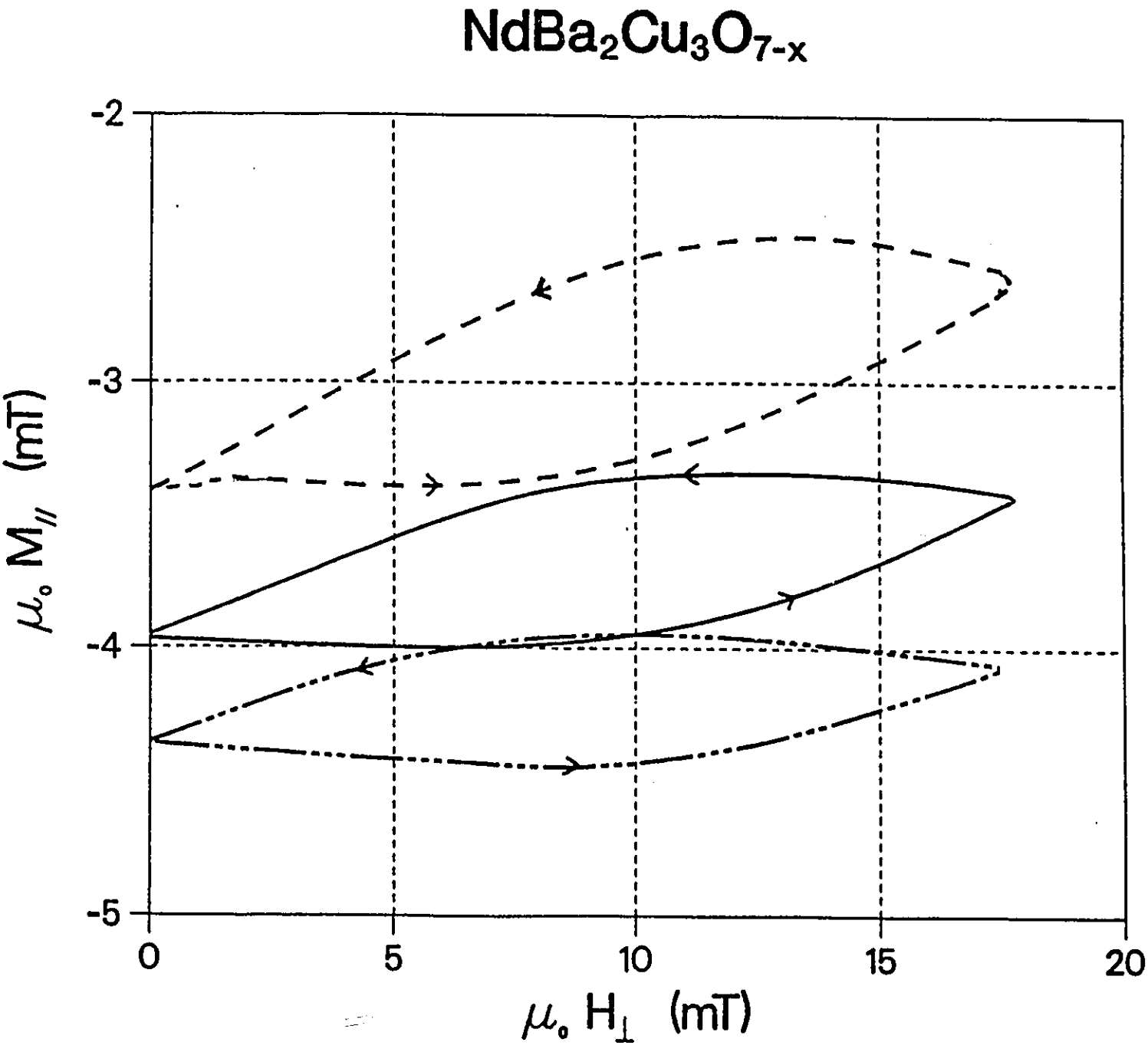

Figure 45: Illustrates the effect of different static bias fields $H_{||}$ on the periodic response of $M_{||}$ to half cycles of H_{perp} for the Nd specimen. Here $\mu_o H_{||} = 8$, 12 and 15.5 mT for the - - - - - - - , ———— , and — - — - — - — curves respectively.

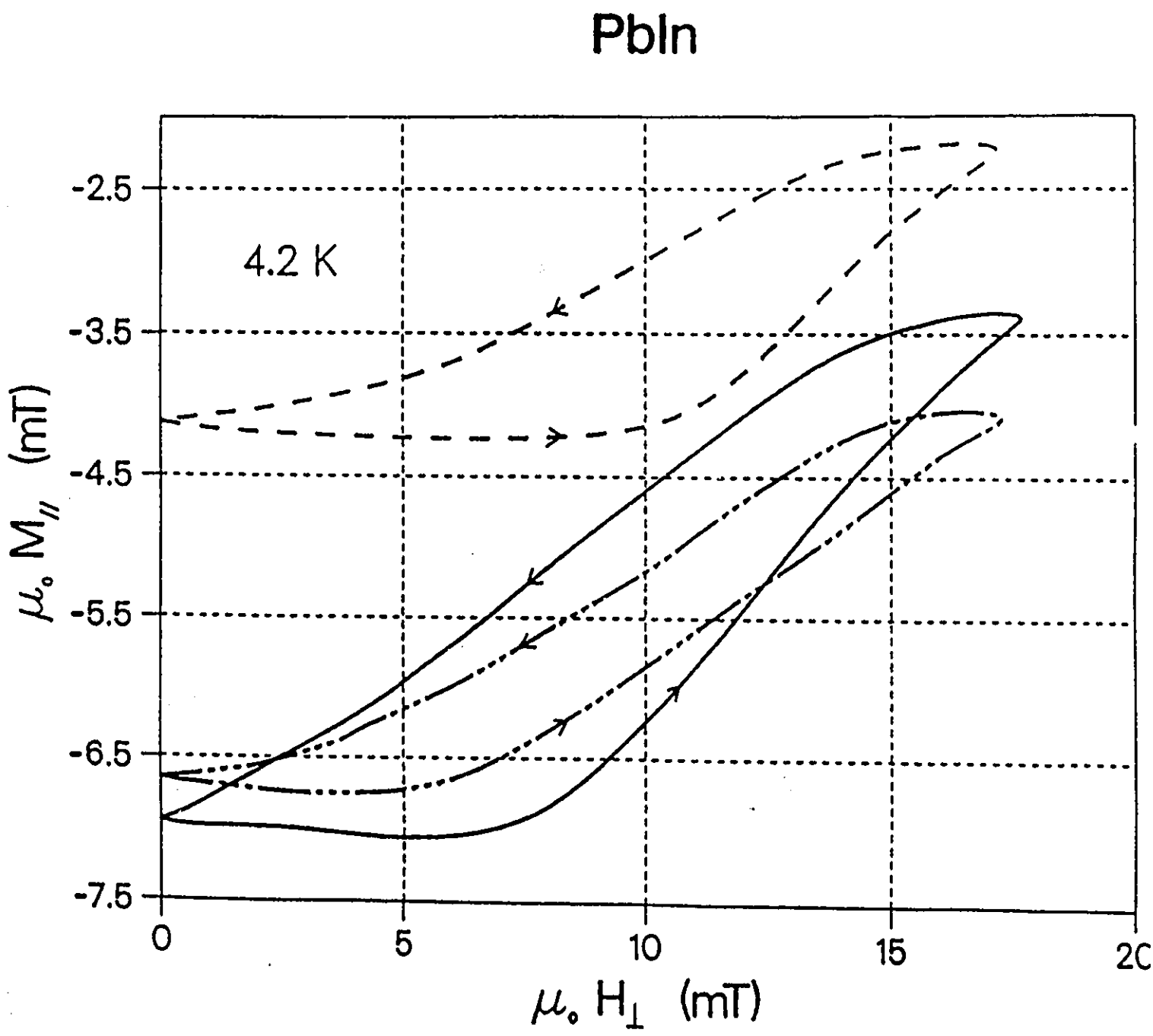

Figure 46: Illustrates the effect of different static bias fields $H_{||}$ on the periodic response of $M_{||}$ to half cycles of H_{perp} for the *PbIn* specimen. Here $\mu_o H_{||} = 5$, 10 and 15 mT for the - - - - - - - - , ———— , and — - — - — - — curves respectively.

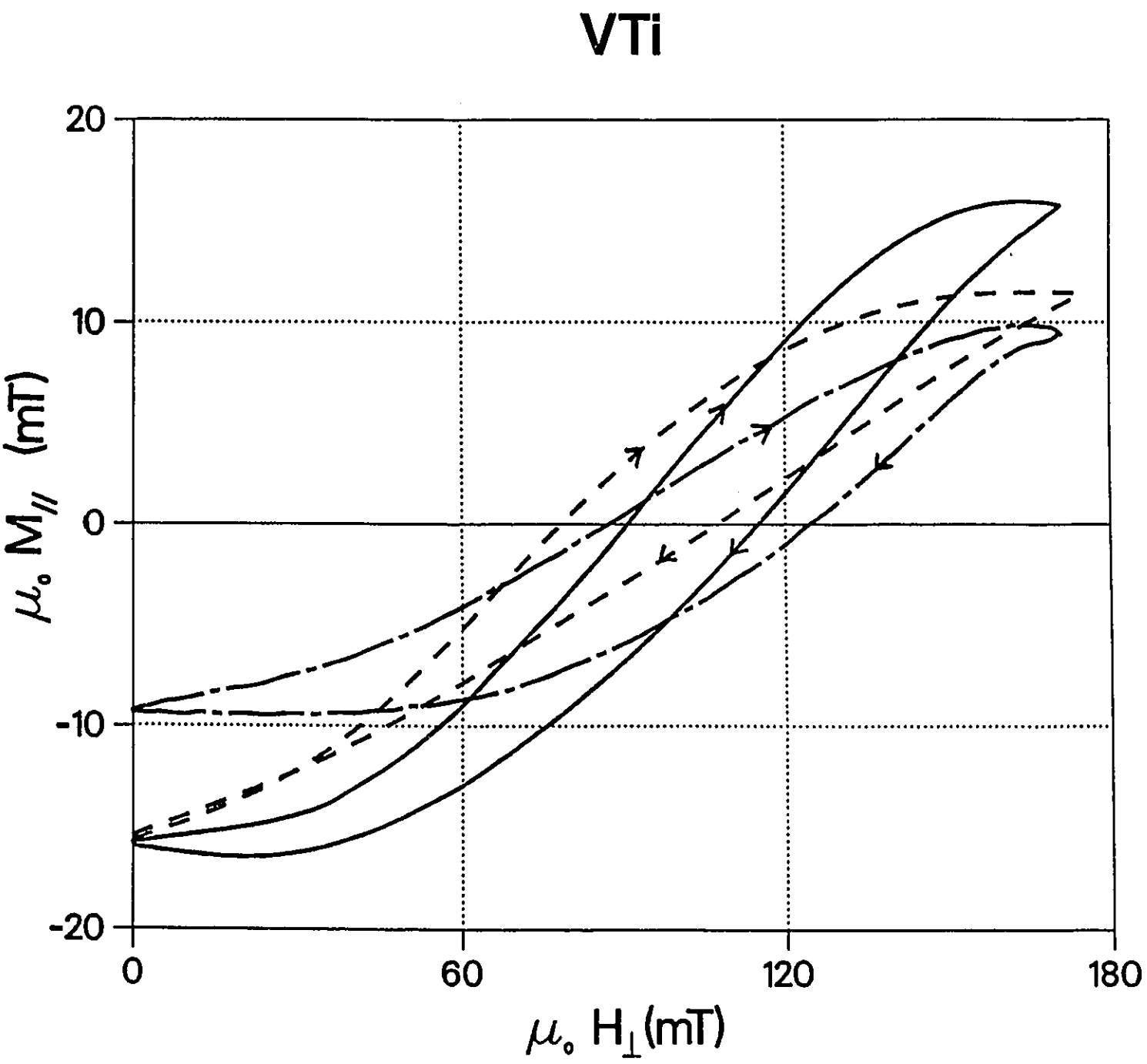

Figure 47: Illustrates the effect of different static bias fields $H_{||}$ on the periodic response of $M_{||}$ to half cycles of H_{perp} for the VTi specimen. Here $\mu_o H|| = 45$, 158, 340 mT for the - - - - - - - , ———— , and — - — - — - — curves respectively.

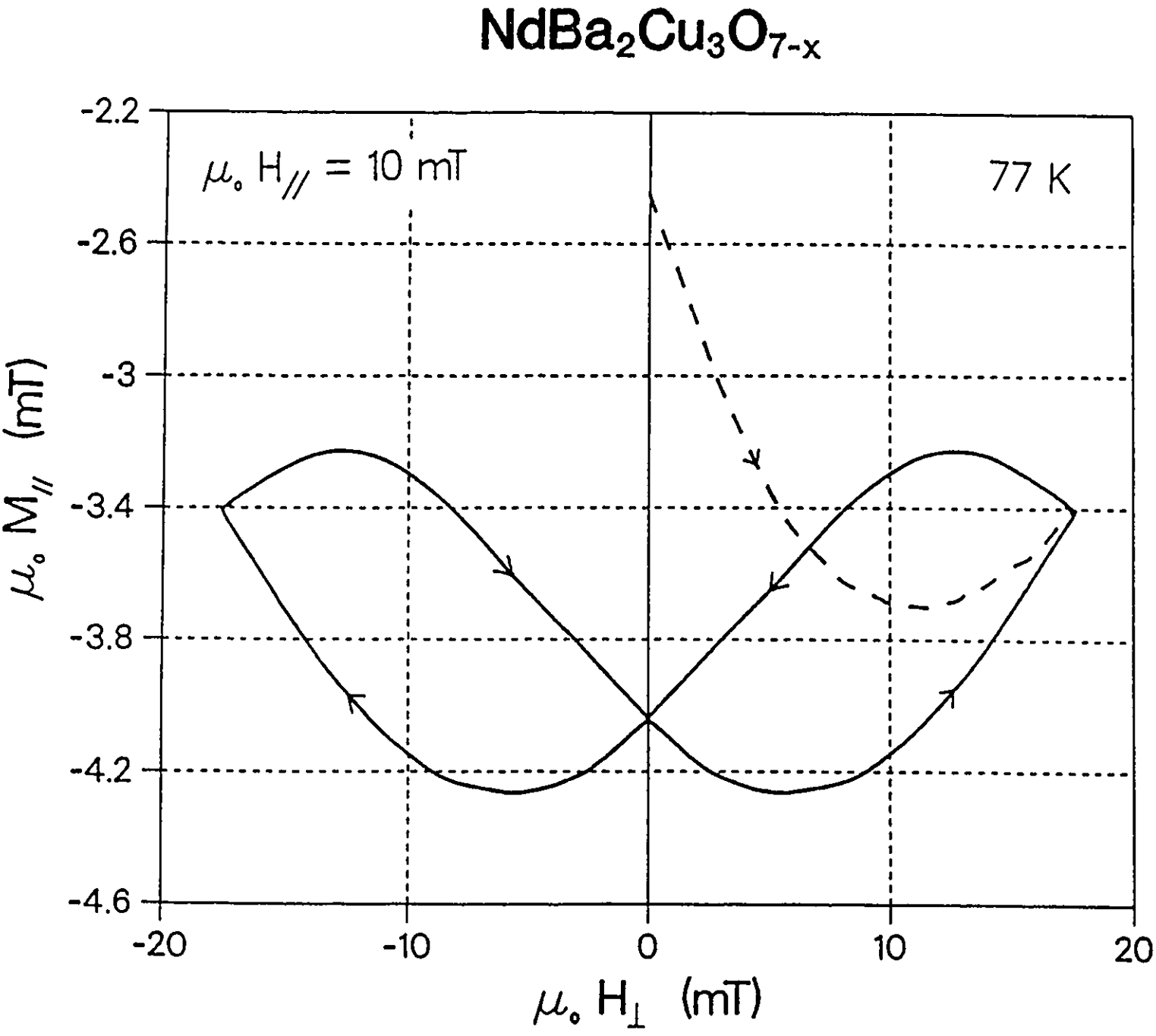

Figure 48: Typical "butterfly" traced periodically by the locus of the magnetic moment along a static bias field $H_{\parallel}$ as $H_{\perp}$ is made to swing symmetrically about $H_{\perp} = 0$ (full wave oscillations). Sample is the Nd at 77 K. Dashed curve displays the initial part of the response.

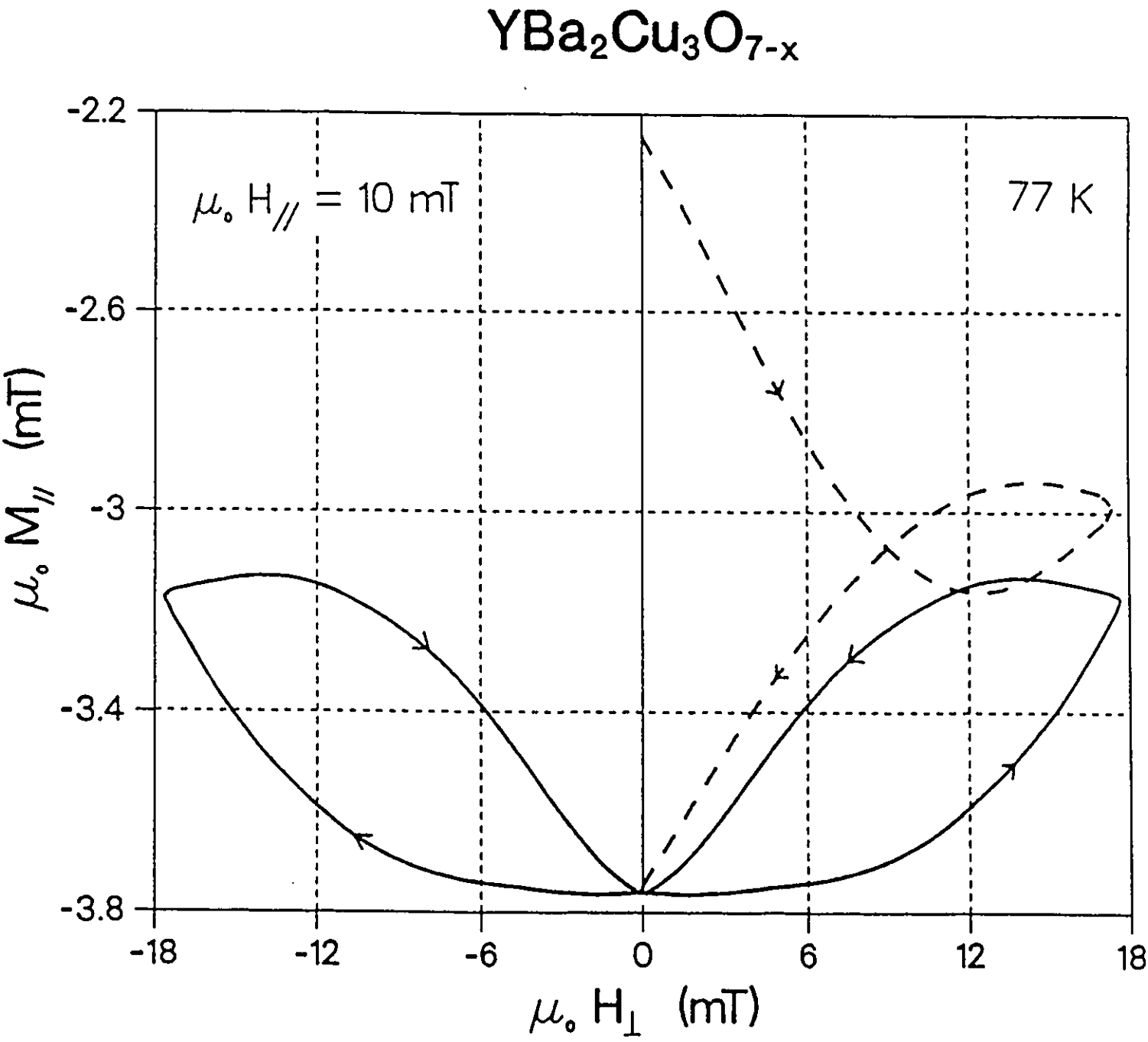

Figure 49: Same as the previous figure except here sample is $YBa_2Cu_3O_{7-x}$.

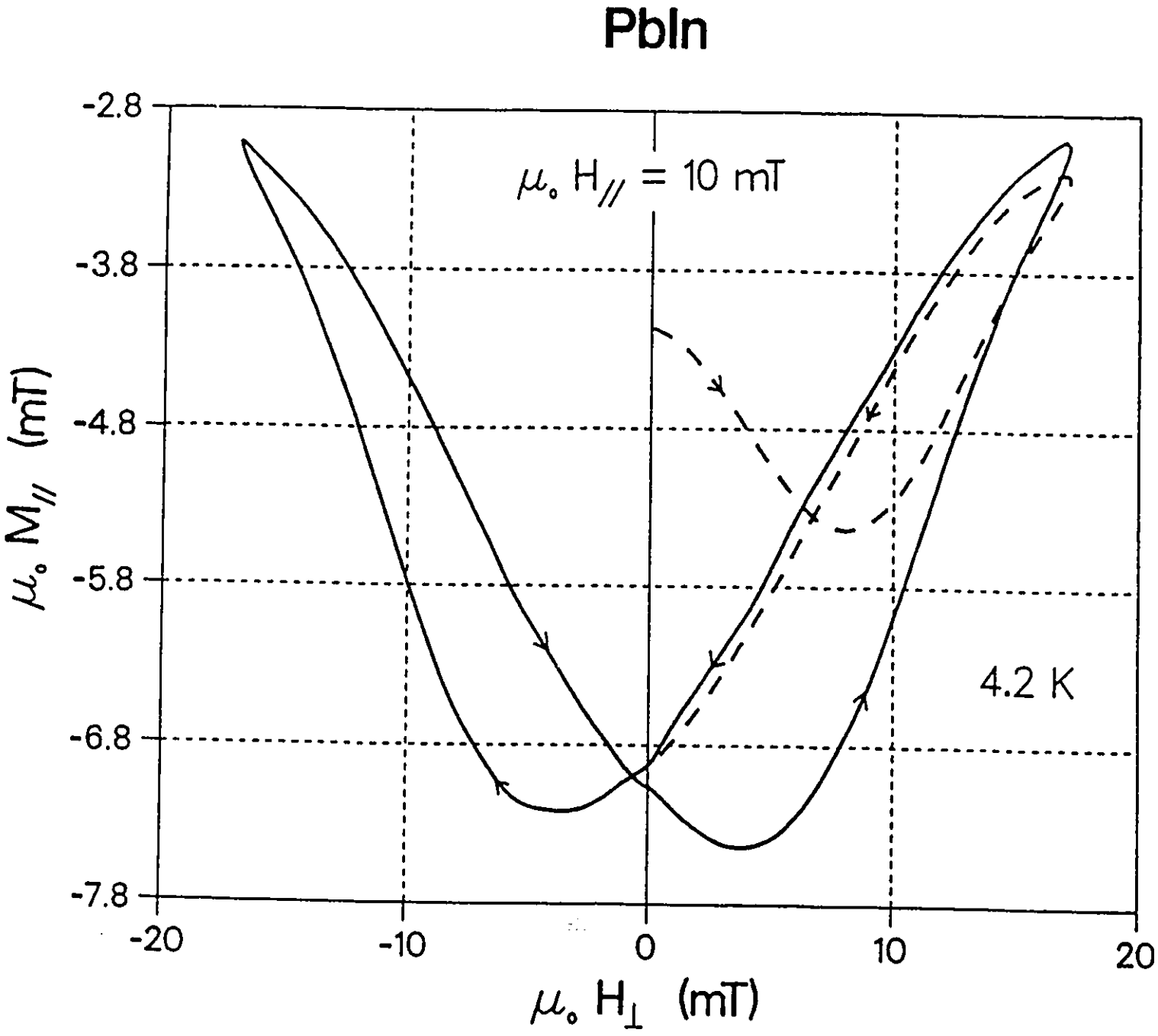

Figure 50: Same as the previous figure except here sample is *PbIn*.

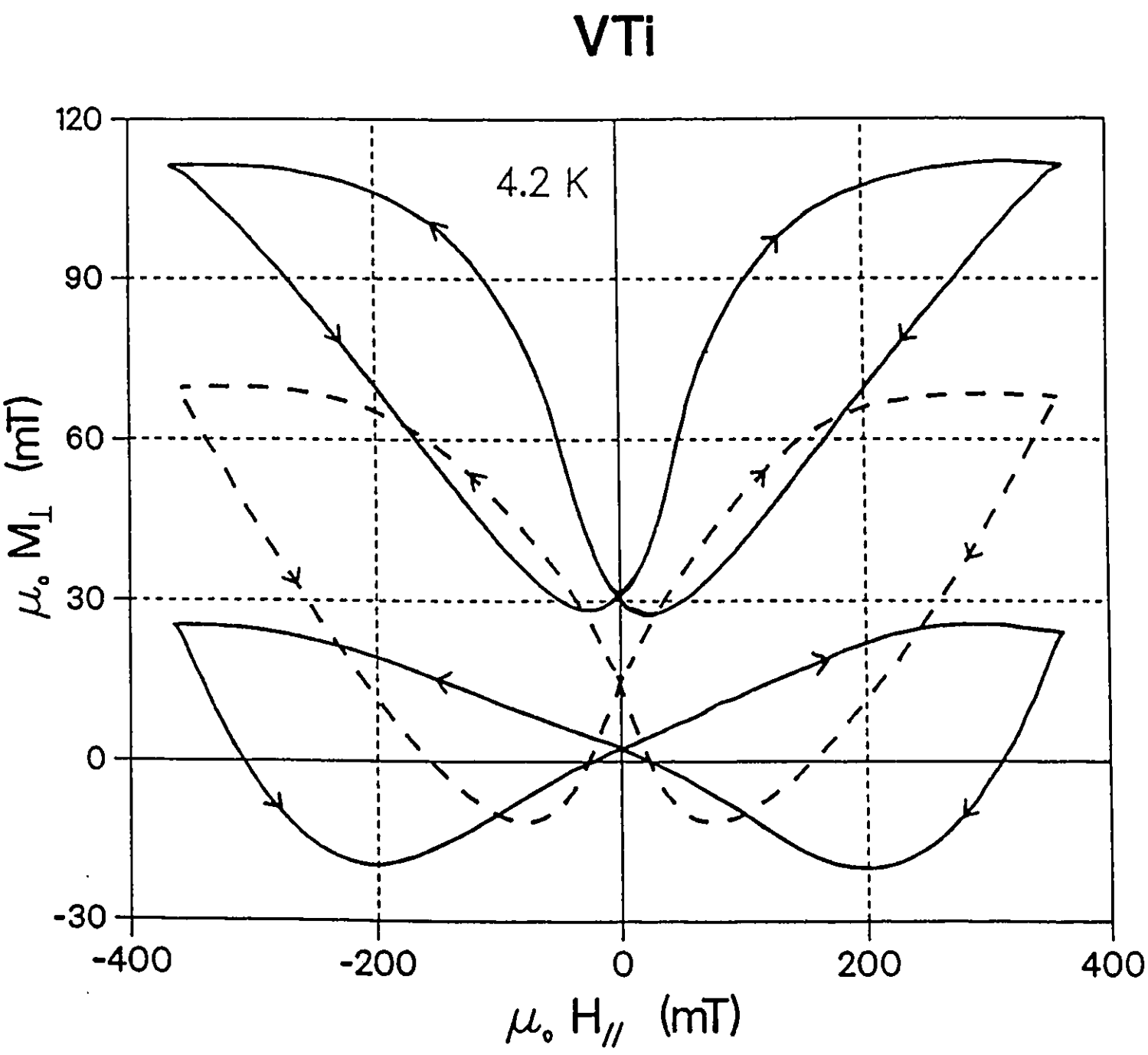

Figure 51: Same as previous three figures except that here the sample is VTi, the static bias field is $H_\perp$ along the width of the ribbon and the varying field is $H_\parallel$ along the length. Also we display "butterflies" observed with $\mu_o H_\perp = 51$, 104 and 204 mT (top,middle and bottom) to show that the sense of circulation (opposite in previous figures) remains constant over a wide range of bias field.

8.4 Analysis of $M_{\parallel}$ vs. $H_{\perp}$

The variety of phenomena we have catalogued so far in this chapter have been investigated theoretically by LeBlanc and Lorrain [35]. These workers exploited a simple double critical state model where $j_{\perp}$ and $j_{\parallel}$ are taken to flow at critical thresholds $j_{c\perp}(B)$ and $j_{c\parallel}(B)$ wherever changes in the magnitude and orientation of the magnetic flux configuration have occurred in the specimen. They assumed infinite slab geometry since this conformed to their ribbon samples. They found that in order to describe the behaviour of the highly hysteretic materials (Nb, $NbTi$, VTi) they had investigated, the ratio of $j_{c\parallel}$ to $j_{c\perp}$ introduced in the computations had to be appreciable (e.g. ≈ 10). These workers also explored the behaviour predicted when $j_{c\parallel} \approx j_{c\perp}$ in this model. Here the calculated curves exhibited many features which bore no resemblance with their observations on strong pinning materials. Consequently they did not pursue their theoretical study of these situations and discarded the results of these exploratory computations. We now recognize that the high T_c materials and the $PbIn$ specimen display many of the features which Lorrain and LeBlanc encountered in their brief theoretical visit to the domain where $j_{c\perp} \approx j_{c\parallel}$ but chose not to pursue since the behaviour did not correspond with their extensive observations on strongly hysteretic materials.

It is indeed encouraging and fascinating that the conceptually simple flux cutting framework pursued by Lorrain and LeBlanc successfully reproduced the vast panoply of intricate responses and complicated trends displayed by strongly hysteretic materials such as the VTi specimen which we have studied also. It is beyond the scope of this thesis and is left to other researchers and future graduate students in our laboratory to apply this model to the analysis of the variety of new behaviour

displayed by semi-reversible materials such as the high T_c and the *PbIn* samples and illustrated in numerous figures of this chapter.

In a qualitative perspective, it is clear that the persistent currents induced by varying $H_\perp$ circulate not only to oppose the entry (or exit) of magnetic flux along $H_\perp$ but flow in a variety of intricate "tilted" patterns which cause the magnetic flux density along the static bias field $H_\parallel$ to be dramatically augmented or diminished.

8.5 Effect of an Orthogonal Bias Field on the Standard Magnetization Curves

In the foregoing we have focused on the magnetic response along the bias field, the static component of $\vec{H}_a = \vec{y}H_\perp + \vec{z}H_\parallel$ since the behaviour along the static component or bias field provides the most spectacular macroscopic manifestation of flux line cutting processes. As noted previously, classical electrodynamics of a lossless conductor predicts zero response along the bias field. Also the observations deviate dramatically from the expectations for a lattice of flux lines where no flux cutting takes place.

In this final section we examine the magnetic behaviour along the component of $\vec{H}_a$ which is made to vary. This response collinear with the varying magnetic field constitutes the more familiar and conventional perspective. For this reason the evolution of the magnetization along the varying component of the applied magnetic field is referred to as the standard magnetization curves. We investigate the effect of the bias field on the standard magnetization curves and emphasize that the static bias field and the varying field are orthogonal to each other.

Since the high T_c samples as well as the *PbIn* specimen are quite isotropic in their magnetic response, it is immaterial whether the bias magnetic field is directed along the length or along the width of the rectangular slab hence whether the varying field component is oriented along the width or the length. The essential feature is that in the flux cutting regime, these two components be orthogonal to each other and lie along the flat faces of the rectangular slab specimen. We will continue to let $M_{||}$ and $H_{||}$ denote the magnetization and the magnetic field along the length of the ribbon and $M_{\perp}$ and $H_{\perp}$, denote these quantities along the width.

Because the pick up coil embracing the length of the slab specimen has many more turns, hence higher sensitivity than that embracing the width, it is experimentally preferable to monitor $M_{||}$ versus $H_{||}$ as $H_{||}$ is varied and let $H_{\perp}$ play the role of the static bias field.

The *VTi* specimen, however, exhibits significant anisotropy. Consequently the directions of the bias and varying fields are not arbitrary and interchangeable. We have, in the preceding, reported on the behaviour when the bias field was directed along the length and the varying field along the width. Thus, in order that the data we present be fully complementary, we will continue to display results obtained in this arrangement for the *VTi* specimen.

There was no bias field present when the solid curves displayed in Figs. 52 through 55 were monitored. Consequently these data exhibit the traditional magnetic response where no flux cutting is taken place. An orthogonal bias field was present, hence conditions for flux cutting prevail, when the dashed curves in these figures were measured. We note that the effect of the bias field is not only quite dramatic but leads to opposite results for different materials.

In the case of the high T_c and the *PbIn* specimens, the maximum capacity of

the induced persistent currents to shield against flux entry is clearly depressed by the static bias magnetic field. In contrast the ability of the VTi to oppose entry of flux is appreciably enhanced by the bias fields.

As regards the response of the high T_c and the $PbIn$ specimens to a decrease in the magnitude of $\vec{H}_a$, the effect of a static bias field, hence of flux cutting, is less clear. It is evident however that the residual trapped flux is diminished when a bias field is present (see lower curves of Figs. 52, 53 and 54). For the VTi sample, however, the role of a bias field is clearcut and is seen to lead to a spectacular augmentation in the ability of the material to imprison magnetic flux. This feature emerges from the relative position of the three bottom curves in Fig. 55.

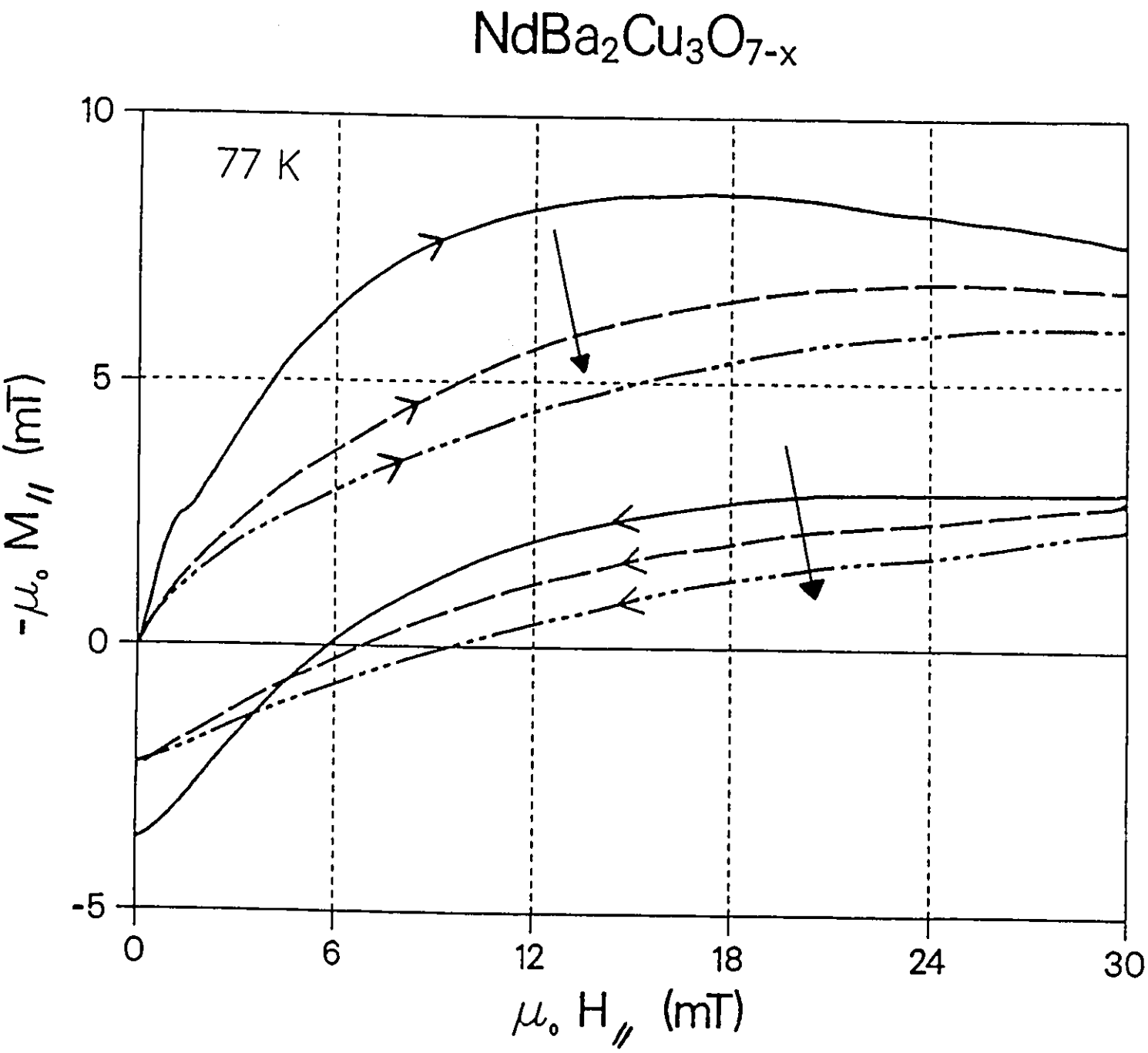

Figure 52: Illustrates the effect of a static bias field $H_\perp$ orthogonal to a varying magnetic field $H_{parallel}$ on the ability of the Nd specimen, (i) to shield against entry of magnetic flux along $H_\parallel$ upon the initial application of $H_\parallel$ (upper 3 curves) and (ii) to retain magnetic flux along $H_\parallel$ as $H_\parallel$ is removed. The stationary bias field $\mu_o H_\perp$ is 0 , 14.7 , and 23 mT for ————, - - - - - - - - - , and — - — - — curves respectively.

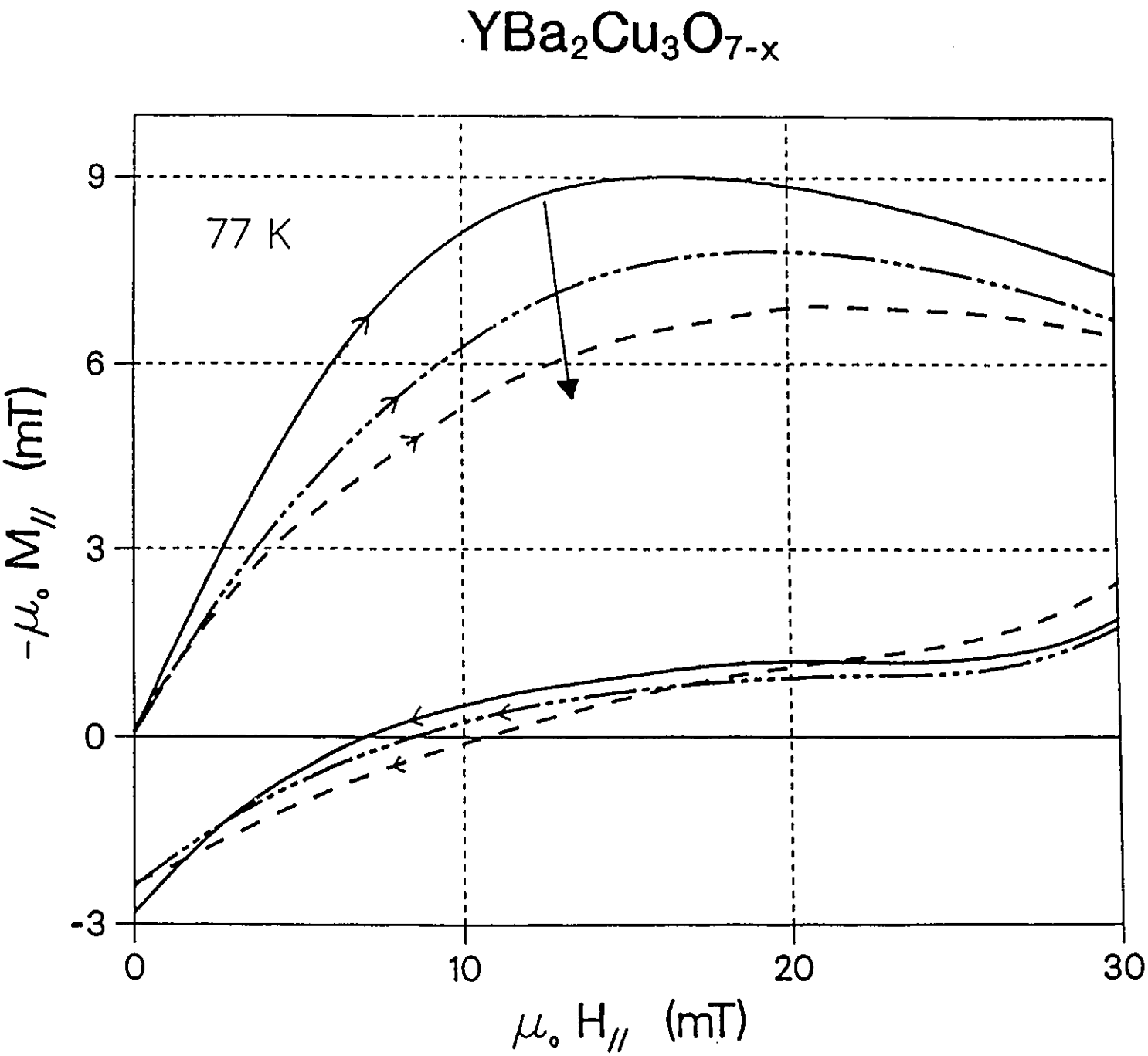

Figure 53: Same as the previous figure except here sample is $YBa_2Cu_3O_{7-x}$. The static bias field $\mu_o H_\perp = 0$, 10 , and 20 mT for the ————, — - — - —, and - - - - - - - - curves respectively.

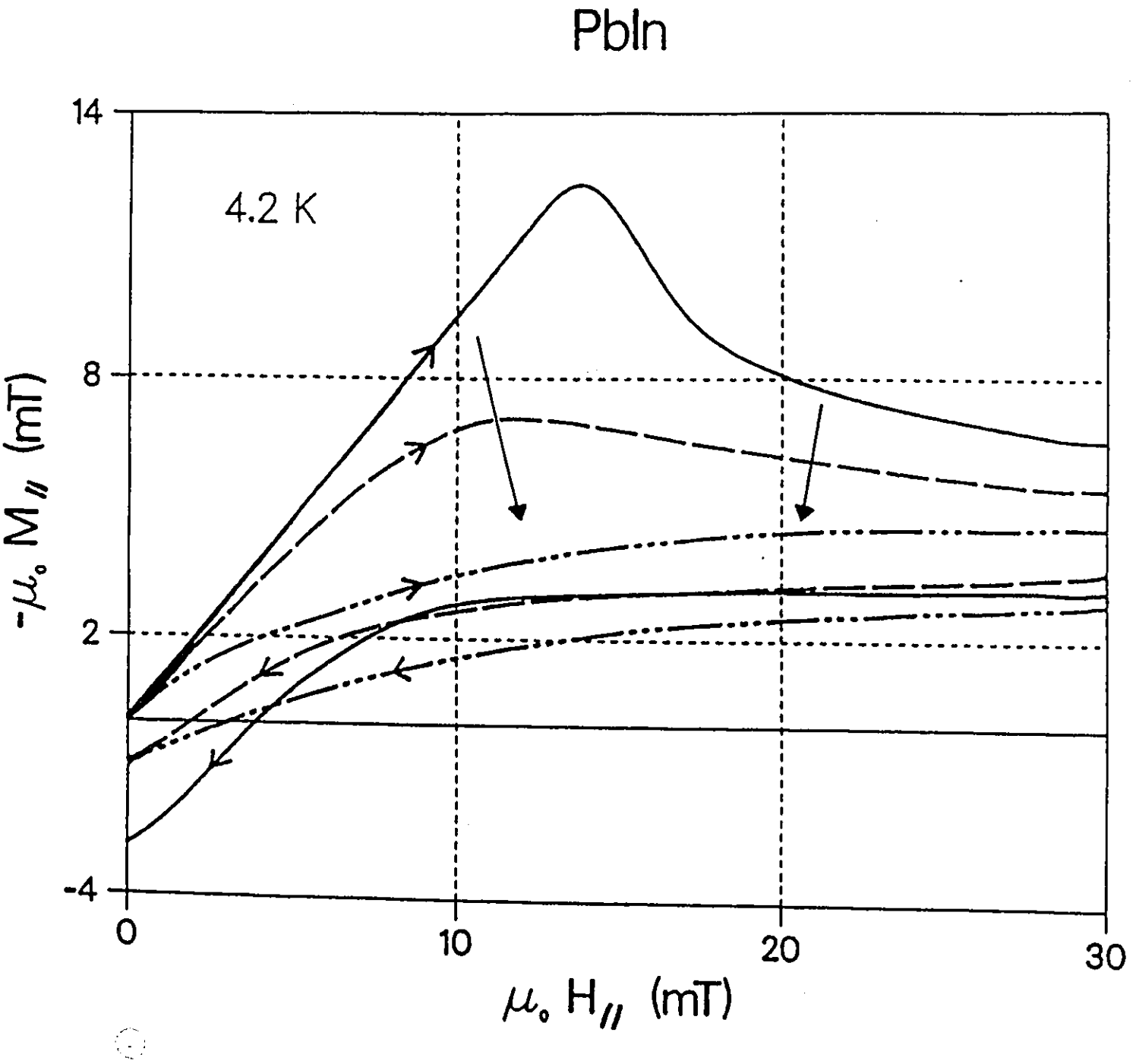

Figure 54: Same as in the previous figure, except that the sample is now *PbIn*. $\mu_o H_\perp = 0$, 10 , 20 mT for the ————, - - - - - - - - , and — - — - — curves respectively.

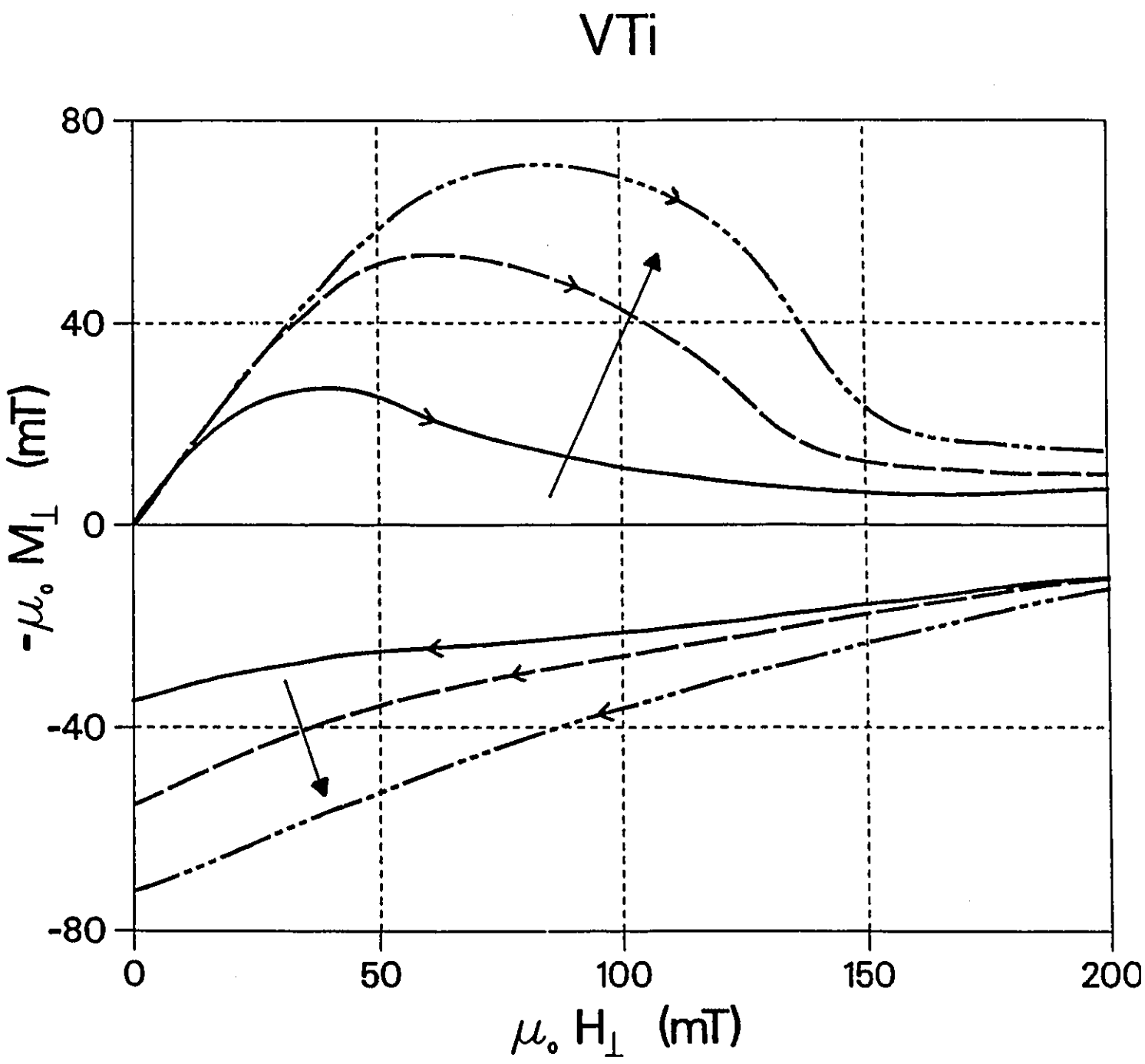

Figure 55: Same as for the previous figures, except here specimen is *VTi*, static bias field is along the length of the ribbon ($H_\parallel$) and the varying field is along the width ($H_\perp$) . $\mu_o H_\parallel$ = 0 , 45 , 90 mT for the ————, - - - - - - - - - , and — - — - — curves. Note that in contrast with the three other specimens, the capacity of the sample to shield against flux entry and to retain magnetic flux along $H_\perp$ is enhanced by a static bias field.

8.6 Analysis of $M_{\parallel}$ vs $H_{\parallel}$ (or $M_{\perp}$ vs $H_{\perp}$) Curves

Timms and LeBlanc [65] and later Lachaine [34], Lorrain [46] and LeBlanc et al. [39] accounted for the phenomena exhibited by hysteretic (strong pinning) materials and illustrated in part in Fig. 55 in the case of our VTi specimen. The latter group of workers exploited the double critical state model already outlined above. This model generated theoretical curves reproducing remarkably well observations similar to that presented in Fig. 55 as well as many other complex features of a vast assortment of pertinent data on the effect of static bias fields on the standard magnetization curves. In order to obtain qualitative and quantitative agreement between theory and experiment, large ratios of $j_{c\parallel}$ to $j_{c\perp}$ (e.g. 5 to 15) had to be introduced in the modeling.

The predictions in the limit where $j_{c\parallel}$ is comparable to $j_{c\perp}$ were not pursued by these researchers since this regime did not appear to be relevant to the extensive body of experimental results accumulated at the time. In the light of our work and recent investigations by Sekerka [61], it is now abundantly clear that the double critical state model should be applied to situations where $j_{c\parallel}/j_{c\perp} \approx 1$. This exercise is left as a challenge to other workers and graduate students in our laboratory.

8.7 Conclusion

We have investigated the magnetic response of sintered high T_c materials, $PbIn$ and a VTi sample in the flux line cutting regime. We adopted a simple recipe to establish the conditions for flux line cutting. Persistent currents are induced to flow with a component $\parallel$ to $\vec{H}_a$ by varying $\vec{H}_a = \vec{y}H_{\perp} + \vec{z}H_{\parallel}$ in such a manner that one

of its two orthogonal components ($H_{\|}$) is maintained fixed while the other ($H_{\perp}$) is made to vary (or vice versa).

We observe that the magnetic flux density along the static bias field ($H_{\|}$) does not remain constant but evolves in a complicated manner as $H_{\perp}$ is impressed, removed and subsequently undergoes half-wave and full-wave oscillations. Inspection of the assortment of illustrative data which we present reveals that the semi-reversible materials (the high T_c and the *PbIn* specimens) exhibit very similar behaviour. The response of the hysteretic *VTi* sample however is generally different and indeed the opposite of that shown by the semi-reversible materials.

We conjecture that the differences in behaviour can be attributed to the fact that the ratio of $j_{c\|}$ to $j_{c\perp}$ is large (≈ 10) in the strong pinning (hysteretic) *VTi* specimen whereas $j_{c\|} \approx j_{c\perp}$ in the other materials. This conjecture will have to be verified by a detailed qualitative analysis exploiting established flux cutting models.

Appendix A

Magnetic Flux Distribution

Rectangular Case

When a uniform externally applied magnetic field is directed along the surfaces of a homogeneous infinite slab or along the axis of an infinite cylinder, the distribution of the magnetic flux is a one-dimensional problem with attendant computational and analytic simplicity. In this appendix we show that the distribution of the magnetic flux in a rectangular specimen of uniform cross-section along its infinite length is mathematically also reduces to a one-dimensional problem when a uniform $\vec{H}_a$ is again directed along the surfaces.

It is well known that the magnetic flux density inside a circular infinitely long solenoid is uniform. This is demonstrated in many text books using Ampere's law,

$$\int \vec{B} \cdot \vec{dl} = \mu_o I_{enclosed} \tag{1}$$

together with symmetry considerations. Let the axis of the solenoid coincide with the z axis.

By symmetry, $\vec{B}$ cannot possess components in the $r-\theta$ *plane* ($x-y$ plane), cannot vary along the z axis, and cannot depend on the azimuthal angle θ, hence,

$$\vec{B} = \vec{z}\,B_z(r) \tag{2}$$

Now applying Ampere's law over a rectangular closed path with two sides parallel to the z axis and two radial edges establishes that,

$$B_z(r_1) = B_z(r_2) \tag{3}$$

when both r_1 and r_2 lie inside the solenoid, hence no current is embraced. Thus B_z is independent of r and is, therefore, uniform. Repeating this procedure with both r_3 and r_4 outside the solenoid gives,

$$B_z(r_3) = B_z(r_4) \tag{4}$$

Thus, B_z is shown to be uniform outside the solenoid. A third application of Ampere's law, now with r_1 inside and r_3 outside the solenoid, yields

$$B_z(r_1) - B_z(r_3) = \mu_o I \tag{5}$$

where I is the current per unit length of the solenoid.

The requirement that the "return" magnetic flux generated by the solenoid be finite, means that the "return" magnetic flux density must be zero, hence

$$B_z(r_3) = \mu_o H_a \tag{6}$$

where H_a is an externally applied uniform magnetic field.

Focusing on B_z at the axis of the solenoid, equation 5 can also be obtained by integrating the Biot-Savart law over the volume of the solenoid.

It is less well known that the magnetic flux density is uniform inside (and outside) an infinitely long solenoid of arbitrary but constant cross-section. Here, again by symmetry, $\vec{B}$ cannot possess components in the $r-\theta$ plane ($x-y$ plane) and cannot vary along the z axis. Symmetry considerations, however, now allow a variation of B_z in the $r-\theta$ plane ($x-y$ plane). Hence we can write,

$$\vec{B} = \vec{z}B_z(r,\theta) = \vec{z}B_z(x,y) \tag{7}$$

Application of Ampere's law for closed paths constructed as above and lying either entirely inside, entirely outside or bracketing the wall of the solenoid leads to,

$$B_z(r_1,\theta_1) = B_z(r_2,\theta_2) = B_z(x_1,y_1) = B_z(x_2,y_2) \tag{8}$$

$$B_z(r_3,\theta_3) = B_z(r_4,\theta_4) = B_z(x_3,y_3) = B_z(x_4,y_4) \tag{9}$$

$$B_z(r_1,\theta_1) - B_z(r_3,\theta_3) = \mu_o I \tag{10}$$

$$B_z(x_1,y_1) - B_z(x_3,y_3) = \mu_o I \tag{11}$$

Again the condition that the "return" magnetic flux be finite requires that outside the solenoid,

$$B_z = \mu_o H_a \tag{12}$$

We stress that the rectangular solenoid is simply a special case of the solenoid of arbitrary cross-section.

It is not well known that the Biot-Savart law can be solved in closed form to yield $\vec{B}(x,y,z)$ at an arbitrary point inside or outside a rectangular solenoid with infinitesimally thin walls. We now develop this result.

Let the four walls of the rectangular solenoid be symmetrically situated with respect to the z-axis, one pair located at, $x = \pm a$ and extending between $-b \leq y \leq b$, the other pair placed at $y = \pm b$ and extending between $-a \leq x \leq a$.

The current elements circulating around the rectangular solenoid have a magnitude,

$$\Delta I = K_y\, dz' = K_x\, dz' \tag{13}$$

and their elemental length vector can be written

$$\vec{dl} = \pm \hat{x}\, dx' \qquad \text{, or} \qquad \vec{dl} = \pm \hat{y}\, dy' \tag{14}$$

where the prime denotes a source quantity.

For simplicity, we let the arbitrary field point lie in the $z = 0$ plane. This choice is immaterial since the solenoid is infinite along the z axis. The general expression for the field point is then,

$$\vec{r} = \hat{x}\, x + \hat{y}\, y \tag{15}$$

To fix ideas we focus on the solenoid wall located at $x = a$. The general expression for the position of an arbitrary current element along this wall then reads,

$$\vec{r'} = \hat{x}\, a + \hat{y}\, y' + \hat{z}\, z' \tag{16}$$

Introducing eqns 13 through 16 into the Biot-Savart law,

$$\Delta \vec{B} = \frac{\mu_o \Delta I\, \vec{dl} \times (\vec{r} - \vec{r'})}{4\pi \mid \vec{r} - \vec{r'} \mid^3} \tag{17}$$

leads to,

$$\Delta \vec{B_a} = \hat{x}\, \Delta B_x^a + \hat{z}\, \Delta B_z^a \tag{18}$$

where,

$$\Delta B_x^a = \frac{\mu_o K_y\, dy'\, z'\, dz'}{4\pi \left[(x-a)^2 + (y-y')^2 + z'^2 \right]^{\frac{3}{2}}} \tag{19}$$

B_x is seen to vanish since the integration over z' performed first yields zero. The integral for B_z reads,

$$B_z^a = \frac{\mu_o K_y (x-a)}{4\pi} \int_{-b}^{+b} dy' \int_{-\infty}^{+\infty} \frac{dz'}{\left[(x-a)^2 + (y-y')^2 + z'^2 \right]^{\frac{3}{2}}} \tag{20}$$

The integration over z' yields,

$$A = \frac{2}{\left[(x-a)^2 + (y-y')^2 \right]} \tag{21}$$

Integrating now over y' cancels out the $(a-x)$ pre-factor and leads to,

$$B_z^a = \frac{\mu_o K_y}{2\pi} \left[\tan^{-1}\left(\frac{b+y}{a-x}\right) + \tan^{-1}\left(\frac{b-y}{a-x}\right) \right] = \frac{\mu_o K_y}{2\pi} \left[\theta_1 + \theta_2\right] = \frac{\mu_o K_y}{2\pi} \theta_a \tag{22}$$

We stress that,

$$\theta_a = \theta_1 + \theta_2 \tag{23}$$

represents the angle subtended between the lines joining the arbitrary field point (x, y) and the edges of the current sheet located at (a, b) and $(a, -b)$ as shown in the accompanying sketch.

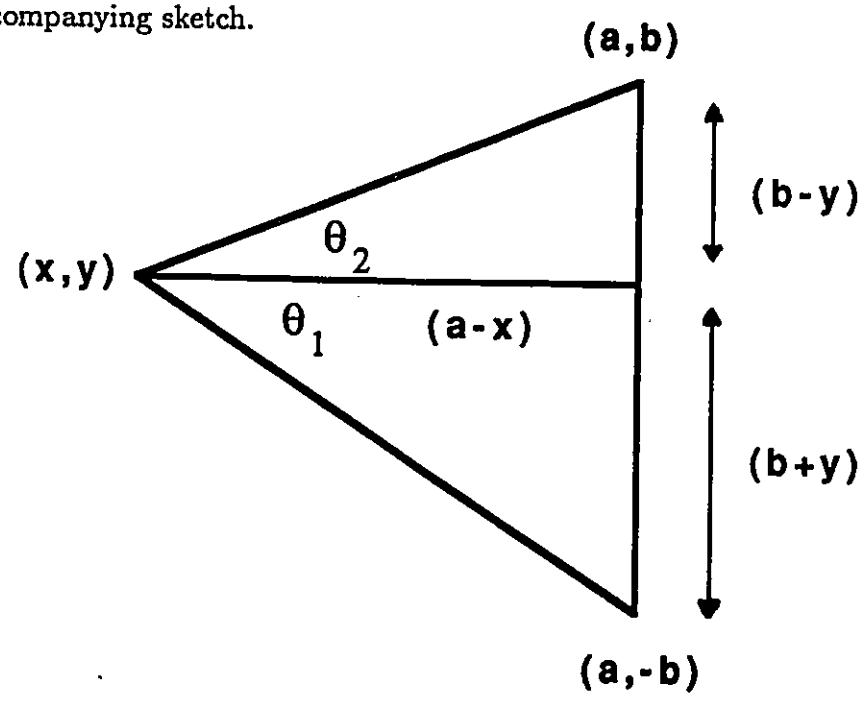

Equation 22 describes the configuration of the magnetic flux density generated in space by a current sheet of width $2b$ straddling the x axis symmetrically at $x = a$. This sheet of finite width is infinite in length along the z axis and carries a uniform surface current K_y per unit length Z flowing along the $+y$ direction. We stress that $B_z^a(x, y)$ is **not** uniform.

We can repeat the procedure followed above for the 3 other sides of the rectangular solenoid and combine all of these results. Alternatively and more expeditiously we note that the sum of the four pairs of subtended angles ($\theta_a = \theta_1 + \theta_2$, etc...) must, (i) equal 2π when the field point (x, y) is situated inside the rectangular solenoid and (ii) yield zero when (x, y) is outside the solenoid.

Both procedures lead to

$$B_z^I = \mu_o I = \mu_o K_y = \mu_o K_x \tag{24}$$

when (x, y) is inside the rectangular solenoid and,

$$B_z^I = 0 \tag{25}$$

when (x, y) is outside.

We stress that the superposition of the four inhomogeneous magnetic fields generated by the four sides of the rectangular solenoid produces a resultant magnetic field which is uniform inside the solenoid and zero outside. The magnetic flux density B_z^I must then be combined with the externally applied $B_a = \mu_o H_a$ to give the final result.

We now proceed to construct a thick-walled rectangular solenoid by concentrically nesting thin walled rectangular solenoids inside each other while maintaining the aspect ratio b/a of the constituents constant. The uniform current $I = K_x = K_y$ circulating around each of these concentric rectangular solenoids

may be chosen to correspond to the critical current I_c for a superconducting material. It is now convenient to rewrite eqn 24 to read,

$$\Delta B_z = \pm \mu_o \Delta I' = \pm \mu_o j_{c\perp_y} \Delta x = \pm \mu_o j_{c\perp_x} \Delta y \tag{26}$$

This gives ΔB_z, the increment in the magnetic flux density, generated by the current $\Delta I'$ flowing (per unit length along Z) around an arbitrary member of the concentric array of nesting rectangular solenoids. The subscripts x and y denote the direction of flow of the current density in the various sides of the rectangular solenoid.

We must envisage the possibility that the critical current densities $j_{c\perp_x}$ and $j_{c\perp_y}$ depend on B and consequently that $j_{c\perp_x}$ may vary along y and similarly that $j_{c\perp_y}$ may vary along x.

However, since we have shown that all of the segments of any particular rectangular solenoid bathe in the same uniform magnetic flux density (generated by the surrounding solenoids and by the solenoid under consideration) we must conclude that $j_{c\perp_x}$ and $j_{c\perp_y}$ will not vary with position along the circumference of the rectangular solenoid under scrutiny. Hence, we can write

$$j_{c\perp_y}(x) = j_{c\perp_y} = j_{c\perp_x}(y) = j_{c\perp_x} = j_{c\perp} \tag{27}$$

Thus the infinitesimal thickness Δx or Δy occupied by $\Delta I'$ in an individual rectangular solenoid will be uniform around the circumference of that solenoid. As a consequence of this and allowing no empty space between the nesting concentric rectangular solenoids, eqn 26 can be written in differential form to read,

$$\frac{dB_z}{dx} = \pm \mu_o j_{c\perp}(x) \tag{28}$$

or equivalently,

$$\frac{dB_z}{dy} = \pm \mu_o j_{c\perp}(y) \tag{29}$$

In either case, the problem has been reduced to one dimension. The depth

$$d_p = a - x_p = b - y_p \tag{30}$$

occupied by the persistent currents circulating in a homogeneous "thick-walled" rectangular solenoid is thus seen to be uniform throughout its cross-section and the B_z profiles to exhibit the same variation with distance from all of the four surfaces.

Appendix B

Calculations of Residual Trapped Flux

We consider two limiting idealized geometries, the infinite slab and infinite cylinder. It is convenient to locate the surfaces of the slab at $x = 0$ and $x = 2X$. In view of the symmetry of the B profiles we need only consider the configuration between $x = 0$ and the midplane at $x = X$. The axis of the cylinder of radius R is situated at $r = 0$. The externally applied field $\vec{H}_a$ is directed along the z-axis. We will, however, omit the subscript z in the expressions for $B(x)$ and $B(r)$.

We develop expressions for the residual trapped flux generated by two procedures denoted H_{cool} and H_{cycle}. To bracket the expected behaviour, we select two extreme dependencies of the depinning critical current density $j_{c\perp}$ on B, the Bean ($j_{c\perp} = \alpha_B$) and the Kim ($j_{c\perp} = \alpha_K/B$) approximations.

B.1 H_{cool} PROCEDURE

We visualize that after cooling from T_c to ambient in a static applied field $H_a = H_{cool}$, which is then reduced to zero, the configuration of the residual trapped flux corresponds to the following. We refer the reader to the accompanying sketch which schematically displays the ensuing B profiles. A region filled with flux retaining persistent currents where $j_\perp = j_{c\perp}$, hence $dB/dx = (dB/dx)_c$ (or $dB/dr = (dB/dr)_c$), surrounds the remaining volume where B is uniform. Let B_s denote the magnetic flux density in this inner region. We stipulate that $B_s = \mu_o H_{cool}$. This assumption is presumably exact for strong pinning materials which exhibit no flux expulsion upon cooling but only approximate in the case of semi-reversible type II superconductors where some flux expulsion (Meissner effect) is observed. For clarity, we focus on the Bean and Kim approximations separately. The variables x and r serve to indicate the applicable geometry (slab or cylinder).

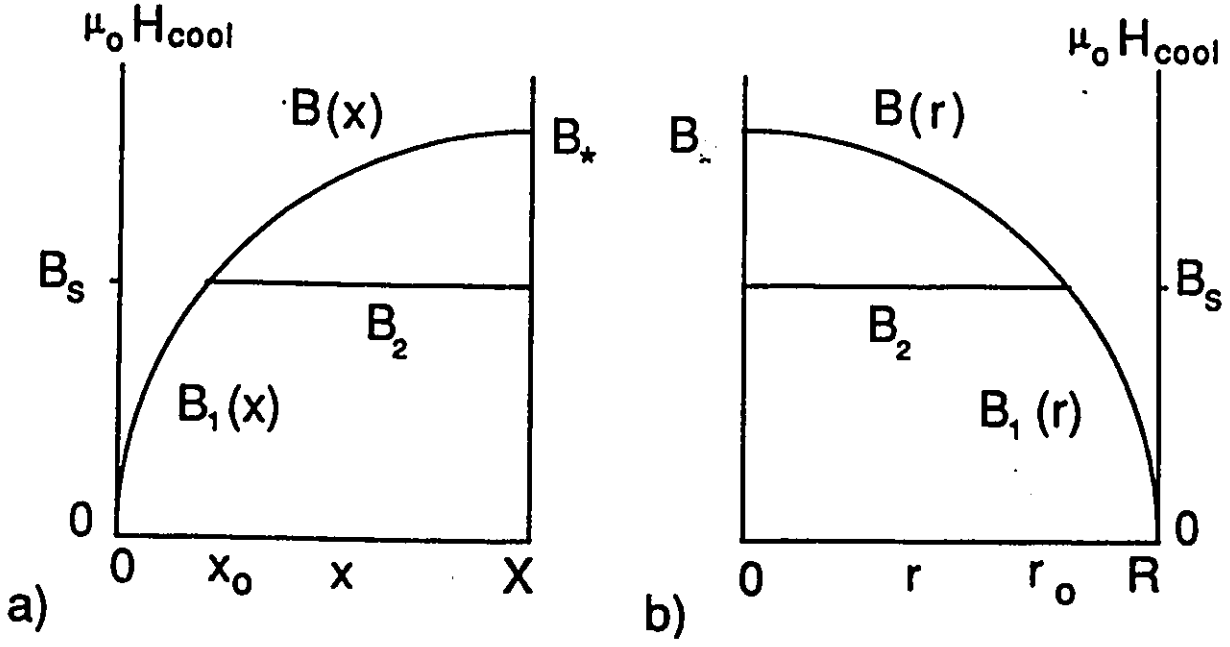

BEAN APPROXIMATION

In the outer volume filled with flux retaining critical persistent currents, the Maxwell-Ampere equation reads,

$$\frac{dB}{dx} = \frac{dB}{dr} = \pm \mu_o j_{c\perp} = \pm \mu_o \alpha_B \tag{1}$$

Integrating leads to,

$$B_1(x) = B_\star \frac{x}{X} \qquad \text{when} \qquad 0 \leq x \leq x_o \tag{2}$$

and

$$B_1(r) = B_\star (1 - \frac{r}{R}) \qquad \text{when} \qquad r_o \leq r \leq R \tag{3}$$

where,

$$B_\star = \mu_o \alpha_B X = \mu_o \alpha_B R \tag{4}$$

and,

$$\frac{x_o}{X} = \frac{B_s}{B_\star} \qquad \frac{r_o}{R} = 1 - \frac{B_s}{B_\star} \tag{5}$$

As stipulated,

$$B_2(x) = B_2(r) = B_s \text{ when } x_o \leq x \leq X \text{ or } 0 \leq r \leq r_o \tag{6}$$

ϕ_{slab}, the magnetic flux trapped in a width Y of the slab and ϕ_{cyl}, the flux in the cylinder can be written,

$$\phi_{slab} = 2Y \left\{ \int_0^{x_o} B_1 \, dx + \int_{x_o}^{X} B_2 \, dx \right\} \tag{7}$$

$$\phi_{cyl} = 2\pi \left\{ \int_0^{r_o} B_2 \, r \, dr + \int_{r_o}^{R} B_1 \, r \, dr \right\} \tag{8}$$

Introducing the appropriate expression for B, the stipulation that $B_2 = B_s = \mu_o H_{cool}$, and the corresponding limits of integration, equation 7 leads to,

$$\phi_{slab} = 2XY B_\star \left[\left(\frac{B_s}{B_\star} \right) - \frac{1}{2} \left(\frac{B_s}{B_\star} \right)^2 \right] \tag{9}$$

and equation 8 to,

$$\phi_{cyl} = \pi R^2 B_\star \left[\left(\frac{B_s}{B_\star} \right) - \left(\frac{B_s}{B_\star} \right)^2 + \frac{1}{3} \left(\frac{B_s}{B_\star} \right)^3 \right] \tag{10}$$

The trapped flux attains a maximum when the specimen is entirely filled with flux retaining persistent circulating currents, hence when,

$$B_s = \mu_o H_{cool} = B_\star \tag{11}$$

Consequently, the maximum trapped flux and residual magnetization read,

$$\phi_{slab_{Max}} = XY B_\star \qquad \text{and} \qquad M_{r_{Max}} = \frac{B_\star}{2\mu_o} \tag{12}$$

$$\phi_{cyl_{Max}} = \frac{\pi R^2 B_\star}{3} \quad , \quad M_{r_{Max}} = \frac{B_\star}{3\mu_o} \tag{13}$$

Normalizing the expressions for the trapped flux and the residual magnetization to the corresponding maximum values and letting W denote these normalized quantities, we can write,

$$W_{slab} = 2u - u^2 \tag{14}$$

and

$$W_{cyl} = 3u - 3u^2 + u^3 \tag{15}$$

where $u = B_s/B_\star$ and $0 \leq u \leq 1$.

KIM APPROXIMATION

In the volume filled with flux retaining critical persistent currents, the Maxwell-Ampere equation reads,

$$\frac{dB}{dx} = \frac{dB}{dr} = \pm \mu_o j_{c\perp} = \pm \mu_o \frac{\alpha_K}{B} \tag{16}$$

Integrating leads to,

$$B_1(x) = B_\star \sqrt{\frac{x}{X}} \qquad \text{when} \qquad 0 \leq x \leq x_o \tag{17}$$

and

$$B_1(r) = B_\star \sqrt{1 - \frac{r}{R}} \qquad \text{when} \qquad r_o \leq r \leq R \tag{18}$$

where,

$$B_\star = \sqrt{2\,\mu_o\,\alpha_K\,X} = \sqrt{2\,\mu_o\,\alpha_K\,R} \tag{19}$$

and,

$$\frac{x_o}{X} = \left(\frac{B_s}{B_\star}\right)^2 \qquad\qquad \frac{r_o}{R} = 1 - \left(\frac{B_s}{B_\star}\right)^2 \tag{20}$$

Introducing the appropriate expressions from above for the B profile and the limits of integration into the definitions for the trapped flux (equations 7 and 8) leads to,

$$\phi_{slab} = 2\,X\,Y\,B_\star \left[\left(\frac{B_s}{B_\star}\right) - \frac{1}{3}\left(\frac{B_s}{B_\star}\right)^3 \right] \tag{21}$$

$$\phi_{cyl} = \pi\,R^2\,B_\star \left[\left(\frac{B_s}{B_\star}\right) - \frac{2}{3}\left(\frac{B_s}{B_\star}\right)^3 + \frac{1}{5}\left(\frac{B_s}{B_\star}\right)^5 \right] \tag{22}$$

Consequently, the maximum trapped flux and residual magnetization attained when $B_s = B_\star$ now read,

$$\phi_{slab_{Max}} = \frac{4}{3}\,X\,Y\,B_\star \qquad \text{and} \qquad M_{r_{Max}} = \frac{2}{3}\,\frac{B_\star}{\mu_o} \tag{23}$$

$$\phi_{cyl_{Max}} = \frac{8}{15}\,\pi\,R^2\,B_\star \qquad \text{and} \qquad M_{r_{Max}} = \frac{8}{15}\,\frac{B_\star}{\mu_o} \tag{24}$$

Equations 21 and 22 in normalized form read,

$$W_{slab} = \frac{3}{2}\left(u - \frac{u^3}{3}\right) \tag{25}$$

$$W_{cyl} = \frac{15}{8}\left[u - \frac{2}{3}u^3 + \frac{u^5}{5}\right] \tag{26}$$

which apply when $0 \leq u \leq 1$.

B.2 H_{cycle} PROCEDURE

A magnetic field $H_a > H_{c1}$ is applied to the virgin sample and causes magnetic flux to penetrate a distance x_p into the infinite slab or a depth $d = R - r_p$ into the cylinder. The volume invaded by the magnetic flux is filled with induced persistent currents at the critical flux depinning density $j_{c\perp}$ which circulate to oppose the entry of the magnetic flux. When B_s, the magnetic flux density just inside the surface of the specimen, is less than $B_\star$, the front of the advancing B profile is situated between the surface ($x = 0$ or $r = R$) and the midplane ($x = X$) or axis ($r = 0$).

The front of the B profile reaches the midplane or cylinder axis when B_s attains $B_\star$. At this juncture, the entire volume of the sample is filled with persistent currents flowing in a flux shielding sense. Any subsequent increase of B_s beyond $B_\star$ causes the magnetic flux density to increase throughout the specimen but does not qualitatively alter the configuration of the current distribution. We let B_2 denote the critical B profiles generated by the application of H_a (see Fig. 1).

H_a is then reduced to zero thereby causing B_s to also diminish to zero. The decrease of B_s allows flux lines to leave the specimen. The decrease of flux threading the sample induces electric currents to flow in the volume from which flux escapes. In the steady state, the persistent currents circulate at the critical flux depinning density $j_{c\perp}$ to oppose the exit of the magnetic flux. Let B_1 denote the B profile in the region occupied by these flux retaining currents (i.e. the volume adjacent to the surface from which flux has departed).

After an excursion of H_a from zero to H_{cycle} to zero, when B_s was not made to exceed B_{**}, the sample then comprises two concentric regions. An outer zone filled with flux retaining persistent currents (B_1 profile) surrounding a region occupied by persistent currents circulating to oppose flux entry (B_2 profile).

The interface between these two regions, hence the intersection of the B_1 and B_2 profiles, is denoted x_i or r_i. The position of this boundary is controlled by the magnitude of the excursion of B_s, hence the choice for H_{cycle}. This interface is seen to migrate inwards as B_s is chosen larger. By symmetry, this frontier lies halfway between the surface of the specimen and the initial depth of penetration of the magnetic flux provided that $B_s < B_*$. The interface approaches the center of the specimen as B_s is chosen greater than B_* and attains the midplane or axis when the excursion of $B_s \geq B_{**}$ (see Fig. 1 (c) and (f)). Consequently sweeps of H_{cycle} which caused B_s to rise above B_{**} leave the specimen filled with a saturated amount of trapped flux. We stress that the final configuration of the currents and of the magnetic flux generated by an excursion of B_s beyond B_{**} is identical to that established in the previous process when $\mu_o H_{cool} \geq B_*$. Thus the maximum trapped flux is the same for both procedures.

We now develop expressions for the remanent trapped flux as a function of B_s, hence of H_{cycle} for slab and cylinder geometry.

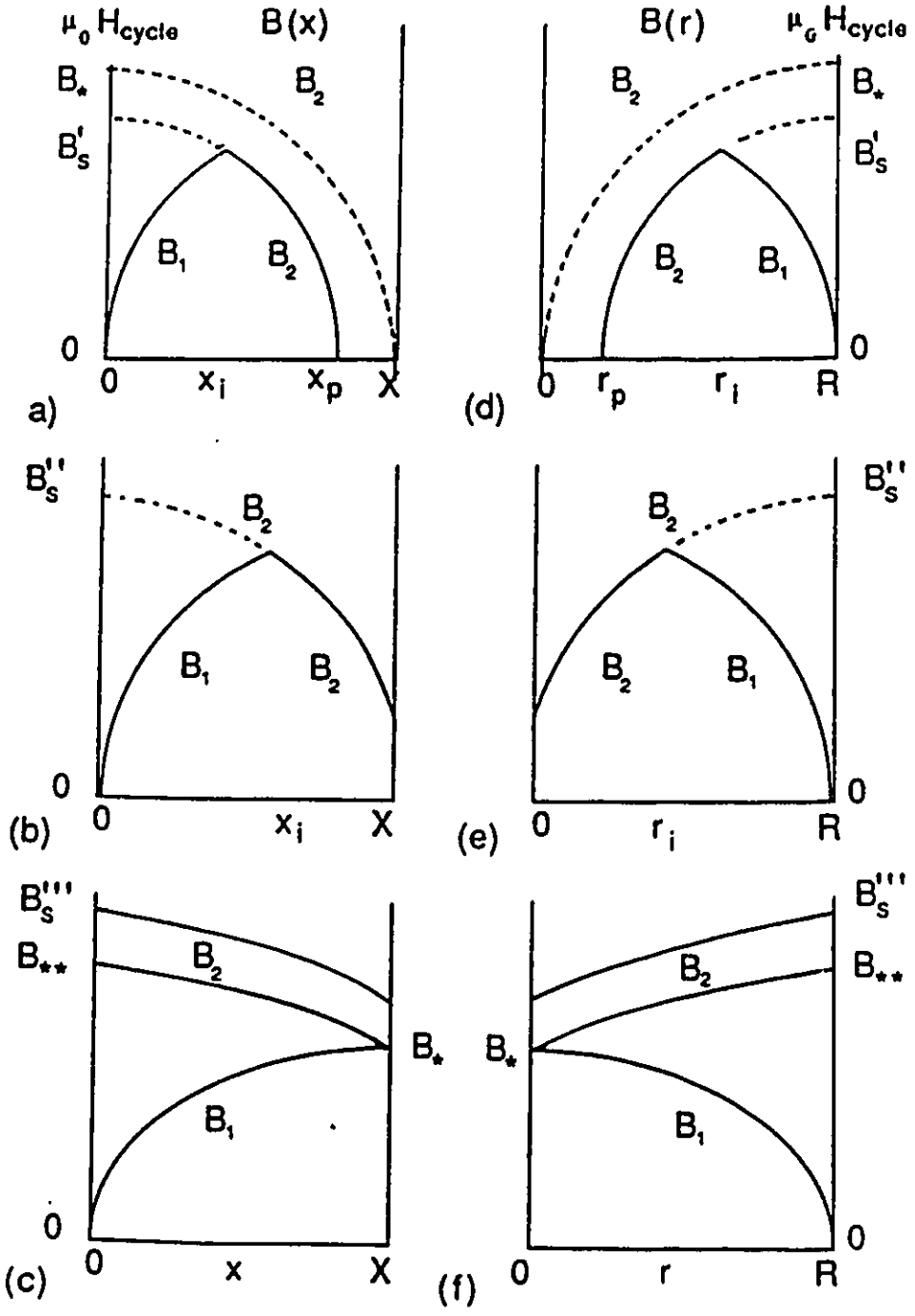

Figure 1: Sketches of the B profiles in the H_{cycle} procedure

BEAN APPROXIMATION

Integration of eqn 1 applied to the B_2 profile leads to

$$B_2(x) = B_s - B_\star \frac{x}{X} \tag{27}$$

$$B_2(r) = B_s - B_\star (1 - \frac{r}{R}) \tag{28}$$

where $B_\star = \mu_o \alpha_B X = \mu_o \alpha_B R$.

Letting $x = x_p$ and $r = r_p$ denote the boundary where $B_2 = 0$ in eqns 27 and 28 we obtain,

$$\frac{x_p}{X} = \frac{B_s}{B_\star} \qquad \frac{r_p}{R} = 1 - \frac{B_s}{B_\star} \tag{29}$$

Integration of eqn 1 applied to the B_1 profile leads to,

$$B_1(x) = B_\star \frac{x}{X} \tag{30}$$

and

$$B_1(r) = B_\star (1 - \frac{r}{R}) \tag{31}$$

Letting $x = x_i$ and $r = r_i$ denote the intersection of the B_1 and B_2 profiles, hence the surface where $B_1 = B_2$ leads to,

$$\frac{x_i}{X} = \frac{1}{2}\frac{B_s}{B_\star} \quad , \quad \frac{r_i}{R} = 1 - \frac{1}{2}\frac{B_s}{B_\star} \tag{32}$$

The magnetic flux remaining in the specimen after an excursion of B_s corresponds to that contained "under" the B_1 plus B_2 profiles and can be written,

$$\phi_{slab} = 2Y \left\{ \int_0^{x_i} B_1 \, dx + \int_{x_i}^{x_p \le X} B_2 \, dx \right\} \tag{33}$$

$$\phi_{cyl} = 2\pi \left\{ \int_{0 \le r_p}^{r_i} B_2 \, r \, dr + \int_{r_i}^{R} B_1 \, r \, dr \right\} \tag{34}$$

Introducing the expressions for B_1 and B_2 and the appropriate limits of integration into eqns 33 and 34, leads to,

$$\phi^A_{slab} = \frac{X\,Y\,B_\star}{2}\left(\frac{B_s}{B_\star}\right)^2 = \frac{X\,Y\,B_\star}{2}\,u^2 \tag{35}$$

$$\phi^A_{cyl} = \frac{\pi\,R^2\,B_\star}{3}\left[\frac{3}{2}u^2\,(1 - \frac{u}{2})\right] \tag{36}$$

which apply until the magnetic flux penetration front reaches the center of the specimen, hence when $0 < B_s \leq B_\star$ (or $0 < u \leq 1$ where $u = B_s / B_\star$).

For the range, $B_\star \leq B_s \leq B_{\star\star}$ where $x_p = X$ and $X/2 \leq x_i \leq X$ (or $r_p = 0$ and $0 \leq r_i \leq R/2$) the integration of equations 33 and 34 yields,

$$\phi^B_{slab} = X\,Y\,B_\star\left[2u - 1 - \frac{u^2}{2}\right] \tag{37}$$

$$\phi^B_{cyl} = \frac{\pi\,R^2\,B_\star}{3}\left[1 - 2\left(1 - \frac{u}{2}\right)^3\right] \tag{38}$$

which apply when, $1 \leq u \leq 2$ since in the Bean approximation (see Figs. 1 (c) and (f)),

$$B_{\star\star} = 2\,B_\star = 2\,\mu_o\,\alpha_B\,R \tag{39}$$

As required, eqns 37 and 38 lead to the same maximum trapped flux as generated by the H_{cool} procedure (see eqns 12 and 13).

KIM APPROXIMATION

Integration of eqn 16 applied to the B_1 profile leads to,

$$B_2(x) = \left[B_s^2 - B_\star^2\,\frac{x}{X}\right]^{\frac{1}{2}} \tag{40}$$

$$B_2(r) = \left[B_s^2 - B_\star^2\left(1 - \frac{r}{R}\right)\right]^{\frac{1}{2}} \tag{41}$$

where

$$B_\star = \sqrt{2\,\mu_o\,\alpha_K\,X} = \sqrt{2\,\mu_o\alpha_K\,R} \tag{42}$$

Denoting the boundary where $B_2 = 0$ by $x = x_p$ and $r = r_p$, these expressions lead to,

$$\frac{x_p}{X} = \left(\frac{B_s}{B_\star}\right)^2 \quad , \quad \frac{r_p}{R} = 1 - \left(\frac{B_s}{B_\star}\right)^2 \tag{43}$$

Integration of equation 16 applied to the B_1 profile leads to,

$$B_1(x) = B_\star\sqrt{\frac{x}{X}} \tag{44}$$

$$B_1(r) = B_\star\sqrt{1 - \frac{r}{R}} \tag{45}$$

Letting $x = x_i$ and $r = r_i$, denote the intersection of the B_1 and B_2 profiles, hence the surface where $B_1 = B_2$ leads to,

$$\frac{x_i}{X} = \frac{1}{2}\left(\frac{B_s}{B_\star}\right)^2 \quad , \quad \frac{r_i}{R} = 1 - \frac{1}{2}\left(\frac{B_s}{B_\star}\right)^2 \tag{46}$$

Introducing the appropriate expressions for B_1 and B_2 and the corresponding limits of integration into the expressions for the magnetic flux (eqns 33 and 34) and integrating yields,

$$\phi^A_{slab} = \frac{2\sqrt{2}}{3}\,X\,Y\,B_\star\left(\frac{B_s}{B_\star}\right)^3 = \frac{2\sqrt{2}}{3}\,X\,Y\,B_\star\,u^3 \tag{47}$$

$$\phi^A_{cyl} = \frac{\sqrt{2}}{3}\,\pi\,R^2\,B_\star\left[2\left(\frac{B_s}{B_\star}\right)^3 - \left(\frac{B_s}{B_\star}\right)^5\right] = \frac{\sqrt{2}}{3}\,\pi\,R^2\,B_\star\left[2\,u^3 - u^5\right] \tag{48}$$

Eqns 47 and 48 are applicable until the front of the B profile reaches the center of the specimen, hence for the range $0 \le u \le 1$.

When the interface between the B_1 and B_2 profiles lies closer to the center of the specimen than to the surface as depicted in Figs. 1 (c) through (f), eqns 47 and 48 are replaced by,

$$\phi^B_{slab} = \frac{2\sqrt{2}}{3}\,X\,Y\,B_\star\left[u^3 - \sqrt{2}\left(u^2 - 1\right)^{\frac{3}{2}}\right] \tag{49}$$

$$\phi^{B}_{cyl} = \frac{\sqrt{2}}{3}\,\pi\,R^2\,B_\star\left[2u^3 - u^5 + \frac{4\sqrt{2}}{5}\left(u^2 - 1\right)^{\frac{5}{2}}\right] \qquad (50)$$

which apply over the range $B_\star \leq B_s \leq B_{\star\star}$, hence, $1 \leq u \leq \sqrt{2}$ since,

$$B_{\star\star} = \sqrt{2}\,B_\star = 2\sqrt{\mu_o\,\alpha_K\,X} = 2\sqrt{\mu_o\,\alpha_K\,R} \qquad (51)$$

Equation 51 is obtained by allowing the B profile to start from 0 and grow without any discontinuity over a range $x = 2X$ or $r = 2R$ (see Figs. 1 (c) and (f)).

As required eqns 49 and 50 yield the same maximum trapped flux as generated by the H_{cool} procedure (see eqns 23 and 24). It is sometimes convenient to normalize the trapped flux to the corresponding maximum values.

B.3 Rectangular Geometry and Limiting Cases

We tabulate expressions for the residual flux trapped by the H_{cool} and H_{cycle} procedures in a rectangular specimen of infinite length along the z axis. We focus on the Bean and Kim approximations and show that each case the resulting formulae reduce to the corresponding one tabulated above when we let the rectangle transform to an infinite slab or become a square. In the latter case, we see that the results are identical to that of the infinite cylinder except that a factor of 4 needs to be replaced by π.

The rectangular sample has a cross section with,

$$\text{Thickness} \qquad 2X = 2a \qquad\qquad \text{Width} \qquad Y = 2b \qquad (52)$$

By symmetry we can focus on one quarter of the cross section. It is convenient to consider the quarter located between $0 \leq x \leq a$ and $0 \leq y \leq b$.

The appropriate element of area dA, threaded by a uniform magnetic flux density $B(x)$, is shaped like the letter L (rotated 180°) as depicted in the accompanying sketch.

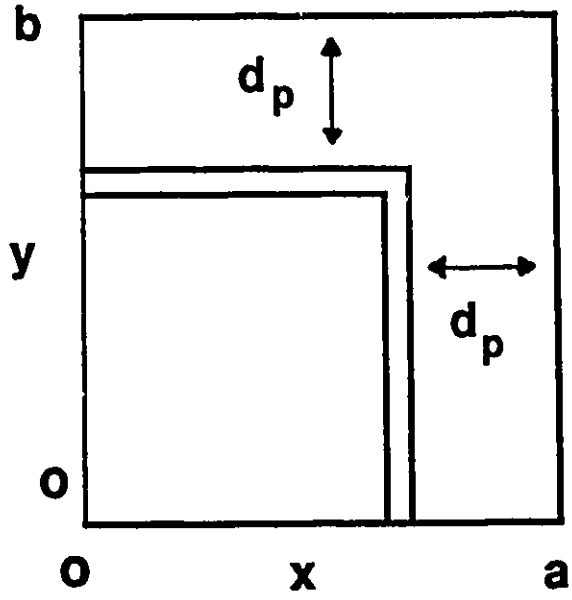

The vertical side of the infinitesimal area dA, can be written,

$$dA_v = y\,dx = (b - d_p)\,dx = [\,b - (a - x)\,]\,dx \tag{53}$$

The horizontal side reads,

$$dA_h = x\,dx \tag{54}$$

We stress that the appropriate element of thickness of the element of area dA_h is dx (and not dy nor $(b/a)\,dx$). The reason for this, as shown in appendix A, is that the depth of penetration and variation of the B profiles is uniform.

Combining 53 and 54 gives

$$dA_l = [\,(b - a) + 2x\,]\,dx \tag{55}$$

The appropriate expressions for the B profiles are listed above for cylindrical geometry where we replace the variable r/R by x/a.

We now tabulate the results of the integrations.

H_{cool} Procedure.

$$\phi^{cool}_{rect,Bean} = 4\,a\,b\,B_\star \left[u - \frac{1}{2}\left(1 + \frac{a}{b}\right) u^2 + \frac{a\,u^3}{3\,b} \right] \tag{56}$$

which simplifies to,

$$\phi^{cool}_{slab,Bean} = 2\,a\,Y\,B_\star \left[u - \frac{u^2}{2} \right] \tag{57}$$

for a segment of width $Y = 2\,b$ of an infinite slab ($a/b = 0$ when $b \rightarrow \infty$ in the parentheses)

For a square sample, $a/b = 1$, and eqn 56 reduces to,

$$\phi^{cool}_{square,Bean} = 4\,a^2\,B_\star \left[u - u^2 + \frac{u^3}{3} \right] \tag{58}$$

$$\phi^{cool}_{rect,Kim} = 4\,a\,b\,B_\star \left[u - \frac{1}{3}\left(1 + \frac{a}{b}\right) u^3 + \frac{a\,u^5}{5\,b} \right] \tag{59}$$

When $a/b = 0$ (infinite slab limit) this reduces to,

$$\phi^{cool}_{slab,Kim} = 2\,a\,Y\,B_\star \left[u - \frac{u^3}{3} \right] \tag{60}$$

When $a/b = 1$ (square limit), this reduces to,

$$\phi^{cool}_{square,Kim} = 4\,a^2\,B_\star \left[u - \frac{2}{3}u^3 + \frac{u^5}{5} \right] \tag{61}$$

H_{cycle} Procedure

In each case we encounter two ranges of the variable, $B_s/B_\star$ as indicated earlier in this appendix.

We tabulate all of the expressions as well as the limiting cases of the infinite slab ($a/b = 0$) and square ($a/b = 1$). The latter, apart from a change in coefficient from 4 to π, corresponds to the cylindrical geometry.

$$\phi^{cycleA}_{rect,Bean} = a\,b\,B_\star \left[u^2 + \frac{a}{b}\left(u^2 - u^3 \right) \right] \tag{62}$$

with infinite slab limit ($a/b = 0$)

$$\phi^{cycleA}_{slab,Bean} = a\,b\,B_\star\,u^2 \tag{63}$$

and square limit ($a/b = 1$)

$$\phi^{cycleA}_{square,Bean} = 4\,a^2\,B_\star \left[\frac{u^2}{2} - \frac{u^3}{4} \right] \tag{64}$$

$$\phi^{cycleB}_{rect,Bean} = 4\,a\,b\,B_\star \left[-\frac{1}{2} + u - \frac{u^2}{4} + \frac{a}{b}\left(\frac{1}{6} - \frac{u^2}{4} - \frac{u^3}{12} \right) \right] \tag{65}$$

with infinite slab limit ($a/b = 0$)

$$\phi^{cycleB}_{slab,Bean} = 2\,a\,b\,B_\star \left[2u - 1 - \frac{u^2}{2} \right] \tag{66}$$

and square limit ($a/b = 1$)

$$\phi^{cycleB}_{square,Bean} = \frac{4\,a^2\,B_\star}{3} \left[-1 + 3u - \frac{3\,u^2}{2} + \frac{u^3}{4} \right] \tag{67}$$

$$\phi^{cycleA}_{rect,Kim} = \frac{4\sqrt{2}}{3}\,a\,b\,B_\star \left[u^3 + \frac{a}{b}\left(u^3 - u^5 \right) \right] \tag{68}$$

with infinite slab limit ($a/b = 0$)

$$\phi^{cycleA}_{slab,Kim} = \frac{4\sqrt{2}}{3}\,a\,b\,B_\star\,u^3 \tag{69}$$

and square limit ($a/b = 1$)

$$\phi^{cycleA}_{square,Kim} = \frac{4\sqrt{2}}{3}\,a^2\,B_\star \left[2u^3 - u^5 \right] \tag{70}$$

$$\phi^{cycleB}_{rect,Kim} = \frac{4\sqrt{2}}{3} a\, b\, B_\star \left[u^3 - \sqrt{2}\left(u^2-1\right)^{\frac{3}{2}} + \frac{a}{b}\left(u^3 - u^5\right)\right] + \frac{4\sqrt{2}}{3} a\, b\, B_\star \left[\frac{\sqrt{2}a}{5b}\left[1+4u^2\right]\left(u^2-1\right)^{\frac{3}{2}}\right] \tag{71}$$

with infinite slab limit ($a/b = 0$)

$$\phi^{cycleB}_{slab,Kim} = \frac{4\sqrt{2}}{3}\, a\, b\, B_\star \left[u^3 - \sqrt{2}\left(u^2-1\right)^{\frac{3}{2}}\right] \tag{72}$$

and square limit ($a/b = 1$)

$$\phi^{cycleB}_{square,Kim} = \frac{4\sqrt{2}}{3}\, a^2\, B_\star \left[2u^3 - u^5 + \frac{4\sqrt{2}}{5}\left(u^2-1\right)^{\frac{5}{2}}\right] \tag{73}$$

SUMMARY

A variety of magnetic phenomena known to occur in classical type II superconductors have been investigated in sintered high T_c ceramic superconductors. In every case we compare the behaviour observed in the high T_c specimens with that encountered in both weak and strong pinning (i.e. semi-reversible and hysteretic) conventional materials.

The elemental interactions of quantized flux lines and the basic physical picture accounting for the macroscopic magnetic behaviour of type II superconductors are outlined and reviewed in the introductory chapter.

The magnetic responses of the four specimens selected for study ($YBa_2Cu_3O_{7-x}$, $NdBa_2Cu_3O_{7-x}$, $Pb_{0.46}In_{0.54}$ and $V_{0.24}Ti_{0.76}$) to the application and cycling of an external magnetic field H_a are extensively documented and compared qualitatively. A hump structure encountered in the initial magnetization curve of the high T_c materials is examined and its role in the calibration is evaluated. We have also monitored the Meissner effect (flux expulsion) which takes place when the samples cool from T_c to ambient in various static H_a.

The Meissner effect (expulsion of magnetic flux during cooling) in ribbon samples of conventional semi-reversible type II superconductors can show a dramatic geometric anisotropy and can be appreciably enhanced when $\vec{H}_a$ is tilted to pierce

the broad faces of the "slab". The rectangular sintered high T_c ceramic samples exhibited no such anisotropic effect.

Hysteresis losses in classical hysteretic type II superconductors subjected to a low frequency alternating magnetic field of fixed amplitude $h_o \lesssim H_\star$ are seen to traverse a minimum as a bias magnetic field H_b directed parallel to h_o is impressed. We searched for but did not find this feature, called the Clem valley, in the sintered high T_c ($YBa_2Cu_3O_{7-x}$) sample. We speculate on the reasons for its absence.

Flux can conveniently be trapped in type II superconductors by, (i) cooling from T_c in a magnetic field which is then removed (H_{cool} procedure) and, (ii) subjecting the specimen, already in the superconducting state, to an excursion of a magnetic field (H_{cycle} procedure). The growth in the amount of flux trapped as a function of H_{cool} and H_{cycle} provides useful information on the dependence of the depinning critical current density $j_{c\perp}$ on the magnetic flux density B. We compare our observations of the evolution of the trapped flux vs. H_{cool} and H_{cycle} in the $YBa_2Cu_3O_{7-x}$ sample with critical state predictions for two extreme geometries (infinite slab and cylinder) in the Bean and Kim limits for $j_{c\perp}$ vs. B. We stress that the threshold magnetic fields H^*_{cool} and H^*_{cycle} required to trap a saturation amount of flux also provide data on the bulk critical current I_b and a check on the calibration of the magnetization.

The sums and the differences of the magnetic moments of type II superconductors observed in an increasing and in a decreasing magnetic field H_a provide data on I_b and the Meissner current I_M and their dependence on H_a, provided that the calibration of the magnetization is appropriate and reliable. We stress that ΔH_c, the sweep of H_a required to cause the magnetization of a specimen to traverse from the upper to the lower branches (or vice versa) of the major hysteresis loop also

provides data on I_b which is independent of the calibration of the magnetization. Thus, ΔH_c can also provide a check on the calibration.

The magnetic responses of the four materials are also investigated and compared in the flux line cutting regime where the persistent circulating currents are made to flow with a component of the current density locally parallel to the magnetic flux density. These configurations were established by directing a varying magnetic field $H_\perp$ orthogonal to a static bias magnetic field $H_\parallel$ (or vice versa) where both are oriented along the broad surfaces of the rectangular specimens. We also examine the effect of the bias field on the capacity of the specimens to oppose flux entry and flux exit. We find that the behaviour of the three semi-reversible materials (the two high T_c samples and the $PbIn$) is usually the opposite of that exhibited by the hysteretic VTi. We attribute these differences in behaviour to changes in the ratio of the flux line cutting critical current density $j_{c\parallel}$ to the flux line depinning critical current density $j_{c\perp}$.

In appendix A we show that the configurations of the persistent critical current density $j_{c\perp}$ and the magnetic flux density $\vec{B}$ in a rectangular slab of infinite length in a uniform H_a directed along the length reduce to a one dimensional problem.

In appendix B we develop closed form expressions for the configurations of the trapped flux versus H_{cool} and H_{cycle} for the rectangular geometry and show that these correspond to the formulae obtained in the limiting cases of the circular cylinder and the infinite slab.

Bibliography

[1] **A.A. Abrikosov,** *J Phys Chem Solids* (1957) **2** 199-208 ; *Soviet Phys J.E.T.P.* (1957) **5** 1174-1182

[2] **C.P. Bean,** *Phys Rev Letters* (1962) **8** 250 ; *Rev Mod Phys* (1964) **36** 31

[3] **C.P. Bean and J.D. Livingston,** *Phys Rev Lett* **12**, 14 (1964)

[4] **J.G. Bednorz and K.A. Muller,** *Z Phys* (1986) **B 64** 189

[5] **M.G. Blamire and J.E. Evetts,** *Phys Rev B* (1986) **33** 5131-5133

[6] **M.G. Blamire and J.E. Evetts,** *Appl Phys Lett* (1985) **46** 1181-1183

[7] **R. Boyer, G. Fillion and M.A.R. LeBlanc,** *J Appl Phys* (1980) **51** 1692-1701

[8] **E.H. Brandt,** *J Low Temp Phys* (1981) **44** 33-57

[9] **E.H. Brandt,** *J Low Temp Phys* (1981) **44** 59-72

[10] **E.H. Brandt,** *J Low Temp Phys* (1981) **42** 557-584

[11] **E.H. Brandt,** *J Low Temp Phys* (1980) **39** 41-61

[12] **E.H. Brandt, J.R. Clem and D.G. Walmsley,** *J Low Temp Phys* (1979) **37** 43-54

[13] **J.F. Bussiere,** *Phys Lett* 58A, 343-346 (1976)

[14] **J.F. Bussiere, M. Garber and S. Shen,** *Appl Phys Lett* **25**, 756-758 (1974)

[15] **A.M. Campbell and J.E. Evetts,** *Adv Phys* (1972) **21** 199

[16] **J.R. Cave and J.E. Evetts,** *Phil Mag B* (1978) **37** 111

[17] **J.R. Cave, J.E. Evetts and A.M. Campbell,** *J Phys* (1978) **39** C6 614-616

[18] **J.R. Cave and M.A.R. LeBlanc,** *J Appl Phys* (1982) **53** 1631-1648

[19] **C.T.M. Chang and M.A.R. LeBlanc,** *Appl Phys Letters* (1967) **10** 344-347

[20] **J.R. Clem and A. Perez-Gonzalez,** *in Proc. Int. Symp. on Flux Pinning and Electromagnetic Properties in Superconductors* Eds Matsushita, T., Yamafuji, K. and Irie, F. Matsukuma Press, Fukuoka, Japan (1985) 196-200

[21] **J.R. Clem and A. Perez-Gonzalez,** *Phys Rev B* (1986) **33** 1601-1610

[22] **J.R. Clem and A. Perez-Gonzalez,** *Phys Rev B* (1984) **30** 5041-5047

[23] **J.R. Clem,** *Phys Rev B* (1982) **26** 2463-2473

[24] **J.R. Clem and S. Yeh,** *J Low Temp Phys* (1980) **39** 173-189

[25] **J.R. Clem,** *J Low Temp Phys* (1980) **38** 353-370

[26] **J.R. Clem,** *J Appl Phys* (1979) **50** 3518-3530

[27] **J.R. Clem,** *Low Temperature Physics - LT B* **Vol. 3** p.102
eds Timmerhaus, O'Sullivan & Hammel (Phenum Pub, New York 1974)

[28] **W.A. Fietz, M.R. Beasley, J. Silcox and W.W. Webb,** *Phys Rev* (1964) **136A** 335-345

[29] **G. Gandolfini, M.A.R. LeBlanc and J. Sekerka,** *Cryogenics* (1989) **29**

[30] **P.G. de Gennes,** *Sol St Comm* **3**, 127 (1965)

[31] **C.Y. Huang, Y. Shapira, E.J. McNiff, P.N. Peters, B.B. Schwartz, M.K. Wu, R.D. Shull and C.K. Chiang,** *Modern Phy Letters B* (1988) **2** 869-874

[32] **Y.B. Kim, C.F Hempstead and A.R. Strnad,** *Phys Rev* (1963) **129** 528

[33] **A. Lachaine and M.A.R. LeBlanc,** *IEEE Trans Magn* (1975) MAG11 336-339

[34] **A. Lachaine,** *Thesis, University of Ottawa, Canada* (1979)

[35] **M.A.R. LeBlanc and J.P. Lorrain,** *J Appl Phys* (1984) **55** 4035-4051

[36] **M.A.R. LeBlanc, W.F Druyvesteyn and C.T.M. Chang,** *Appl Phys Letters* (1965) **6** 189-191

[37] **M.A.R. LeBlanc and C.T.M. Chang,** *Solid State Commun* (1968) **6** 679-683

[38] **M.A.R. LeBlanc,** *Phys Letters* (1964) **10** 260-261

[39] **M.A.R. LeBlanc and J.P. Lorrain,** *Cryogenics* (1984) **24** 143-155

[40] **M.A.R. LeBlanc, G. Fillion and J.P. Lorrain,** *J Appl Phys* (1986) **59** 3208-3223

[41] **M.A.R. LeBlanc, G. Fillion, W.E. Timms, A. Zahradnitsky and J.R. Cave,** *Cryogenics* (1981) **21** 491-500

[42] **M.A.R. LeBlanc and H.G. Mattes,** *J. de Physique* **39** C6 - 654-656 (1978)

[43] **M.A.R. LeBlanc, D.J. Griffiths and B.C. Belanger,** *Phys Rev Lett* **18**, 844-848 (1967)

[44] **H. London,** *Phys letters* (1963) **6** 162

[45] **J.P. Lorrain, M.A.R LeBlanc and A. Lachaine,** *Can J Phys* (1979) **57** 1458-1477

[46] **J.P. Lorrain,** *Thesis, University of Ottawa, Canada* (1983)

[47] **T. Matsushita,** *Phys Rev B* (1988) **38** 820-824

[48] **T. Matsushita, T. Honda, Y. Hasegawa and Y. Monju,** *J Appl Phys* **54**, 6526 (1983)

[49] **W. Meissner and R. Ochsenfeld,** *Naturwissenschaften* (1933) **21** 787

[50] **J.F. Nicholson and P.T. Sikora,** *J Low Temp Phys* (1974) **17** 275

[51] **H.K. Onnes,** *Commun Phys Lab Univ Leiden* (1911) **120b** 3

[52] **A. Perez-Gonzalez and J.R. Clem,** *J Appl Phys* (1985) **58** 4326-4335

[53] **A. Perez-Gonzalez and J.R. Clem,** *Phys Rev B* (1985) **32** 2909-2914

[54] **A. Perez-Gonzalez and J.R. Clem,** *Phys Rev B* (1985) **31** 7048-7058

[55] **H. Riemersma,** *J Appl Phys* (1964) **35** 1802

[56] **D.G. Schweitzer and B. Bertman,** *Phys Rev* **152**, 293-299 (1966)

[57] **D.G. Schweitzer and A.D. McInturff,** *Sol St Comm* **6**, 885-887 (1968)

[58] **D.G. Schweitzer and M. Garber,** *Phys Rev* **160**, 348-358 (1967)

[59] **D.G. Schweitzer,** *Phys Lett* **24A**, 718-719 (1967)

[60] **D.G. Schweitzer, M. Garber and B. Bertman,** *Phys Rev* **159**, 296-300 (1967)

[61] **J. Sekerka,** *M. Se. thesis, University of Ottawa, Canada* (1989)

[62] **F.F. Ternowskii and L.N. Shekhata,** *Soviet Phys* JETP **35**, 1202 (1972)

[63] **J.D. Thompson, M.P. Maley and J.R. Clem,** *J Appl Phys* **50**, 3530 (1979)

[64] **W.E. Timms and D.G. Walmsley,** *J Phys F: Metal Phys* (1976) **6** 2107-2118

[65] **W.E. Timms and M.A.R. LeBlanc,** *J Phys F: Metal Phys* (1974) **4** 136-153

[66] **H.A. Ullmaier and W.F. Gauster,** *J Appl Phys* **37**, 4519 (1966)

[67] **D.G. Walmsley,** *J Phys F: Metal Phys* (1972) **2** 510-528

[68] **D.G. Walmsley,** *J Phys F: Metal Phys* (1972) **2** 529-546

[69] **M.K. Wu, J.R. Ashburn, C.J. Torng, P.H. Hor, R.L. Meng, L. Gao, Z.J. Huang, Y.Q. Wang and C.W. Chu,** *Phys Rev Letters* (1987) **58** 908